Thèse n° 10 244

Tailor-made Piezoelectric Elastomer Materials

Présentée le 17 mars 2023

Faculté des sciences et techniques de l'ingénieur
SMX - Enseignement
Programme doctoral en chimie et génie chimique

pour l'obtention du grade de Docteur ès Sciences

par

Francis OWUSU

Acceptée sur proposition du jury

Prof. A. Züttel, président du jury
Prof. F. Nüesch, Dr D. M. Opris, directeurs de thèse
Prof. R. Gerhard, rapporteur
Prof. A. Kilbinger, rapporteur
Prof. D. Damjanovic, rapporteur

École
polytechnique
fédérale
de Lausanne

2023

Deeds never die, until forgotten!

Thank you for the selfless love

to my parents, in loving memory

" Dua kontonkyikuronkyi na ɛma yehunu odwumfo pa,
Nyansapɔ, wɔsane no badwemma "

Acknowledgements

I would like to express my sincerest gratitude, foremost, to my thesis advisors Dr. Dorina M. Opris and Prof. Dr. Frank A. Nüesch for their invaluable advice, continuous support, and patience during my study. The immense knowledge and experience shared in every discussion served as a motivation to sail me through my academic research journey.

My gratitude extends to the entire team of Functional Polymer Laboratory for the enormous assistance throughout this pursuit. Most especially, Beatrice Fischer for the constant help in thermal and GPC characterizations, Dr. Daniel Rentsch for his support with NMR spectroscopy, Cristian Walder for his extensive knowledge of instruments and equipment, and Isabella Gartman for the administrative assistance. Additionally, a special thank you goes to the wonderful colleagues, in the persons of Patrick, Johannes, Cansu, Yerlan, Martin, Jana, Dnyaneshwar, Wei-Hsu, Mohammed, Yauhen, Yulia, Anand, Sonja, Sina, Matthias, Karen, Elena, Mihail, Thulasinath, Michael, John, René, Jakob, and Roland, for the emotional support and of course relevant technical and scientific discussions.

During these years, I got assistance from many people, and I would need another 100 pages to write everything. Particularly, Prof. Martin Negri for the collaborative works and the timely suggestions and discussions, Dr. Martin Tress for sharing his extensive knowledge on the topic of dielectric spectroscopy, and Dr. Frank Clemens for his valuable scientific discussions.

Furthermore, I gratefully acknowledge the Swiss National Science Foundation, the European Research Council, and the Swiss Federal Laboratories of Materials Science and Technology (Empa) for providing financial support and the infrastructure throughout my research period.

Lastly, a heartfelt appreciation goes to my family and friends. Without their tremendous understanding and encouragement over the past few years, it would be impossible for me to complete my studies.

Dübendorf, February 23, 2023

F. O.

Abstract

Recent advancements in miniature devices with higher computational capabilities and ultralow power consumption have accelerated the development of wearable sensors, actuators, and energy harvesters everywhere. The ultimate aim of such a technological revolution is to create an ecosystem of connected devices and transform physical objects into information sources. To achieve this, flexible materials with the versatility to be designed into complex architectures will be of relevance. Among the different energy transducing technologies, piezoelectricity has been earmarked as one of the leading routes due to its simple conversion mechanism, relatively high power density, and easy integration into various systems. However, conventional piezoelectric materials are limited in many applications due to their rigidity, high density, lack of machinability, inability to conform to delicate parts of systems and arbitrary interfaces. For this reason, there is an appreciable demand for developing new materials, which can sustain large mechanical deformation while retaining superb characteristics in their performance.

This thesis systematically presents processing steps for preparing highly elastic piezoelectric materials solely from organic constituents. The approach combines selected organic reactions available in the synthesis toolbox and composite preparation technique. Novel polar amorphous polymers bearing different dipole moieties were synthesized, processed into nano-particles, and embedded as fillers in a polydimethylsiloxane (PDMS) matrix.

To this end, we employed the power and versatility of ring-opening metathesis polymerization (ROMP) to synthesize polar amorphous polymers with high dielectric relaxation strength and glass transition temperature (T_g) significantly above room temperature. The collection of novel polymers was thoroughly characterized by NMR spectroscopy, gel permeation chromatography (GPC), thermogravimetric analysis (TGA), and differential scanning calorimetry (DSC). The dielectric behaviors were further investigated by broadband dielectric spectroscopy (BDS), and thermally stimulated depolarization current (TSDC) techniques. Structure-property relationships were established to evaluate the optimal material with promising properties to be used as a filler in the composite preparation.

The polar amorphous polymer with optimal characteristics is then processed into particulate forms by the nanoprecipitation method. Sub-micrometer particles with sizes ranging from 90 nm to 2 µm could be obtained. Elastomeric composites were then prepared by impregnating different weight fractions of the filler particles into PDMS matrix. Following the successful processing of the blends into chemically cross-linked thin films, piezoelectric activity was induced by electric poling. The piezoelectric properties of the prepared elastic composites showed strong dependence on the filler

weight fraction, particle size, stereo-regular configuration of the polar polymer particles, and the poling technique employed. A quasi-stable transverse piezoelectric coefficient (d_{31}) of 37 pC N^{-1} could be recorded for the best-performing material poled by corona discharge. In addition, these piezoelectric materials could withstand large mechanical deformations (maximum strain at break up to 400%) as a peculiar advantage compared to the prevailable piezoelectric polymer and ceramic materials.

Keywords: Polar amorphous polymers, Ring-opening metathesis polymerization (ROMP), PDMS matrix, composite film processing, corona poling, elastic electrets, molecular dipoles, piezoelectric elastomers, piezoelectric polymers, transverse piezoelectric charge coefficient

Zusammenfassung

Jüngste Fortschritte bei der Miniaturisierung von Bauteilen mit höherer Rechenleistung und ultraniedrigem Stromverbrauch haben die Entwicklung von tragbaren Sensoren, Aktoren und Geräte für die Energiegewinnung überall beschleunigt. Das ultimative Ziel einer solchen technologischen Revolution ist die Schaffung eines Ökosystems vernetzter Geräte und die Umwandlung physischer Gegenstände in Informationsquellen. Um dies zu erreichen, sind flexible Materialien, welche sich in komplexe Strukturen einfügen lassen, von großer Bedeutung. Unter den verschiedenen Energieumwandlungstechnologien hat sich die Piezoelektrik aufgrund ihres einfachen Umwandlungsmechanismus, ihrer relativ hohen Leistungsdichte und ihrer einfachen Integration in verschiedene Systeme als einer der führenden Richtungen herauskristallisiert. Aufgrund ihrer Steifigkeit, hohen Dichte, eingeschränkten Prozessierbarkeit, Untauglichkeit für die Anpassung an empfindliche Systemteile und willkürlichen Zwischenflächen sind herkömmliche piezoelektrisch Materialien in vielen Anwendungen begrentzt. Aus diesem Grund besteht ein erheblicher Bedarf an der Entwicklung neuer Materialien, die großen mechanischen Verformungen standhalten können und gleichzeitig hervorragende Leistungswerte aufweisen.

Diese Dissertationsarbeit befasst sich mit systematischen Prozessschritten zur Herstellung hochelastischer piezoelektrischer Materialien, welche ausschließlich aus organischen Bestandteilen bestehen. Der Ansatz führt ausgewählte organische Reaktionen, die in der Synthese-Toolbox verfügbar sind, mit der Technik der Kompositpräparation zusammen. Somit wurden neuartige polare amorphe Polymere mit unterschiedlichen Dipolanteilen synthetisiert, zu Nanopartikeln verarbeitet und als Füllstoffe in eine Polydimethylsiloxan (PDMS) Matrix eingebettet.

Zu diesem Zweck nutzten wir die Leistungsfähigkeit und Vielseitigkeit der ringöffnenden Metathesepolymerisation (ROMP), um polare amorphe Polymere mit hoher dielektrischer Relaxationsstärke und einer deutlich über Raumtemperatur liegenden Glasübergangstemperatur (T_g) zu synthetisieren. Die Anzahl neuartiger Polymere wurde durch NMR-Spektroskopie, Gelpermeationschromatographie (GPC), thermogravimetrische Analyse (TGA) und Differentialscanningkalorimetrie (DSC) eingehend charakterisiert. Weiter wurde das dielektrische Verhalten mittels breitbandiger dielektrischer Spektroskopie (BDS) und thermisch stimuliertem Depolarisationsstrom (TSDC) untersucht. Die gewonnene Struktur-Eigenschafts-Beziehungen erlaubten, das optimale Material mit vielversprechenden Eigenschaften für die Verwendung als Füllstoff bei der Herstellung von Kompositen zu ermitteln.

Das polare amorphe Polymer mit den optimalen Eigenschaften wurde dann mit der Methode der Nanopräzipitation in Partikelform verarbeitet. Submikrometerpartikel mit Teilchengrössen von 90 nm

bis 2 µm konnten erhalten werden. Anschließend wurden elastomere Verbundwerkstoffe hergestellt, indem verschiedene Gewichtsanteile der Füllstoffpartikel in die PDMS-Matrix dispergiert wurden.

Nach der erfolgreichen Verarbeitung der Mischungen zu chemisch vernetzten dünnen Filmen wurde die piezoelektrische Aktivität durch elektrische Polung induziert. Die piezoelektrischen Eigenschaften der hergestellten elastischen Verbundwerkstoffe zeigten eine starke Abhängigkeit vom Gewichtsanteil des Füllstoffs, der Teilchengröße, der stereoregulären Konfiguration der polaren Polymerteilchen und der angewandten Polungstechnik. Ein quasistabiler transversaler piezoelektrischer Koeffizient (d_{31}) von 37 pC N^{-1} konnte für das leistungsstärkste Material, das durch Koronaentladung gepolt wurde, ermittelt werden. Darüber hinaus konnten diese piezoelektrischen Materialien großen mechanischen Verformungen standhalten (maximale Bruchdehnung bis zu 400 %), was ein besonderer Vorteil gegenüber den bisher verfügbaren piezoelektrischen Polymer- und Keramikmaterialien ist.

Schlüsselwörter: Polare amorphe Polymere, ringöffnende Metathesepolymerisation (ROMP), PDMS-Matrix, Verbundfilmverarbeitung, Corona-Poling, elastische Elektrete, molekulare Dipole, piezoelektrische Elastomere, piezoelektrische Polymere, transversaler piezoelektrischer Ladungskoeffizient

Contents

List of Figures

List of Schemes

List of Tables

List of Abbreviations

$\Delta\varepsilon$	Dielectric relaxation strength
ADP	Ammonium dihydrogen phosphate
$BaTiO_3$	Barium Titanate
BDS	Broadband dielectric spectroscopy
CAD	Computer-aided design
$CDCl_3$	Deuterated chloroform
CNT	Carbon nanotubes
COC	Cyclo-olefin copolymers
COP	Cyclo-olefin polymers
d_{31}	Transverse piezoelectric coefficient
d_{33}	Longitudinal piezoelectric coefficient
DCC	N,N'-dicyclohexylcarbodiimide
DCM	Dichloromethane
DE	Dielectric elastomers
DIW	Direct ink writing
DLP	Digital light processing
DMA	Dynamic mechanical analysis
DMSO	Dimethyl sulfoxide
DSC	Differential scanning calorimetry
E_b	Dieelectric breakdown field
EDC	2,6-Dimethyl-4*H*-pyran-4-one and 1-ethyl-3-(3-dimethylaminopropyl) carbodiimide
FDM	Fused deposition modeling

FEP	Fluorinated ethylene propylene
g_{31}	Transverse piezoelectric voltage coefficient
GPC	Gel permeation chromatography
HFIP	Hexafluoroisopropanol
HPLC	High-performance liquid chromatography
ICDs	Implantable cardioverter defibrillators
IEEE	Institute of Electrical and Electronics Engineers
IoT	Internet of Things
k_{31}	Electromechanical coupling coefficient
KNLN	Potassium Sodium Lithium Niobate
LC	Liquid crystalline
LCEs	Liquid crystalline elastomers
LC-MS	Liquid chromatography–Mass spectrometry
LEDs	Light-emitting diodes
$LiNbO_3$	Lithium Niobate
$LiTaO_3$	Lithium Tantalate
LSM	Lithium Sulfate Monohydrate
M_n	Number average molecular weight
MWCNTs	Multi-wall carbon nanotubes
NMR	Nuclear magnetic resonance
NPs	Nanoparticles
P(NaSS-*co*-AN)	Poly(sodium *p*-styrenesulphonate-*co*-acrylonitrile)
PµSL	Projection micro-stereolithography
PAN	Polyacrylonitrile
$PbTiO_3$	Lead(II) Titanate

PDI	Polydispersity indices
PDMS	Polydimethylsiloxane
PEG	Poly(ethylene glycol)
PEN	Poly(ethylene naphthalate)
PET	Poly(ethylene terephthalate)
PMN-PT	Lead Magnesium Niobate–Lead Titanate
PO	Polyolefins
PP	Polypropylene
PRX	Polyrotaxane
PTFE	Polytetrafluoroethylene
PU	Polyurethane
PVC	Polyvinyl chloride
PVDF	Polyvinylidene difluoride
PVVA	Poly(vinylidenecyanide vinyl acetate)
PZT	Lead Zirconate Titanate
ROMP	Ring-opening metathesis polymerization
$scCO_2$	Supercritical carbon dioxide
SEM	Scanning electron microscope
SLA	Stereolithography
T_d	Decomposition temperature
T_g	Glass-transition temperature
TGA	Thermogravimetric analysis
THF	Tetrahydrofuran
TSDC	Thermally stimulated depolarization current
UV	Ultraviolet

UV-vis	Ultraviolet-visible
ZnO	Zinc Oxide
α-CD	A-cyclodextrin
ε'	Real dielectric permittivity
ε''	Imaginary dielectric permittivity
ε_0	Dielectric permittivity of vacuum
ε_r	Relative dielectric permittivity

CHAPTER 1
Introduction

Extensive connectivity of the Internet of Things (IoT) is proliferating into almost 'everything' we interact with in our daily lives. This technological revolution aims to create an ecosystem of connected devices that can transform physical objects into information sources.[1-7] To sustain such a plethora of networked devices will require further considerations on vital enablers such as sensors, actuators, and energy harvesters. From the material scientists' perspective, this can only be realized by tailoring materials with compatible and excellent properties to fabricate devices for target applications. Specifically, devices such as pacemakers and implantable cardioverter defibrillators (ICDs) used by persons with life-threatening arrhythmia need to be sensitive in performance and flexible enough to conform to the site of application.[8-9] Additionally, they should have a reliable power supply to prolong performance and possibly eliminate periodic surgeries intended for replacing batteries in such devices.[9-10] For this reason, there is a surging demand for smart materials that tend to sense or harness energy from bending and stretching motions.

1.1 Problem Statement and Objectives

Piezoelectric materials have been widely exploited in the fabrication of smart devices due to their unique electromechanical properties. Depending on the application, these smart elements can either operate as a motor in actuator mode or a generator in energy harvester and sensor mode. Hence, they have been vastly employed in consumer electronics, musical instruments, automobiles, medical and defense applications. Ceramic-based materials led by the prominent lead zirconate titanate (PZT) family dominate most applications due to their superb piezoelectric properties. However, piezoelectric ceramics exhibit characteristic drawbacks such as rigidity, brittleness, toxicity, high density, low breakdown field strength, and lack of design flexibility, which limit their extensive application in flexible and stretchable devices.[2, 9, 11-15] Promisingly, there are alternative design approaches which have been adopted to create synergy between piezoelectric ceramics and polymers to induce flexibility.[11, 16] However, challenges attributed to the two components' intrinsic behavior restrict processing such composites. An example is the large disparity between the dielectric permittivity of ceramics and polymers, which can result in a non-uniform electric field distribution in the composite when poling. In addition, thermal stability concerns of polymers at a

temperature above 300 °C can restrain setting an optimal condition for the poling of ceramic constituents, which may result in either insufficient poling or dielectric breakdown.[17-19] Although reported to show comparatively weak electromechanical behavior, piezoelectric polymers have received tremendous research attention due to their mechanical flexibility, biocompatibility, lightweight, ease of processing, cost-efficiency, high impact resistance, high dielectric breakdown, and low acoustic and mechanical impedance.[20-21] Among the available choices, materials that can retain piezoelectric activity when significantly stretched are rarely apparent due to limitations regarding the ductility of most polymeric materials. Exclusively, in the emerging fields of wearable and implantable electronics, piezoelectric elastomers are demanded to sustain large deformations while exhibiting impressive responses.

Due to the characteristic drawbacks associated with the fabrication of stretchable piezoelectric materials from ceramics and ceramic-polymer composites, we have considered a new perspective in processing piezoelectric elastomers that embraces two main steps. The first step involves the synthesis of polar polymers in which the dipole units can be electrically aligned and frozen-in to induce net macroscopic polarization. Ideally, polymers with inherent dipole domains or randomized dipolar groups as part of their amorphous structures and T_g sufficiently high above room temperature, upon electrical poling, can give rise to thermodynamically quasi-stable oriented dipolar phases responsible for piezoelectricity. Quite a number of such polymers are readily synthesizable and can be modified by varying polar units to tune their dielectric properties. The polymers, following a successful synthesis, are subsequently processed into nanoparticles and made into a composite with a non-polar polydimethylsiloxane (PDMS) elastomer. In the final step, the reinforced elastomer composites are rendered piezoelectric by poling in a strong electric field at temperatures above the T_g of the particulate polar polymer fillers. A dipole structural anisotropy can be retained by cooling the composite material to room temperature under the electric field. A schematic illustration of the poling process can be found in Figure 1.1. To maximize piezoelectric efficiency, the composite system should retain sufficient polarization in the particulate fillers while maintaining low elastic modulus due to the intrinsic property of the PDMS matrix. The first proof of concept is clearly elaborated in another thesis work where piezoelectric elastomers were fabricated from particles of a polar poly [(methyl methacrylate)-*co*-(disperse Red 1 methacrylate)] reinforced in a PDMS matrix. [22] However, the reported piezoelectric properties generally show a drastic decay in the first few days after poling until pseudo-stable value could be recorded.

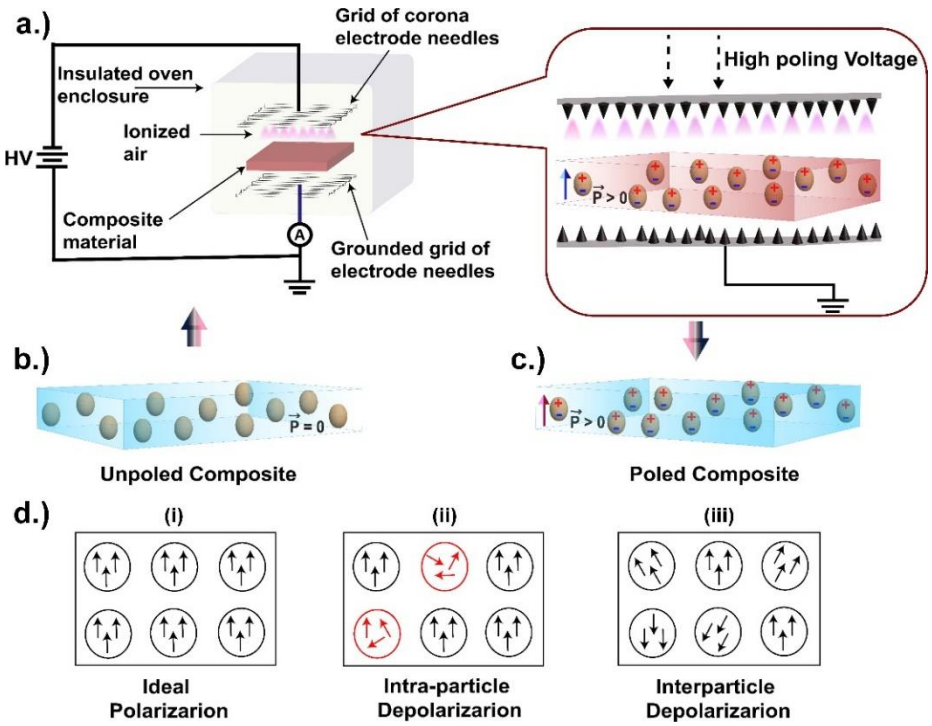

Figure 1.1 Schematic illustration of electrical poling: a.) thermally assisted corona treatment; b.) Un-poled composite; c.) poled composite; d.) dynamics of possible depolarization mechanisms

Further investigation to substantiate the established concept will be provided in this thesis. The design strategy combines reactions from the organic synthesis toolbox and a composite processing technique to prepare all-organic piezoelectric elastomer materials. The aim is to thoroughly understand the mechanism behind time-dependent decay in the piezoelectric response of such elastic piezoelectric composites. To achieve this, we synthesized different polar amorphous polymers containing double bonds in their main chains with varying pendant dipolar moieties. The rationale is to establish structure-property relations among the different polar polymers. By introducing double bonds in the polymer backbone chains, we hypothesize getting enough rigidity in the molecular structure of the polar polymer, which may help limit dipolar relaxations possibly caused by a high degree of intramolecular chain rotations (Figure 1.1 d.(ii)). Furthermore, we investigate the contribution effects of particle size and interfaces between polar polymer fillers and PDMS matrix in the decay of piezoelectric response (Figure 1.1 d.(iii)). Finally, the influence of the type of poling treatment on net macroscopic polarization and eventual piezoelectric performance is studied.

1.2 Synthetic Strategies

The approach will consider feasible synthetic pathways to achieve polar glassy polymers with sufficient rigidity in the polymer backbones such that the degree of bond rotations in the chains, which may further effect relaxation in the dipolar pendant groups at the molecular level, is minimized.

Ring-opening metathesis polymerization (ROMP) is peculiarly an interesting method among the living polymerization techniques, which presents a unique feature of preserving carbon double bonds within the backbone of synthesized polymers. The choice of monomers ranges from cyclic olefins to bi- and oligocyclic structures.[23] Nonetheless, the bicyclic olefin norbornene monomers predominate most ROMP due to high ring strain within their chemical structure, which promotes efficient polymerization. Additionally, this class of monomers can easily be modified with a wide range of functional groups, giving rise to polymers with otherwise inaccessible structures and properties. Monomers of functionalized norbronenes, as such, readily prevent secondary metathesis of the polymer backbone as an additional advantage over other monomer classes for ROMP.[23-24] For these reasons, we chose this synthetic route to prepare new polar polymers from functionalized norbornene monomers with different dipole substituents, as shown in Scheme 1.1.

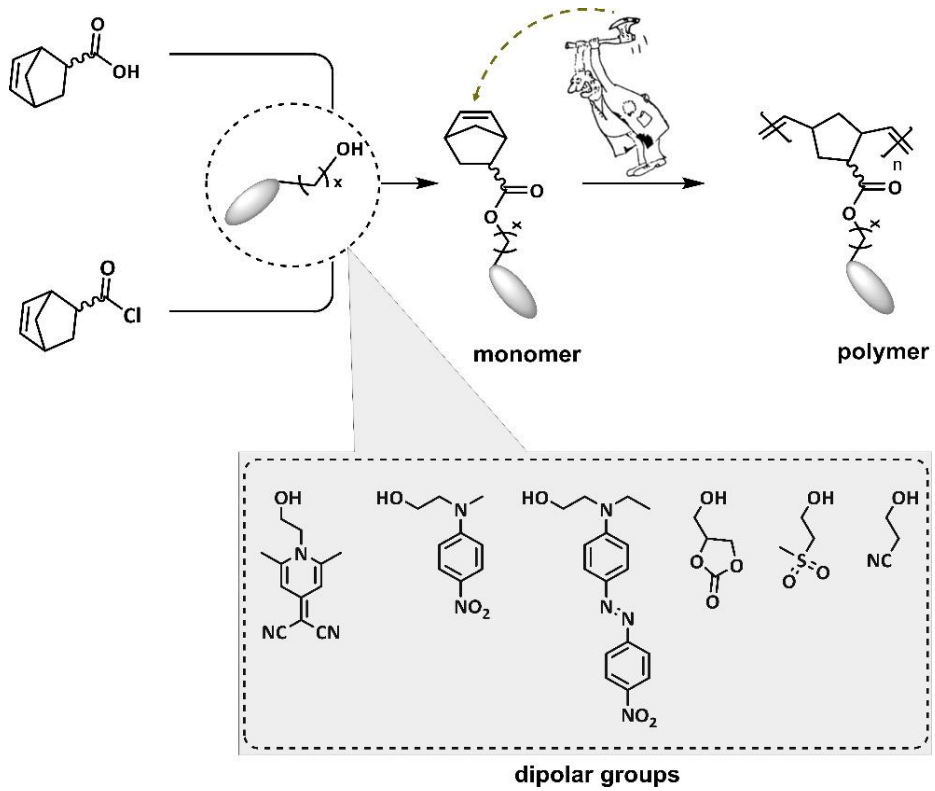

Scheme 1.1 Synthesis route for preparing polar glassy polymer

Following a successful synthesis, the polymers will be processed into nanoparticles by a solvent displacement technique known as nanoprecipitation or *Ouzo effect*.[25-27] This technique is a basic physical phenomenon that occurs at least in ternary liquid systems and involves the formation of sub-micrometer particles during a solvent exchange between a polymer solution and a non-solvent. The solvent employed for the polymer solution should be miscible with the non-solvent used as the precipitating medium. Producing polymer particles by this process complies with the nucleation theory and consists of steps such as particle nucleation, growth, and aggregation. Colloidal or pseudo-colloidal suspensions are formed under the right conditions, which promote a super-saturation of polymer molecules in a ternary polymer/solvent/non-solvent system and favor rapid particle formation with little or no particle growth when a metastable state is attained. The metastable region is located between the miscibility limits (binodal phase) and the stability limits (spinodal phase) of the ternary system created. A schematic illustration of the phenomenon is shown in Figure 1.2. The resulting particles primarily depend on the polymer behavior in the solution phase, the nature and ratio of non-solvent, the densities of the individual components, and their mutual solubility and concentration.[25, 28] Thus, the particle size is strongly affected by the initial polymer concentration, and the ratio between solvent and non-solvent.[28] We will therefore capitalize on this technique to process polymer particles with varying size distributions and investigate their influence on piezoelectric response when made into composites with PDMS.

The chemistry of PDMS and its curing techniques have been well established, which is evidenced by a great variety of formulations that are commercially available.[29-31] By a solution processing strategy, we will impregnate the polar polymer filler particles in PDMS matrix. Additionally, we will adopt a condensation curing technique, which requires silanol-terminated PDMS in the presence of organo-functional silane crosslinker and condensation catalysts (Tin- or Titanium-based catalysts), in transforming composites solutions into 3D networks. The choice of processing steps are crucial in fabricating composite materials with excellent filler dispersion in the matrix. Therefore, we will employ ball milling to break down large aggregates of filler particles and 3-roll milling to homogeneously disperse particles in matrix solution via shearing. The processing solvent will be carefully considered to selectively solubilize PDMS matrix and its associate crosslinking agents while keeping the polar polymer filler particles intact without any significant shape change or dissolution. Finally, blade casting will be used to process composite films out of the mixture.

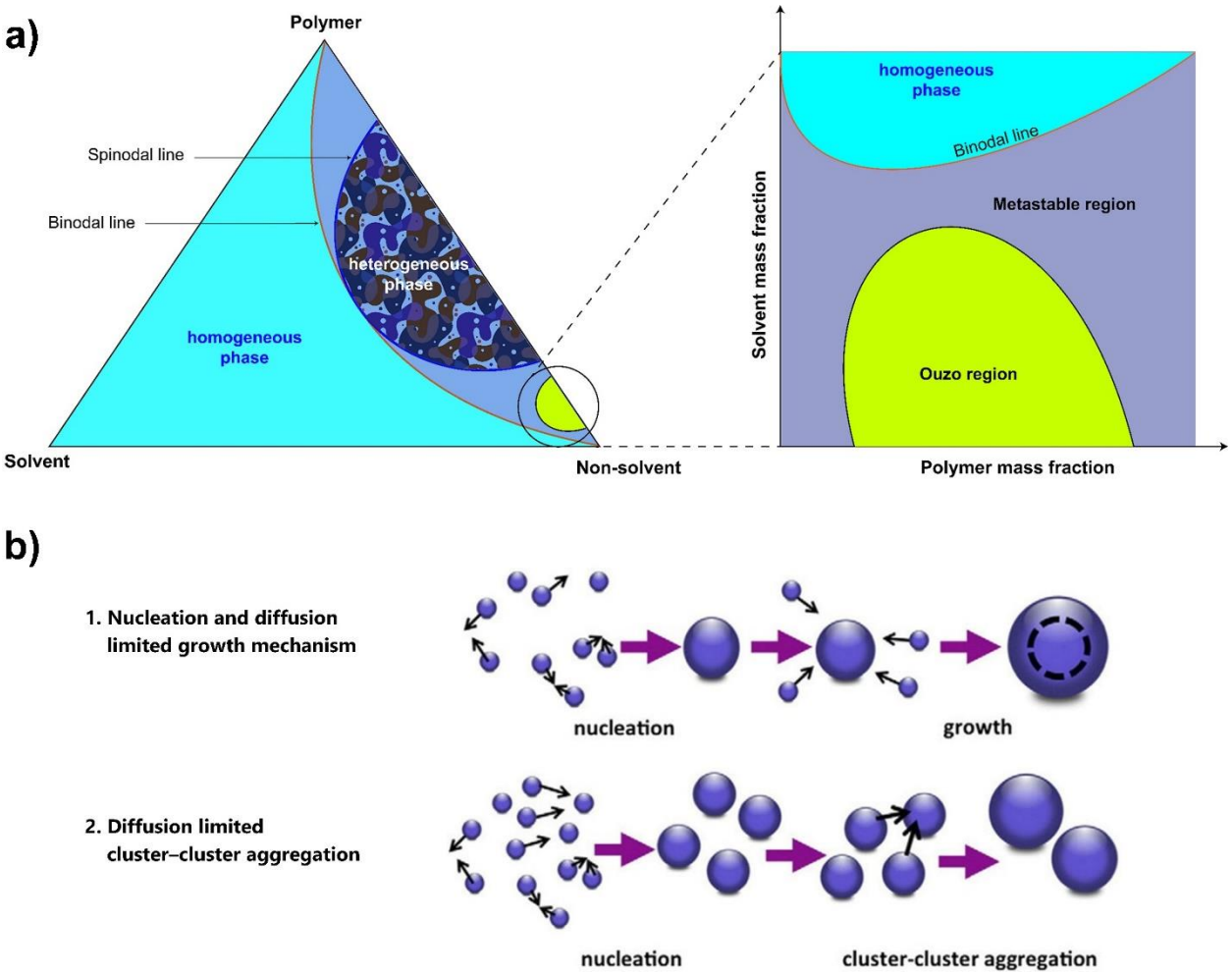

Figure 1.2 a.) Ternary phase diagram of a polymer/solvent/non-solvent system; b.) Schematic description of particle formation mechanisms. Adopted and reproduced with permission.[32-33] Copyright 2014, Advanced Drug Delivery Reviews, Elsevier, Copyright 2019, Materials Chemistry Frontiers, RSC.

1.3 Brief Outline

In the following, a brief overview of the thesis is given:

Chapter 2 presents a systematic review of different processing techniques employed in fabricating flexible and stretchable piezoelectric materials. As part of this, a brief history of piezoelectricity and the underlying fundamental principles from the material development perspective are covered. Thorough discussions on fabrication strategies with typical examples of materials processed by these methods and the associated challenges are summarized. In **Chapter 3,** we have employed ROMP to synthesize polar polymers with different dipolar groups as side chains and screened the potential to be used as stable piezo-electrets by studying their dielectric relaxation dynamics. Functionalization of a norbornene monomer with six (6) different dipolar moieties was initially achieved by conventional esterification. Homopolymerization of five (5) out of the 6 pre-modified

monomers was successfully performed. The impact of derivatization on the structural, thermal and dielectric properties of each polar polymer was thoroughly investigated. In **Chapter 4**, the polar polymer with optimal properties was processed into highly stretchable piezoelectric materials by combining with PDMS. The pre-synthesized polar polymers were initially processed into particulate forms with different particle sizes by solvent displacement. Composites with different filler contents and particle sizes of the particulate polar polymer forms in PDMS were processed by blade casting into thin films. A total of six (6) different elastic films with varying compositions were investigated. The possibility of applying these films in stretchable sensors, energy harvesters, and flexible electronics was preliminarily investigated by assessing their mechanical properties, dielectric behavior, and piezoelectric responses as a function of time, frequency, and strain. **Chapter 5** presents a summarized conclusion of all the results achieved and an outlook for future research and potential applications

1.4 References

[1] M. Shirvanimoghaddam, K. Shirvanimoghaddam, M. M. Abolhasani, M. Farhangi, V. Z. Barsari, H. Liu, M. Dohler, M. Naebe, *IEEE Access* **2019**, 7, 94533.

[2] Y. Liu, H. Wang, W. Zhao, M. Zhang, H. Qin, Y. Xie, *Sensors (Basel)* **2018**, 18, 645.

[3] S.-T. Han, H. Peng, Q. Sun, S. Venkatesh, K.-S. Chung, S. C. Lau, Y. Zhou, V. A. L. Roy, *Advanced Materials* **2017**, 29, 1700375.

[4] F. Xu, X. Li, Y. Shi, L. Li, W. Wang, L. He, R. Liu, *Micromachines* **2018**, 9, 580.

[5] F. Narita, M. Fox, *Advanced Engineering Materials* **2018**, 20, 1700743.

[6] Z. Yang, S. Zhou, J. Zu, D. Inman, *Joule* **2018**, 2, 642.

[7] H. Maiwa, DOI: 10.5772/64162 **2016**.

[8] D. Calero, S. Paul, A. Gesing, F. Alves, J. A. Cordioli, *BioMedical Engineering OnLine* **2018**, 17, 23.

[9] S. Lee, Q. Shi, C. Lee, *APL Materials* **2019**, 7, 031302.

[10] X. Zhang, J. Ai, Z. Ma, Z. Du, D. Chen, R. Zou, B. Su, *Journal of Materials Chemistry C* **2019**, 7, 8527.

[11] V. L. Stuber, D. B. Deutz, J. Bennett, D. Cannel, D. M. de Leeuw, S. van der Zwaag, P. Groen, *Energy Technol.* **2019**, 7, 177.

[12] C. Falconi, *Nano Energy* **2019**, 59, 730.

[13] V. Jella, S. Ippili, J.-H. Eom, S. V. N. Pammi, J.-S. Jung, V.-D. Tran, V. H. Nguyen, A. Kirakosyan, S. Yun, D. Kim, M. R. Sihn, J. Choi, Y.-J. Kim, H.-J. Kim, S.-G. Yoon, *Nano Energy* **2019**, 57, 74.

[14] R. A. Surmenev, T. Orlova, R. V. Chernozem, A. A. Ivanova, A. Bartasyte, S. Mathur, M. A. Surmeneva, *Nano Energy* **2019**, 62, 475.

[15] J. Wu, Springer Singapore, Singapore 2018, 1 Online.

[16] I. Babu, G. de With, *Composites Science and Technology* **2014**, 91, 91.

[17] J. S. Harrison, Z. Ounaies, in *Encyclopedia of Polymer Science and Technology*, DOI: 10.1002/0471440264.pst427 **2002**.

[18] K. Arlt, M. Wegener, *Ieee Transactions on Dielectrics and Electrical Insulation* **2010**, 17, 1178.

[19] M. Xie, Y. Zhang, M. J. Kraśny, C. Bowen, H. Khanbareh, N. Gathercole, *Energy & Environmental Science* **2018**, 11, 2919.

[20] S. Mishra, L. Unnikrishnan, S. K. Nayak, S. Mohanty, *Macromolecular Materials and Engineering* **2019**, 304, 1800463.

[21] M. Smith, S. Kar-Narayan, *International Materials Reviews* **2022**, 67, 65.

[22] Y. S. Ko, F. Nüesch, D. M. Opriş, *Poleable Dielectric Elastomer Composites*, Ecole Polytechnique Fédérale de Lausanne, Lausanne **2017**.

[23] S. Hilf, A. F. M. Kilbinger, *Nature Chemistry* **2009**, 1, 537.

[24] A. Leitgeb, J. Wappel, C. Slugovc, *Polymer* **2010**, 51, 2927.

[25] S. A. Vitale, J. L. Katz, *Langmuir* **2003**, 19, 4105.

[26] E. Aschenbrenner, K. Bley, K. Koynov, M. Makowski, M. Kappl, K. Landfester, C. K. Weiss, *Langmuir* **2013**, 29, 8845.

[27] S. Stainmesse, A. M. Orecchioni, E. Nakache, F. Puisieux, H. Fessi, *Colloid and Polymer Science* **1995**, 273, 505.

[28] I. Y. Perevyazko, A. Vollrath, C. Pietsch, S. Schubert, G. M. Pavlov, U. S. Schubert, *Journal of Polymer Science Part A: Polymer Chemistry* **2012**, 50, 2906.

[29] D. M. Opris, M. Molberg, C. Walder, Y. S. Ko, B. Fischer, F. A. Nüesch, *Advanced Functional Materials* **2011**, 21, 3531.

[30] P. Mazurek, S. Vudayagiri, A. L. Skov, *Chemical Society Reviews* **2019**, 48, 1448.

[31] D. Wang, J. Klein, E. Mejía, *Chemistry – An Asian Journal* **2017**, 12, 1180.

[32] E. Lepeltier, C. Bourgaux, P. Couvreur, *Advanced Drug Delivery Reviews* **2014**, 71, 86.

[33] E. Middha, P. N. Manghnani, D. Z. L. Ng, H. Chen, S. A. Khan, B. Liu, *Materials Chemistry Frontiers* **2019**, 3, 1375.

CHAPTER 2

Processing of Piezoelectric Elastomers in Retrospect: A Systematic Review

by

*Francis Owusu,[a,b] Thulasinath Raman Venkatesan,[a] Frank A. Nüesch,[a,b,c] Martin R. Negri,[d,e] and Dorina M. Opris [a]**

[a] *Laboratory for Functional Polymers Swiss Federal Laboratories for Materials Science and Technology Empa Überlandstrasse 129, Dübendorf CH-8600, Switzerland*

[b] *Institute of Chemical Sciences and Engineering Ecole Polytechnique Federale de Lausanne (EPFL) Station 6, Lausanne CH-1015, Switzerland*

[c] *Institute of Materials Science and Engineering Ecole Polytechnique Federale de Lausanne (EPFL) Station 6, Lausanne CH-1015, Switzerland*

[d] *Institute of Physical Chemistry of Materials, Environment and Energy (INQUIMAE). University of Buenos Aires. National Council for Scientific and Technical Research (CONICET). Argentina.*

[e] *Department of Inorganic, Analytical and Physical Chemistry. School of Exact and Natural Sciences. University of Buenos Aires. Argentina.*

2.1 Abstract

Piezoelectrics play a significant role in modern electronics and electric devices. Thermal or mechanical stress on such materials induce a change in polarization generating an electric response. This response makes piezoelectrics indispensable in electronic and electric devices. However, most ferroelectrics are rigid and brittle and thus difficult to integrate into the next-generation wearable electronics that comply with human skin or organs. To facilitate the incorporation of piezoelectrics into stretchable electronic devices, researchers have focused on developing piezoelectric materials with improved properties and significant advances have been achieved regarding flexibility. However, marrying piezoelectricity and elasticity proved challenging. Such materials are important in sensors and energy harvesting. Here approaches to piezoelectric elastomers are reviewed and potential future research directions are pointed out.

2.2 Introduction

Electroactive materials describe a gamut of materials that exhibit very interesting and useful properties that include piezo-, pyro-, and ferroelectric properties. The term 'Electrets' is often used to describe this interesting and useful class of materials. Piezoelectricity, primarily found in crystalline materials, has propelled its application in myriad areas ranging from sensors and actuators to energy harvesting.[1-2] In particular, piezoelectric ceramics and fluorinated polymers have captivated much interest and attention over the last century. Similarly, dielectric elastomers (DE), a relatively new class of electroactive polymers originally developed for actuator applications in the early 1990s has extended its portfolio also to include other applications such as energy generators, sensors, etc.[3-4]

While piezoelectric ceramics such as lead-zirconate-titanate (PZT) show very good piezoelectric activity, they are brittle and thus, are not suitable to be used in flexible devices. In the case of PVDF, the workhorse piezoelectric polymer along with its derivative copolymers, are flexible and stretchable to a certain extent, but show lower piezoelectric response than ceramics.[3] On the other hand, dielectric elastomers polymers are soft, flexible, and can be easily stretched, offering several advantages over ceramic and semi-crystalline polymers to be used in electroactive applications. However, traditional DE do not showcase intrinsic piezoelectric behavior. Hence, several methods have been used to develop novel piezoelectric elastomers, which combine the functionality of conventional piezoelectric materials with the inherent stretchability of elastic materials.

Fabrication of piezoelectric elastomers with controlled structural morphology and physicochemical and electromechanical properties plays a significant role in assessing their suitability for specific applications. Depending on the processing history, these smart elastomers can offer additional freedom in fashioning them into complex architectural devices. Such unlimited-shaped devices can

be significant in the technological hub of the IoT, ranging from wearable electronics, stretchable wireless sensor networks, soft robotics, and energy harvesting.[5-11]

Different approaches to designing stretchable piezoelectric materials have been strewed in the literature with a common intention of intermarrying piezoelectricity and elasticity. For example, Zhang et al. prepared bioinspired piezoelectric elastomer composites made of (Ba,Ca)(Zr,Ti)O_3 (BCZT) ceramic and polydimethylsiloxane (PDMS) elastomer matrix. A porous 3D interconnected ceramic scaffold prepared from a sea sponge-like polyurethane sacrificial template was infiltrated with PDMS and chemically crosslinked.[12] Another study by Cheng et al. presented the design of a self-powered flexible tactile sensor that can detect triaxial dynamic force from a ternary phase composite prepared by random mixing of PDMS, polyvinylidene fluoride terpolymer P(VDF-TrFE-CTFE), and multi-wall carbon nanotubes (MWCNTs).[13] Other prototype wearable devices fabricated from similar ternary phase PVDF-PDMS-CNT elastomer nanocomposite have been studied by Guang Yang and coworkers. They reported excellent performance of this material, functioning as a self-powered insole sensor for monitoring human motions and also as an implantable artificial artery.[14] A different processing approach to fabricate elastomers with intrinsic piezoelectric behavior has recently been reported by Zhou and coworkers.[15] A crosslinked elastic network of a copolymer of poly(sodium *p*-styrenesulphonate-*co*-acrylonitrile) (P(NaSS-*co*-AN)) showed an inherently high piezoelectric charge coefficient (d_{33}) of 40 pC/N and a recoverable elasticity under 100% strain. Functionally graded polyrotaxane (PRX) elastomers composed of poly(ethylene glycol) (PEG) and α-cyclodextrin (α-CD) have also been designed and investigated by Ji-Hun Seo and coworkers.[16-17] These elastomers showed superior mechanical properties comparable to commercially available PDMS and good ferroelectric behavior with remnant polarization of 0.03 μC/cm^2, similar to that of PVDF. Other material scientists have reported on the possibilities of exploring additive manufacturing in the processing of piezoelectric elastomers.[18-21] The advantages of this processing technique are the infinite potential for rapid prototyping, high material utilization, production precision, and the absence of shape restrictions in device fabrication, among others.

Regardless of the meteoric rise of piezoelectric elastomers in the last decade, there is a need to close gaps in tailoring suitable materials for optimal and sustainable implementation industrially.[5, 21-24] There are reported numbers of published reviews on the synthesis and fabrication of piezoelectric materials and their application in the field of wearable electronics, soft robotics, energy harvesting, sensors, actuators, and bio-implantable, among others.[25-27] Park et al. presented a brief overview of flexible and stretchable piezoelectric nanocomposite generators for realizing self-powered energy systems focusing on development history, power performance, and applications.[28] Chorsi et al. thoroughly reviewed different piezoelectric biomaterials focusing on operational principles, possible applications in biosensors and bioactuators, and their future opportunities and challenges.[22] Zhou et al. gave an overview of the recent development in new intrinsically stretchable piezoelectric

materials and rigid inorganic piezoelectric materials with novel stretchable structures for potential application in sensors and energy harvesters.[29] Chen et al. discussed recent progress in adopting additive manufacturing for piezoelectric material design, summarizing the advantages of the technology and its technical impact on production.[21] Another recent review by Vallem et al. briefly summarized the various modes of converting ambient energy sources into electricity using soft and stretchable materials, shedding more light on the harvesting mechanisms and the design strategies to render such devices into soft or stretchable embodiments.[30] However, a compilation of processing techniques deployed so far in designing stretchable piezoelectric materials has rarely been summarized. With the above-raised concerns, we present a comprehensive overview of the different processing techniques reported in the literature to produce piezoelectric elastomers. First, we will briefly present the history of piezoelectricity and the underlying fundamental principles from the material perspective. Subsequently, the processing techniques employed in preparing piezoelectric elastomers will be thoroughly covered, giving typical examples of materials and their inherent properties. To conclude, a summary of associated challenges in designing piezoelectric elastomers will be discussed. To profit most from this review, it is also noteworthy that there is no such as an ideal processing technique for fabricating the best piezoelectric material unless the application is specifically described.

2.3 Brief History and Fundamental Principles of Piezoelectricity

The concept of piezoelectricity revolves around a complex phenomenon that extends across areas of classical physics, electronics, material science, engineering, etc. In connection with the multidisciplinary nature, research publications on this subject are vastly dispersed, and few books on this topic are usually compilations of authors' research works. Therefore, piezoelectricity may not necessarily be taught for didactic purposes and can be difficult to understand sometimes. In this section, we will briefly cover the historical milestones of piezoelectricity with a focus on the underlying principles of the phenomenon.

2.3.1 Historical Milestones

The term *piezoelectricity*, which Wilhelm Gottlieb Hankel proposed in 1881, combines two Greek words and means "pressure-induced electrostatic charge". By the simplest and broadest definition, piezoelectricity is a phenomenon that involves electromechanical interconversion between mechanical stress and electrical polarization.[31-32] The phenomenon was first experimentally discovered in 1880 by Pierre and Jacques Curie, focusing on the mechano-electrical transduction effect, also termed *direct piezoelectricity*, in hemihedral crystals of quartz, tourmaline, zincblende, topaz, boracite, calamine, and Rochelle salt. As a result of the difficulties and lack of knowledge in

quantifying the magnitude of this effect, the Curie brothers got stuck in answering only qualitative questions. Not long after, Gabriel Lippmann, in 1881, theoretically predicted the existence of the electro-mechanical transduction effect, likewise known as *converse piezoelectricity*, based on general thermodynamic considerations. This was again verified experimentally by the Curie brothers, consequently paving the way for systematic quantitative evaluations to reveal the rules governing charge development by pressure.[3, 33]

The early history of piezoelectricity until the scientific community acclaimed the works of the Curie brothers answered interesting questions about how and why the phenomenon was discovered and how the related knowledge was developed. Although scientific discoveries usually have similarities regarding historical patterns, piezoelectricity seems to defy customary trends. The Curie brothers deliberately experimented on this phenomenon, which was not discovered accidentally. The discovery was not based on an empirical confirmation of established theory nor a result of any ‘crisis state'. Neither was it an accomplishment based on a new instrument nor an experimental method. However, contingency, theoretical speculations, and derivations based on knowledge of pyroelectric phenomena coupled with experimentation resulted in the discovery of piezoelectricity. [33-34]

Scientists in the late 19th century enthusiastically embraced the seminal publications of the Curie brothers. Consequently, piezoelectricity was first discovered and investigated in inorganic single-crystal or polycrystalline materials.[35] The first decade following the discovery was dedicated to understanding the basic properties of the phenomenon with a focus on relations between elastic forces and electric fields. The theory that embraced these properties was successfully formulated based on the pinnacle works of Woldemar Voigt between 1890 and 1894.[36] Technological applications were not the main concern in the early study of piezoelectricity. Not until the early 1910's when the phenomenon in quartz was deployed outside the laboratory in sonar to track German submarines during the First World War.[33, 37] The use of quartz was further exploited in the field of frequency control to stabilize oscillators often employed in timekeeping devices which exceeded that of astronomy-based references in stability. However, the avalanche in the electronic applications of piezoelectricity was realized with barium titanate ($BaTiO_3$), which was demonstrated in 1946 to show forth piezoelectric effect when electrically poled. Phonograph pickups were, as a consequence, the first commercial device made from $BaTiO_3$ piezoceramics circa 1947.[1] Following the report of piezoelectricity in $BaTiO_3$ ceramics, a large array of ceramic materials have been discovered to possess this effect.[38] For example, the solid binary solution of lead zirconate titanate (PZT) discovered in 1954 exhibits outstanding piezoelectric properties. A number of other single crystal materials such as lithium niobate ($LiNbO_3$), lithium tantalate ($LiTaO_3$), lithium sulfate monohydrate (LSM), ammonium dihydrogen phosphate (ADP) have also exhibited piezoelectric effect. Since then, the advent of man-made piezoelectric materials has found wide applications in sonar, piezo-ignition systems, accelerometers, hydrophones, microphones, ultrasonic transducers, frequency-controlled

oscillators in watches and radars, as well as surface acoustic wave devices employed as major signal processors and detectors in modern telecommunication systems.[39-40]

Observation of the piezoelectric phenomenon was fortunately not restricted to only ceramic materials. Eiichi Fukada and other scientists in the 1950s and 1960s pioneered the field of piezoelectricity in wood, collagenous tissues, and bio- and synthetic polymers.[41-47] Particularly interesting to the wider scientific community was the discovery of the piezoelectric effect in poly(vinylidene fluoride) (PVDF) by Heiji Kawai in 1969.[48] Further investigations in the 1970s were carried out on copolymers of PVDF with vinyl fluoride, trifluoroethylene, and tetrafluoroethylene by several scientists.[3, 49-50] The effects in these synthetic polymers were at least an order of magnitude higher than previously observed in other biomaterials and represent the state-of-the-art piezoelectric polymers.[51-52] In later years, piezoelectricity has been investigated in several other polymer-based materials ranging from biopolymers, amorphous polar polymers, solid and cellular polymer electrets, ceramic-polymer hybrids, electret elastomers, etc.[31, 40, 53-70] For instance, in 2001, the VTT Technical Research Centre of Finland reported on a film made from polypropylene with a cellular structure that exhibited piezoelectric sensitivity of 200 pC/N.[71] Thus far, the thermal stability of the piezoelectric response, which is only guaranteed up to 60 ºC, has been the major limitation for many applications. In the same year, Reimund Gerhard and coworkers observed in corona-charged sandwich films of porous amorphous Teflon® a strong piezoelectric effect up to 600 pC/N, which was thermally stable up to 120 ºC.[72] Additionally, a Swiss company named Algra group introduced printable piezoelectric composite materials with sensitivity up to 1,000 pC/N in device configurations and are commercially employed in touch switches and keyboards.[3] Details of these materials remain a company secret. In summary, piezoelectricity has received enormous research attention over the years and is progressively drifting the search toward sustainability with a keen interest in flexible and stretchable polymeric materials.

2.3.2 Origin of the Piezoelectric Effect in Different Materials and Related Equations

Theoretically, piezoelectricity can be understood as an electromechanical coupling between mechanical and electrical states. The phenomenon can be explained with a simple molecular model, as shown in Figure 2.1.[73] Before applying mechanical stress, both the gravity centers of the positive and negative charges coincide, resulting in an electrically neutral molecule, as indicated in Figure 2.1a. When pressure is exerted, the internal reticular structure is deformed, which causes the opposite charge centers in the molecule to separate and eventually leads to the generation of a small dipole, as shown in Figure 2.1b. An ideal situation for a material containing such molecules is that the opposite-facing poles of each molecule are mutually canceled, and fixed charges appear on the

surface of the bulk material, as illustrated in Figure 2.1c. That is to say, the application of mechanical stress results not only in a strain response but also in an electrical polarization.

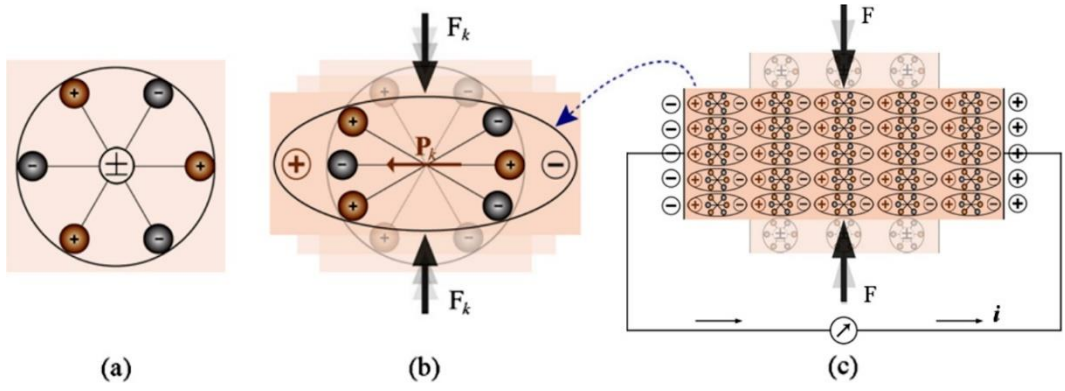

Figure 2.1 Piezoelectric effect explained with a simple molecular model: (a) An unperturbed molecule with no piezoelectric polarization (though prior electric polarization may exist); (b)The molecule subjected to an external force (F_k), resulting in polarization (P_k) as indicated; (c)The polarizing effect on the surface when a piezoelectric material is subjected to an external force. Reproduced with permission.[74] Copyright 2013, Robotic Tactile Sensing, Springer.

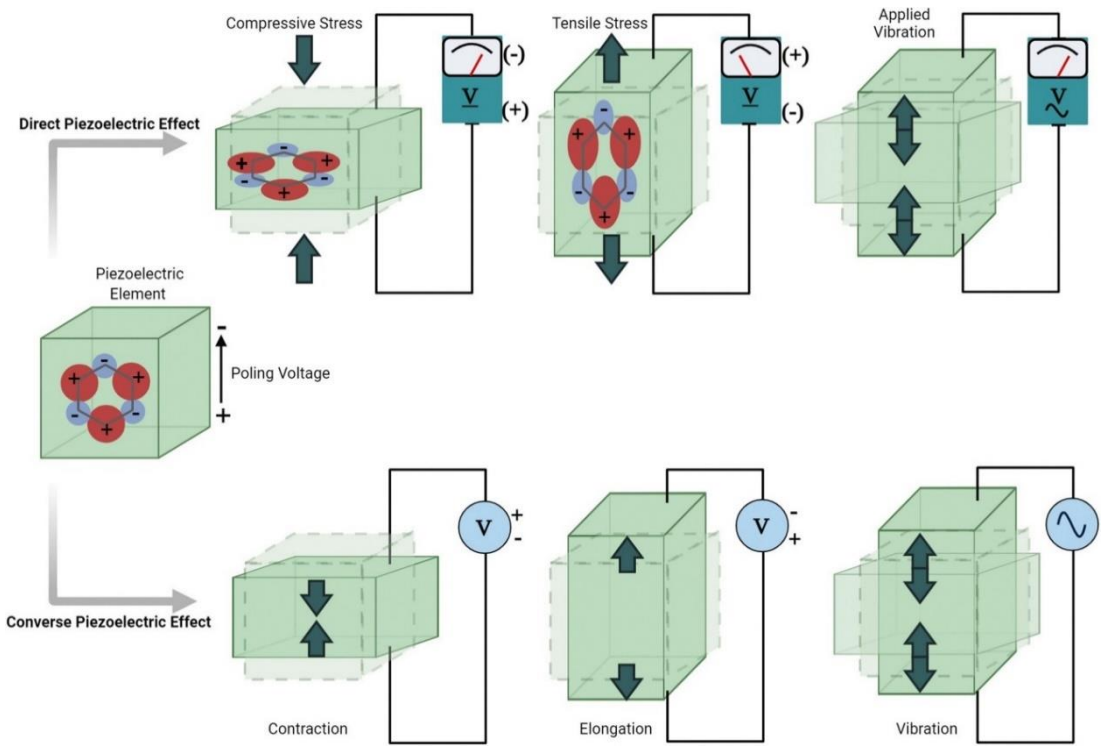

Figure 2.2 The Piezoelectric effect. The *direct piezoelectric effect* generates an electric voltage in response to a mechanical force, whereas the *converse piezoelectric effect* produces mechanical stimulation in response to an electric voltage. Reproduced with permission.[75] Copyright 2021, Bioelectricity.

In principle, the *piezoelectric effect* is a reversible process. Thus, the *direct effect* displaces charges in response to applied mechanical stress, and the *converse effect* gives off mechanical strain when an external electric field is applied, as schematically illustrated in Figure 2.2. Thermodynamic principles have been used to model these phenomena to interpret or quantify observed experimental results, as referenced in the IEEE Standards on Piezoelectricity, even though other models were developed based on microscopic theories with appreciable clarifications.[76-77]

Linear approximations are employed to describe the *piezoelectric effect* and are valid in small mechanical deformations and electric fields. However, the phenomena may exhibit nonlinearity above certain thresholds upon applying an electric field or mechanical stress. This review focuses on the linear theory of piezoelectricity in which the elastic, piezoelectric, and dielectric coefficients are treated as constants independent of the magnitude and frequency of the applied mechanical stress and electric field as clearly described in the scope of the IEEE standards.[76]

Following energy exchange and thermodynamic considerations, appropriate constitutive equations could be formulated as follows:

$$\begin{bmatrix} S \\ D \end{bmatrix} = \begin{bmatrix} s^E & d^t \\ d & \varepsilon^T \end{bmatrix} \begin{bmatrix} T \\ E \end{bmatrix} \tag{2.1}$$

Direct piezoelectric effect $$D = \varepsilon^T E + dT \tag{2.2}$$

Converse piezoelectric effect $$S = d^t E + s^E T \tag{2.3}$$

Where *D* and *E* denote the dielectric displacement and electric field components; *S* and *T* refer to the mechanical strain and stress components; *s*, *ε*, and *d* represent the elastic compliance, the dielectric permittivity, and the piezoelectric coefficient, respectively. The superscripts *E* and *T* indicate that the respective quantities are measured at a constant electric field and constant mechanical stress, respectively, and superscript t stands for the transpose. It is equally possible to develop second partial derivatives of the Gibbs free energies for the four different configurations of natural variables ((T,D), (T,E), (S,D) and (S,E)) and obtain four matrix equation couples that describe the same piezoelectric system, but based on different boundary conditions. These equations can easily be found in the literature.[78]

Numerous mechanistic and phenomenological models are proposed in the literature to explain the philosophy behind the origination of the piezoelectric effect in different kinds of material systems.[1, 14, 29, 34, 51, 54, 57, 71, 73, 75, 77, 79-93] However, a more simplified and semi-quantitative model (termed as a *charge-spring model*) proposed by Reimund Gerhard has specifically been useful in the design of soft, flexible and stretchable piezoelectric materials as well as predicting their electromechanical behaviors.[31, 94] This model generally considers a piezoelectric material as a two-phase system with a *dipole* phase and a *matrix* phase, which is elastically non-affine. The dipole phase usually comprises nano-, micro-, or macroscale units such as ionic charges of opposite polarity in the lattice of inorganic solid, polar molecules, ionic crystalline particles, polar crystallites in a semi-crystalline polymer, polar particles with opposite charges on their opposing faces, cavities with internal surface charges of one or both polarities, etc. The matrix phase can be the boundary layers between or around ionic charges, the polymer matrix of a composite, the amorphous phase of a semi-crystalline polymer, the cell walls of a polymer foam, etc.

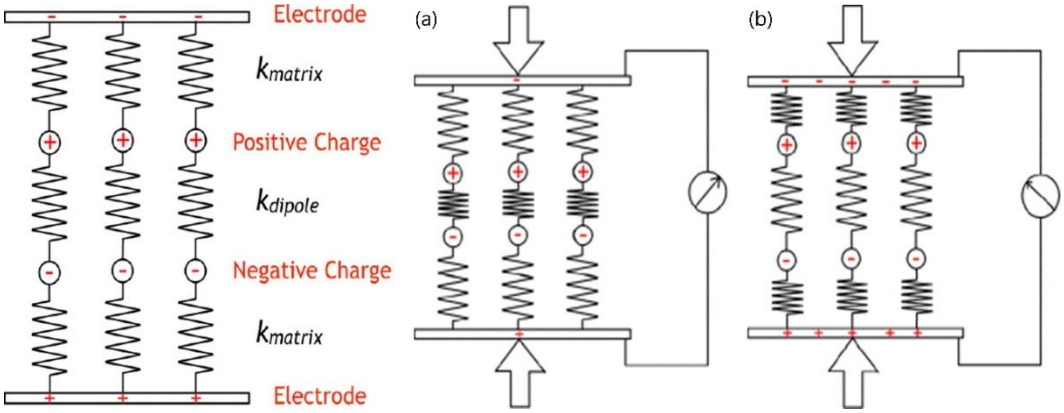

Figure 2.3 Charge-spring model for an elastically heterogeneous material with a dipole phase, a matrix phase and interface charges between them: (a) Non-affine deformation $k_{matrix} >> k_{dipole}$ leads to a dipole-moment change (so-called primary piezoelectricity); (b) Non-affine deformation with $k_{matrix} << k_{dipole}$ leads to a dipole-density change (so-called secondary piezoelectricity). Reproduced with permission.[94] Copyright 2014, SPIE.

All these material systems are considered the same way, except the length scales of the two phases and their deformations which are reckoned differently. The dimension of the two phases, in particular the lengths of the respective springs in the model, may range from a few nanometers in crystalline materials to micrometers or even millimeters in semi-crystalline polymers or various composites.

This concept can be represented by the arrangement of charges and springs, as shown in Figure 2.3. In an ideal case, electric polarization P in a material of volume V can be represented mathematically by the vector sum of its dipole moments μ as:

$$\vec{P} = \frac{1}{V}\sum_{i=1}^{N}\vec{\mu_i}$$

(2.4)

By definition, dipole moment μ is the product of charge magnitude q_i and the distance l_i between the centers of the opposite charges, which can be expressed as $\vec{\mu_i} = q_i\vec{l_i}$. Following this expression, equation (2.4) can be rewritten as;

$$\vec{P} = \frac{1}{V}\sum_{i=1}^{N} q_i\,\vec{l_i}$$

(2.5)

Applying a mechanical stress component *T* to a poled material gives a corresponding linear electrical response called *direct piezoelectricity*, which is described by the *d* coefficient. Considering all relevant definitions, the *d* coefficient can be expressed as the sum of local linear changes in the dipole moments, which has been termed as *dipole-moment effect* or *"primary piezoelectricity"* and the dipole density, also termed as *matrix effect* or *"secondary piezoelectricity".* These two contributing terms are illustrated in Figure 2.3 (a) and (b), respectively, and can be mathematically expressed in the following response equation;

$$\frac{\partial\vec{P}}{\partial T} = -\frac{1}{V^2}\frac{\partial V}{\partial T}\sum_{i=1}^{N} q_i\,\vec{l_i} + \frac{1}{V}\sum_{i=1}^{N} q_i\left(\frac{\partial\vec{l_i}}{\partial T}\right)$$

(2.6)

In a special case of a thin film material system subjected to compression in the thickness direction, equation 2.6 can further be simplified to achieve an approximated relation that considers only the unified thicknesses of the respective phases *t*, the bipolar interfacial charge density σ (the overall polarization P_3) and the respective Young's moduli of the dipole (Y_D), and the matrix (Y_M) phases;

$$d_{33} \approx \frac{\partial P_3}{\partial T_{33}} \approx -\frac{\sigma}{t}\frac{l_D}{Y_M} + \frac{\sigma}{t}\frac{l_D}{Y_D} \approx -\frac{P_3}{Y_M} + \frac{P_3}{Y_D}$$

(2.7)

Detail readings for further understanding can be found in the literature.[31, 35, 94-95]

2.4 Processing of Piezoelectric Elastomers

This section will emphasize strategies developed over the years to achieve piezoelectric elastomer materials to meet precisely advanced technological application requirements.

2.4.1 Ceramic-Polymer Compositing

To quickly remind the readers about bulk piezoelectric ceramics, it should be mentioned that though they undoubtedly exhibit high piezoelectric performance, they are too brittle to be integrated into flexible and stretchable electronics. Therefore tailoring heterogeneous composite with locally tuned elastic properties would extend the lifetime of functional devices employed at mechanically incompatible interfaces and create materials for application in flexible and stretchable electronics. Processing ceramic-polymer composites involves mixing melt polymers or polymeric solution with ceramic particles. In preparing such diphasic hybrid materials, it is important to consider the relevant properties of the individual phases, their relative amounts, and the preferable manner of interconnection.[96] The concept of connectivity implies the number of dimensions a component phase in the composite can be self-connected. A diphasic composite system can have at least ten predictable connectivity patterns, ranging from 0-0, where neither phase is self-connected, to 3–3, where each phase is self-connected in three dimensions.[97-98] The first digit denotes the connectivity of the filler particles, while the second represents the host matrix. Typically in a piezoelectric elastomer material made from ceramic filler and a passive polymer matrix, the success of such a hybrid system can be traced to a well-designed connectivity of each phase making up the composite. The connectivity patterns help control the effectiveness of stress transfer in the hybrid material and enhance the anisotropy of property coefficients. Thus, the number of dimensions in which the piezoelectric ceramic filler particles and the elastomeric polymer matrix are self-connected influences the piezoelectric coefficient and the elastic modulus of the resultant material.[98-100]

A typical traditional method for processing such hybrid materials involves random dispersion of the ceramic filler particles in a continuous polymeric phase, which mostly results in a 0-3 connectivity pattern. Achieving good connectivity in the ceramic phase by such an easy technique usually requires increasing the volume fraction above the percolation threshold, which eventually compromises the mechanical flexibility and elasticity of the resulting composite. We will, in this context, describe some processing techniques that have been deployed practically to attain 0-3, 1-3, and 3-3 connectivity patterns in piezoelectric ceramic-polymer composites, as illustrated in Figure 2.4. In 0-3 composites, the active filler phase has zero connectivity, while the inactive matrix phase has three-dimensional connectivity. The 1-3 case refers to active filler connectivity in one dimension, while the matrix phase is continuous in all three dimensions. The 3-3 denotes each phase is self-connected in all three dimensions.

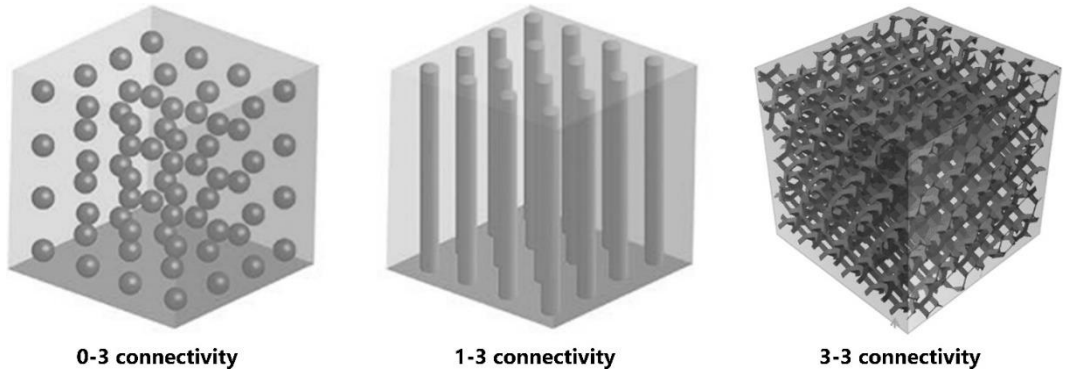

Figure 2.4 Schematic illustration of ceramic-polymer composite connectivity patterns. Reproduced with permission.[9, 101] Copyright 2018, Energy & Environmental Science, Copyright 2018, Advanced Engineering Materials

2.4.1.1 Piezoelectric composites with 0-3 connectivity

The 0-3 type piezoelectric filler composites have the advantages of easy synthesis and manufacturing in different shapes and film thicknesses with large areas. Various fillers and matrices were investigated. Because of the favorable combination of piezoelectric and elastic properties, PZT and $BaTiO_3$ fillers and PDMS matrix were the most explored. Already in 1959, Lutsch dispersed $BaTiO_3$ particles in an organic resin and poled it in a strong electric field above the Curie temperature of the filler. He found a strong influence of the particle size on the piezoelectric response, e.g., the smaller the filler size, the lower the response.[102] Later, Qian et al. developed $BaTiO_3$ composites in a silicone matrix. A piezodevice with a size of 5 × 6 cm^2 gave peak-to-peak values of a voltage of 38 V and a current of 0.8 μA and could charge a capacitor of 1 μF to 14 V in 800 s.[103]

Composites of PZT particles with different sizes of 30, 50, and 80 μm in a rubber matrix poled at 50 $kVcm^{-1}$ gave a d_{33} of 29, 36, and 46 pC/N and a d_{31} of -8, -11, and -11 pC/N, respectively.[104] Banno investigated composites of PZT and $PbTiO_3$ in chloroprene rubber and reported a piezoelectric coefficient d_{31} of about -5 pC/N.[105-106] Changing the ratio between the PZT/ $PbTiO_3$ did not lead to a significant difference in the d_{31} response. Choudhry et al. dispersed different piezoelectric nanoparticles ($BaTiO_3$, ZnO, and PZT) in a PDMS matrix and found that the PZT-based composites are superior, giving an open circuit voltage (~27 V), short-circuit current (429.23 μA), and power density (402 mW/m^2) under real-time human walking.[107] Lead magnesium-niobate (85 vol%) in poly(acrylonitrile butadiene) rubber poled at 7 - 8 kV/mm and 80 °C showed a d_{33} = 33 pC/N.[108] Later, a composite film of lead magnesium niobate-lead titanate (PMN-PT) in an elastic matrix sandwich between silver nanowires stretchable electrodes and poled at 50 kV cm^{-1} gave an output of 4 V and 500 nA and exhibited no significant degradation during about 15000 stretching-relaxation cycles.[109] A piezoelectric device (5 cm × 4 cm) consisting of PZT (65 vol%) in a silicone elastomer

matrix, when strained 50% at 6.4 cm s^{-1} strain rate and a frequency of 0.7 Hz generated an output voltage of 20 V, a current of 0.55 μA, and a power density of 3.93 μW/cm^3.[110] Liu et al. made a ternary composite of graphene and PZT in silicone. The PZT:PDMS composite and the optimized ternary-based piezoelectric composite with 0.33% graphene exhibit slightly smaller output voltage but much greater short-circuit current density of 13.23 μA cm^{-2} under foot stepping. The output power of 32 nW (59 mV and 553 nA) and 1.9 nW were measured for the 0.33% graphene/PZT/PDMS composite and the PZT/PDMS, respectively.[111] An elastic PZT composite in a hydrogenated styrene−butadiene block copolymer, which can be stretched to about 950%, gave a maximum output current density of 9.704 mA·m^{-2} and an open circuit voltage of about 100 V. The device can power 40 green LEDs and charge a 10 μF capacitor from about 0 V to 6 V in about 500 s.[112] The piezoelectric response of 0-3 composites increases with the amount of piezoelectric filler used. Unfortunately, this has a detrimental effect on mechanical properties. To circumvent this problem, Niu et al. used agglomerated PMN-PT particles and increased the amount of active filler to 92 wt.% while the composites could still be stretched by 30% (Figure 2.5). The generators produced a power density of about 81.25 μW/cm^3. The best material showed a peak-to-peak voltage of 50 V and could charge a capacitor of 10 μF up to ∼10 V in 20 min.[113]

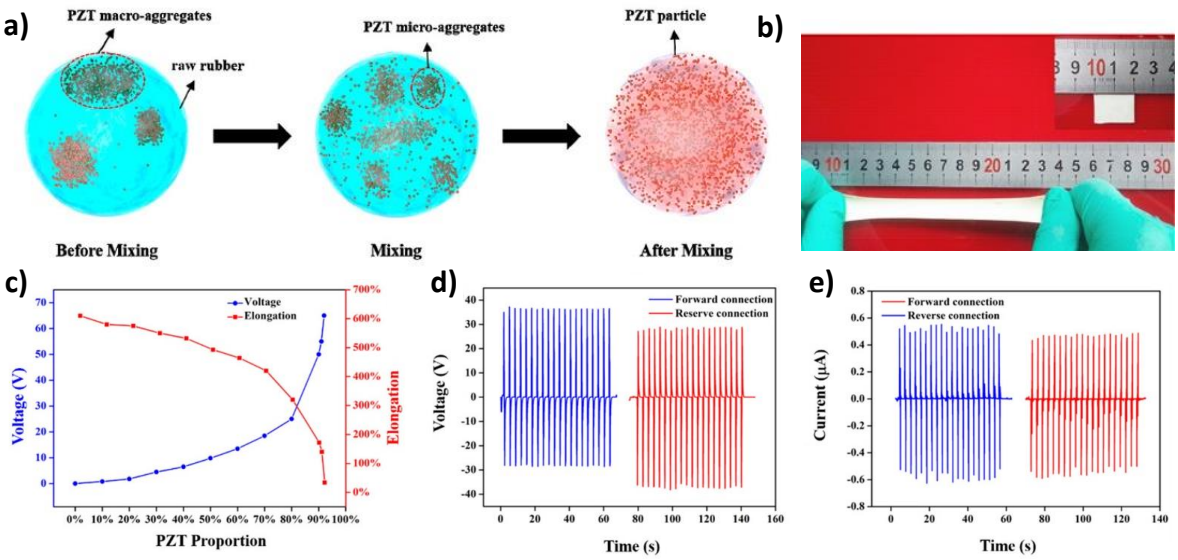

Figure 2.5 PZT-based stretchable piezoelectric nanogenerator (HSPG): a) fabrication process; b) the piezoelectric composite is stretched to 575%; c) the maximum output voltages and elongations at break of HSPGs with different PZT proportions; the measured d) output voltage and e) currents of the HSPG with forward and reverse connection. Reproduced with permission.[113] Copyright 2019, ACS Sustainable Chemistry & Engineering

2.4.1.2 Piezoelectric composites with 1-3 connectivity

Several strategies have been used to synthesize composites with 1-3 connectivity, however, dielectrophoresis is the most explored. It was first reported in 1949 by W. M. Winslow when describing a phenomenon whose origin is electrically induced by the alignment of small particles in liquid fluid suspensions.[114] The technique has since been employed as a relevant step in processing piezoelectric elastomer composites with ceramic particles as the filler phase and elastomeric polymers as the matrix phase. In principle, such hybrid materials are subjected to an AC electric field before crosslinking, which evokes a translational force causing the particles to reorient with respect to the electric field.[115] The non-uniform electric field, as a result, induces space charge separation on each suspended particle which then generates a dipole. The induced dipoles from the displacement of double layer and/or space charges at the fluid-particle interface then associate with each other via electrostatic dipolar-dipolar interactions. Eventually, the resultant translational motion causes rotation and axial displacements on the suspended particles leading to fibrils of chain-like arrangements, called *dieletrophoresis* or *electrorheological effect*.[116-117] A schematic illustration of this processing technique can be found in Figure 2.6. The advantage of this technique over the traditional method is that a relatively low volume fraction of filler particles can be used to achieve quasi 1-3 connectivity patterns in the resulting composite materials. Additionally, effective stress transfer can be attained in the structured particle phase resulting in excellent piezoelectric properties whiles preserving the composite material's elastic integrity.

For instance, Gao et al. recently adopted this unidirectional particle alignment engineering technique to fabricate a flexible piezoelectric touch sensor and wearable keyboard with outstanding sensitivity and extraordinary mechanical stability.[99-100] The sensing element, which was a diphasic composite prepared from 8 vol% of $(Ba_{0.85}Ca_{0.15})(Ti_{0.90}Zr_{0.10})O_3$ (BCZT) particles in a PDMS matrix, gave an impressive open circuit voltage of 28.8 V and a piezoelectric voltage coefficient (g_{33}) of 0.10 V m N^{-1}. By optimizing the poling conditions of this same material composition, the scientists reported an outstanding g_{33} value of 0.60 V m N^{-1} attributed to synergistic enhancement in the stress-transfer capability of the aligned active particles in the composite material.[100] Another study by Stuber et al. presented the design of a quasi 1-3 connectivity pattern of potassium sodium lithium niobate (KNLN) ceramic fibers in a flexible PDMS matrix by dielectrophoresis.[98] The energy harvesting performance of the structured composite materials was determined by the product of piezoelectric coefficients, $d_{33} \cdot g_{33}$, which is a measure of the energy density per unit volume that can be harvested. However, these hybrid materials exhibited piezoelectric properties, which are dependent on the aspect ratio of filler particles, their interconnectivity after aligning in the PDMS matrix, and poling efficiency.

Thus, the higher the aspect ratio of the filler fibers used, the shorter the inter-particle distance becomes when electrically aligned and the higher the electromechanical coupling.

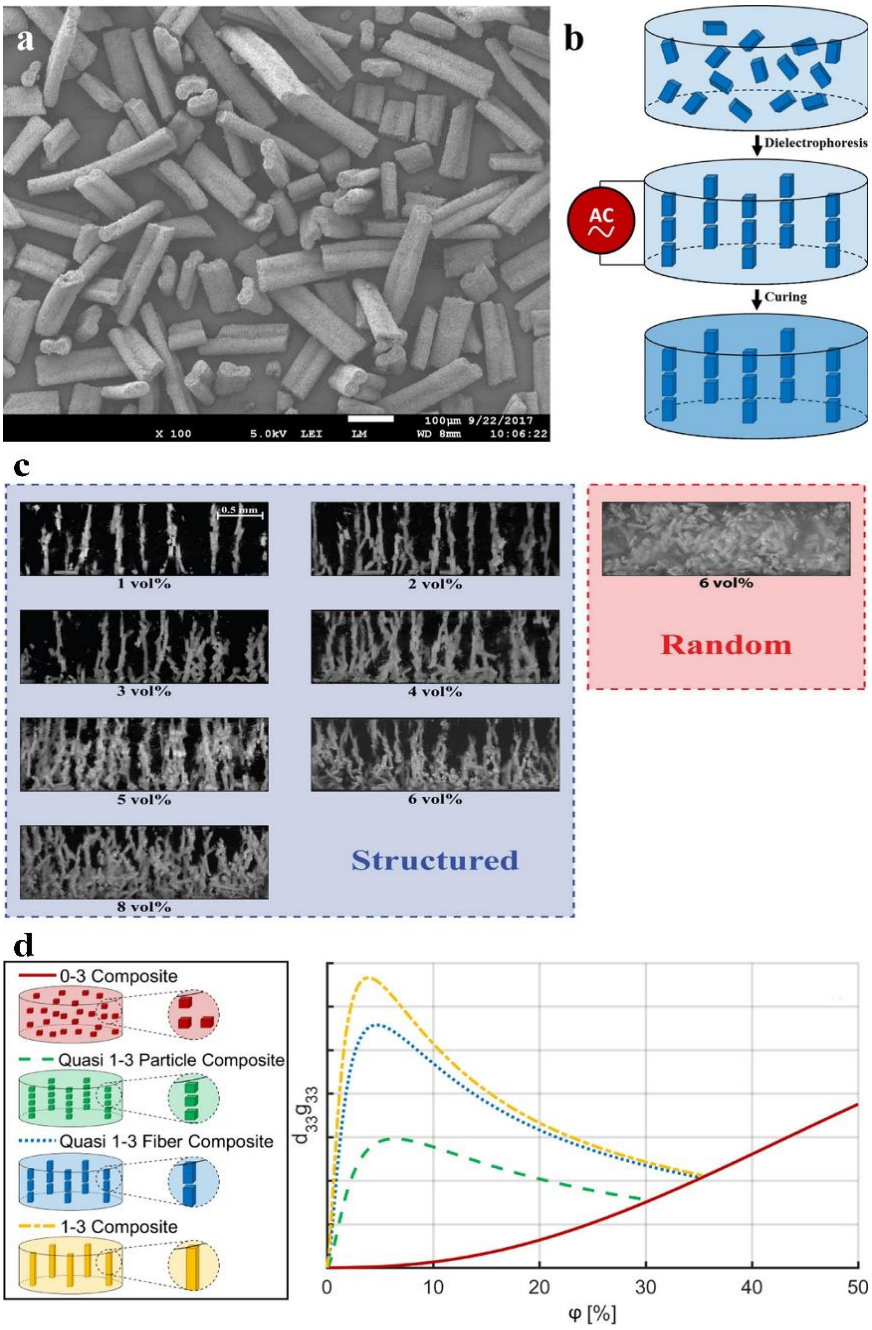

Figure 2.6 Schematic representation of dielectrophoresis process: a.) SEM micrograph of KNLN fibers; b.) Typical alignment mechanism of piezoelectric particles; c.) Microstructure of dielectrophoretically aligned KNLN fibers in a PDMS matrix; d.) Connectivity schemes of ceramic-polymer composite materials and corresponding arbitrary illustration of the energy harvesting figure of merit, $d_{33} \cdot g_{33}$ as a function of volume fraction, φ, of piezoelectric filler. Reproduced with permission.[98] Copyright 2019, Energy Technology.

The measured figure of merit, $d_{33} \cdot g_{33}$, was 18 pm^3J^{-1}, reported to be comparable to that of state-of-the-art ceramic PZT. Pseudo-1-3 piezoelectric PZT/polymer composites in different polymeric matrices (silicone gel, silicone rubber, urethane rubber, and poly(methyl methacrylate)) and poled at the different electric fields have also been reported. An increase in the piezoelectric response with the poling field and reducing the elastic modulus of the matrix were demonstrated.[118]

Another less explored possibility of achieving composites with 1-3 connectivity is making ribbons and pillars of piezoelectric filler on a substrate which are then transferred to an elastic matrix. For instance, crystalline piezoelectric nanothick ribbons of PZT on a host substrate were transferred onto PDMS. They showed among the highest electromechanical energy conversion with a transverse piezoelectric constant, d_{31} = 49 pm/V, which could be increased to an even higher value of d_{31}=79 pm/V when the structure was poled at ~100 kV/cm for 14 h (Figure 2.7(a-d)).[119]

To overcome the mechanical incompatibility between inorganic piezoelectrics and elastomeric substrates, PZT was shaped as wavy ribbons (5-10 μm wide and 250-500 nm thick) before transferring to a stretched PDMS film (Figure 2.7(e)).[120] Finally, releasing the pre-strain in the PDMS lead to periodic de-adhesion and buckling of PZT ribbons. A current density of 2.5 μA/mm2 was calculated, comparable to the current density measured in PZT nanowire-based devices.

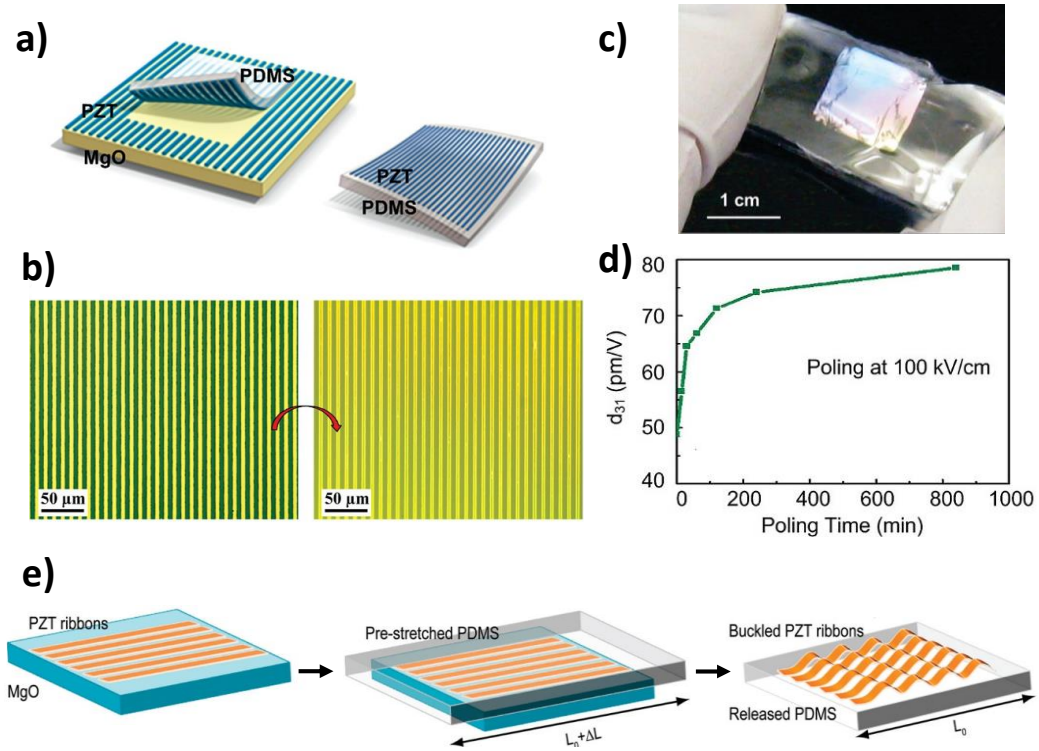

Figure 2.7 a) PZT ribbons synthesized on a MgO substrate, which is subsequently etched (left) and PZT ribbons are transferred onto a PDMS substrate (right); b) optical micrograph of PZT ribbons before and after transfer; c) photograph of PZT ribbons on PDMS top surface; d) d_{31} at different poling times and a poling field of ~100 kV/cm; and e) formation of wavy/buckled piezoelectric PZT ribbons on a stretchable PDMS film in three steps from left to right: PZT ribbons on a sacrificial MgO substrate which is subsequently etched and transferred to a prestrained PDMS film. Reproduced with permission.[119-120] Copyrights 2010 and 2011, ACS Nano Letters.

2.4.1.3 Piezoelectric composites with 3-3 connectivity

In 3-3 composites, the piezoelectric filler and the matrix have three-dimensional connectivity. Their synthesis involves two major steps, as illustrated in Figure 2.8(A). The first step is fabricating cellular ceramic struts with tailored microstructure containing a high porosity (typically above 70 vol. %). Methods employed to produce such macroporous ceramics with three-dimensional (3D) arrangements include, but are not limited to, replication of porous polymer templates, sacrificial template technique, and direct foaming of a liquid slurry. Detailed descriptions of methods regarding the versatility and ease of fabrication, as well as the influence on the microstructure and mechanical strength of the macroporous ceramics, can be found in the literature.[121-123] The final step involves infiltrating the macroporous interconnected structure with an elastomeric polymer solution and curing it into cross-linked networks.

For instance, Rittenmyer et al. mixed plastic spheres with PZT powder in an organic binder and sintered the mixture to give a ceramic skeleton, which was backfilled with PDMS and poled after curing. Composites containing 50% PZT showed a piezoelectric d_{33} response of about 250 pC/N.[124] Hikita, showed that the voltage output coefficient of the porous PZT increased with increasing volume fraction of porosity. A high voltage coefficient of 100 × 10^{-3} Vm/N was obtained in samples with a volume fraction porosity of 0.6 and thus showed almost the same piezoelectric response as the starting porous PZT.[125] Varaprasad et al. prepared a porous La-doped PZT 3D structure and infiltrated it with silicone using poly(methyl methacrylate) particles glued by polyvinyl alcohol as a sacrificial template. Best materials had a 50 wt. % filler, and it was poled at 100 °C and 25 kV/cm. A d_{33} coefficient of 90 pC/N and a piezoelectric voltage coefficient g_{33} of 110 × 10^{-3} V m/N were reported.[126]

Li et al., first made a porous PZT structure via freeze drying and calcination followed by impregnation with PDMS to give a 3-3 piezoelectric composite with a piezoelectric constant d_{33} ~ 146 pC N^{-1}, which is almost 10 times higher than the conventional 0–3 piezoelectric composite.[127] Qing Wang and co-workers designed energy harvesters based on 3-3 connectivity patterned composites prepared from ceramic skeletons infiltrated with PDMS.[12, 101, 128] The piezoceramic 3D interconnected architectures were prepared using polyurethane (PU) foam and bio-fibril cellulose as templates. Thus, a sol-gel or slurry of the piezoceramic phase is either dip-coated on the PU foam or freeze-casted in a blend with cellulose solution. Depending on the templating approach, the resulting wet mold is dried using an oven or a freeze-dryer. Afterward, the dried sample is calcined at an elevated temperature to burn out the sacrificial template. Finally, a solution of PDMS is infiltrated into the macroporous ceramic skeleton via vacuum suction and cured. A model based on Fourier spectral iterative perturbation method was employed to rationalize mechanical stress transfer and corresponding induced polarization distribution within composites.[12] The numerical data generated were in good agreement

with reported experimental data revealing that the piezoelectric performance of 3D interconnected structures is an order of magnitude higher than randomly dispersed composite materials. The reason is that the interconnected structures create a continuous pathway for stress transfer within the 3D architecture. In contrast, the randomly dispersed composite relaxes and dissipates most of the stress within the soft matrix rather than transferring to the active ceramic phase.

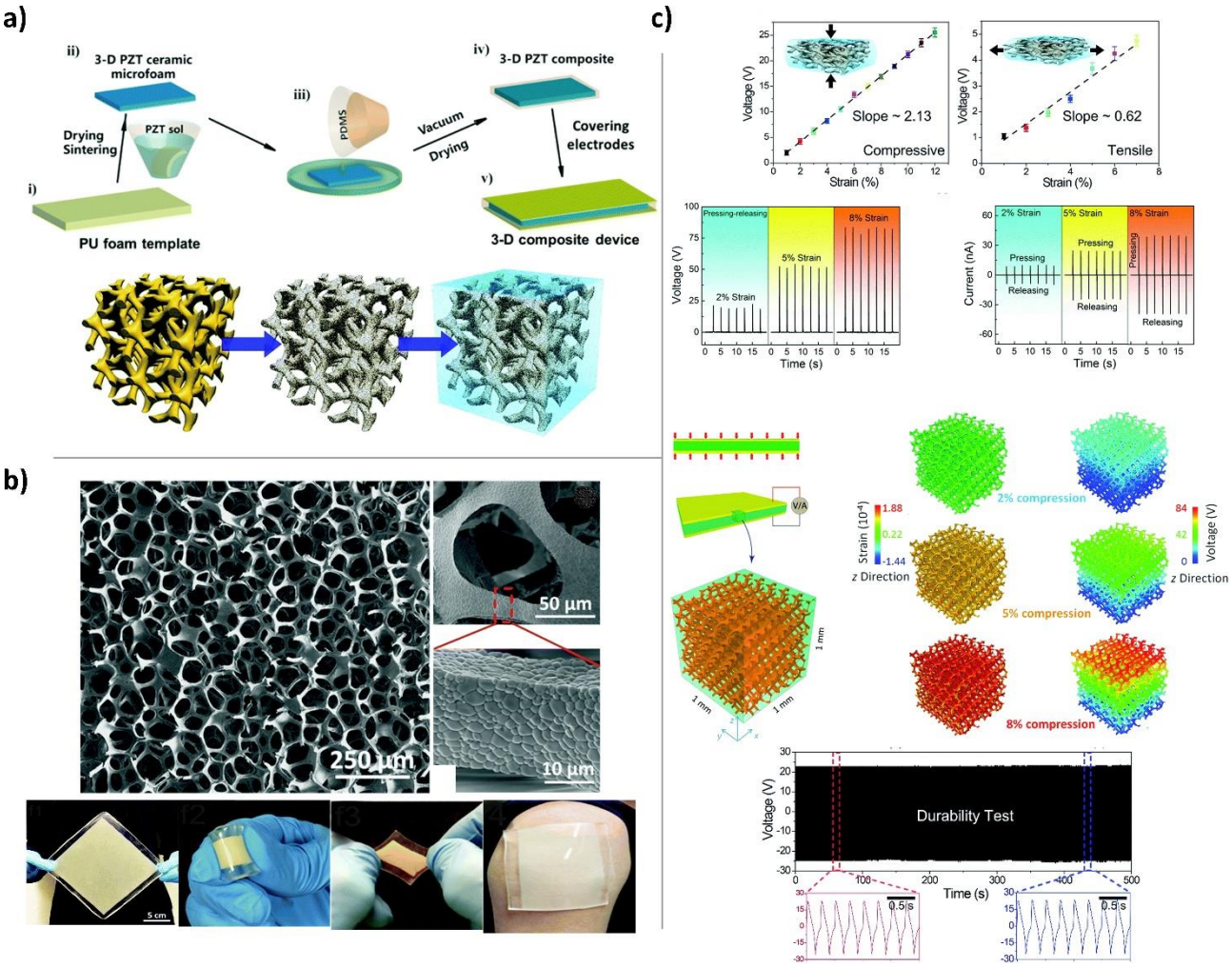

Figure 2.8 Fabrication and structures of the 3-D ceramic-polymer composites. a) Representation of the composite preparation procedure; b) The SEM micrographs of the macroporous ceramic skeleton and representative pictures of the composite demonstrates the possibility to bend and stretch by fingers and good conformation with the human body; c) Piezoelectric responses show output electrical signals under different compressive and tensile strains. Reproduced with permission.[12, 101] Copyrights 2018, The Royal Society of Chemistry.

2.4.2 All-organic Elastomeric Compositing

This processing method technically considers only organic-based components in the preparation of composite materials. The strategy is based on incorporating polar organic or polymeric molecules with the tendency to retain a net macroscopic polarization into the elastic network of a nonpolar polymer matrix after poling. Usually, polymers with inherent polar crystalline domains, such as PVDF and its copolymers, odd-numbered nylons (nylon 7 and 11) etc., and polar amorphous polymers with glass-transitions (T_g) high above room temperature are used as active phase components.[53] The dipolar segments in such active components, upon structuring, either by electrical poling or mechanical stretching, give rise to thermodynamically stable or quasi-stable oriented phases responsible for piezoelectricity. On the other hand, polymers that can maintain mechanical integrity by exhibiting recoverable strain deformations at different temperatures and frequencies, such as PDMS, etc., are used as matrices.[129] Figure 2.9(b) gives a typical schematic representation of such composite material systems and the process of generating polarization and piezoelectricity. When such a composite system is mechanically stretched or compressed, the dipole density changes due to fixed guest dipoles, leading to current flow.

Zhang et al. employed this processing technique in designing a flexible piezoelectric nanogenerator with a PVDF-PDMS composite material as the energy harvesting element.[130] The process starts with the fabrication of a mesoporous β-phase PVDF film by freeze-casting a solution of PVDF in DMSO solvent. The DMSO is then sublimed at low pressure (0.8 Pa) at ambient temperature (18–25 °C). The resulting interconnected network with controlled porosity was infiltrated with PMDS solution and cured at an elevated temperature (70 °C). Following this simple but effective processing technique, the researchers demonstrated by basic electromechanical evaluations that the mechanical properties of the piezoelectric nanogenerator can be tailored to conform to biological tissues whiles maintaining an appreciable piezoelectric output. The tensile and compressive test revealed that the piezoelectric nanogenerator exhibits elastomeric behavior with Young's modulus as low as 0.8 MPa. The recorded modulus falls within the specified range for certain human organs, such as blood vessels, known to range from 0.1 - 1 MPa. Subjecting this device to 0.3 MPa compressive stresses at a frequency of 20 Hz gave an average open-circuit voltage of 2.87 V and a short-circuit current of 3.42 µA. An artificial artery system with this nanogenerator integrated into its fabrication further demonstrated the capabilities of harvesting mechanical energy from blood pressure fluctuations. By mimicking regular heartbeat activity, an average output voltage of 0.35 V could be achieved, proving potential application as a self-sufficient power supply for implantable devices. Mechanical mixing of PDMS with PVDF and CNT fillers allowed Hu et al. to achieve materials that gave a voltage of 2 V for PDMS/PDVF and 2.75 V for PDMS/PVDF/CNT, respectively. The functionality of the device was demonstrated by using the energy harvested to operate a light-emitting diode (LED).[14] Park et al. reported a flexible and stretchable piezoelectric sensor consisting

of poly(vinylidenefluoride-*co*-trifluoroethylene) electrospun nanofiber sandwiched between two elastomer films on which surface electrodes were sputtered. The developed sensors could be stretched and folded multiple times. Their functionality was demonstrated in a high-precision sensor and a skin-attachable pulse monitoring device.[131] Duan et al. first made PVDF micro/nanofibers by combining helix electrohydrodynamic printing and buckling-driven self-assembly and embedded them in PDMS to give highly stretchable generators.

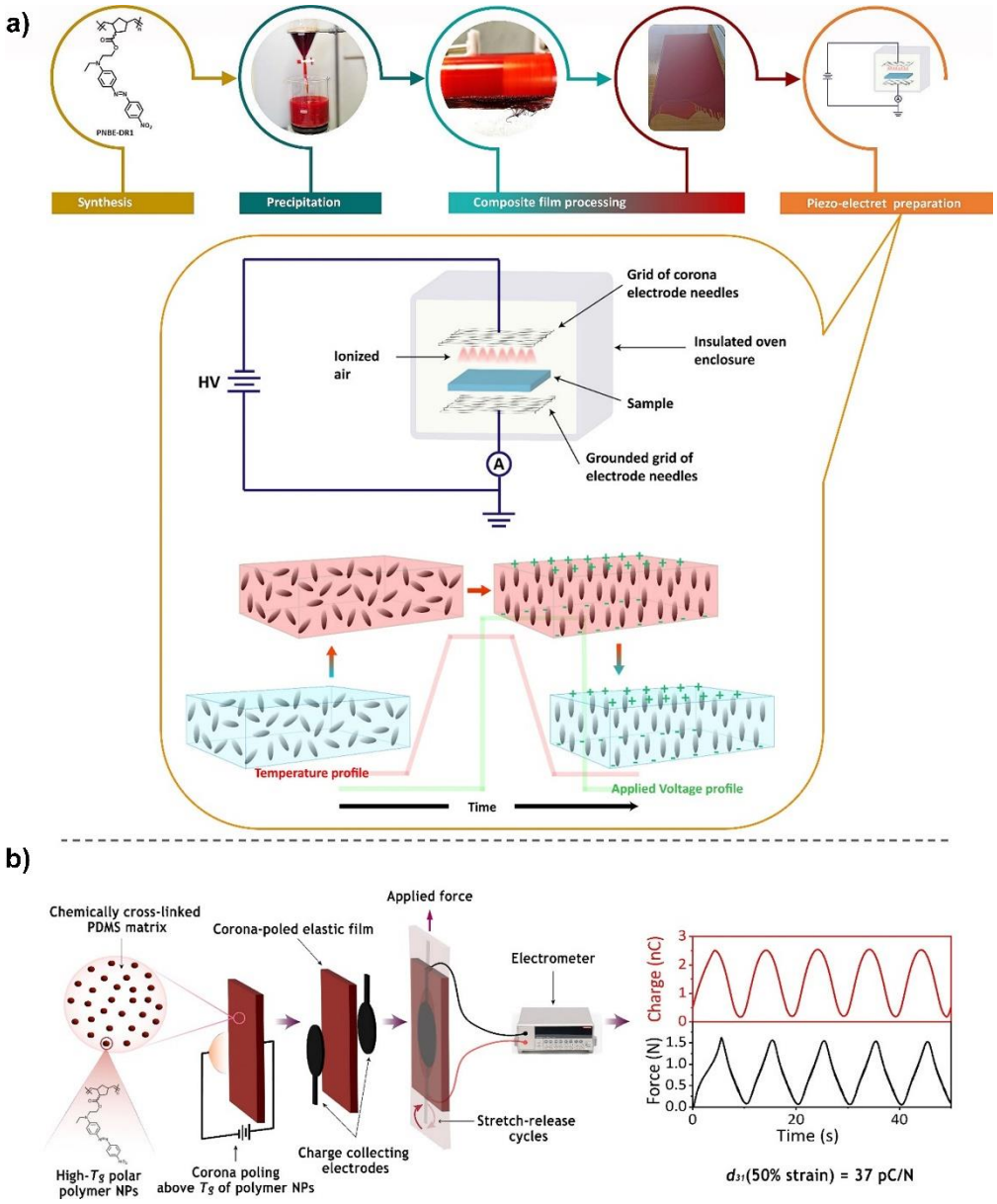

Figure 2.9 A typical approach for preparing all polymer-based piezoelectret elastomer: a) Flow diagram showing steps through synthesis and precipitation of polar polymer particles, processing into composites film with PDMS (using a three-roll-mill and Blade casting), and corona poling in a strong electric field at elevated temperatures; b) Piezoelectric charge generation after poling. Adopted and reproduced with permission.[70] Copyright 2022, Advanced Functional Materials.

A peak current of 200 nA at 200% strain was measured when liquid-metal in PDMS served as electrodes.[132]

In another communication by Moody et al., a design concept of doping nonpolar polymers with polar organic moieties proved a promising approach to fabricating flexible piezoelectric composite materials.[133] The independent selection of matrix and dopant permits easy processing and tailorable properties. Thus, mechanical properties significantly depend on the choice of host matrix, while electric polarization relies on the selected dopant molecule. The dopant may not necessarily be inherently piezoelectric, but the possibility of creating long-range molecular ordering when incorporated into a polymer matrix unveils this synergistic piezoelectric behavior. Here, a highly polar 2-chloro-4-nitroaniline (CNA) molecule as a dopant was mixed with a polyurethane host matrix and before crosslinking, portioned into a poling fixture consisting of two electrodes. The sample mold was then cured at room temperature under an applied voltage bias. A quasi-static d_{33} piezocoefficient up to 244 ± 30 pC/N could be measured. Additionally, typical finger taps gave a peak current and power output of 5 nA and 5 nW, respectively. Nonetheless, the reported piezoelectric response showed strong dependence on the electric field applied during poling treatments, which also has an eventual effect on the stability of retained polarization. Thus, samples poled at low electric fields record piezoelectric coefficients decaying over orders of tens of minutes. Poling at a significantly higher electric field causes additional polarization stability, possibly conferred by the long-range cooperative effect, which delays the depolarization profile and the decay in piezoelectric response for days. The mechanism for a decrease in piezoelectric response over time is hypothesized to be caused by rotational diffusion of the dopants due to weak interfacial interactions between the dopant and host matrix, which then leads to depolarization. Larger dopants would likely improve stability by decreasing the rotational diffusion and increasing interaction with the matrix by crosslinking dopants into the polymer.

Underlying concepts of this processing technique have been further substantiated by the investigation works of D.M. Opris and coworkers. As illustrated in Figure 2.9(a), a general workflow was followed as the design strategy for preparing piezoelectric elastomers. The first step involves the synthesis of polar amorphous polymers with T_gs considerably high above room temperature. Unlike inorganic ceramics, these amorphous polymers rely on the presence of molecular dipole units to exhibit piezoelectricity. Besides, the dipoles should be oriented, stabilized in their aligned state and responsive to strain when mechanically stressed.[53] The next steps require transforming these polar polymers into particles by solvent displacement technique, reinforcing them in an elastic PDMS matrix and blade casting into thin films. Finally, quasi-permanent polarization, responsible for the piezoelectric effect, is achieved by poling the films in a strong electric field at temperatures above the T_g of the filler particles. Under such conditions, the dipolar moieties orient in the direction of the electric field, and the achieved orientation is frozen-in by cooling the material back to room

temperature with the field on. In order to maximize piezoelectric efficiency, the proposed system should retain sufficient polarization in the polar filler particles while maintaining low elastic modulus by the intrinsic property shown in the PDMS matrix. Preliminary experiments were conducted to prove this design concept in a typical sample, which was prepared using particles of a polar amorphous polymer, poly [(methyl methacrylate)-*co*-(disperse Red 1 methacrylate)] reinforced in a PDMS matrix. Mechanical properties of the resulting composite could be tailored to obtain an elastic modulus of 10 MPa, which is two orders of magnitude lower than that of commercial PVDF, and a strain at break of 300%. After electrode contact poling the prepared sample, the longitudinal piezoelectric coefficient (d_{33}) as a function of polarization was studied. The reported d_{33} values showed a quadratic growth from an amplitude of 3 to 27 pC/N with increasing polarization.[68] The same research group carried out further investigations to ascertain the stability of piezoelectric response in this material when it is operated in transverse (d_{31}) mode.[69] The observed piezoelectric properties generally experienced a non-exponential decay revealing a strong onset decrease and a pseudo-stable state over one month study period. A stable transverse piezoelectric coefficient (d_{31}) as high as 12 pC/N was recorded, which also proved to be thermally stable up to 50°C.

To thoroughly understand the mechanism behind the time dependent decay in piezoelectric response, a different polar amorphous polymer containing double bonds in its main chains was synthesized and introduced as filler in another study.[70] The hypothetical reason behind this was to introduce enough rigidity into the molecular structure of the polar polymer, which may help limit dipolar relaxations possibly caused by a high degree of intramolecular chain rotations. Additionally, the contributing effects of filler particle size and filler-matrix interface on the eventual decay in remnant polarization were evaluated. Finally, the influence of the type of poling treatment on polarization and the eventual piezoelectric performance was studied. The published findings revealed piezoelectric properties with a similar decay profile as previously reported. Hence, the reason for introducing double bonds in the polar polymer main chains to limit depolarization could not be substantiated. This confirms that thermodynamic instability in oriented structures of polar amorphous polymers is a general intrinsic behavior.[53] Immense theoretical simulations will be required to understand these molecular dynamics in more detail. Concerning particle size variation, the piezoelectric response was reported to increase with decreasing particle size of the polar filler polymer. The observed behavior is likely due to effective stress transfer in composite systems with smaller filler particles than larger ones.[134] Additionally, large interfacial boundaries present in composites with smaller filler particles may possibly serve as charge traps to retain polarization. Another investigation was carried out to deconvolute the possible effect of interfacial relaxation on charge decay, which periodic mechanical strains may cause during operation. This was achieved by performing piezoelectric measurements on two samples that were processed under the same conditions. One was periodically strained for three weeks and the other left stands after poling. The recorded piezoelectric responses were similar, suggesting that charge decay in the prepared

piezoelectric elastomer composite is not significantly influenced by the mechanism of mechanical deformation. Final studies also confirmed that samples subjected to corona poling treatment showed threefold higher piezoelectric properties compared to the ones treated by contact poling. A transverse piezoelectric coefficient up to 37 pC/N could be recorded for the best-performing material poled by corona discharge.

2.4.3 Porous Piezoelectret Elastomer by Foaming techniques

Porous piezoelectret elastomer can also be considered as a composite consisting of a gas phase dispersed in a solid polymer matrix. Thermoplastic polymers such as polyolefins (PO), cyclo-olefin polymers (COP) and their copolymers (COC), polyurethanes (PU), polyvinyl chloride (PVC), poly(ethylene terephthalate) (PET), poly(ethylene naphthalate) (PEN), and fluoropolymers have commonly been used in the preparation of such cellular materials. The technique presents a simple and easy way of preparing flexible and stretchable materials with outstanding electromechanical behavior. Processing requires a combination of foaming and poling methods. Foaming is generally performed by mechanical, physical and chemical means, which is sometimes coupled with extrusion and injection molding processing techniques.[92, 135-136] Alternatively, cellular materials can be achieved by sugar-templating strategies and stretching of particulate-filled polymers to initiate voids at the filler-polymer interfaces through delamination.[137-138] Piezoelectricity can be induced in such voided materials through ionization of the air pockets by applying a sufficiently high electric field. This can be achieved through direct electrode contact poling, corona discharge poling or soft X-ray poling. A typical preparation procedure is schematically represented in Figure 2.10(a-c).

The inner Townsend breakdown triggers whenever the applied charging voltage exceeds a specific threshold value and is responsible for charge deposition in the voids, as shown in Figure 2.10(c).[92] Trapped charges with opposite polarities are then formed on the interior upper and lower surfaces of the voids, to create a dipole-like macroscopic structure. Such compliant polymers, also termed *piezoelectrets* or *ferroelectrets*, containing polarized cavities can respond to electrical or mechanical stimuli similar to the piezoelectric material. Analogous to a displacement of ionic or molecular dipoles in a regular piezoelectric material, the deformation of the charged voids is the cause of the piezoelectric effect. Following a sequence of well-designed preparation steps, the thermal stability, annealing history, dimension, shape and porosity of resulting foamed materials affect piezoelectric response.[92, 139] Since there is a need to maintain polarization in the charged pores, the polymer should ideally be a good dielectric, electrically insulating, and able to retain trapped charges.

Fang et al. reported a cellular PEN piezoelectret fabricated from a commercial PEN polymer film through physical foaming in supercritical carbon dioxide ($scCO_2$), inflation, biaxial stretching, and electrical charging.[139-140] The PEN film was initially soaked in $scCO_2$ at high pressure (150 bar) for

a few hours. The $scCO_2$-saturated polymer was then subjected to heat treatment for a few seconds at a temperature above the glass-transition temperature (T_g) of PEN. The sudden increase in the volume of the $scCO_2$ fluid upon phase change led to the foaming of the film. Subsequently, the voided film was inflated by exposing it to high-pressure gas until the voids were sufficiently filled with pressurized gas and further heat treated to improve the cellular geometry. After inflation, the foamed PEN film was subjected to biaxial stretching to decrease void heights and change geometry to lens-shaped voids. Electrical charging of the voided film was achieved by either electrode contact poling or corona discharge poling under different poling conditions. Piezoelectricity arises from the combination of internally separated and trapped charges and anisotropy in the cellular polymer matrix with very low elastic stiffness. The densities of the prepared foamed PEN films and the poling conditions influenced the reported piezoelectric coefficients (d_{33}). Thus, relatively high d_{33} coefficients could only be achieved in samples with an optimal density approximating 1.1 g/cm^3 and lower elastic stiffness. Generally, samples charged under higher voltages gave off a stronger piezoelectric response. The contact-poled samples exhibited low piezoelectric properties compared to the corona-poled counterparts. Piezoelectric d_{33} coefficients up to 140 pC/N, which proved thermally stable until 80 °C could be achieved. Additionally, samples poled at elevated temperatures below T_g show improved thermal stability in terms of their piezoelectric response than those poled at room temperature.[139]

In another preliminary communication, Galantini et al. presented a piezoelectret elastomer fabricated using cellular polyurethane films and charging by the corona process.[141] The foamed films were prepared via mold casting of an emulsion containing liquid polyurethane precursors (diisocyanate and polyol) and a pre-optimized ratio of distilled water (10 wt. %) suitable for designing porous structures with excellent elasticity and dielectric properties. The molded films were sufficiently cured at ambient temperature for 2 days and subsequently at elevated temperature (60 °C) under vacuum for 24 hours. An adequate enough processing voltage (4.5 kV) was precautionarily applied to corona-charge the prepared cellular samples, and the induced electromechanical properties were evaluated. Wang et al. made a 300 μm thick cellular polydimethylsiloxane (PDMS) structure with micrometer-sized voids internally coated with a thin polytetrafluoroethylene (PTFE) sandwich between two stretchable gold electrodes. An electric field of up to 35 MV m^{-1} was applied to ionize the air in the voids and inject charges onto the inner voids surfaces. The resulting structure is stretchable, has an elastic modulus of about 300 kPa, a stress sensitivity of about 10 mV Pa^{-1}, and shows a piezoelectric coefficient d_{33} of about 1000 pC N^{-1}.[142]

Lacour et al. made a stack of ten polypropylene films consisting of alternating positive/negative charged cellular polypropylene films with a d_{33} = 200 pC/N glued by thin PDMS layers sandwiched between two stretchable electrodes. This piezoelectric device was compliant with human skin and exhibited good pressure sensitivity.[143]

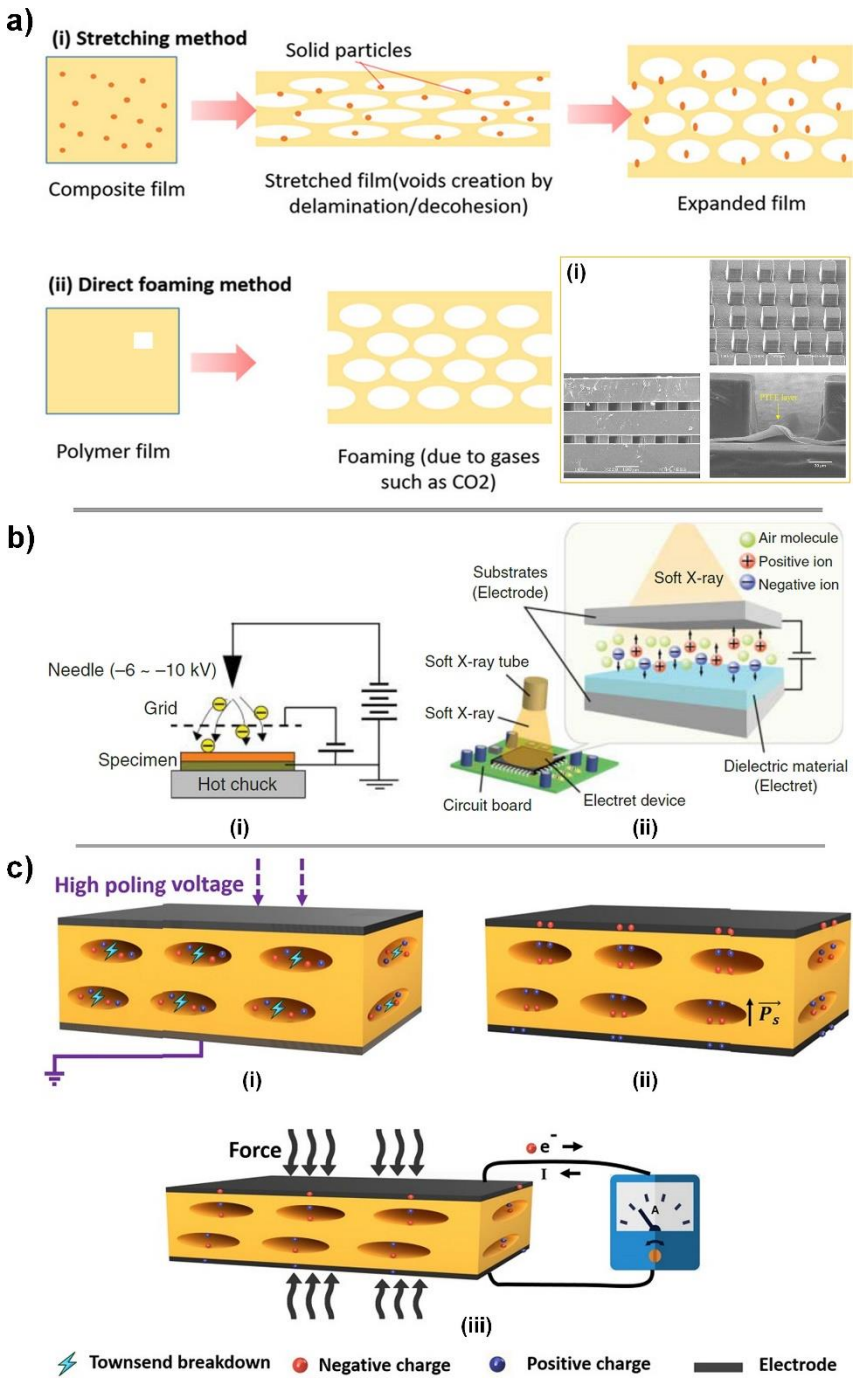

Figure 2.10 Schematic illustration of the preparation and working mechanism of cellular piezoelectrets: a) Route of foaming (i) SEM images of the top view, cross-sectional view, and close view of cellular PDMS microstructures; b) Electric poling methods (i) typical corona charging system and (ii) through-substrate soft-X-ray charging; c) Mechanism of piezoelectret operation (i) Townsend breakdown under a high poling voltage following Paschen's law for a breakdown in air, (ii) charged sample having positive/negative electrical charges on the opposite faces of the polymer surfaces with the polarization of Ps, (iii) piezoelectrically induced charge flow when an external force applied along the polarization direction. Reproduced with permission.[92, 138, 144-145] Copyright 2015, Micro Energy Harvesting, Copyright 2019, Nano Energy, Copyright 2022, Advanced Energy and Sustainability Research.

Zhong et a. designed a sandwich-structure piezoelectret composed of two fluorinated ethylene propylene (FEP) electret films which sandwich an Ecoflex film with holes as a spacer. The electrical connections were made using a gold (Au) and an aluminum (Al) electrode on the top and bottom of the piezoelectret, respectively. A piezoelectric coefficient as high as 4050 pC/N and a stable response was reported.[146] Tsai et al. developed cellular PDMS films internally coated with a thin layer of PTFE. The charges generated in the voids during poling are deposited on the PTFE. The designed structure showed an elastic modulus of about 300 kPa and a piezoelectric coefficient d_{33} of about 1500 pC/N.[145] Similarly, Kachroudi et al. made micro-structured cellular polydimethylsiloxane (PDMS) with an area of 2×2 cm^2 and a total thickness of 150 μm consisting of two bulk layers separated by the microstructured one and coated with two gold electrodes and charged it at 1 kV and 4 kV and a frequency of 0.5 Hz. The device showed a piezoelectric coefficient d_{33} of 350 pC/N, which is ten times larger than polyvinylidene fluoride.[60]

Recently, Hu et al. used the sugar-templating method coupled with corona poling to design a soft and stretchable piezoelectret with outstanding electromechanical behavior.[147] The porous material was first prepared by simply mixing a solution of silicone-based elastomeric kit (Sylgard 184 PDMS) in proportionate amounts with polytetrafluoroethylene (PTFE) fillers and sugar particles. The resulting viscous mixture was mold-cast and sufficiently cured at elevated temperatures. The cured mold was repeatedly soaked in warm water to dissolve the sacrificial sugar template and oven-dried thereafter. Uniformly distributed porous structures, composed of PTFE particles immobilized in the PDMS matrix, were obtained and the extent of porosity could be tuned by the amount of sugar particles added. Following electrical treatment, the pores are internally charged, generating "pseudo" macroscopic dipoles. The direct piezoelectric coefficient was evaluated by a quasi-static and dynamic method. A quasi-static piezoelectric coefficient (d_{33}^{eff}) up to 477 pC/N could be attained when the polarized porous piezoelectret was subjected to 5 N external load. The piezoelectric performance was proven to strongly depend on the PTFE filler content, the extent of polarization, which directly informs the number of macroscopic dipoles generated, porosity and the charge retention capabilities of the piezoelectret, and the measuring frequency. As reported, the d_{33} coefficient was almost stable after a week of periodic measurements. Ma et al. made a porous structure by mixing a polydimethylsiloxane (PDMS) matrix with PZT particles and NaCl powder, whereby the NaCl powder served as a sacrificial filler. The formed composite was polarized at an electric field of 1.6 kV/mm. A generator with dimensions of 2 × 2 × 0.3 cm^3 gave an open-circuit voltage of 29 V and a short-circuit current of 116 nA under 30 N.[148]

2.4.4 Intrinsic Piezoelectric Elastomer Synthesis

Organic synthetic methods have also been employed in the de novo design and processing of elastomers with piezoelectric properties. The strategy used here is to carefully select reaction pathways from the organic toolbox that can eventually affect structural modifications and long-range intermolecular assembly of dipolar moieties when an electrical or mechanical stimulus is applied. Molecular structure illustrations of elastomers with intrinsic piezoelectric behavior can be found in Figure 2.11.

One of the earliest preliminary studies on the synthesis of elastic materials which exhibit intrinsic piezoelectricity was conducted by Rudolf Zentel in the late 1980s.[149-152] A consideration based on incorporating mesogenic molecular moieties in polymer main chains and/or as side groups and crosslinking into liquid crystalline elastomers (LCEs). Synthetic techniques used, thus far, in fabricating LCEs include free radical copolymerization of acrylates or methacrylates,[153-154] hydrosilylation of silicon hydride and alkene,[155-157] azeotropic or melt polycondensation of diols with allylmalonic acid or diethyl allylmalonate, polyaddition of epoxy and carboxylic acid[149, 158-159], and other reactions involving click chemistry. Li et al. recently published a comprehensive review of emerging synthetic approaches to LCEs.[160] LCEs combine the orientability of mesogenic groups into ordered liquid crystalline (LC) phases with elasticity and flexibility inherent to rubbers. Piezoelectric properties can be achieved depending on the chirality of the mesogens and the retained LC phases in the LCEs. Thus, applying sufficient mechanical stress to these crosslinked elastomers causes conformational changes in the polymer main chains and effects reorientation in the LC phase. This eventually can transform the chiral phase with zero net polarization into structures with macroscopic polarization making them promising materials in electro-optics, energy harvesting, flexible electronics, and actuator technologies.[151, 161-163]

In 2010, Heinze et al. investigated a homologous series of chiral LCEs to understand further how varying amounts of chiral dopant influenced the crystal phase ordering and the electromechanical properties. Hydrosilylation step-growth reaction was employed to synthesize chiral smectic C* main chain LCEs, with chirality achieved by doping a smectic C host system. The effect of shear stress in reorienting the LC phase was studied by measuring spontaneous polarization and X-ray diffraction.

Generally, exposure to shear deformation caused a macroscopic realignment of the chiral Smectic C* phase leading to electric polarization. The formation of charges on the elastomer surface due to polarization was linearly dependent on smaller shear angles with an onset of a distant nonlinearity above 25° angle. Additionally, the measured spontaneous polarization showed a linear dependence on the amount of chiral dopant with a value up to 370 $\mu C/m^2$attainable. That is to say, doping LCEs with chiral mesogens induces the formation of domains with permanent electric dipole moments, which cause them to exhibit piezoelectric properties.

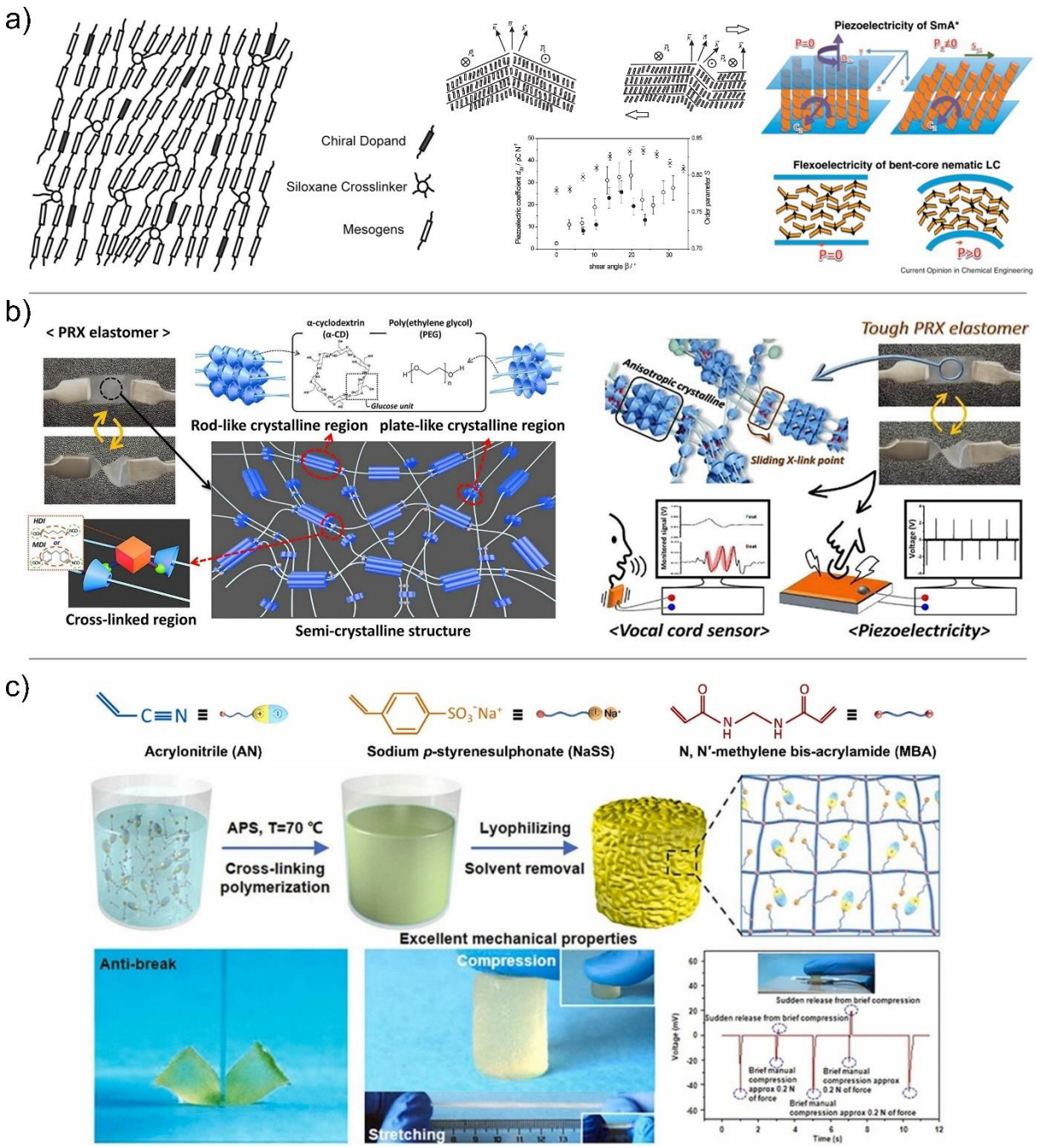

Figure 2.11 Schematic illustration of the molecular structures of elastomers with intrinsic piezoelectric behavior and the physical mechanism for generating piezoelectricity: a) Structural representation of main-chain smectic C* LCEs. A chiral dopant is added to induce the formation of domains with a permanent electric dipole moment. Effects of shear on making the elastomer piezoelectric by phase conversion reflect in the increase of the piezoelectric coefficient; b) Internal structure of PRX elastomers composed of ring-shaped α-CD host molecules threaded on linear PEG guest polymer chains and representation of electrical signal generated by voice pitch and finger touch; c) Fabrication procedure for poly(sodium *p*-styrenesulphonate-*co*-acrylonitrile) copolymer crosslinked network with representative photographs and electric signal generation. Reproduced with permission.[16, 164-165] Copyright 2010, Macromolecules, Copyrights 2013, 2021 and 2022 Elsevier.

Following this publication, Papadopoulos et al., in the same year, studied further the piezoelectric behavior on one of the doped smectic C* liquid crystal elastomers as a function of shear, static mechanical stress, frequency, and temperature.[164] The investigation confirmed that processing by shear effectively produces electromechanically active LCEs and the exact set shear parameters are crucial in realizing optimal performance. The optimum direct piezoelectric coefficient (d_{33} = 35 pC/N) was measured for samples processed at a shear angle of 22°, which is in agreement with the report by Heinze et al. Although the reported elastic modulus was almost independent of frequency over three decades (1 -1,000 Hz), the d_{33} value shows a clear decrease with increasing frequency. This is attributed to large mechanical losses at frequencies above 10 Hz. The elastomer exhibited a constant d_{33} value with increasing static mechanical stress up to ~0.3 MPa (corresponding to a static strain deformation of approximately 3%) but decreased drastically thereafter. The plummeting electromechanical response at larger static deformations is ascribed to distortion in the morphology of the LC phase monodomain. Furthermore, the elastomer showed an increasing d_{33} response as a function of temperature until the smectic C*-to-isotropic phase transition is reached, after which a sharp irreversible drop is observed. In summary, the d_{33} value does not change by more than a factor of 2 within a broad frequency, temperature, and static deformation range.

A recent study by Zhou and coworkers unveiled another technique to fabricate elastomers with inherent piezoelectric properties.[15] This facile process involves a one-pot free radical crosslinking copolymerization of acrylonitrile, sodium p-styrene sulphonate, and N-methylene bisacrylamide in dimethyl sulfoxide (DMSO), which yielded a poly(sodium p-styrenesulphonate-*co*-acrylonitrile) organogel. The organogel was then freeze-dried to remove DMSO and form an elastic copolymer network with highly polar groups. The structural morphology could be retained due to the electrostatic repulsion and spatial resistance caused by the sodium p-styrenesulphonate ionic monomer coupled with the loosely crosslinked network induced by freeze-drying. This eventually limits the possibility of intermolecular dipolar interactions of the acrylonitrile units and enhances the internal mobility of the highly polar nitrile side groups. Subjecting this elastomer to mechanical deformation facilitates change in polarization due to dipole movement and rotation from the randomized zero net polarization equilibrium position to a non-zero net polarization state. Thus, the bulk elastomer can be easily polarized by mechanical stress courtesy of its low Young’s modulus and the abundant interspaced nitrile side groups with high polarity. The fabricated soft tissue-like elastomer could therefore display excellent electromechanical behavior with an appreciably high piezoelectric charge coefficient of 40 pC/N and a recoverable elasticity under 100% strain. Additionally, this elastomer exhibited a fast and stable electrical response, good mechanical damping qualities, and excellent sensitivity attributed to the stress-induced polarization behavior inherent to the material. Due to this material's elastic and piezoelectric responsiveness, it has been demonstrated and proposed for application as a potential artificial skin for simultaneous impact protection and self-sensing, as well as continuous human pulse monitoring.

Functionally graded polyrotaxane (PRX) elastomers composed of ring-shaped α-cyclodextrin (α-CD) host molecules threaded on linear poly(ethylene glycol) (PEG) guest polymer chains have also been demonstrated to exhibit piezoelectric effect by Ji-Hun Seo and coworkers.[16] This polymer was crosslinked with diisocyanates via urethane bond formation by taking advantage of the hydroxyl groups on α-CDs. The elastic properties could be tuned by the type and amount of crosslinker used. Among the non-crosslinked adjacent α-CD bundles, the PRX polymer chains could associate through hydrogen bonding to form hexagonally packed anisotropic crystalline domains. The level of anisotropy and crystallinity, which is informed by the blend ratio of PRX polymers with different chain lengths, determines the piezoelectric activity. Meanwhile, the partially crosslinked α-CD molecules maintain a “slide-ring” pulley effect responsible for the mechanical integrity of the elastomer. The PRX elastomer was therefore reported to show superior mechanical properties comparable to commercially available PDMS and piezoelectric charge coefficient ($\boldsymbol{d_{33}}$) of 7 pC/N. A piezoelectric device fabricated from the elastomer with optimal characteristics gave a stable open-circuit voltage of 3.7 V, a current density of 360 nA cm^{-2}, and a power density of 1.34 μW cm^{-2} upon repeated cyclic test. The scientists then attached this device to a nose mask and reported an enhanced piezosensitivity against the mechanical vibrations generated by respiratory signals proving the novelty of employing this smart elastomer as an energy harvester.[16-17] A. G. B. da Cruz et al. made a collagen blend in 10% natural rubber. While the d_{14} of the blend decreased from 0.057 pC/N for neat collagen to 0.042 pC/N, the addition of NR increased the thermal stability.[166] Also, a polyurethane elastomer poled at 25 MV/m was reported to show a d_{31} of 184 pC/N.[167] Unfortunately, polyurethanes are a broad class of polymers; thus, it is difficult to determine the exact molecular composition showing these outstanding properties.

2.4.5 Additive Manufacturing

The underlying concept of this processing technique can be dated back to the invention work of Charles Hull in 1986, which paved the way for designing complex architectures from printable functional materials. Generally, additive manufacturing refers to the fabrication of three-dimensional (3D) complex structures via controlled deposition of materials in printable ink forms. The inks employed include metals, ceramics, polymers, and their hybrid blends. The operation begins with designing 3D virtual models segmented into numerous 2D horizontal cross-sections based on computer-aided design (CAD) software. Successive printing of a new 2D layer on top of previous layers leads to the fabrication of a coherent 3D object.[21, 168] Further extensions known as 4D printing, which considers time-dependent variables to trigger printing through external stimuli such as electromagnetism, temperature, pH, and light, have also been reported.[169-171] The technique serves as a big umbrella that describes several processes of constructing designed parts in a layer-by-layer fashion. These include stereolithography, selective layer sintering, direct ink writing, solvent

evaporation-assisted 3D printing, fused deposition modelling, digital light processing, electric poling-assisted additive manufacturing, and many more. Figure 2.12(a) shows graphical representations of some additive manufacturing techniques. A detailed description of these processes can be found in other reviews.[21, 172-173] The technology has gained widespread application due to its advantages, such as low manufacturing cost, high material utilization, production precision, and the absence of structural restrictions during printing.

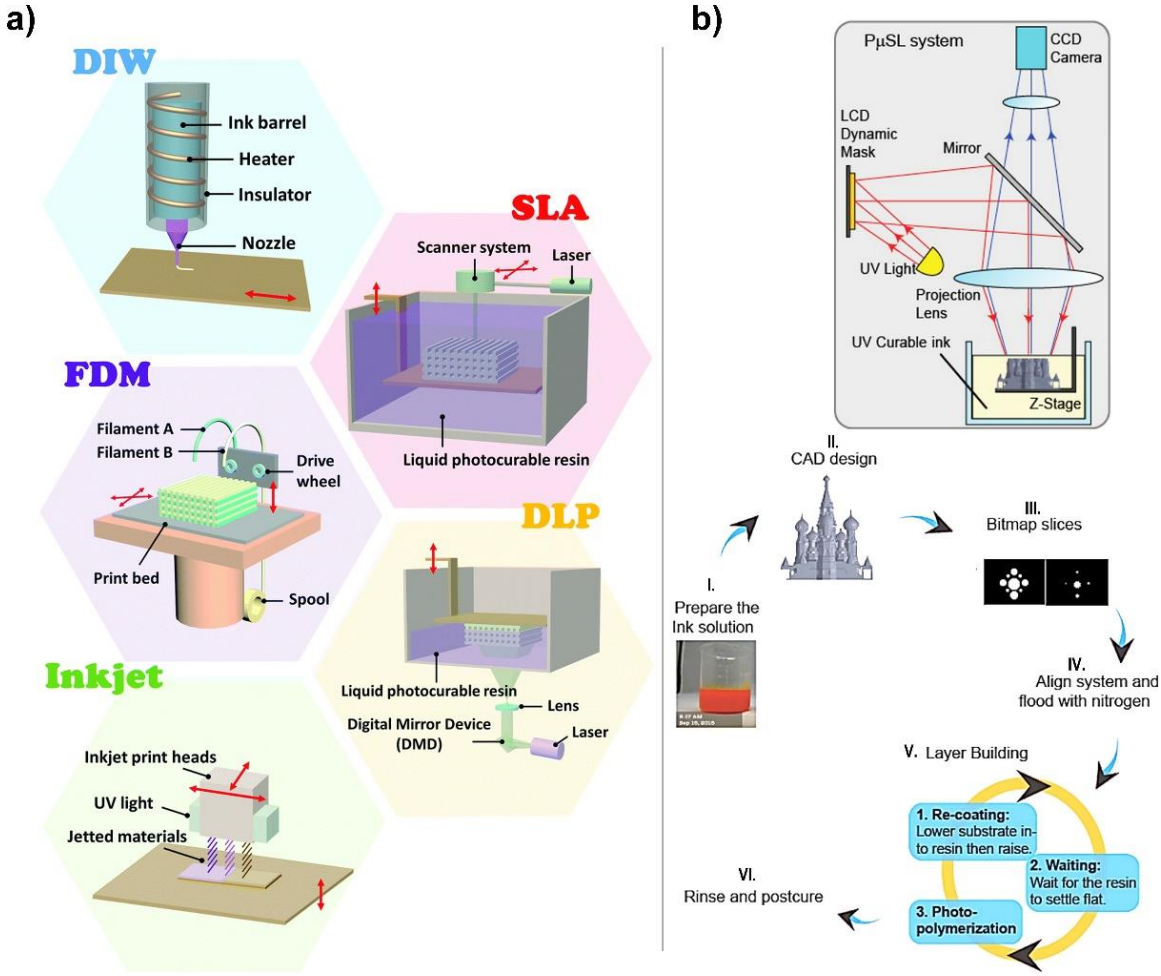

Figure 2.12 Schematic illustration of additive manufacturing techniques: a.) Extrusion-based direct ink writing (DIW) and fused deposition modeling (FDM) form 3D projects in a line-by-line and then layer-by-layer manner. Photopolymerization-based stereolithography (SLA) and digital light processing (DLP) can print in sub-micron resolution with high fidelity. SLA employs a laser beam and scanner system, while DLP relies on a digital mirror device (DMD) to achieve dynamic pattern generation. Inkjet printing uses a thermal or piezoelectric actuator to jet materials. Reproduced with permission; b.) A typical projection micro-stereolithography (PμSL) system and the 3D printing process flow. Reproduced with permission.[18, 171] Copyright 2017, Procedia CIRP, Copyright 2022, Materials Horizons.

Additively assembled piezoelectric elastomers are gradually gaining popularity for their optimized application in sensors, actuators, energy harvesters and tissue engineering.[19-20, 174] Cheng Sun and coworkers recently developed a piezoelectric polymer photo-curable ink suitable for 3D printing by projection micro-stereolithography (PµSL) processing technique.[18] The formulated ink contained PDVF particles as the piezo-active phase, 1,6-hexanediol diacrylate monomer as a matrix, Irgacure 819 as a photoinitiator, Sudan I as a UV absorber, and diethyl fumarate as a solvent to adjust the viscosity. Considering a trade-off between manufacturability and piezoelectric characteristics, the ink could be optimized to contain 35 wt.% PVDF, 40 wt.% 1,6-hexanediol diacrylate, 2.2 wt.% photoinitiator, 0.12 wt.% UV absorber and 22.68 wt.% solvent. A schematic illustration of the PµSL system and the 3D printing process flow is shown in Figure 2.12(b). Following a 3D CAD model, the substrate on which the printing is to be made is vertically mounted and aligned with a movement precision of 0.5 µm. The printing process is then initiated, and after depositing each layer, the resin is exposed to UV light via a dynamic mask to cure in a controlled photopolymerization fashion. By repeating these steps for each layer, complex 3D structures with customized geometries could be rapidly designed. On completion, the fabricated device was rinsed in diethyl fumarate to remove the uncured residues and further exposed to UV irradiation to cure the structures completely. A piezoelectric voltage coefficient (g_{33}) of 105 mV m/N following a poling treatment was reported, comparable to that of pure PVDF film.

2.5 Summary and Future Perspective

The rapid technological advancement towards a more humane future increasingly demands energy harvesters, sensors, and actuators that can be easily integrated into devices. In respect of this, piezoelectric materials with improved elastic integrity, excellent electromechanical transduction effect, ease of processing, and pliability at complex interfaces, among other advantages, become relevant aspects for the outlined applications. Approaching this from the material design perspective will concurrently require looking into the fabrication methods. We have therefore presented a concise overview of processing techniques adopted in the development of piezoelectric elastomers. The basic history and fundamental mechanisms of piezoelectricity from the materials' viewpoint have been briefly discussed. As described, the performance of piezoelectric elastomers can be enhanced through several effective processing strategies. Compositing techniques have been employed in fabricating stretchable hybrid materials, which take advantage of the elastic properties of elastomer matrices and the piezoelectric behavior of the filler. However, designing such materials to give collegial properties than the separate properties of each component will require significant effort in optimizing fabrication conditions and understanding the structural-property relations. For instance, ceramic-polymer-based composite materials prepared by random dispersion of ceramic fillers in the elastic matrices often result in limited connectivity. Hence, issues pertaining to permittivity mismatch

between the two phases arise, which result in non-uniform electric field distribution when poling. This causes weak levels of polarization and piezoelectric activity. Higher connectivity of the ceramic phase can be achieved with dielectrophoresis and 3D interconnected structures designed from sacrificial templates. Although higher dimensional connectivity of the ceramic component results in impressive piezoelectric performance, they are restricted when subjected to high mechanical strains. Therefore, the tradeoff between elasticity and piezoelectricity will demand a further understanding of the interfacial effect to gain more structural insight into the composites. Also, careful domain and interfacial engineering may assist in designing composites with intriguing performance. Other processing strategies discussed have likewise achieved a certain level of development, but intrinsic material characteristics and availability are bottlenecks for implementation. For example, the emergence of additive manufacturing provides new advantages for integrating piezoelectric elements into devices by eliminating tedious assembly and packaging steps during fabrication to improve manufacturing efficiency and performance of the device. However, the technology is not very matured for piezoelectric elastomer materials and still limited to experimentation and prototyping. It is, therefore, necessary to discover materials that can withstand processing conditions, and at the same time, present high performance. These problems hinder the development of piezoelectric elastomer materials, and solving key technical problems should be the focus of future research.

2.6 References

[1] W. Heywang, K. Lubitz, W. Wersing, in *Springer series in materials science 114*, DOI: 10.1007/978-3-540-68683-5, Springer, Berlin 2008, Online.

[2] H. S. Nalwa, *Ferroelectric polymers: chemistry: physics, and applications*, CRC Press, **1995**.

[3] S. Bauer, F. Bauer, in *Piezoelectricity: Evolution and Future of a Technology*, DOI: 10.1007/978-3-540-68683-5_6, Springer Berlin Heidelberg, Berlin, Heidelberg **2008**, p. 157.

[4] F. Carpi, D. De Rossi, R. Kornbluh, R. Pelrine, P. Sommer-Larsen, *Dielectric Elastomers as Electromechanical Transducers: Fundamentals, Materials, Devices, Models and Applications of an Emerging Electroactive Polymer Technology* **2008**, DOI: Doi 10.1016/B978-0-08-047488-5.00033-2Ix.

[5] M. Shirvanimoghaddam, K. Shirvanimoghaddam, M. M. Abolhasani, M. Farhangi, V. Z. Barsari, H. Liu, M. Dohler, M. Naebe, *IEEE Access* **2019**, 7, 94533.

[6] Y. Liu, H. Wang, W. Zhao, M. Zhang, H. Qin, Y. Xie, *Sensors (Basel)* **2018**, 18, 645.

[7] S.-T. Han, H. Peng, Q. Sun, S. Venkatesh, K.-S. Chung, S. C. Lau, Y. Zhou, V. A. L. Roy, *Advanced Materials* **2017**, 29, 1700375.

[8] F. Xu, X. Li, Y. Shi, L. Li, W. Wang, L. He, R. Liu, *Micromachines* **2018**, 9, 580.

[9] F. Narita, M. Fox, *Advanced Engineering Materials* **2018**, 20, 1700743.

[10] Z. Yang, S. Zhou, J. Zu, D. Inman, *Joule* **2018**, 2, 642.

[11] H. Maiwa, “Piezoelectric Energy Harvesting,” Piezoelectric Materials, InTech 2016, doi:10.5772/64162.

[12] Y. Zhang, C. K. Jeong, T. Yang, H. Sun, L.-Q. Chen, S. Zhang, W. Chen, Q. Wang, *Journal of Materials Chemistry A* **2018**, 6, 14546.

[13] X. Cheng, Y. Gong, Y. Liu, Z. Wu, X. Hu, *Smart Materials and Structures* **2020**, 29, 075007.

[14] S. Hu, Z. Shi, W. Zhao, L. Wang, G. Yang, *Composites Part B: Engineering* **2019**, 160, 595.

[15] R. Fu, L. Tu, Y. Guan, Z. Wang, C. Deng, P. Yu, G. Tan, C. Ning, L. Zhou, *Nano Energy* **2022**, 103, 107784.

[16] J. Seo, J. Hur, M.-S. Kim, T.-G. Lee, S. J. Seo, S. H. Han, J.-H. Seo, *Chemical Engineering Journal* **2021**, 426, 130792.

[17] J. Seo, B. Kim, M.-S. Kim, J.-H. Seo, *ACS Macro Letters* **2021**, 10, 1371.

[18] X. Chen, H. O. T. Ware, E. Baker, W. Chu, J. Hu, C. Sun, *Procedia CIRP* **2017**, 65, 157.

[19] J.-I. Park, G.-Y. Lee, J. Yang, C.-S. Kim, S.-H. Ahn, *Journal of Composite Materials* **2015**, 50, 1573.

[20] E. Cesewski, A. P. Haring, Y. Tong, M. Singh, R. Thakur, S. Laheri, K. A. Read, M. D. Powell, K. J. Oestreich, B. N. Johnson, *Lab Chip* **2018**, 18, 2087.

[21] C. Chen, X. Wang, Y. Wang, D. Yang, F. Yao, W. Zhang, B. Wang, G. A. Sewvandi, D. Yang, D. Hu, *Advanced Functional Materials* **2020**, 30, 2005141.

[22] M. T. Chorsi, E. J. Curry, H. T. Chorsi, R. Das, J. Baroody, P. K. Purohit, H. Ilies, T. D. Nguyen, *Advanced Materials* **2019**, 31, 1802084.

[23] X. Tang, X. Wang, R. Cattley, F. Gu, A. D. Ball, *Sensors (Basel)* **2018**, 18, 4113.

[24] N. A. Spaldin, R. Ramesh, *Nature Materials* **2019**, 18, 203.

[25] Q. Zheng, B. Shi, Z. Li, Z. L. Wang, *Advanced Science* **2017**, 4, 1700029.

[26] C. Covaci, A. Gontean, *Sensors (Basel)* **2020**, 20, 3512.

[27] G. Clementi, F. Cottone, A. Di Michele, L. Gammaitoni, M. Mattarelli, G. Perna, M. López-Suárez, S. Baglio, C. Trigona, I. Neri, *Energies* **2022**, 15, 6227.

[28] K. I. Park, C. K. Jeong, N. K. Kim, K. J. Lee, *Nano Converg.* **2016**, 3, 12.

[29] H. Zhou, Y. Zhang, Y. Qiu, H. Wu, W. Qin, Y. Liao, Q. Yu, H. Cheng, *Biosensors and Bioelectronics* **2020**, 168, 112569.

[30] V. Vallem, Y. Sargolzaeiaval, M. Ozturk, Y.-C. Lai, M. D. Dickey, *Advanced Materials* **2021**, 33, 2004832.

[31] R. Gerhard, SPIE, **2016,** 9798, 97980T

[32] J. Chen, Q. Qiu, Y. Han, D. Lau, *Renewable and Sustainable Energy Reviews* **2019**, 101, 14.

[33] S. Katzir, *Archive for History of Exact Sciences* **2003**, 57, 61.

[34] S. Katzir, *Historical Studies in the Physical and Biological Sciences* **2003**, 34, 69.

[35] R. Gerhard, in *Electromechanically Active Polymers: A Concise Reference*, 1st ed. (Ed: F. Carpi), Polymers and Polymeric Composites Series, Springer, Berlin **2016**, p. 489. DOI: 10.1007/978-3-319-31530-0_21

[36] S. Katzir, *Studies in History and Philosophy of Science Part B: Studies in History and Philosophy of Modern Physics* **2003**, 34, 579.

[37] A. Jain, P. K. J., A. K. Sharma, A. Jain, R. P.N, *Polymer Engineering & Science* **2015**, 55, 1589.

[38] G. H. Haertling, *Journal of the American Ceramic Society* **1999**, 82, 797.

[39] Y.-h. Xu, Ferroelectric Materials and Their Applications, Elsevier, Amsterdam, **1991**, 60.

[40] E. K. Akdogan, M. Allahverdi, A. Safari, *IEEE Transactions on Ultrasonics, Ferroelectrics, and Frequency Control* **2005**, 52, 746.

[41] E. Fukada, *Journal of the Physical Society of Japan* **1955**, 10, 149.

[42] E. Fukada, I. Yasuda, *Journal of the Physical Society of Japan* **1957**, 12, 1158.

[43] C. A. Bassett, R. O. Becker, *Science* **1962**, 137, 1063.

[44] M. H. Shamos, L. S. Lavine, M. I. Shamos, *Nature* **1963**, 197, 81.

[45] E. Fukada, I. Yasuda, *Japanese Journal of Applied Physics* **1964**, 3, 117.

[46] M. H. Shamos, L. S. Lavine, *Nature* **1967**, 213, 267.

[47] E. Fukada, *Wood Science and Technology* **1968**, 2, 299.

[48] H. Kawai, *Japanese Journal of Applied Physics* **1969**, 8, 975.

[49] N. A. Suttle, *Materials & Design* **1988**, 9, 318.

[50] J. S. Harrison, Z. Ounaies, Piezoelectric Polymers. In Encyclopedia of Polymer Science and Technology, (Ed.), **2002**, https://doi.org/10.1002/0471440264.pst427

[51] M. Smith, S. Kar-Narayan, *International Materials Reviews* **2022**, 67, 65.

[52] E. Fukada, *Annals of the New York Academy of Sciences* **1974**, 238, 7.

[53] Z. Ounaies, J. A. Young, J. S. Harrison, in *Field Responsive Polymers*, Vol. 726, American Chemical Society **1999**, Ch. 6, p. 88.

[54] C. Park, Z. Ounaies, K. E. Wise, J. S. Harrison, *Polymer* **2004**, 45, 5417.

[55] E. Fukada, *IEEE Transactions on Dielectrics and Electrical Insulation* **2006**, 13, 1110.

[56] S. Bauer, R. Gerhard-Multhaupt, G. M. Sessler, *Phys. Today* **2004**, 57, 37.

[57] S. R. Anton, K. Farinholt, A. Erturk, *Journal of Intelligent Material Systems and Structures* **2014**, 25, 1681

[58] E. Fukada, *IEEE Transactions on Ultrasonics, Ferroelectrics, and Frequency Control* **2000**, 47, 1277.

[59] J. S. Hundal, R. Nath, *Journal of Physics D: Applied Physics* **1998**, 31, 482.

[60] A. Kachroudi, S. Basrour, L. Rufer, A. Sylvestre, F. Jomni, *Smart Materials and Structures* **2016**, 25, 105027.

[61] G. M. Sessler, *Journal of Electrostatics* **2001**, 51-52, 137.

[62] S. Zhang, Y. Wang, X. Yao, P. Le Floch, X. Yang, J. Liu, Z. Suo, *Nano Letters* **2020**, 20, 4580.

[63] M. Krause, I. Graz, S. Bauer-Gogonea, S. Bauer, B. Ploss, M. Zirkl, B. Stadlober, U. Helbig, *Ferroelectrics* **2011**, 419, 23.

[64] C. Baur, D. J. Apo, D. Maurya, S. Priya, W. Voit, in *Polymer Composites for Energy Harvesting, Conversion, and Storage*, Vol. 1161, American Chemical Society **2014**, Ch. 1, p. 1.

[65] J.-J. Choi, B.-D. Hahn, J. Ryu, W.-H. Yoon, B.-K. Lee, D.-S. Park, *Sensors and Actuators A: Physical* **2009**, 153, 89.

[66] K. Kim, W. Zhu, X. Qu, C. Aaronson, W. R. McCall, S. Chen, D. J. Sirbuly, *ACS Nano* **2014**, 8, 9799.

[67] R. A. Surmenev, T. Orlova, R. V. Chernozem, A. A. Ivanova, A. Bartasyte, S. Mathur, M. A. Surmeneva, *Nano Energy* **2019**, 62, 475.

[68] Y. S. Ko, F. A. Nüesch, D. Damjanovic, D. M. Opris, *Advanced Materials* **2017**, 29, 1603813.

[69] Y. S. Ko, F. A. Nüesch, D. M. Opris, *Journal of Materials Chemistry C* **2017**, 5, 1826.

[70] F. Owusu, F. A. Nüesch, D. M. Opris, *Advanced Functional Materials* **2022**, 32, 2207083.

[71] M. Paajanen, J. Lekkala, H. Valimaki, *IEEE Transactions on Dielectrics and Electrical Insulation* **2001**, 8, 629.

[72] A. Mellinger, M. Wegener, W. Wirges, R. Gerhard-Multhaupt, *Applied Physics Letters* **2001**, 79, 1852.

[73] A. Arnau, D. Soares, in *Piezoelectric Transducers and Applications*, DOI: 10.1007/978-3-540-77508-9_1 (Ed: A. A. Vives), Springer Berlin Heidelberg, Berlin, Heidelberg **2008**, p. 1.

[74] R. S. Dahiya, M. Valle, *Robotic tactile sensing : technologies and system*, Springer, Dordrecht ; New York **2013**.

[75] A. Carter, K. Popowski, K. Cheng, A. Greenbaum, F. S. Ligler, A. Moatti, *Bioelectricity* **2021**, 3, 255.

[76] IEEE Standard on Piezoelectricity, ANSI/IEEE Std 176-1987 **1988** Pages 0_1, DOI: 10.1109/IEEESTD.1988.79638.

[77] B. A. Capron, D. W. Hess, *IEEE Transactions on Ultrasonics, Ferroelectrics, and Frequency Control* **1986**, 33, 33.

[78] E. Defaÿ, Integration of ferroelectric and piezoelectric thin films concepts and applications for microsystems, ISTE, London **2011**, DOI: 10.1002/978111861663.

[79] S. O. R. M. A. J. Fleming, in *Piezoelectric Transducers for Vibration Control and Damping*, DOI: 10.1007/1-84628-332-9_2 (Eds: S. O. R. Moheimani, A. J. Fleming), Springer London, London **2006**, p. 9.

[80] W. A. Smith, B. A. Auld, *IEEE Transactions on Ultrasonics, Ferroelectrics, and Frequency Control* **1991**, 38, 40.

[81] E. Fukada, M. Date, *Journal of Macromolecular Science, Part B* **1973**, 8, 463.

[82] E. Fukada, *Quarterly Reviews of Biophysics* **1983**, 16, 59.

[83] R. Hayakawa, Y. Wada, Piezoelectricity and related properties of polymer films, Fortschritte der Hochpolymeren-Forschung, Springer Berlin Heidelberg **1973**, 1-55.

[84] L. Eric Cross, Ferroelectric Ceramics: Tailoring Properties for Specific Applications, Birkhäuser Basel **1993**, 1-85

[85] T. J. Lewis, presented at Annual Report Conference on Electrical Insulation and Dielectric Phenomena, 20-24 Oct. 2002, **2002**.

[86] S. Katzir, *THE BEGINNINGS OF PIEZOELECTRICITY A Study in Mundane Physics*, **2006**.

[87] D. Damjanovic, M. D. Maeder, P. D. Martin, C. Voisard, N. Setter, *Journal of Applied Physics* **2001**, 90, 5708.

[88] R. Kressmann, *Journal of Applied Physics* **2001**, 90, 3489.

[89] S. Bauer, *IEEE Transactions on Dielectrics and Electrical Insulation* **2006**, 13, 953.

[90] R. Dahiya, M. Valle, *de Robotic Tactile Sensing., Springer* **2013**.

[91] M. Stewart, M. G. Cain, in *Characterisation of Ferroelectric Bulk Materials and Thin Films*, DOI: 10.1007/978-1-4020-9311-1_3 (Ed: M. G. Cain), Springer Netherlands, Dordrecht **2014**, p. 37.

[92] Y. Zhang, C. R. Bowen, S. K. Ghosh, D. Mandal, H. Khanbareh, M. Arafa, C. Wan, *Nano Energy* **2019**, 57, 118.

[93] T. Yamada, T. Ueda, T. Kitayama, *Journal of Applied Physics* **1982**, 53, 4328.

[94] R. Gerhard, presented at 2014 IEEE Conference on Electrical Insulation and Dielectric Phenomena (CEIDP), 19-22 Oct. 2014, **2014**.

[95] R. Gerhard, S. Bauer, X. Qiu, presented at 2016 IEEE Conference on Electrical Insulation and Dielectric Phenomena (CEIDP), 16-19 Oct. 2016, **2016**.

[96] S. B. Lang, D. K. Das-Gupta, in *Handbook of Advanced Electronic and Photonic Materials and Devices*, DOI: https://doi.org/10.1016/B978-012513745-4/50036-6 (Ed: H. Singh Nalwa), Academic Press, Burlington **2001**, p. 1.

[97] R. E. Newnham, D. P. Skinner, L. E. Cross, *Materials Research Bulletin* **1978**, 13, 525.

[98] V. L. Stuber, D. B. Deutz, J. Bennett, D. Cannel, D. M. de Leeuw, S. van der Zwaag, P. Groen, *Energy Technol.* **2019**, 7, 177.

[99] X. Gao, M. Zheng, X. Yan, J. Fu, M. Zhu, Y. Hou, *Journal of Materials Chemistry C* **2019**, 7, 961.

[100] X. Gao, M. Zheng, X. Yan, J. Fu, Y. Hou, M. Zhu, *Nanoscale* **2020**, 12, 5175.

[101] G. Zhang, P. Zhao, X. Zhang, K. Han, T. Zhao, Y. Zhang, C. K. Jeong, S. Jiang, S. Zhang, Q. Wang, *Energy & Environmental Science* **2018**, 11, 2046.

[102] A. Lutsch, *Nature* **1959**, 184, 1458.

[103] S. Qian, L. Qin, J. He, N. Zhang, J. Qian, J. Mu, W. Geng, X. Hou, X. Chou, *Materials Letters* **2020**, 261, 127119.

[104] R. Tandon, D. Chaubey, R. Singh, N. Soni, *Journal of materials science letters* **1993**, 12, 1182.

[105] H. Banno, *Ferroelectrics* **1983**, 50, 3.

[106] K. Ogura, M. Nishiki, H. Banno, *Japanese Journal of Applied Physics* **1992**, 31, 278.

[107] I. Choudhry, H. R. Khalid, H.-K. Lee, *ACS Applied Electronic Materials* **2020**, DOI: 10.1021/acsaelm.0c00636.

[108] X. Jiang, S. Wen, L. Zhang, L. Liu, *Polymer-Plastics Technology and Engineering* **2008**, 47, 1273.

[109] C. K. Jeong, J. Lee, S. Han, J. Ryu, G.-T. Hwang, D. Y. Park, J. H. Park, S. S. Lee, M. Byun, S. H. Ko, K. J. Lee, *Advanced Materials* **2015**, 27, 2866.

[110] X. Chou, J. Zhu, S. Qian, X. Niu, J. Qian, X. Hou, J. Mu, W. Geng, J. Cho, J. He, C. Xue, *Nano Energy* **2018**, 53, 550.

[111] Y. Liu, L. Zhao, L. Wang, H. Zheng, D. Li, R. Avila, K. W. C. Lai, Z. Wang, Z. Xie, Y. Zi, X. Yu, *Advanced Materials Technologies* **2019**, 4, 1900744.

[112] X. Huang, Q. Qin, X. Wang, H. Xiang, J. Zheng, Y. Lu, C. Lv, K. Wu, L. Yan, N. Wang, C. Xia, Z. L. Wang, *ACS Nano* **2021**, 15, 19783.

[113] X. Niu, W. Jia, S. Qian, J. Zhu, J. Zhang, X. Hou, J. Mu, W. Geng, J. Cho, J. He, X. Chou, *ACS Sustainable Chemistry & Engineering* **2019**, 7, 979.

[114] W. M. Winslow, *Journal of Applied Physics* **1949**, 20, 1137.

[115] H. A. Pohl, K. Pollock, J. S. Crane, *Journal of Biological Physics* **1978**, 6, 133.

[116] M. A. Gutiérrez, H. Khanbareh, S. van der Zwaag, *Computational Materials Science* **2016**, 112, 139.

[117] C. A. Randall, D. V. Miller, J. H. Adair, A. S. Bhalla, *J. Mater. Res.* **1993**, 8, 899.

[118] S. Mamada, N. Yaguchi, M. Hansaka, M. Yamato, H. Yoshida, *Journal of Applied Polymer Science* **2015**, 132.

[119] Y. Qi, N. T. Jafferis, K. Lyons, C. M. Lee, H. Ahmad, M. C. McAlpine, *Nano Letters* **2010**, 10, 524.

[120] Y. Qi, J. Kim, T. D. Nguyen, B. Lisko, P. K. Purohit, M. C. McAlpine, *Nano Letters* **2011**, 11, 1331.

[121] M. Scheffler, P. Colombo, *Cellular Ceramics: Structure, Manufacturing, Properties and Applications*, **2005**.

[122] P. Colombo, *Philos Trans A Math Phys Eng Sci* **2006**, 364, 109.

[123] A. R. Studart, U. T. Gonzenbach, E. Tervoort, L. J. Gauckler, *Journal of the American Ceramic Society* **2006**, 89, 1771.

[124] K. Rittenmyer, T. Shrout, W. A. Schulze, R. E. Newnham, *Ferroelectrics* **1982**, 41, 189.

[125] K. Hikita, K. Yamada, M. Nishioka, M. Ono, *Ferroelectrics* **1983**, 49, 265.

[126] A. M. Varaprasad, K. Uchino, *Ferroelectrics Letters Section* **1987**, 7, 89.

[127] J. Li, Y. Yang, H. Jiang, Y. Wang, Y. Chen, S. Jiang, J.-M. Wu, G. Zhang, *Composites Part B: Engineering* **2022**, 232, 109617.

[128] Y. Zhang, C. K. Jeong, J. Wang, H. Sun, F. Li, G. Zhang, L.-Q. Chen, S. Zhang, W. Chen, Q. Wang, *Nano Energy* **2018**, 50, 35.

[129] Y. S. Ko, F. Nüesch, D. M. Opriş, *Poleable Dielectric Elastomer Composites*, Ecole Polytechnique Fédérale de Lausanne, Lausanne **2017**.

[130] Z. Zhang, C. Yao, Y. Yu, Z. Hong, M. Zhi, X. Wang, *Advanced Functional Materials* **2016**, 26, 6760.

[131] S.-H. Park, H. B. Lee, S. M. Yeon, J. Park, N. K. Lee, *ACS Applied Materials & Interfaces* **2016**, 8, 24773.

[132] Y. Duan, Y. Ding, J. Bian, Z. Xu, Z. Yin, Y. Huang, in *Polymers*, Vol. 9, 2017.

[133] M. J. Moody, C. W. Marvin, G. R. Hutchison, *Journal of Materials Chemistry C* **2016**, 4, 4387.

[134] C. Li, X. Tian, T. He, *International Journal of Energy Research* **2021**, 45, 7235.

[135] A. Mohebbi, F. Mighri, A. Ajji, D. Rodrigue, *Advances in Polymer Technology* **2018**, 37, 468.

[136] F.-L. Jin, M. Zhao, M. Park, S.-J. Park, in *Polymers*, Vol. 11, 2019.

[137] W. R. McCall, K. Kim, C. Heath, G. La Pierre, D. J. Sirbuly, *ACS Applied Materials & Interfaces* **2014**, 6, 19504.

[138] M. A. Ansari, P. Somdee, *Advanced Energy and Sustainability Research* **2022**, 3, 2200063.

[139] P. Fang, X. Qiu, W. Wirges, R. Gerhard, L. Zirkel, *IEEE Transactions on Dielectrics and Electrical Insulation* **2010**, 17, 1079.

[140] P. Fang, M. Wegener, W. Wirges, R. Gerhard, L. Zirkel, *Applied Physics Letters* **2007**, 90, 192908.

[141] F. Galantini, G. Gallone, F. Carpi, *IEEE Transactions on Dielectrics and Electrical Insulation* **2012**, 19, 1203.

[142] J.-J. Wang, J.-W. Tsai, Y.-C. Su, *Journal of Micromechanics and Microengineering* **2013**, 23, 075009.

[143] S. P. Lacour, I. Graz, D. Cotton, S. Bauer, S. Wagner, presented at 2011 Annual International Conference of the IEEE Engineering in Medicine and Biology Society, 30 Aug.-3 Sept. 2011, **2011**.

[144] Y. Suzuki, Electrostatic/Electret-Based Harvesters, In Micro Energy Harvesting, Ed. D. Briand, E. Yeatman, S. Roundy, Wiley, **2015**, p. 149, DOI: https://doi.org/10.1002/9783527672943.ch8.

[145] J.-W. Tsai, J.-J. Wang, Y.-C. Su, *Sensors and Actuators A: Physical* **2014**, 215, 176.

[146] J. Zhong, Y. Ma, Y. Song, Q. Zhong, Y. Chu, I. Karakurt, D. B. Bogy, L. Lin, *ACS Nano* **2019**, 13, 7107.

[147] H. Hu, *Polymer Engineering & Science* **2022**, n/a.

[148] S. W. Ma, Y. J. Fan, H. Y. Li, L. Su, Z. L. Wang, G. Zhu, *ACS Applied Materials & Interfaces* **2018**, 10, 33105.

[149] R. Zentel, G. Reckert, *Die Makromolekulare Chemie* **1986**, 187, 1915.

[150] R. Zentel, *Liquid Crystals* **1988**, 3, 531.

[151] R. Zentel, *Angewandte Chemie* **1989**, 101, 1437.

[152] R. Zentel, G. Reckert, S. Bualek, H. Kapitza, *Die Makromolekulare Chemie* **1989**, 190, 2869.

[153] M. Portugall, H. Ringsdorf, R. Zentel, *Die Makromolekulare Chemie* **1982**, 183, 2311.

[154] R. Zentel, H. Ringsdorf, *Die Makromolekulare Chemie, Rapid Communications* **1984**, 5, 393.

[155] H. Finkelmann, H.-J. Kock, G. Rehage, *Die Makromolekulare Chemie, Rapid Communications* **1981**, 2, 317.

[156] G. H. F. Bergmann, H. Finkelmann, V. Percec, M. Zhao, *Macromolecular Rapid Communications* **1997**, 18, 353.

[157] B. Donnio, H. Wermter, H. Finkelmann, *Macromolecules* **2000**, 33, 7724.

[158] B. Reck, H. Ringsdorf, *Die Makromolekulare Chemie, Rapid Communications* **1985**, 6, 291.

[159] M. Engel, B. Hisgen, R. Keller, W. Kreuder, B. Reck, H. Ringsdorf, H. W. Schmidt, P. Tschirner, *Pure and Applied Chemistry*, **1985**, 57, 1009.

[160] Y. Li, T. Liu, V. Ambrogi, O. Rios, M. Xia, W. He, Z. Yang, *ACS Applied Materials & Interfaces* **2022**, 14, 14842.

[161] W. Meier, H. Finkelmann, *Die Makromolekulare Chemie, Rapid Communications* **1990**, 11, 599.

[162] S. U. Vallerien, F. Kremer, E. W. Fischer, H. Kapitza, R. Zentel, H. Poths, *Die Makromolekulare Chemie, Rapid Communications* **1990**, 11, 593.

[163] H. Harald, M. Wolfgang, F. Heino, presented at Proc.SPIE **1991**.

[164] P. Papadopoulos, P. Heinze, H. Finkelmann, F. Kremer, *Macromolecules* **2010**, 43, 6666.

[165] A. Jákli, N. Éber, *Current Opinion in Chemical Engineering* **2013**, 2, 120.

[166] A. G. B. da Cruz, J. C. Góes, S. D. Figueiró, J. P. A. Feitosa, N. M. P. S. Ricardo, A. S. B. Sombra, *European Polymer Journal* **2003**, 39, 1267.

[167] R. Liu, Q. Zhang, L. E. Cross, *Journal of Applied Polymer Science* **1999**, 73, 2603.

[168] X. Tian, J. Jin, S. Yuan, C. K. Chua, S. B. Tor, K. Zhou, *Advanced Energy Materials* **2017**, 7, 1700127.

[169] S. Tibbits, The emergence of “4D printing”, *TED conference*, **2013**.

[170] H. A. Alshahrani, *Journal of Science: Advanced Materials and Devices* **2021**, 6, 167.

[171] Z. Guan, L. Wang, J. Bae, *Materials Horizons* **2022**, 9, 1825.

[172] C. Zhang, Y. Li, W. Kang, X. Liu, Q. Wang, *SusMat* **2021**, 1, 127.

[173] H. Ikram, A. Al Rashid, M. Koç, *Polymer Composites* **2022**, 43, 6355.

[174] D. McCoul, S. Rosset, S. Schlatter, H. Shea, *Smart Materials and Structures* **2017**, 26, 125022.

CHAPTER 3

Synthesis of Polar Polynorbornenes with High Dielectric Relaxation Strength as Candidate Materials for Dielectric Applications

This chapter is based on the publication

Synthesis of polar polynorbornenes with high dielectric relaxation strength as candidate materials for dielectric applications

by

*Francis Owusu,[a,b] Martin Tress,[c] Frank A. Nüesch,[a,b,d] Sandro Lehner,[e] and Dorina M. Opris [a]**

[a] *Swiss Federal Laboratories for Materials Science and Technology Empa, Laboratory for Functional Polymers, Überlandstr. 129, CH-8600, Dübendorf, Switzerland.*

[b] *Institute of Chemical Sciences and Engineering, Ecole Polytechnique Federale de Lausanne, EPFL, Station 6, CH-1015 Lausanne, Switzerland*

[c] *Leipzig University, Peter Debye Institute for Soft Matter Physics, Linne ́straße 5, 04103 Leipzig, Germany*

[d] *École Polytechnique Fédérale de Lausanne (EPFL), Institut des Matériaux, Station 12, CH 1015, Lausanne, Switzerland.*

[e] *Swiss Federal Laboratories for Materials Science and Technology Empa, Laboratory for Advanced Fibers, Lerchenfeldstrasse 5, 9014 St. Gallen, Switzerland*

Reprinted with permission from

Materials Advances, 2022, 3, 998 – 1006
DOI: 10.1039/D1MA00704A
http://dx.doi.org/10.1039/D1MA00704A

Author Contributions:

F. Owusu performed the synthesis and characterization of compounds as well as contributed to the manuscript

3.1 Abstract

Materials with high dielectric permittivity and dielectric relaxation strength are searched for thermal and pressure sensors and electrical energy generators. However, most polymers have either a too low dielectric permittivity or are so polar that their glass transition temperature (T_g) is too high that decomposition and side reactions occur before an electric field can polarize the polar groups. Here, we use the power and versatility of ring-opening metathesis polymerization (ROMP) to synthesize polar polymers with high dielectric relaxation strength and T_g significantly below the decomposition temperature. We first synthesized six polar norbornene monomers by conventional esterification, which were then polymerized by ROMP using Grubbs first and third-generation catalysts. The structure of the polynorbornenes obtained were verified by multinuclear NMR spectroscopy, molecular weights determined by gel permeation chromatography (GPC), and thermal properties evaluated by thermogravimetric analysis (TGA) and differential scanning calorimetry (DSC). Additionally, their dielectric permittivity, conductivity, and dielectric losses were measured at different temperatures and frequencies ranging between $0.1 - 10^6$ Hz.

3.2 Introduction

The design and synthesis of polymers responsive to different stimuli is a research field that gained significant attention from polymer chemists.[1] A large body of research has been focused on achieving polymeric materials that respond to pH, humidity, temperature, light, and magnetic field. However, little attention has been given to the synthesis of electroactive polymers despite their potential in various applications.[2]

Electret polymers have a quasi-permanent polarization and respond to mechanical or thermal stress by generating an electric signal, and thus show piezo and pyroelectric effects.[3] These effects were known, but a significant advance in this field was achieved only when the piezoelectric response in polyvinylidene difluoride (PVDF) was discovered in 1969.[4] Since then, many applications for this polymer were found, which range from sensors, actuators, energy conversion to electronic devices.[5-6] However, PVDF is environmentally unfriendly and difficult to process. A further advance of the field was achieved when small air voids in highly insulating polymer foams were polarized by corona discharge.[7] Such foams show a high piezoelectric response, but humidity negatively influences their performance.[8]

Quasi-permanent polarization can be introduced in amorphous polar polymers by poling in a strong electric field when heated above T_g and cooled below T_g.[9] Research in this direction attracted the attention of polymer chemists in the 1990s, as for example Hall Jr.,[10] Feast,[11] and Wegner.[12]

Polyacrylonitrile and poly(vinylidenecyanide vinyl acetate) (PVVA) show a large dielectric relaxation strength ($\Delta\varepsilon$), but they are either environmentally unfriendly or have a high T_m. PVVA has amongst the highest $\Delta\varepsilon$ = 30.[13] While this is attractive, it's very high T_g (170 °C) complicates the poling process due to possible thermal decomposition and side reactions. To achieve a practical piezoelectric response, polymers with as high as possible $\Delta\varepsilon$ are desirable. The dielectric relaxation strength is defined as the difference between the ε_r and ε_∞ and is related to the density of polar groups (N) and the dipole moment (μ). The polarization (P) is given by:

$$P = \varepsilon_0 \Delta\varepsilon(T) E_p \tag{3.1}$$

where ε_0 is the vacuum permittivity, $\Delta\varepsilon\ (T)$ the dielectric relaxation strength at the poling temperature, and E_p the poling field.

Polymers with large $\Delta\varepsilon$ can be accessed by increasing the dipole density and dipole strength of polar groups grafted to the polymer chain. Polar groups can be introduced to a polymer chain either by post-polymerization modification or by polymerizing polar monomers. Ring-opening polymerization (ROMP) is a powerful tool for synthesizing polymers with different functional groups.[14-15] Norbornene-based monomers are predominantly employed due to their high ring strain, ensuring excellent polymerization propagation. Additionally, this monomer class can easily be modified with a wide range of functional groups, giving rise to polymers with otherwise inaccessible structures and properties.[16-17] Due to this versatility, polynorbornenes with pendant groups to the polymer backbone have recently spotlighted material research. This is also due to the materials' attractive optical and electro-optic properties,[18] good mechanical and adhesive properties,[19-21] multi-shape memory effect,[22] and the excellent dielectric behavior.[23-28] To increase the dielectric permittivity, functional moieties with large dipole moments as side chains have typically been considered.[29] For instance, Feast reported the synthesis of poly[2,3-bis(trifluoromethyl)norbornadiene] and its dielectric and pyroelectric properties.[11] Most recently, Bonardd et al. reported on the synthesis of new poly(itaconate) polymers containing pendant sulfone and nitrile groups, which showed an interesting dielectric behavior in a broad temperature range, proving their potential as promising candidates for energy storage applications.[30-31]

There are only a few systematic experimental studies available on how different dipole moieties as pendant groups of poly norbornenes affect dielectric properties. Here, we report the synthesis of six polar norbornene monomers and their ROM polymerization. Furthermore, we report the thermal and dielectric properties of these polynorbornenes. Gratifyingly, some of these polymers show high $\Delta\varepsilon$ and a T_g suitable for room temperature applications.

3.3 Experimental

3.3.1 Materials

All reagents were purchased from Sigma Aldrich and utilized without further purification unless otherwise stated. 2,6-Dimethyl-4*H*-pyran-4-one and 1-ethyl-3-(3-dimethylaminopropyl) carbodiimide (EDC) were acquired from ABCR GmbH and TCI Chemicals, respectively. Ethyl acetate, ethanol, methanol, heptane, dichloromethane (DCM), toluene, and tetrahydrofuran (THF) were purchased from VWR Chemicals and deuterated solvents from Deutero GmbH. N-(2-Hydroxyethyl)-N-Methyl-4-nitroaniline was synthesized according to the literature.[32] DCM was dried over calcium hydride. Millipore Milli-Q system processed deionized water was taken for all experimental work-ups.

3.3.2 Standard measurements and instrumentation

^{1}H and ^{13}C NMR spectra were recorded on a Bruker Avance-400 spectrometer (400 MHz at room temperature) using $CDCl_3$ as a solvent if not otherwise stated. Mass spectra of monomers were obtained using a Bruker Daltonics HPLC-ESI-qTOF-MS spectrometer. Elemental analyses were conducted with a LECO TruSpec Micro and a LECO 628 O Micro employing IR spectroscopy as a detection unit.

The average molecular weights and polydispersity indices (PDI) of polymers were determined by two different gel permeation chromatography (GPC) systems with THF or hexafluoroisopropanol (HFIP) as eluents. The THF-based setup was equipped with Agilent 1260 Infinity, using two tandem-connected mixed-bed columns (1×PLgel 5 µm MIXED-C Guard and 2×PLgel 5 µm MIXED-C Analytical), coupled to a 390-MDS refractive index detector. Both systems employed a flow rate of 1 ml/min and were kept at 35 − 40 °C. Polystyrene and poly(methyl methacrylate) were used as calibration standards for the THF and HFIP eluent systems, respectively.

The thermal behavior of the synthesized polymers was investigated using a Perkin Elmer DSC 8000 differential scanning calorimeter. The samples were initially heated to 150 °C at a rate of 20 °C/min to remove any thermal history. Heat-cool-heat cycles were scanned from 0 to 200 °C at a rate of 20 °C/min unless otherwise stated. Thermogravimetric analysis (TGA) was conducted using a Perkin Elmer TGA7 at a heating rate of 10 °C/min under a nitrogen gas flow.

Broadband dielectric spectroscopy (BDS) measurements were performed using a Novocontrol Alpha-A Frequency Analyzer equipped with quatro cryosystem temperature control. Samples were prepared by making pellets of the polymers with the aid of a hydraulic press, sandwiching between two metal

electrodes with 100 µm glass fibres as spacers, and melt pressing in a 110 °C to 130 °C temperature range. Dielectric spectra were obtained by applying an external electric field of 10 kV/m in a frequency and temperature range of 0.1 to 1 MHz and −100 to 160 °C, respectively.

3.3.3 Synthetic methods

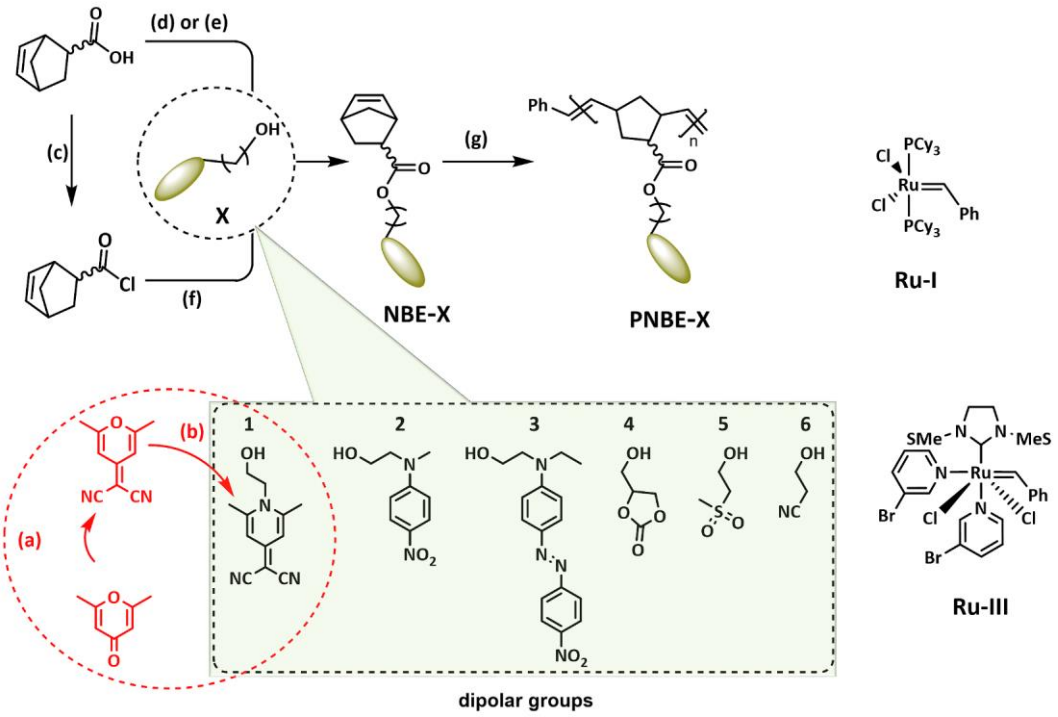

Scheme 3.1 Synthesis of monomers and respective homopolymers: (a) malononitrile, acetic anhydride, 4 h, reflux; (b) ethanolamine, methanol, 2 h, rf; (c) thionyl chloride, anhydrous chloroform 4 h, rf; (d) 4-dimethylaminopyridine, N,N'-dicyclohexylcarbodiimide, dry DCM, 24 h, 45 °C; (f) *N*,*N*-Dimethylaniline, anhydrous chloroform, 13 h, 0 °C to rf; (g) Grubbs 1st or 3rd generation catalysts, dry DCM, 18 h, 40 °C.

3.3.3.1 Synthesis of 2-(1-(2-hydroxyethyl)-2,6-dimethylpyridin-4(1H)-ylidene)malononitrile

2,6-Dimethyl-4*H*-pyran-4-one (20.00 g, 161.1 mmol) and malononitrile (10.64 g, 161.1 mmol) were dissolved in acetic anhydride (80 ml) and the solution charged into a 200 ml round bottom flask. The reaction mixture was refluxed at 130 °C for 4 h to obtain crude **4*H*-PMal** intermediate (Scheme 1). The intermediate was purified by washing the unreacted acetic acid with warm water and recrystallizing from heptane to produce a dark brown powder (87 % yield).

A 200 ml round bottom flask was charged with **4*H*-PMal** intermediate (15.00 g, 87 mmol), ethanolamine (44.7 ml, 745 mmol) and methanol (100 ml). The reaction was refluxed at 70 °C for 2 h and then it was left to stand overnight. The separated solid was collected by filtration, dried, and recrystallized in ethanol to give compound **1** as brown flakes (yield 60%). ^{1}H NMR (DMSO-d_6) *δ* 6.68 (s, 2H, Ar–**H**), 5.17 (t, *J* = 5.4 Hz, 1H, O**H**), 4.17 (t, *J* = 5.6 Hz, 2H, N–C$\mathbf{H_2}$), 3.70 (q, *J* = 5.4 Hz, 2H, C$\mathbf{H_2}$–OH), 2.53 (s, 6H, Ar–C$\mathbf{H_3}$); ^{13}C NMR (DMSO-d_6) δ 155.40 ($\mathbf{C_{Ar}}$=C(CN)$_2$), 150.92 ($\mathbf{C_{Ar}}$ –CH$_3$), 119.43 (**C**N), 113.07 ($\mathbf{C_{Ar}}$ –H), 59.76 (=**C**(CN)$_2$ and **C**H$_2$–OH), 51.13 (N–**C**H$_2$) , 21.03 (Ar–**C**H$_3$); MS (ESI) m/z calcd. for $C_{12}H_{13}N_3NaO$ [M+Na]$^+$: 238.0951; found: 238.0950; Anal. Calcd. for $C_{12}H_{13}N_3O$ (%): C 66.96, H 6.09, N 19.52, O 7.43; found: C 66.91, H 6.01, N 19.43 O 7.31. (Figure S3.1- Figure S3.6)

3.3.3.2 General preparation procedure for monomers (NBE-1 to NBE-4) via Steglich esterification

A dried 2-necked round bottom flask was charged with 5-norbornene-2-carboxylic acid (1 equiv.), functional alcohol **1**–**4** (1 equiv.), and 4-dimethylaminopyridine (2 equiv.) dissolved in anhydrous dichloromethane (60 ml). N,N'-dicyclohexylcarbodiimide (DCC) / 1-ethyl-3-(3-dimethylaminopropyl) carbodiimide (EDC) (2 equiv.) was added at 0 °C to the reaction mixture, which was then stirred for 5 min at 0 °C and refluxed for 24 h at 45 °C. The resulting crude mass was concentrated in vacuum and purified via column chromatography eluting with heptane and ethyl acetate (3:2). (Figure S3.7 - Figure S3.34)

NBE-1 was obtained as light yellow powder (59% yield): ^{1}H NMR *δ*: 6.65 (s, 2H), 6.19 (ddd, J = 12.9, 5.7, 3.0 Hz, 1H), 5.96 (ddd, J = 117.3, 5.7, 3.0 Hz, 1H), 4.41 – 4.18 (m, 4H), 3.22 – 3.07 (m, 1H), 3.01 – 2.87 (m, 2H), 2.53 (s, 6H), 1.94 (ddd, J = 11.8, 9.4, 3.7 Hz, 1H), 1.52 – 1.25 (m, 3H). ^{13}C NMR (101 MHz, Chloroform-d) δ 175.78, 174.23, 156.07, 147.86, 147.84, 138.42, 138.31, 135.38, 131.80, 118.36, 113.85, 113.83, 61.17, 61.07, 49.74, 46.83, 46.74, 46.53, 46.36, 45.72, 43.17, 42.85, 42.48, 41.59, 30.59, 29.41, 21.01, 20.99. MS (ESI) m/z calcd. for $C_{20}H_{21}N_3NaO_2$ [M+Na]$^+$: 358.1526; found: 358.1529. Anal. Calcd. for $C_{20}H_{21}N_3O_2$ (%): C 71.62, H 6.31, N 12.53, O 9.54; found: C 71.47, H 6.37, N 12.53 O 9.26. Refractive index: 1.565; Density: 1.238

NBE-2 was obtained as viscous yellow liquid (92% yield): ^{1}H NMR δ 8.18 – 8.10 (m, 2H), 6.74 – 6.66 (m, 2H), 6.16 (ddd, J = 14.8, 5.7, 3.0 Hz, 1H), 6.10 – 5.81 (m, 1H), 4.36 – 4.19 (m, 2H), 3.78 – 3.65 (m, 2H), 3.14 (d, J = 2.2 Hz, 4H), 2.97 – 2.86 (m, 2H), 1.94 – 1.80 (m, 1H), 1.48 – 1.40 (m, 1H), 1.41 – 1.23 (m, 2H). ^{13}C NMR (101 MHz, $CDCl_3$) δ 176.14, 174.66, 153.43, 138.16, 138.07, 137.43, 135.54, 132.09, 126.18, 126.16, 110.53, 110.50, 60.98, 60.82, 50.90, 50.85, 49.68, 46.48, 46.36, 45.65, 43.28, 43.05, 42.50, 41.58, 38.97, 38.96, 30.37, 29.27. MS (ESI) m/z calcd. for $C_{17}H_{20}N_2NaO_4$

$[M+Na]^+$: 339.1315; found: 339.1315. Anal. Calcd. for $C_{17}H_{20}N_2O_4$ (%): C 64.54, H 6.37, N 8.86, O 20.23; found: C 64.68, H 6.54, N 8.92. Refractive index: 1.582; Density: 1.237

NBE-3 was obtained as a reddish powder (95 % yield): ^{1}H NMR δ 8.43 – 8.24 (m, 2H), 8.04 – 7.82 (m, 4H), 6.90 – 6.74 (m, 2H), 6.24 – 6.13 (m, 1H), 6.01 (ddd, J = 77.5, 5.7, 3.0 Hz, 1H), 4.30 (dt, J = 26.8, 6.3 Hz, 2H), 3.70 (dt, J = 15.8, 6.3 Hz, 2H), 3.56 (q, J = 7.2 Hz, 2H), 3.24 – 3.10 (m, 1H), 3.05 – 2.87 (m, 2H), 2.02 – 1.89 (m, 2H), 1.44 (ddd, J = 11.1, 7.6, 4.1 Hz, 2H), 1.28 (t, J = 7.1 Hz, 3H). ^{13}C NMR (101 MHz, $CDCl_3$) δ 175.69 (d, J = 106.1 Hz), 174.71, 156.76, 151.32, 147.36, 143.82, 138.14, 138.02, 136.86, 135.63, 132.53, 132.19, 126.27, 124.66, 122.64, 111.47, 61.32, 61.18, 55.94, 55.74, 49.81, 49.76, 49.70, 48.85, 48.79, 46.81, 46.57, 46.39, 45.71, 45.65, 45.61, 44.36, 43.31, 43.08, 42.75, 42.54, 41.63, 34.94, 33.97, 32.87, 32.80, 31.27, 31.14, 30.85, 30.44, 29.29, 26.48, 26.41, 25.53, 25.47, 25.40, 24.99, 24.86, 24.70, 12.30. MS (ESI) m/z calcd. for $C_{24}H_{26}N_4NaO_4$ $[M+Na]^+$: 457.1846; found: 457.1848. Anal. Calcd. for $C_{24}H_{26}N_4O_4$ (%): C 66.34, H 6.03, N 12.89, O 14.73; found: C 67.97, H 6.94, N 12.13. Refractive index: 1.422; Density: 1.185

NBE-4 was obtained as viscous, lightly yellow liquid (90 % yield): ^{1}H NMR δ 6.28 – 6.15 (m, 1H), 6.14 – 5.88 (m, 1H), 5.02 – 4.84 (m, 1H), 4.57 (td, J = 8.6, 2.8 Hz, 1H), 4.44 – 4.16 (m, 3H), 3.32 – 3.18 (m, 1H), 3.09 – 2.99 (m, 1H), 2.95 (dp, J = 5.3, 2.2 Hz, 1H), 2.01 – 1.88 (m, 1H), 1.45 (ddddd, J = 18.6, 9.5, 6.8, 5.2, 2.1 Hz, 2H), 1.30 (dq, J = 8.3, 1.7 Hz, 1H). ^{13}C NMR δ 175.79, 174.25, 154.47, 138.34, 138.20, 138.15, 135.51, 132.14, 131.96, 73.92, 73.90, 73.89, 73.84, 66.02, 65.99, 62.98, 62.87, 49.79, 49.72, 46.66, 46.63, 46.37, 45.84, 43.20, 43.18, 42.93, 42.51, 42.50, 41.65, 30.47, 29.23. MS (ESI) m/z calcd. for $C_{12}H_{14}NaO_5$ $[M+Na]^+$: 261.0733; found: 261.0731. Anal. Calcd. for $C_{12}H_{14}O_5$ (%): C 60.50, H 5.92, O 33.58; found: C 60.83, H 6.22. Refractive index: 1.482; Density: 1.268

3.3.3.3 General preparation procedure for monomers NBE-5 and NBE-6

A dried 2-necked round bottom was charged with the respective functional alcohol (2 equiv.), and *N*,*N*-dimethylaniline (2 equiv.). 5-Norbornene-2-carbonyl chloride (1 equiv.) was diluted with 15 ml of dry chloroform and added over 15 min to the reaction vessel at 0 °C. The mixture was then stirred at RT for 1 h and further heated to reflux for another 12 h. The reaction was then quenched by adding 10 ml of 6 N H_2SO_4. Afterward, the organic phase was separated and the aqueous phase extracted thrice with DCM. The collected organic phases were combined, washed with 6 ml of 6 N H_2SO_4, followed by further washing with 2 × 20 ml deionized water, 2 × 20 ml conc. $NaHCO_3$ and 20 ml of brine solution. The crude product in the solution was dried over anhydrous Na_2SO_4 and then vacuum evaporated. Finally, the product was purified by column chromatography eluting with heptane and ethyl acetate (3:2). (Figure S3.35 - Figure S3.44)

NBE-5 was obtained as colourless liquid (81 % yield): ^{1}H NMR *δ*: 6.21 (ddd, J = 22.6, 5.7, 3.0 Hz, 1H), 6.03 (ddd, J = 66.8, 5.7, 3.0 Hz, 1H), 4.60 – 4.43 (m, 2H), 3.39 – 3.28 (m, 2H), 3.22 (dq, J = 3.6, 2.0 Hz, 1H), 3.09 – 2.98 (m, 1H), 3.02 (s, 3H), 2.98 – 2.93 (m, 1H), 2.01 – 1.88 (m, 1H), 1.56 – 1.36 (m, 2H), 1.34 – 1.25 (m, 1H). ^{13}C NMR δ 175.57, 174.02, 138.29, 138.24, 135.51, 132.01, 57.83, 57.70, 54.04, 49.72, 46.50, 46.40, 45.77, 43.21, 42.94, 42.54, 42.30, 42.27, 41.63, 30.50, 29.31. MS (ESI) m/z calcd. for $C_{11}H_{16}NaO_4S$ $[M+Na]^+$: 267.0662; found: 267.0662. Refractive index: 1.475; Density: 1.267

NBE-6 was obtained as colourless liquid (89 % yield): ^{1}H NMR δ 6.20 (ddd, J = 23.0, 5.7, 3.0 Hz, 1H), 6.06 (ddd, J = 60.4, 5.7, 2.9 Hz, 1H), 4.35 – 4.18 (m, 2H), 3.27 (dq, J = 3.8, 2.1 Hz, 1H), 3.11 – 2.98 (m, 1H), 2.98 – 2.91 (m, 1H), 2.72 (dt, J = 16.1, 6.3 Hz, 2H), 2.00 – 1.90 (m, 1H), 1.55 – 1.38 (m, 2H), 1.31 (dt, J = 8.2, 1.6 Hz, 1H). ^{13}C NMR *δ*: 175.77, 174.25, 138.20, 138.11, 135.61, 132.18, 116.89, 116.86, 58.59, 58.47, 49.72, 46.71, 46.36, 45.79, 43.17, 42.95, 42.55, 41.67, 30.41, 29.24, 18.10, 18.08. MS (ESI) m/z calcd. for $C_{11}H_{13}NNaO_2$ $[M+Na]^+$: 214.0838; found: 214.0839. Refractive index: 1.482; Density: 1.133

3.3.3.4 General procedure for ring-opening metathesis polymerization (ROMP).

Polymers were prepared via ROMP using Grubb's 1st or 3rd generation catalysts, as shown in Scheme 1 below. A 2-necked round bottom flask was charged with the respective monomer **NBE-X** and DCM. For quantities, see Table 3.1. The system was initially degassed by two freeze-vacuum-thaw cycles followed by the addition of the catalyst while frozen and a third degassing. The reaction was run under argon and at 40 °C for 18 h. After confirming total monomer conversion by TLC, ethyl vinyl ether was added, and the resulting mixture stirred for a further 1 h. The product mixture was concentrated under vacuum and then precipitated into excess methanol. The polymer was further purified by five consecutive dissolution (DCM) and re-precipitation cycles (MeOH). The obtained polymers were dried to constant weight under vacuum at 50 °C.

PNBE-2 was obtained as green solid (98 % yield). ^{1}H NMR (DMSO) *δ*: 7.94 (br s, 2H), 6.71 (br s, 2H), 5.01 (br d, J = 45.8 Hz, 2H), 4.09 (br d, J = 68.8 Hz, 2H), 3.66 (br s, 2H), 2.99 (br s, 3H), 2.93 – 2.16 (br m, 3H), 2.07 – 0.55 (br m, 4H). ^{13}C NMR (DMSO) *δ*: 175.03, 174.00, 154.02, 136.30, 134.54, 133.51, 132.71, 130.76, 129.51, 126.09, 111.07, 61.23, 50.41, 48.10, 44.95, 42.27, 38.88, 37.49, 36.38. (Figure S3.45- Figure S3.47)

PNBE-3 was obtained as dark red solid (95 % yield).^{1}H NMR *δ*: 8.26 (br d, J = 9.0 Hz, 2H), 7.87 (br s, 4H), 6.78 (br d, J = 12.2 Hz, 2H), 5.28 (br dd, J = 44.0, 21.3 Hz, 2H), 4.45 – 3.87 (br m, 2H), 3.56 (br d, J = 55.7 Hz, 4H), 3.26 – 2.61 (br m, 3H), 1.85 (br d, J = 86.3 Hz, 4H), 1.46 – 1.10 (br m, 3H).

^{13}C NMR *δ*: 174.28, 156.47, 154.00, 151.31, 147.31, 143.67, 134.52, 133.31, 132.48, 130.71, 129.80, 126.40, 124.64, 122.57, 111.50, 60.93, 50.12, 48.71, 45.61, 42.71, 40.51, 37.70, 36.10, 32.77, 31.11, 26.18, 25.45, 24.83, 12.36. (Figure S3.48 - Figure S3.50)

PNBE-4 was obtained as off-white solid (98 % yield).^{1}H NMR (DMSO) *δ*: 5.60 – 4.88 (br m, 3H), 4.58 (br q, J = 7.8 Hz, 1H), 4.45 – 4.00 (br m, 3H), 3.01 (br t, J = 65.8 Hz, 3H), 2.19 – 1.06 (br m, 4H). ^{13}C NMR (DMSO) *δ*: 174.86, 173.93, 155.11, 135.27, 134.91, 133.75, 132.89, 132.04, 130.98, 129.76, 129.30, 74.77, 74.69, 74.61, 66.51, 66.46, 63.76, 63.66, 49.96, 48.32, 48.08, 45.35, 42.28, 40.89, 40.75, 37.50, 36.48, 35.94, 35.53. (Figure S3.51 - Figure S3.53)

PNBE-5 was obtained as off-white solid (96 % yield). ^{1}H NMR (DMSO) *δ*: 5.58 – 5.06 (br m, 2H), 4.51 – 4.12 (br m, 2H), 3.48 (br m, J = 8.9, 7.9 Hz, 2H), 3.02 (br s, J = 5.2 Hz, 3H), 3.28 – 2.53 (br m, 3H), 2.13 – 1.19 (br m, 4H). ^{13}C NMR (DMSO) *δ*: 174.90, 173.89, 135.18, 131.03, 129.88, 58.18, 57.87, 53.20, 53.12, 47.96, 42.22, 42.14, 42.07, 37.48, 36.47, 35.90. (Figure S3.54 - Figure S3.56)

PNBE-6 was obtained as off-white solid (95 % yield). ^{1}H NMR (DMSO) *δ*: 5.59 – 5.03 (br m, 2H), 4.17 (br dddd, *J* = 32.8, 15.8, 11.1, 5.4 Hz, 2H), 3.29 – 2.54 (br m, 5H), 2.14 – 1.33 (br m, 4H). ^{13}C NMR (DMSO) *δ*: 174.99, 173.94, 133.80, 132.87, 130.99, 129.75, 118.94, 59.39, 59.24, 59.19, 47.99, 45.39, 42.41, 37.48, 36.51, 35.96, 17.96, 17.88. (Figure S3.57- Figure S3.59)

3.4 Results and discussion

The synthesis of different polar norbornene monomers (**NBE-X**) is outlined in Scheme 3.1. Monomers **NBE-1** to **NBE-4** were prepared by an esterification reaction with 5-norbornene-2-carboxylic acid, a mixture of endo and exo, whereas monomers **NBE-5** and **NBE-6** were obtained by esterification reaction of 5-norbornene-2-carboxylic acid chloride, respectively. Monomers were purified by column chromatography over silica gel to achieve a mixture of 80 % endo and 20 % exo-products according to the integration of the olefinic protons in the ^{1}H NMR spectra. The structure of all monomers was confirmed by ^{1}H and ^{13}C NMR spectroscopy, MS spectrometry, and elemental analysis (Figure S3.1 - Figure S 3.44).

Homopolymerizations of **NBE-X** were carried out with Grubbs I and III catalysts in DCM at 40 °C for 18 h. Ethyl vinyl ether was used as a quencher. The polymers were isolated in yields of over 90%. Clear evidence for polymerization is provided by ^{1}H NMR spectroscopy of the vinylene groups. While those of the monomers appear at *δ* = 5.8 - 6.5 ppm those of the polymer absorb at *δ* = 5.4 ppm. Additionally, all signals of the polymers are broadened. Figure 3.1 shows representative ^{1}H NMR spectra of monomer **NBE-3** and of polymer **PNBE-3**. Because the molecular weights of the prepared polymers were relatively high, end groups could not be detected in the ^{1}H NMR spectra. It must be

stated that the polymerization of the **NBE-1** monomer was unsuccessful. A possible reason might be the stabilization of the reactive metal-carbene complex center by this monomer, thereby inhibiting the polymerization propagation step.

The polymerizations were conducted using varying monomer/catalyst ratios (Table 3.1). The molecular weights (M_n) and polydispersities (*PDI*) were determined by GPC in THF, HFIP, or 20 mM sodium trifluoroacetate solution in HFIP using polystyrene and poly(methyl methacrylate) standards (Table 3.1). Figure 3.2(a) shows the GPC elugrams of **PNBE-3** of different molecular weights. For all other elugrams see the supporting information. The molecular weights of the polymers increased with increasing monomer/catalyst ratio. The molecular weights calculated based on the ratio of monomer to catalyst are generally higher than those measured by GPC, which is expected as the GPC is a relative method and the standards used for calibration have a different chemical structure. Some polymers show slight bimodality, presumably due to side reactions in the later stage of the polymerization.

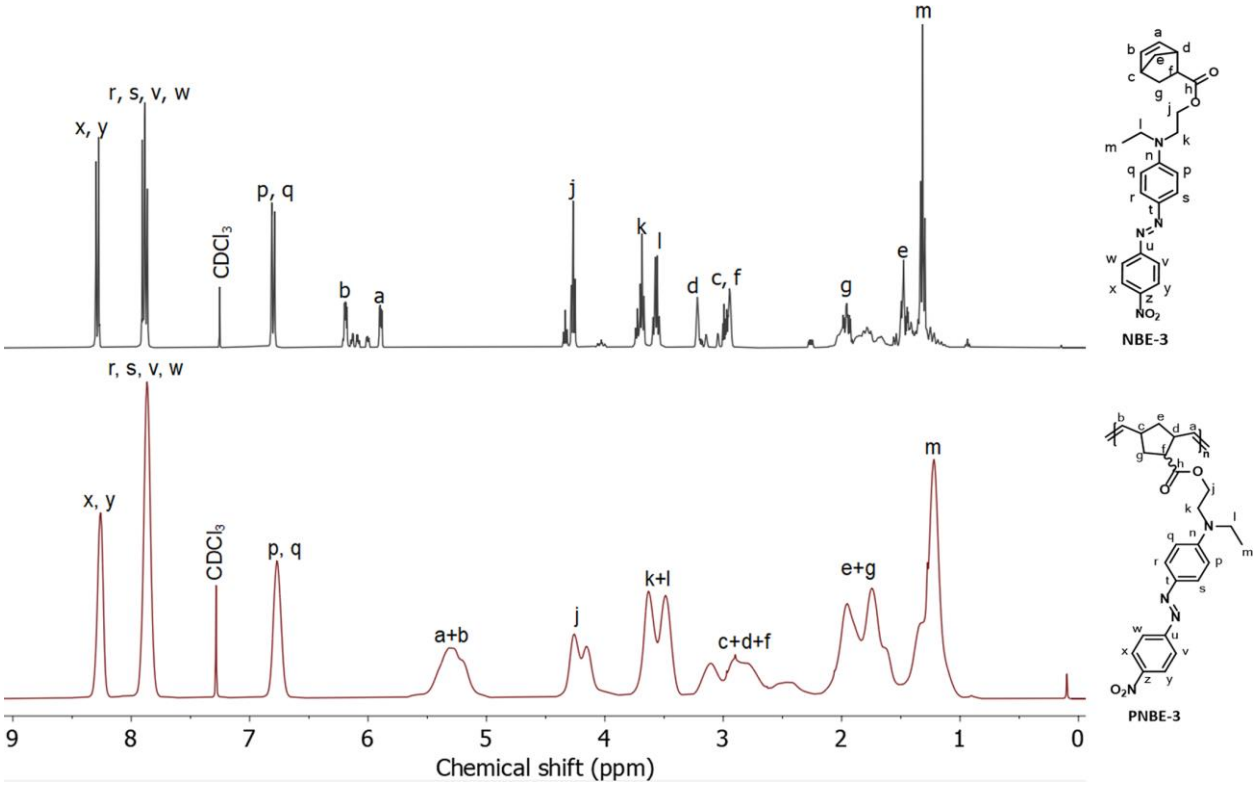

Figure 3.1 ^{1}H NMR spectra in $CDCl_3$ of monomer NBE-3 (top) and its corresponding polymer PNBE-3 (bottom).

Table 3.1 Polymerization of norbornene monomers: Monomer to catalyst ratio [M]:[Cat.], the catalyst used, polymerization degree (n), number average molecular weight Mn, polydispersity index (PDI), and yield.

ID	[M]:[Cat]	Cat.	n	M_n (Da)	*PDI*	Yield (%)
PNBE-2	75:1	Ru-I	99	31’300 [a]	1.29	92
PNBE-2	150:1	Ru-I	194	61’300 [a]	1.36	95
PNBE-2	200:1	Ru-III	198	62’800 [a]	2.40	94
PNBE-2	300:1	Ru-I	565	178’700 [a]	1.51	96
PNBE-2	400:1	Ru-III	403	127’600 [a]	2.40	97
PNBE-2	800:1	Ru-III	1161	367’400 [a]	1.59	96
PNBE-3	150:1	Ru-I	117	50’700 [b]	1.46	90
PNBE-3	200:1	Ru-III	120	52’200 [b]	1.33	95
PNBE-3	300:1	Ru-I	134	58’300 [b]	1.87	93
PNBE-3	400:1	Ru-III	205	88’900 [b]	1.46	97
PNBE-3	800:1	Ru-III	490	213’000 [b]	1.56	98
PNBE-4	75:1	Ru-I	131	31’100 [c]	1.60	93
PNBE-4	150:1	Ru-I	146	34’900 [c]	1.91	92
PNBE-4	200:1	Ru-III	-	-	-	94
PNBE-4	300:1	Ru-I	136	32’400 [c]	1.81	93
PNBE-4	400:1	Ru-III	-	-	-	95
PNBE-4	800:1	Ru-III	-	-	-	95
PNBE-5	200:1	Ru-III	177	43’200 [a]	2.48	96
PNBE-5	400:1	Ru-III	302	73’800 [a]	2.41	95
PNBE-5	800:1	Ru-III	1956	257’900 [a]	1.54	97
PNBE-6	200:1	Ru-III	187	35’700 [b]	1.69	97
PNBE-6	400:1	Ru-III	276	52’800 [b]	1.88	96
PNBE-6	800:1	Ru-III	470	89’900 [b]	2.03	97

[a] GPC in 20 mM sodium trifluoroacetate in HFIP; [b] GPC in THF; [c] GPC in HFIP as eluents.

The thermal behavior of **PNBE-X** was investigated by differential scanning calorimetry (DSC) and thermogravimetric analysis (TGA) (Figure 3.2(b-c), Figure S3.60 - Figure S3.69). All polymers are

amorphous and show a T_g. Figure 3.2(b) shows the DSC curves of polymers **PNBE-X**. The corresponding T_g and ΔC_p values of the transitions are listed in Table 3.2.

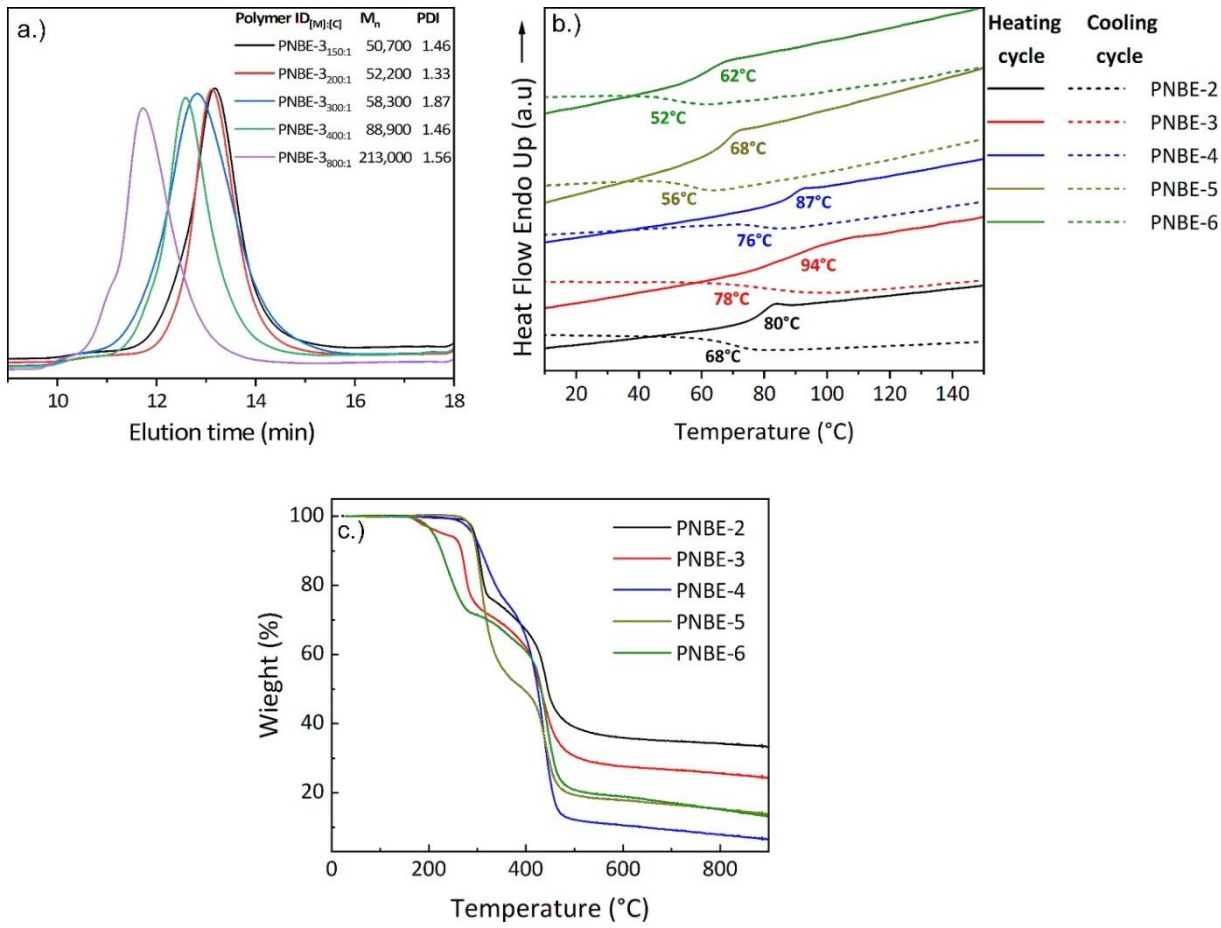

Figure 3.2 Molecular weight and thermal characterization; (a) GPC elugrams of **PNBE-3** polymers using different monomer/catalyst ratios; (b) DSC curves and (c) TGA thermograms of **PNBE-X**.

Table 3.2 T_g values and ΔC_p of the glass transition, decomposition temperature $T_{d,5\%}$, activation energy E_a, room temperature dielectric permittivity, and dielectric relaxation strength $\Delta\varepsilon$.

Sample	M_n (Da)	T_g[a] **[°C]**	T_g[b] **[°C]**	C_p **[Jg^{-1} °C^{-1}]**	$T_{d,5\%}$ **[°C]**	E_a **[kJ/mol]**	ε[c]	$\Delta\varepsilon_{max}$[d]
PNBE-2	178’700	80/68	73	0.34	294	44.15 ± 0.36	3.37	19.06
PNBE-3	213’000	106/95	77	0.34	222	49.66 ± 0.35	3.84	15.08
PNBE-4	32’400	87/76	76	0.31	289	36.08 ± 0.64	4.97	11.24
PNBE-5	73’800	68/56	-	0.23	294	46.50 ± 0.70	4.78	-

PNBE-6	52’800	62/52	-	0.25	254	38.66 ± 0.70	8.93	-

[a] T_g taken from DSC measurements; [b] estimated by impedance spectroscopy (IS); [c] taken at 25 °C; [d] taken at maximum relaxation

The lowest T_g of 62 °C was measured for **PNBE-6** that carries nitrile groups, while the highest T_g of 106 °C was measured for **PNBE-3**, which has *N*-Ethyl-*N*-(2-hydroxyethyl)-4-(4-nitrophenylazo)aniline (disperse red 1) as a dipole. TGA was carried out to test the thermal stability and decomposition behavior. Polymers **PNBE-2**, **PNBE-4**, and **PNBE-5** turned out to be stable up to a temperature of 290 °C (Figure 3.2(c)), while polymers **PNBE-6** and **PNBE-3** decompose above 200 °C. The molecular weight of the polymers has a negligible impact on thermal behavior, which indicates that the synthesized polymers are in the polymeric regime, where the T_g is molecular weight independent.

Broadband dielectric spectroscopy (DBS) was applied at temperatures between -100 °C to 140 °C to identify the type of mobile segments in the polymers and elucidate the dynamic changes. The measurements were conducted in capacitor geometry, where 100 µm thick films of PNBE-X were placed between two metal electrodes with a diameter of 20 mm. The PNBE-X polymers show several relaxation processes within the set temperature range. Figure 3.3 gives an illustration of how the real part ε' and imaginary part ε'' of the complex permittivity, the real part of the conductivity σ' and the loss tangent $tan\ \delta$ evolve with the temperature at different frequencies for PNBE-2. Generally, there is a noticeable increase in ε' with increasing temperature over the specified frequency range, as shown in Figure 3.3(a). However, the ε' remains virtually constant from - 60 °C to 70 °C because the orientation motions are restricted to small angles. Above 70 °C the increment becomes very pronounced, which is attributed to the thermal activation of the dipole motions in the polymer. Thus, the presence of pendant dipolar moieties on the polymer chains experiences enough hindrances, which impose potential energy barriers to their mobility below certain temperatures. Such energy impositions are dependent on the packing density, the intrinsic chain flexibility, rotational restrictions, softness of potential related to angle changes, and the intra- and intermolecular dipole interactions.[31, 33] Adding enough thermal energy to the system helps overcome these energy barriers, and segmental rotation allows reorientation of the dipoles reflected in an increased polarization. Thus, the orientation polarization of the dipoles occurs above T_g. The relaxation peak for the orientation polarization process is shifted to higher frequencies with increasing the temperature. Above 100 °C, the ionic conductivity contributes to the increase in dielectric permittivity at low frequencies. This is also supported by the dielectric loss, which shows an increase at low frequencies with a slope approximation of –1 and a sudden rise in the conductivity of the material, as shown in Figure 3.3(b-d). The temperature increases the ionic conductivity and shifts this process to higher frequencies. To relate the bulk dielectric behavior of **PNBE-X** polymers with respect to structural and molecular

motions of their dipolar segments, an approximation was made by fitting the experimental data with a Havriliak-Negami (HN) relaxation function.

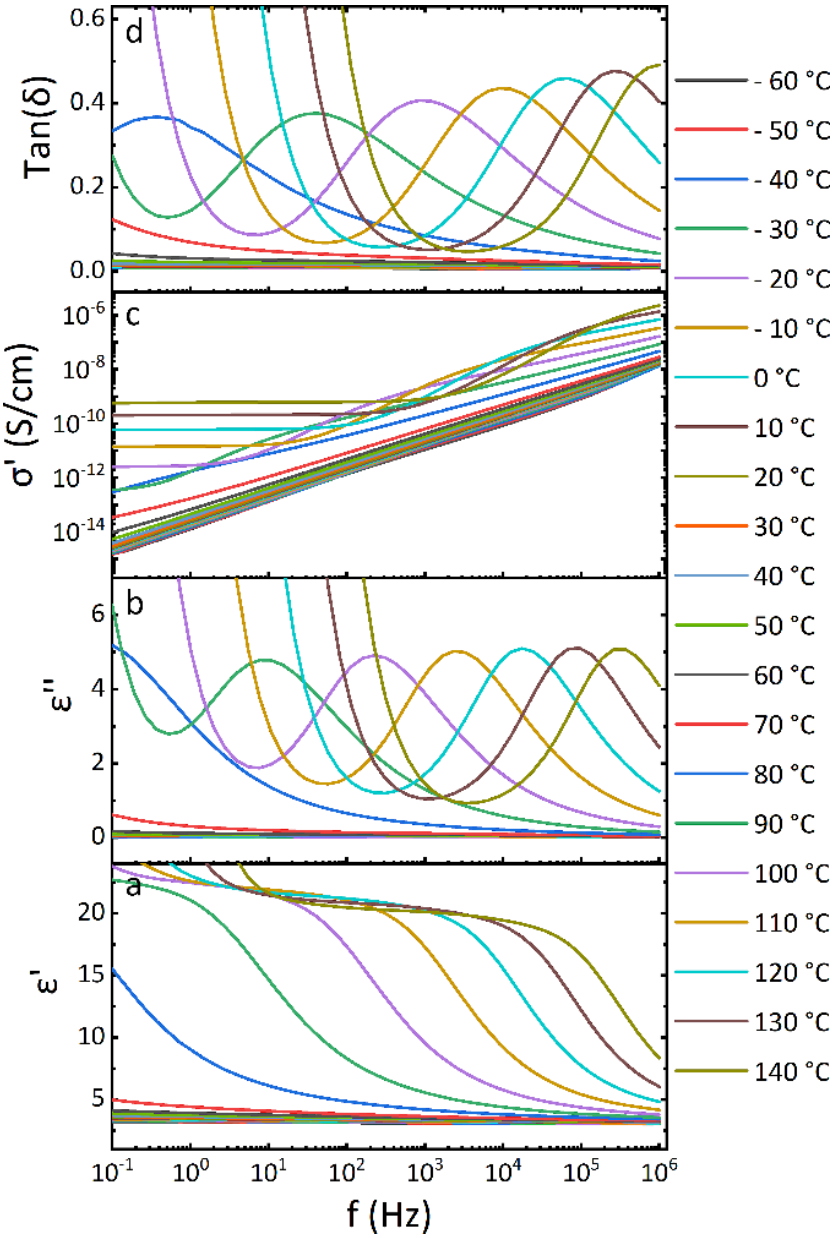

Figure 3.3 Isothermal dielectric response of PNBE-2 as a function of frequency; (a) real permittivity *ε'*, (b) dielectric loss *ε''*, (c) real conductivity *σ'* and (d) loss *tan δ*.

This was achieved through fitting isothermal data of ε'' by a superposition of the HN-function and a conductivity contribution as shown in equation (3.2) below;[34]

$$\boldsymbol{\varepsilon''} = \frac{\boldsymbol{\sigma_0}}{\boldsymbol{\varepsilon_0}}\frac{\boldsymbol{a}}{\boldsymbol{\omega^s}} + \mathbf{Im}\left[\frac{\Delta\boldsymbol{\varepsilon}}{(\mathbf{1} + (\boldsymbol{i\omega\tau})^{\alpha})^{\gamma}}\right]$$

(3.2)

where ε'' is the imaginary permittivity, σ_0 is the d.c.-conductivity, a is a constant, ε_0 the permittivity of vacuum, $\omega = 2\pi f$ the angular frequency, $\Delta\varepsilon$ the dielectric relaxation strength, τ the relaxation time, α and γ describe the symmetric and asymmetric broadening of the relaxation peak, i the imaginary unit $(i = \sqrt{-1})$. The exponent $s < 1$ are observed for ionic charge carriers, which cause electrode polarisation. The parameters of relevance to understand the dynamic transitions taken place at the molecular level and the possibility to polarize these polymers are τ and $\Delta\varepsilon$.

Generally, two distinct regimes revealing molecular motions responsible for α- and β-relaxation processes in glass-forming materials were easily fitted, as illustrated in Figure 3.4(a). Complete sets of fits for all polymers can be found in the supporting information (Figure S3.70- Figure S3.82). The relaxation times for the β-processes, as shown in Figure 3.4(b), exhibit Arrhenius temperature dependences over the temperature range in which the process is resolvable. The Arrhenius fits describe the experimentally determined relaxation times. The activation energies, which depend on both internal rotational barriers and the environment of the dipolar fluctuating unit, obtained from the fitting for the **PNBE-X** polymers are listed in Table 3.2.

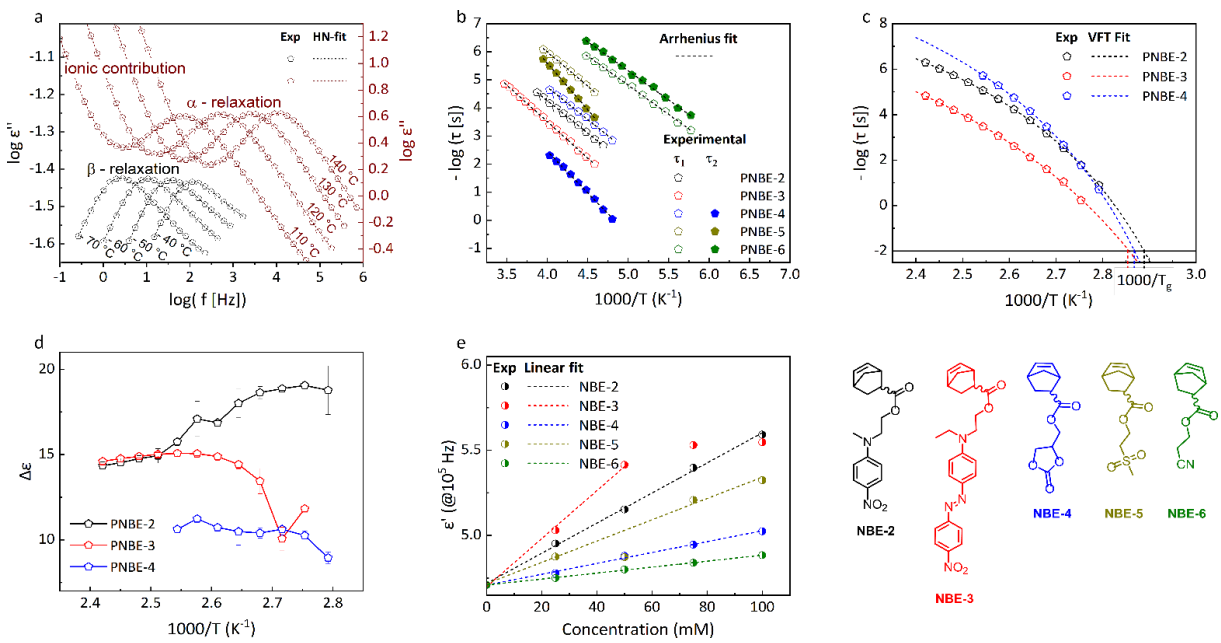

Figure 3.4 Dielectric relaxation of PNBE-X polymers and the dipolar dynamics of their respective monomers; (a) isothermal illustration of the imaginary part ε'' of the complex dielectric function vs frequency for two temperature regimes; below T_g (*β*-relaxation) and above T_g (*α*-relaxation) for PNBE-3; (b) Arrhenius fitting of *β*-relaxation mechanisms for PNBE-X; (c) VFT plot of *α*-relaxation processes for PNBE-2, PNBE-3, and PNBE-4; and (d) temperature dependence of dielectric relaxation strength for PNBE-2, PNBE-3, and PNBE-4 in the *α*-

relaxation regime; (e) dielectric permittivity as a function of concentration for NBE-X in chloroform. From the slopes the respective dipole moments were calculated.

Contrary, the α-relaxation processes for **PNBE-X** polymers exhibit clear non-Arrhenius temperature dependencies, well represented by a Vogel–Fulcher-Tammann (VFT) fit function with parameters in good agreement with experimental values as shown in Figure 3.4(c). The degree of deviation from an Arrhenius-type temperature dependence provides a useful classification of glass-forming systems. Additionally, at the calorimetric glass transition temperature T_g, the α-relaxation reaches a peak frequency approximated to 10^{-3} Hz.[34] The T_g of glass-forming materials can be extrapolated from the α-relaxation processes obeying a VFT-temperature dependence. As a result, the T_g for **PNBE-2**, **PNBE-3**, and **PNBE-4** could be estimated by DBS techniques as listed in Table 3.2. While the β-processes are believed to be due to localized motions of the pendant dipolar moieties, the α-processes are attributed to segmental relaxations of the polymer chains. For amorphous polymers, $\Delta\boldsymbol{\varepsilon}$ is said to decrease with increasing temperature above T_g.[34] Figure 3.4(d) shows the temperature dependence of $\Delta\boldsymbol{\varepsilon}$ for **PNBE-2**, **PNBE-3**, and **PNBE-4** polymers within the α-relaxation regime. This temperature dependency was more pronounced in **PNBE-2** polymer than in the **PNBE-3** and **PNBE-4** polymers. The maximum dielectric relaxation strengths were estimated to be 19.06, 15.08, and 11.24 for **PNBE-2**, **PNBE-3,** and **PNBE-4**, respectively. For **PNBE-5** and **PNBE-6** we could not assess the relaxation strength because of the high ionic conductivity of the samples.

To clarify the observed trend in dielectric relaxation strengths $\Delta\boldsymbol{\varepsilon}$ of **PNBE-X** polymers, the molecular dipole moments of the corresponding **NBE-X** monomers were evaluated experimentally. The $\Delta\boldsymbol{\varepsilon}$ is proportional to the dipole moments of contributing dipolar units within a material. [34] The dipole moments of **NBE-X** were determined from dielectric spectroscopy measurements of solutions of **NBE-X** in chloroform at ambient temperature and 10^5 Hz. To avoid dipolar interactions, dilute solutions of the monomers in chloroform were prepared. The dielectric permittivity was measured as a function of solute concentration, as shown in Figure 3.4(e). Dipole moments were thereafter estimated by modified Onsager equation according to Böttcher[35-36] and a model according to Hedestrand-Guggenheim-Smith.[37-38] The obtained results are listed in Table 3.3. For the equations used, please see supporting information. The dipole moment was obtained from the slope of $\boldsymbol{\varepsilon}'$ versus molar concentration (Figure 3.4(e)). As expected, the highest dipole moment was found for **NBE-1**, but this monomer did not polymerize (Table 3.3). The second highest dipole was found for **NBE-3**. However, this high dipole moment is not reflected in the relaxation strength of P**NBE-3**, which was lower than for **NBE-2**, which has a lower dipole moment. The low relaxation strength of P**NBE-3** may be related to the different dipole moments of cis-trans isomers of disperse red 1 or the antiparallel orientation of the dipoles, which is likely favored by the π-π interactions.

Table 3.3 Dipole moments of **NBE-X** determined by Hedestrand-Guggenheim-Smith (HGS) model and Böttcher model

Monomer	ρ [g/cm^3]	n	Dipole moment (Debye)	
			μ_{HGS}	$\mu_{Böttcher}$
NBE-1	1.238	1.565	12.21±2.38	11.54±1.09
NBE-2	1.237	1.582	8.67±1.26	9.34±1.28
NBE-3	1.185	1.422	11.54±1.37	10.90±1.76
NBE-4	1.268	1.482	4.52±0.87	7.67±1.47
NBE-5	1.267	1.475	6.41±1.32	8.63±1.51
NBE-6	1.133	1.482	3.00±0.42	7.07±1.63

3.5 Conclusions

Six polar norbornene monomers were synthesized and five of them were successfully polymerized by ROMP using Grubbs I and III generation catalysts. The molecular weight of the polymers, as revealed by GPC, shows an increasing correlation with the theoretical monomer-to-catalyst feed ratio. The synthesized polymers show moderate room temperature dielectric permittivity, typical for high T_g polar glassy polymers. All polymers show an increase in the dielectric relaxation strength at temperatures above the T_g. Because of their high dielectric relaxation strength, we propose the novel polymers to be useful as electrets and to find applications in thermal sensors and thermal energy harvesting. Work in this direction is underway.

3.6 Supporting Information

3.6.1 Synthesis of 2-(1-(2-hydroxyethyl)-2,6-dimethylpyridin-4(1H)-ylidene)malononitrile

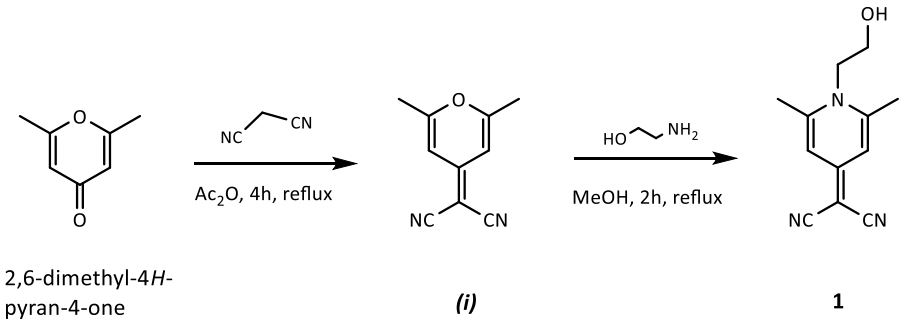

Scheme S 3.1 Synthesis of compound 1

Compound **1** was designed and synthesized as shown in Scheme S1. Initially, 2,6-dimethyl-4*H*-pyran-4-one (20.00 g, 161.10 mmol), malononitrile (10.64 g, 161.10 mmol), and acetic anhydride (80 ml) were charged into a 200 ml round bottom flask. The system was refluxed at 130 °C for 4 hours to obtain crude of *compound (i)* intermediate. The intermediate was purified by washing with warm water and recrystallizing from heptane to produce a dark brown powder (yield, 87 %). Furtherly, a 200 ml round bottom flask was charged *compound (i)* intermediate (15.00 g, 87.11 mmol), ethanolamine (44.7 ml, 740.46 mmol) and methanol (100 ml). The reaction was then refluxed at 70 °C for 2 hours and left to stand overnight. The separated solid was collected by filtration, dried, and recrystallized in ethanol to produced compound **1** as brown flakes (yield, 60%).

^{1}H NMR (400 MHz, DMSO-d_6) δ 6.68 (s, 2H, Ar–H), 5.17 (t, J = 5.4 Hz, 1H, OH), 4.17 (t, J = 5.6 Hz, 2H, N–CH_2), 3.70 (q, J = 5.4 Hz, 2H, CH_2–OH), 2.53 (s, 6H, Ar–CH_3). ^{13}C NMR (101 MHz, DMSO-d_6) δ 155.40 (C_{Ar}=C(CN)$_2$), 150.92 (C_{Ar} –CH_3), 119.43 (CN), 113.07 (C_{Ar} –H), 59.76 (=C(CN)$_2$ and CH_2–OH), 51.13 (N–CH_2) , 21.03 (Ar–CH_3). MS (ESI) m/z for $C_{12}H_{13}N_3NaO$ $[M+Na]^+$: calc. = 238.0951; found = 238.0950 Elemental analysis $C_{12}H_{13}N_3O$ (%): calc. C 66.96, H 6.09, N 19.52, O 7.43; found: C 66.91, H 6.01, N 19.43 O 7.31

3.6.2 Synthesis of bicyclo[2.2.1]het-5-ene-2-carbonyl chloride

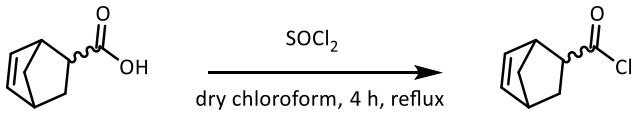

(ii)

Scheme S 3.2 Synthesis of compound (ii)

A 2-necked round bottom flask was charged with 5-norbornene-2-carboxylic acid (15 g, 108.56 mmol), thionyl chloride (19.37 g, 162.84 mmol), and anhydrous chloroform (10 ml). The reaction mixture was refluxed for 4 hours under argon protection. The solvent was then evaporated and the residue was distilled at 1 mbar (40 °C) to give the corresponding acyl chloride as colorless oily liquid (yield, 83%).

^{1}H NMR (400 MHz, $CDCl_3$) δ 6.26 (ddd, *J* = 19.1, 5.7, 3.1 Hz, 1H), 6.06 (dd, *J* = 5.8, 2.5 Hz, 1H), 3.48 (dd, *J* = 7.9, 4.2 Hz, 1H), 3.45 (s, 1H), 3.01 (dt, *J* = 4.2, 2.3 Hz, 1H), 2.09 – 1.92 (m, 1H), 1.60 – 1.40 (m, 2H), 1.36 (d, *J* = 8.3 Hz, 1H). ^{13}C NMR (101 MHz, $CDCl_3$) δ 176.81, 175.04, 139.04, 138.69, 134.88, 131.61, 77.23, 56.43, 56.32, 49.22, 47.16, 46.90, 46.29, 42.89, 41.85, 31.22, 30.09.

3.6.3 Structure characterization of 2-(1-(2-hydroxyethyl)-2,6-dimethylpyridin-4(1H)-ylidene)malononitrile

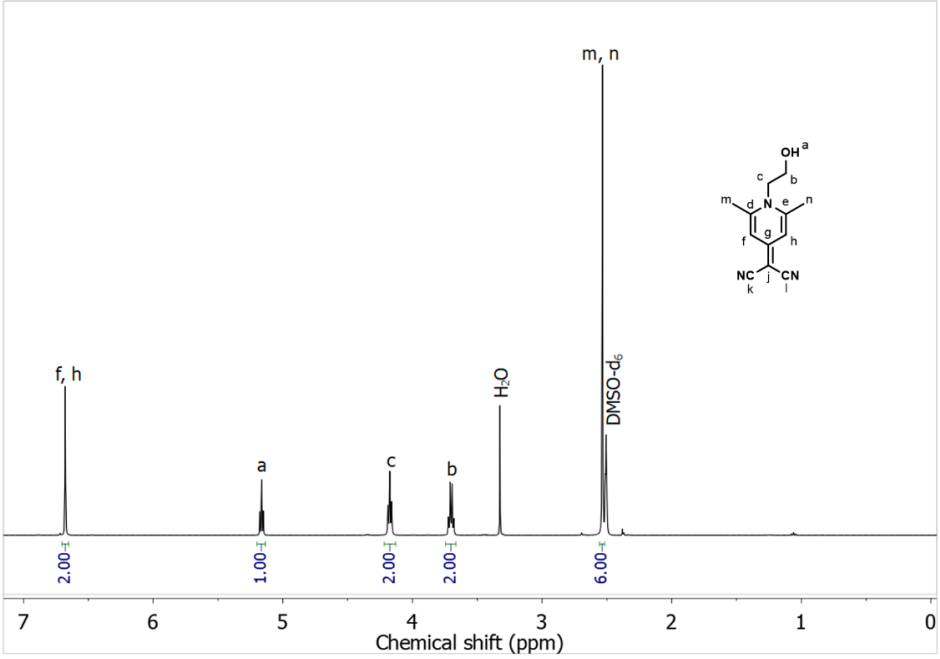

Figure S 3.1 ^{1}H NMR spectrum of 2-(1-(2-hydroxyethyl)-2,6-dimethylpyridin-4(1H)-ylidene)malononitrile

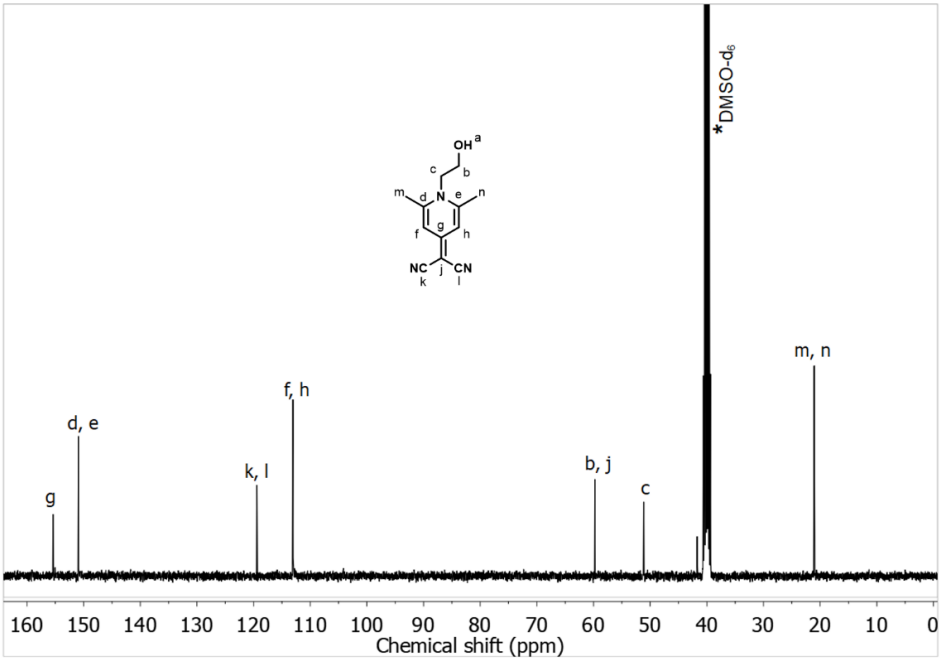

Figure S3.2 ^{13}C NMR spectrum of 2-(1-(2-hydroxyethyl)-2,6-dimethylpyridin-4(1H)-ylidene)malononitrile

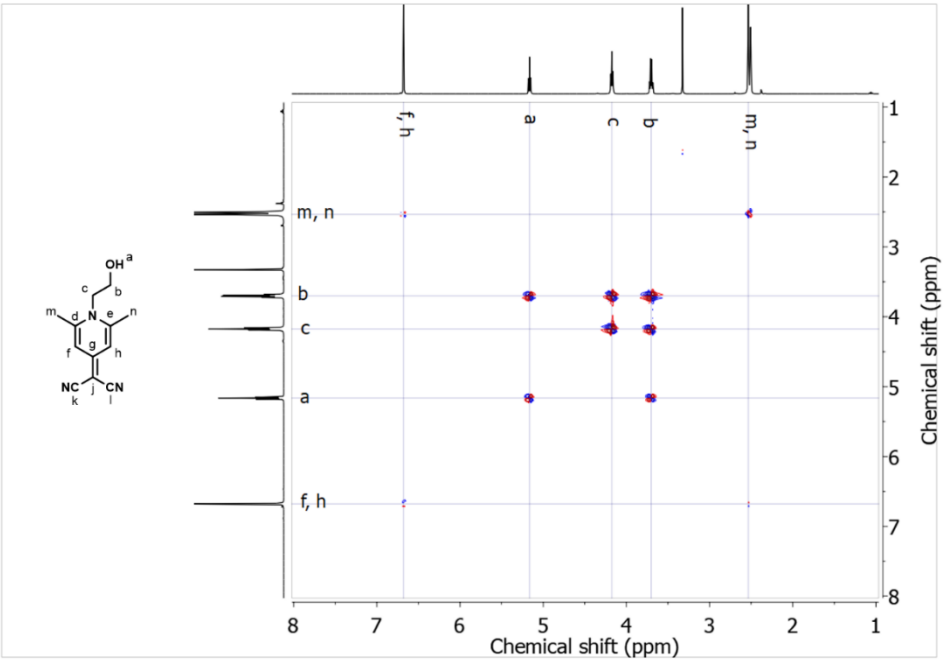

Figure S3.3 COSY of 2-(1-(2-hydroxyethyl)-2,6-dimethylpyridin-4(1H)-ylidene)malononitrile

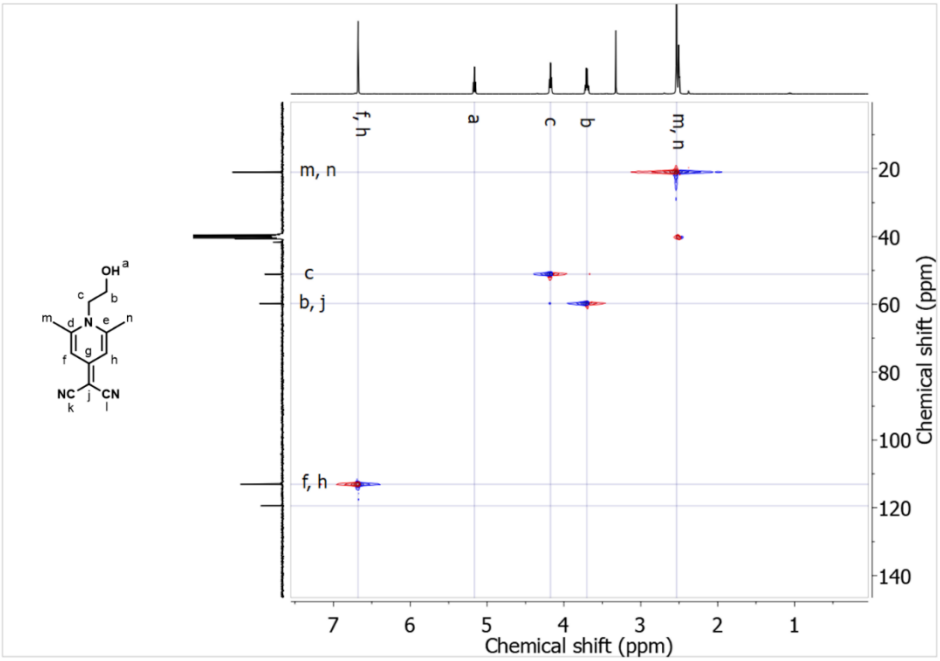

Figure S3.4 HSQC of 2-(1-(2-hydroxyethyl)-2,6-dimethylpyridin-4(1H)-ylidene)malononitrile

Eidgenössische Technische Hochschule Zürich

Laboratorium für Organische Chemie

ETH-Hönggerberg - HCI E304 8093 Zürich Tel: 044/633 43 58

Mikroelementaranalyse

Name: Owusu Francis Gruppe: Opris EMPA
Labor: LA182 Tel: 058/765 48 01

Substanz: 1
Molekularformel: C12 H13 N3 O Mr = 215.25g/mol

Schmelzpunkt:
gereinigt: ??????????????????????????? getrocknet: HV

Bestimmungen: C H N O

Eingang: 19.09.19 Ausgang: 23.09.19

M-166261 Operator: PK

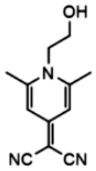

$C_{12}H_{13}N_3O$
M= 215.26 g/mol

Berechnete Gewichtsanteile:

[C] 66.96% [H] 6.09% [N] 19.52% [O] 7.43%

Gefundene Gewichtsanteile:

Einwaage: 0.910mg LECO TruSpec Micro
[C] 66.91% [H] 6.01% [N] 19.43% 19.09.19

Einwaage: 1.048mg LECO RO-628
[O] 7.31% 23.09.19

Figure S3.5 Elemental analysis of 2-(1-(2-hydroxyethyl)-2,6-dimethylpyridin-4(1H)-ylidene)malononitrile

Acquisition Parameter

Method:	ETH_HyStar_HPLC_QTOF_POS_LowMass_Loop-AS.m			Acquisition Date:	10.10.2019 15:57:20
File Name:	D:\Data\bmax0051xx\BMAX005105_44666.d			Operator:	Daniel Wirz
Source Type	ESI	Ion Polarity	Positive	Set Nebulizer	1.6 Bar
Focus	Not active	Set Capillary	4500 V	Set Dry Heater	200 °C
Scan Begin	50 m/z	Set End Plate Offset	-500 V	Set Dry Gas	8.0 l/min
Scan End	1300 m/z	Set Collision Cell RF	200.0 Vpp	Set Divert Valve	Source

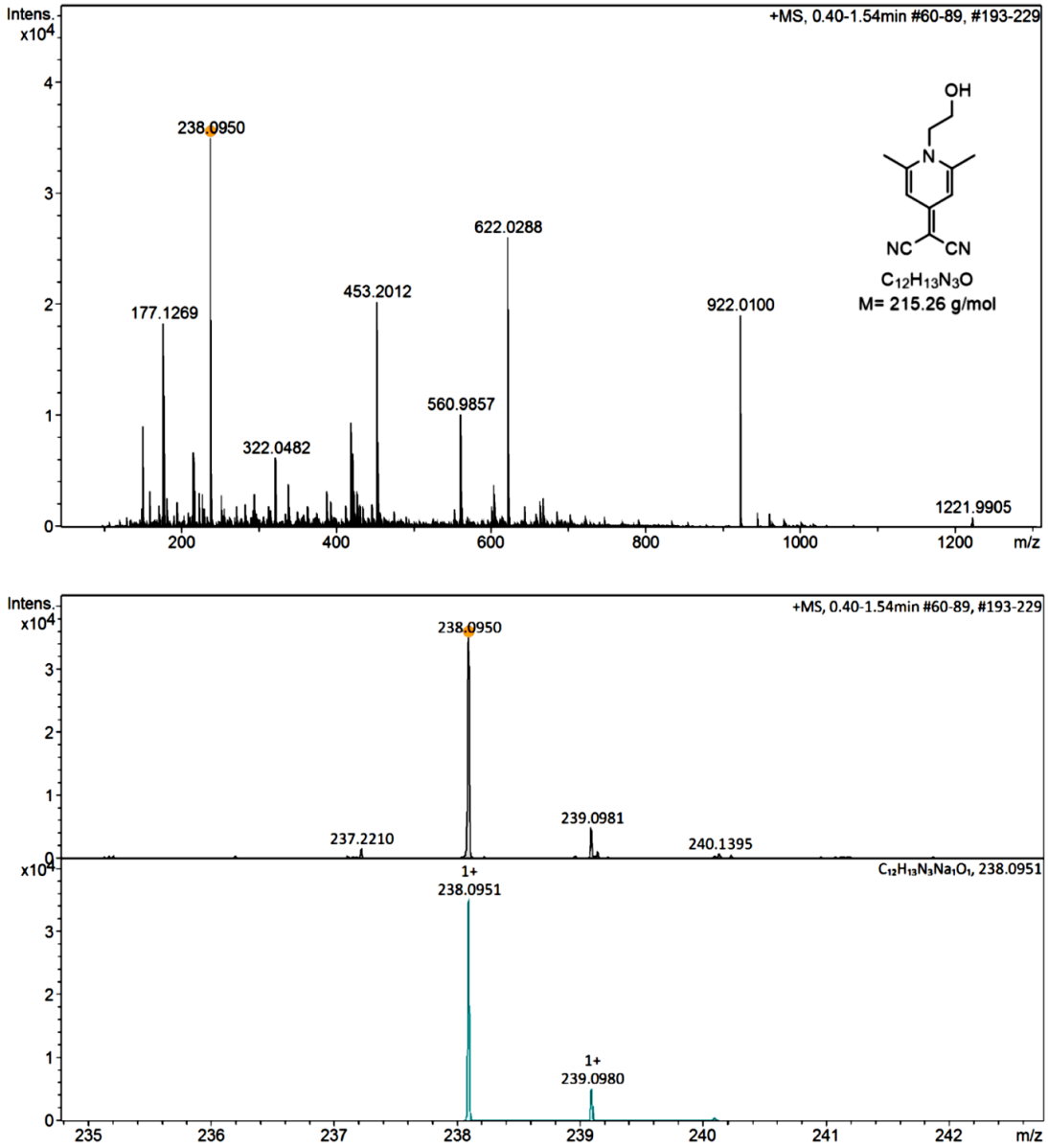

Figure S3.6 Mass spectra of 2-(1-(2-hydroxyethyl)-2,6-dimethylpyridin-4(1H)-ylidene)malononitrile

3.6.4 Structure characterization of bicyco[2.2.1]hept-5-ene-2-carbonyl chloride

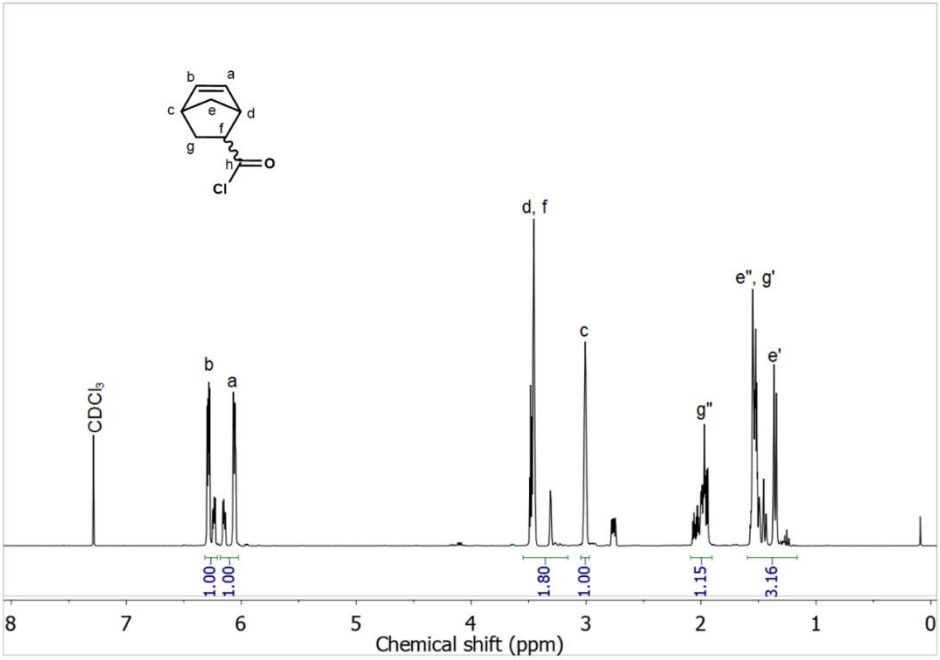

Figure S 3.7 ^{1}H NMR spectrum of bicyclo[2.2.1]hept-5-ene-2-carbonyl chloride

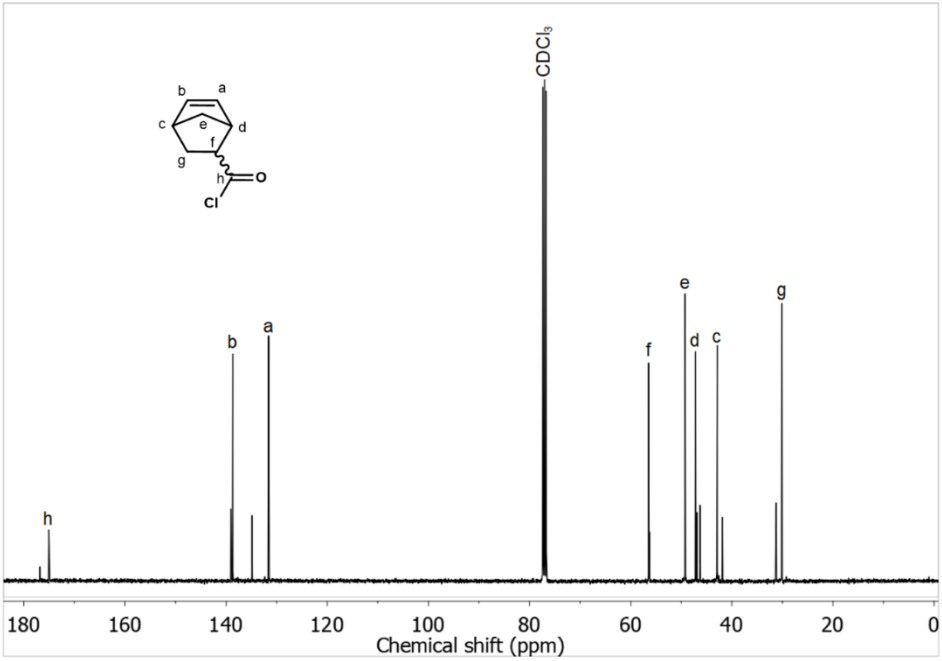

Figure S3.8 ^{13}C NMR spectrum of bicyclo[2.2.1]hept-5-ene-2-carbonyl chloride

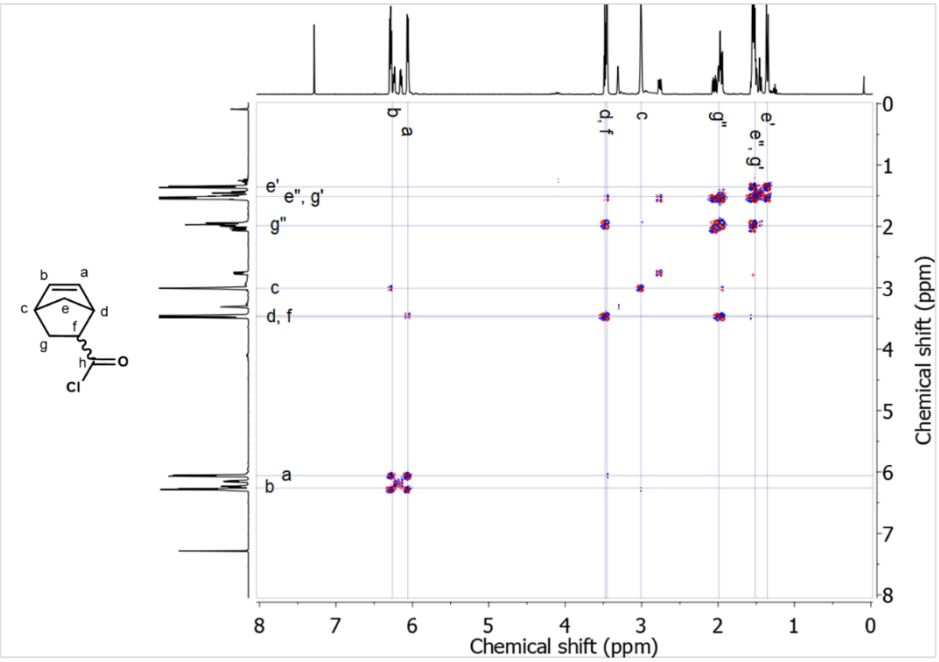

Figure S3.9 COSY of bicyclo[2.2.1]hept-5-ene-2-carbonyl chloride

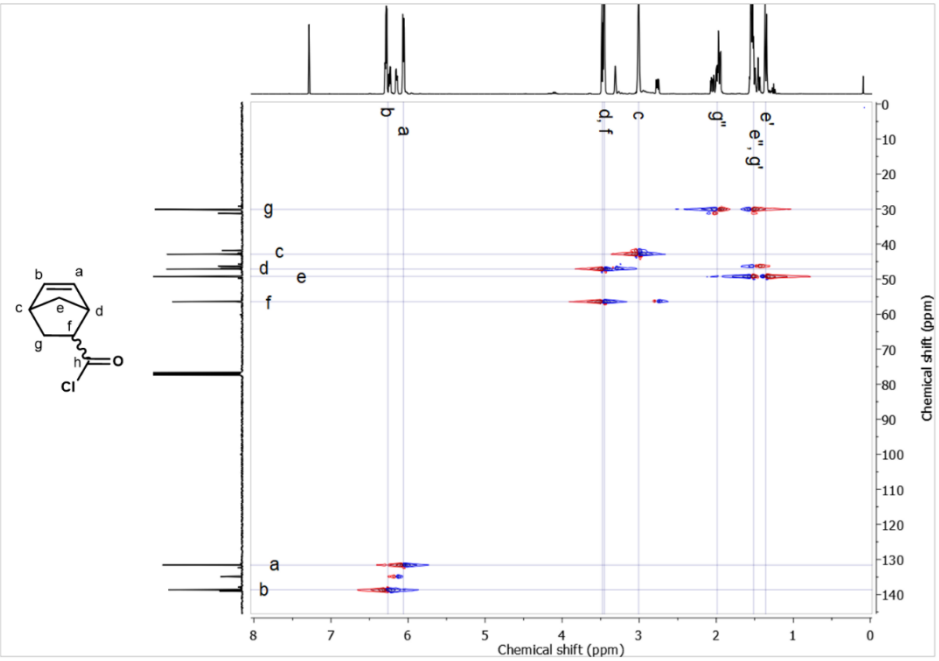

Figure S3.10 HSQC of bicyclo[2.2.1]hept-5-ene-2-carbonyl chloride

3.6.5 Structure characterization of monomers

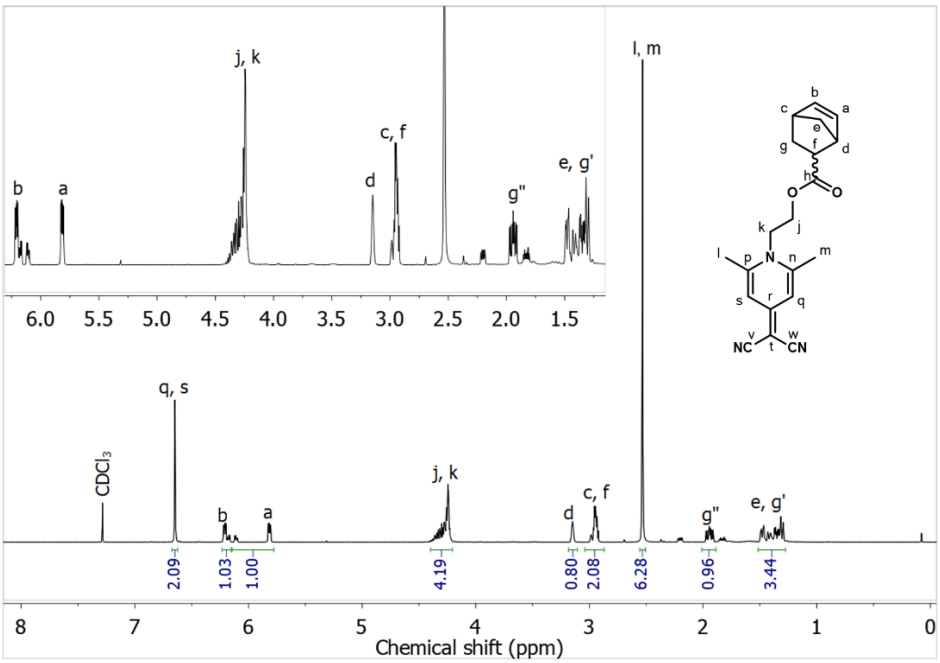

Figure S3.11 ^{1}H NMR spectrum of **NBE-1**

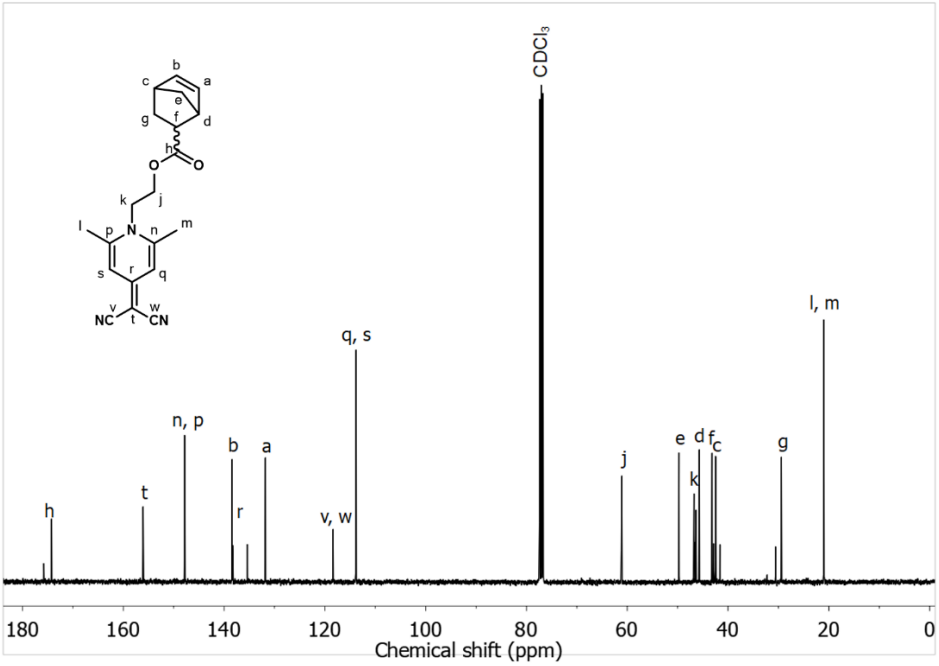

Figure S3.12 ^{13}C NMR spectrum of **NBE-1**

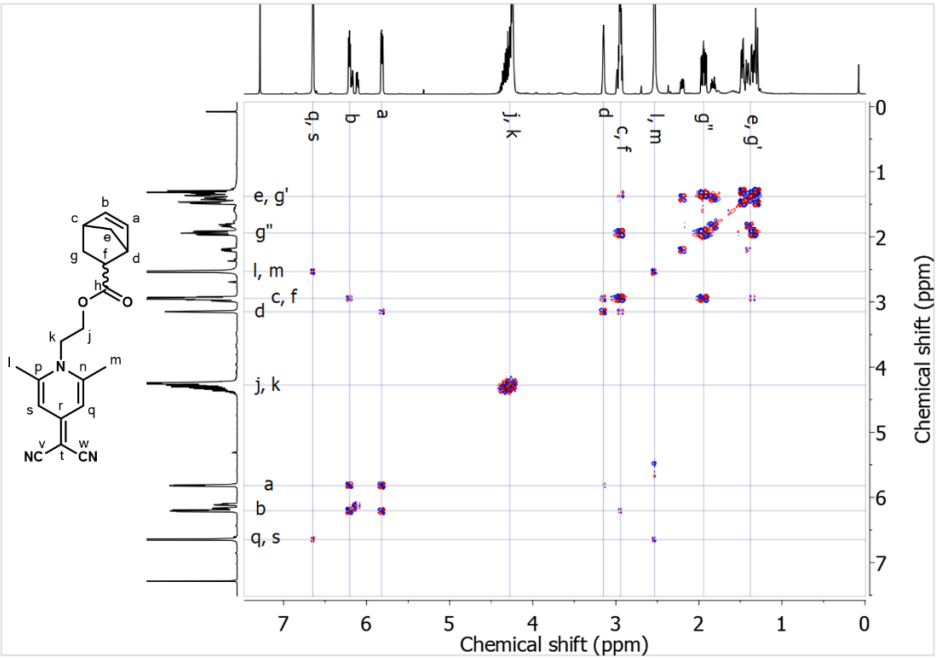

Figure S3.13 COSY of **NBE-1**

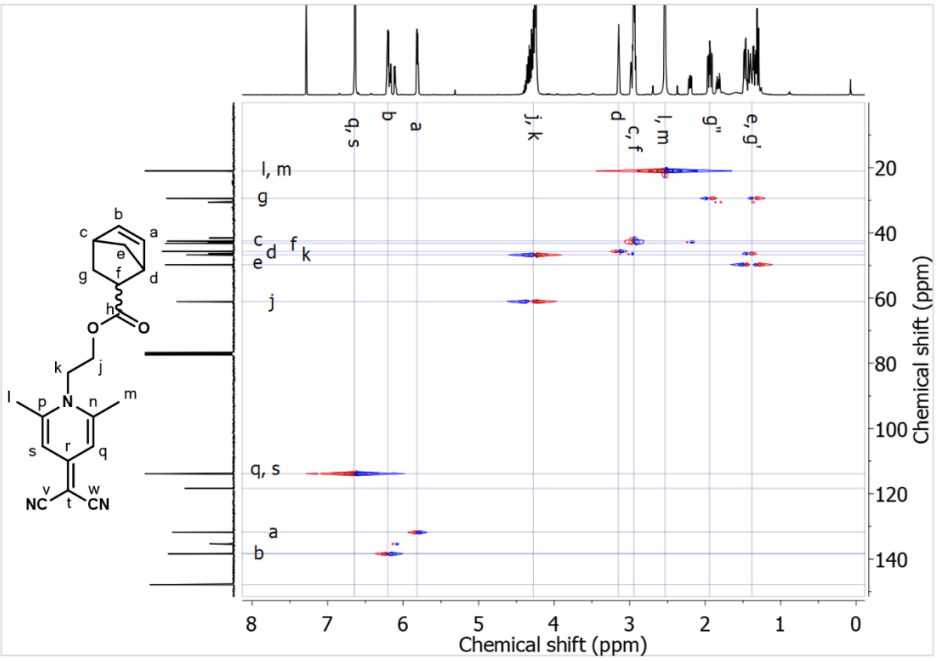

Figure S3.14 HSQC of **NBE-1**

Eidgenössische Technische Hochschule Zürich

Laboratorium für Organische Chemie

ETH-Hönggerberg - HCI E304 8093 Zürich Tel: 044/633 43 58

Mikroelementaranalyse

Name: Owusu Francis Gruppe: Opris EMPA
Labor: LA182 Tel: 058/765 48 01

Substanz: NBE-1
Molekularformel: C20 H21 N3 O2 Mr = 335.40g/mol
HV

Schmelzpunkt:
gereinigt: ??????????????????????????? getrocknet:

Bestimmungen: C H N O

Eingang: 19.09.19 Ausgang: 23.09.19

M-166263 Operator: PK

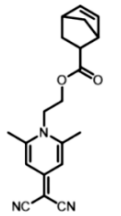

$C_{20}H_{21}N_3O_2$
M = 335.41 g/mol

Berechnete Gewichtsanteile:

[C] 71.62% [H] 6.31% [N] 12.53% [O] 9.54%

Gefundene Gewichtsanteile:

Einwaage: 0.886mg LECO TruSpec Micro
[C] 71.47% [H] 6.37% [N] 12.53% 19.09.19

Einwaage: 0.990mg LECO RO-628
[O] 9.26% 23.09.19

Figure S3.15 Elemental analysis of **NBE-1**

Acquisition Parameter

Method:	ETH_HyStar_HPLC_QTOF_POS_LowMass_Loop-AS.m			Acquisition Date:	10.10.2019 16:03:16
File Name:	D:\Data\bmax0051xx\BMAX005107.d			Operator:	Daniel Wirz
Source Type	ESI	Ion Polarity	Positive	Set Nebulizer	1.6 Bar
Focus	Not active	Set Capillary	4500 V	Set Dry Heater	200 °C
Scan Begin	50 m/z	Set End Plate Offset	-500 V	Set Dry Gas	8.0 l/min
Scan End	1300 m/z	Set Collision Cell RF	200.0 Vpp	Set Divert Valve	Source

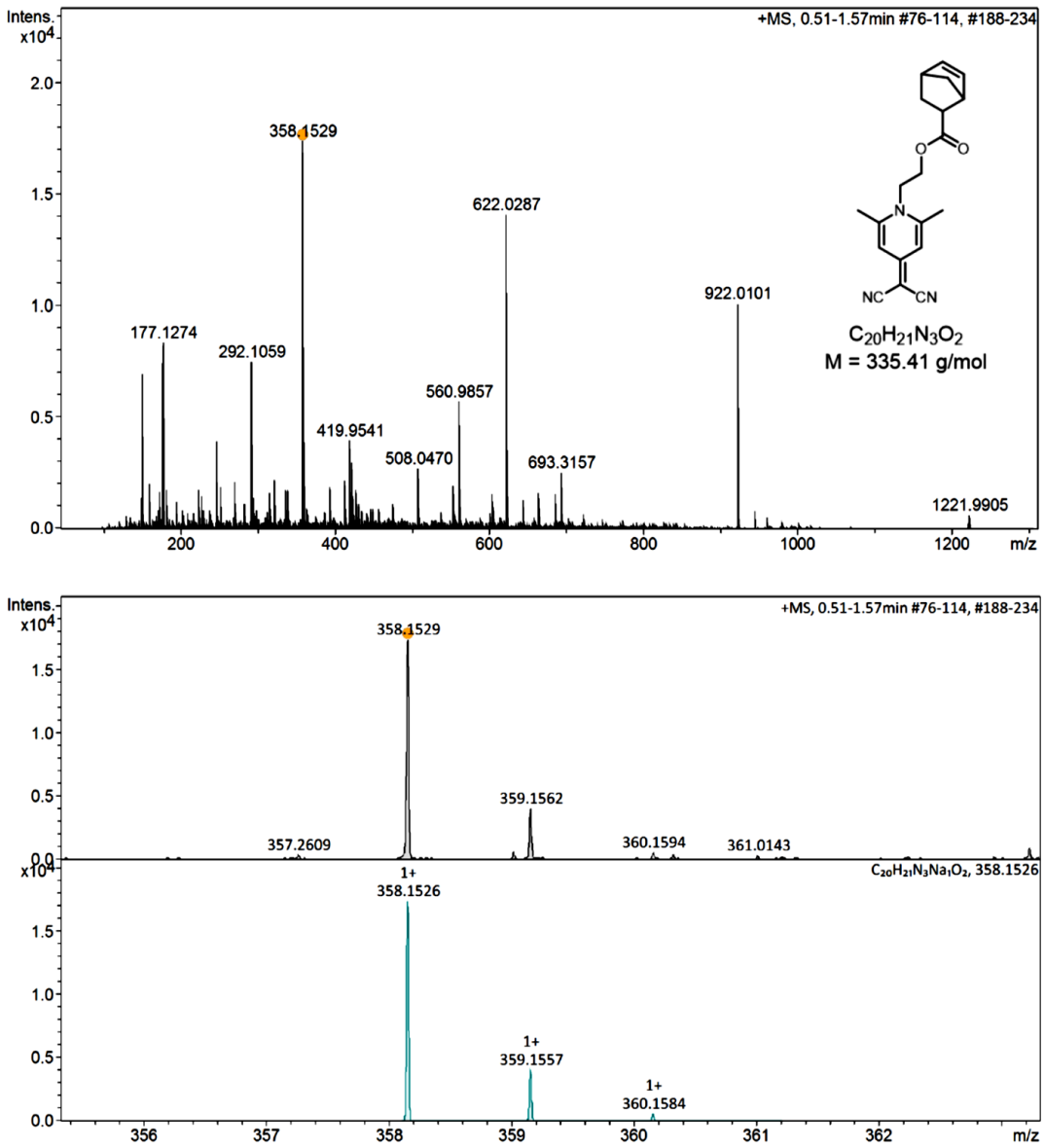

Figure S3.16 Mass spectra of **NBE-1**

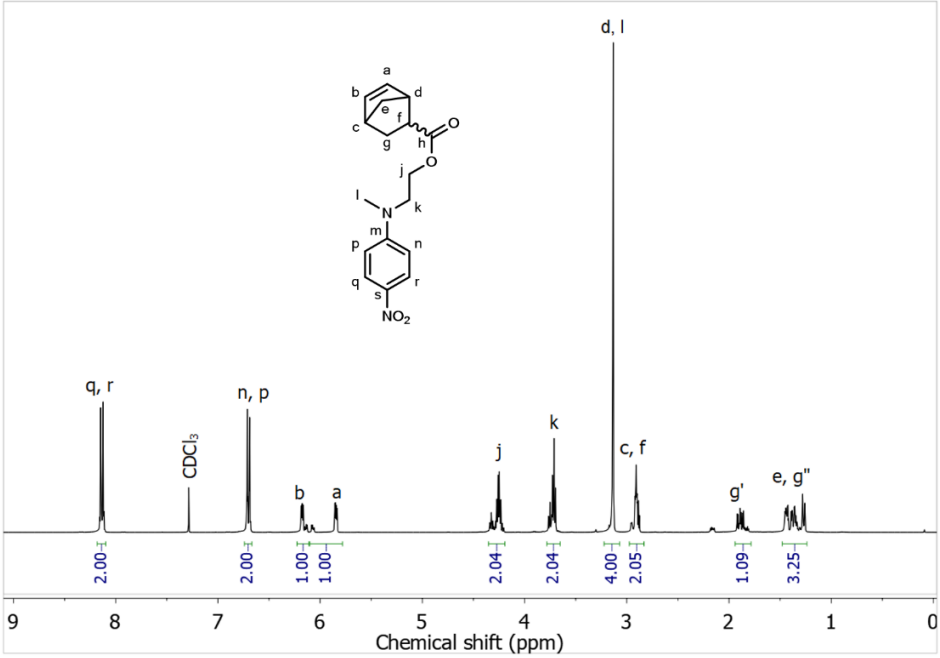

Figure S3.17 ^{1}H NMR spectrum of **NBE-2**

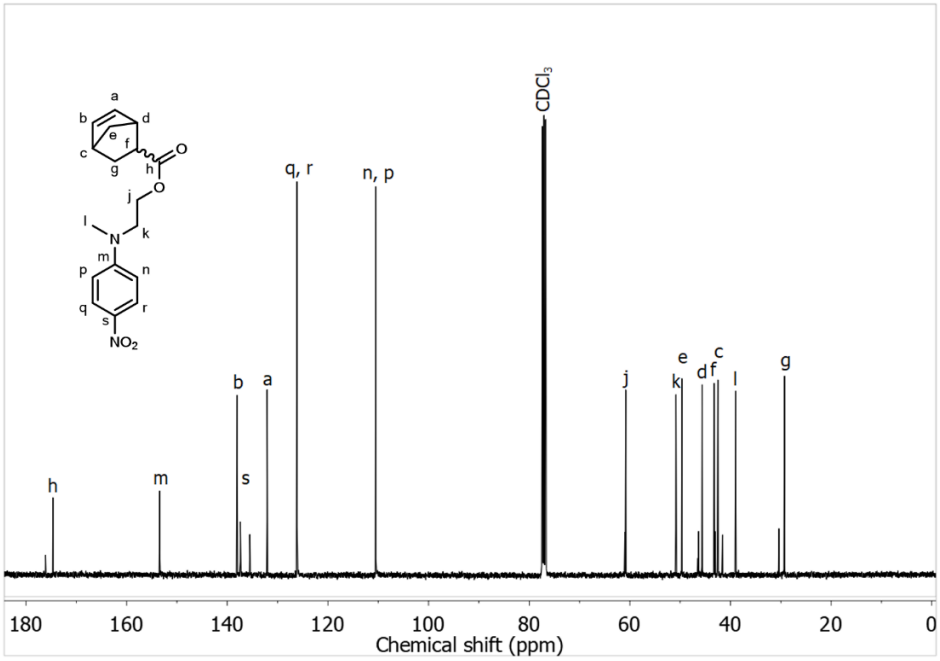

Figure S3.18 ^{13}C NMR spectrum of **NBE-2**

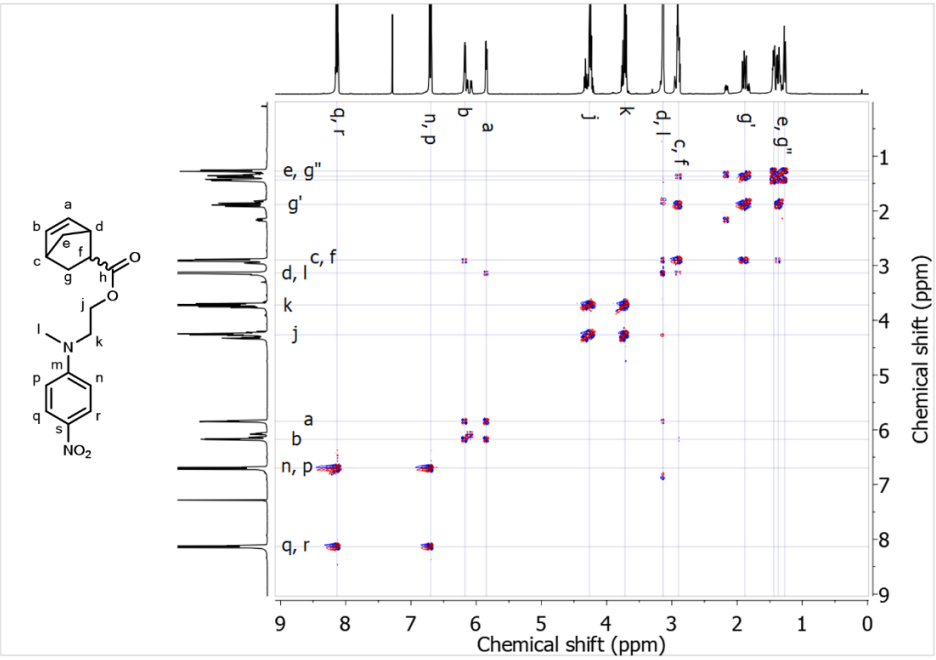

Figure S3.19 COSY of **NBE-2**

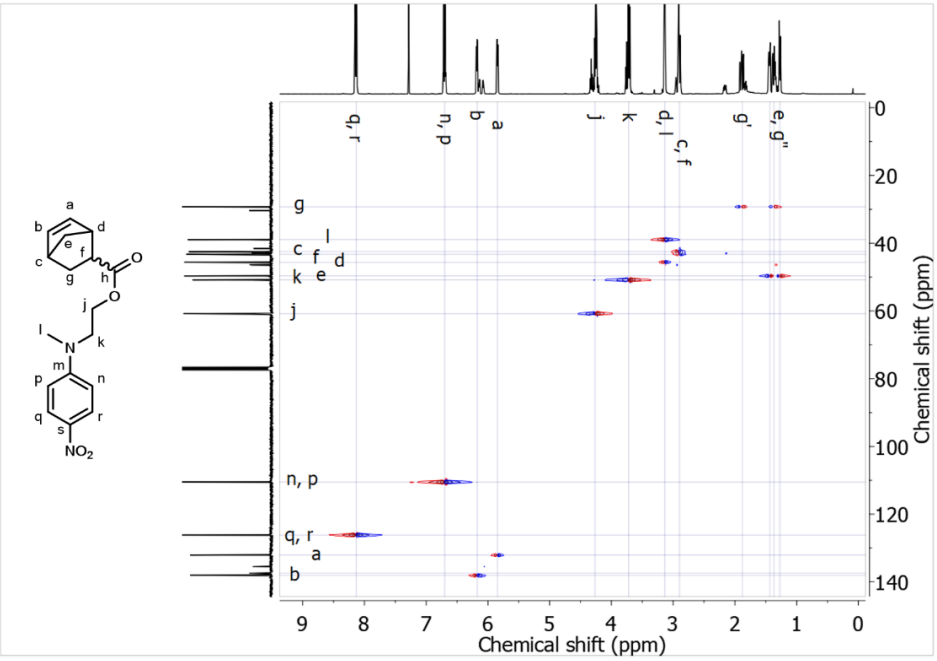

Figure S3.20 HSQC of **NBE-2**

Eidgenössische Technische Hochschule Zürich

Laboratorium für Organische Chemie

ETH-Hönggerberg - HCI E304 8093 Zürich Tel: 044/633 43 58

Mikroelementaranalyse

Name: Owusu Francis Gruppe: Opris EMPA
Labor: LA182 Tel: 058/765 48 01

Substanz: NBE-2
Molekularformel: C17 H20 N2 O4 Mr = 316.36g/mol

Siedepunkt:
gereinigt: ??????????????????????? getrocknet: HV

Bestimmungen: C H N

Eingang: 19.09.19 Ausgang: 19.09.19

M-166262 Operator: PK

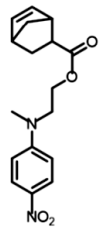

$C_{17}H_{20}N_2O_4$
M = 316.36 g/mol

Berechnete Gewichtsanteile:

[C] 64.54% [H] 6.37% [N] 8.86% [O] 20.23%

Gefundene Gewichtsanteile:

Einwaage: 0.959mg LECO TruSpec Micro
[C] 64.68% [H] 6.54% [N] 8.92% 19.09.19

Von flüssigen Proben können nur CHN bestimmt werden.

Figure S3.21 Elemental analysis of **NBE-2**

Acquisition Parameter

Method:	ETH_HyStar_HPLC_QTOF_POS_LowMass_Loop-AS.m			Acquisition Date:	10.10.2019 16:00:19
File Name:	D:\Data\bmax0051xx\BMAX005106.d			Operator:	Daniel Wirz
Source Type	ESI	Ion Polarity	Positive	Set Nebulizer	1.6 Bar
Focus	Not active	Set Capillary	4500 V	Set Dry Heater	200 °C
Scan Begin	50 m/z	Set End Plate Offset	-500 V	Set Dry Gas	8.0 l/min
Scan End	1300 m/z	Set Collision Cell RF	200.0 Vpp	Set Divert Valve	Source

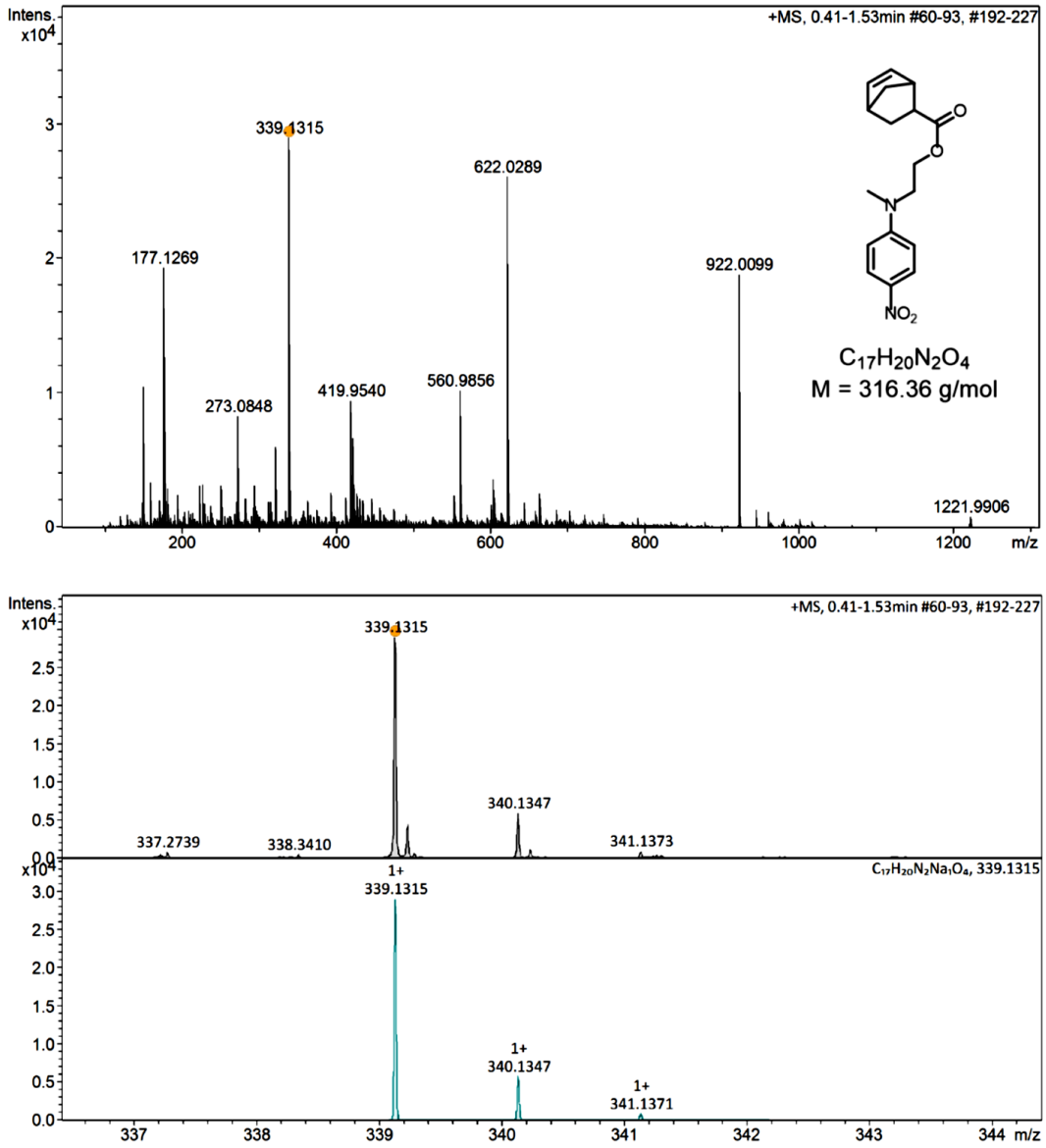

Figure S3.22 Mass spectra of **NBE-2**

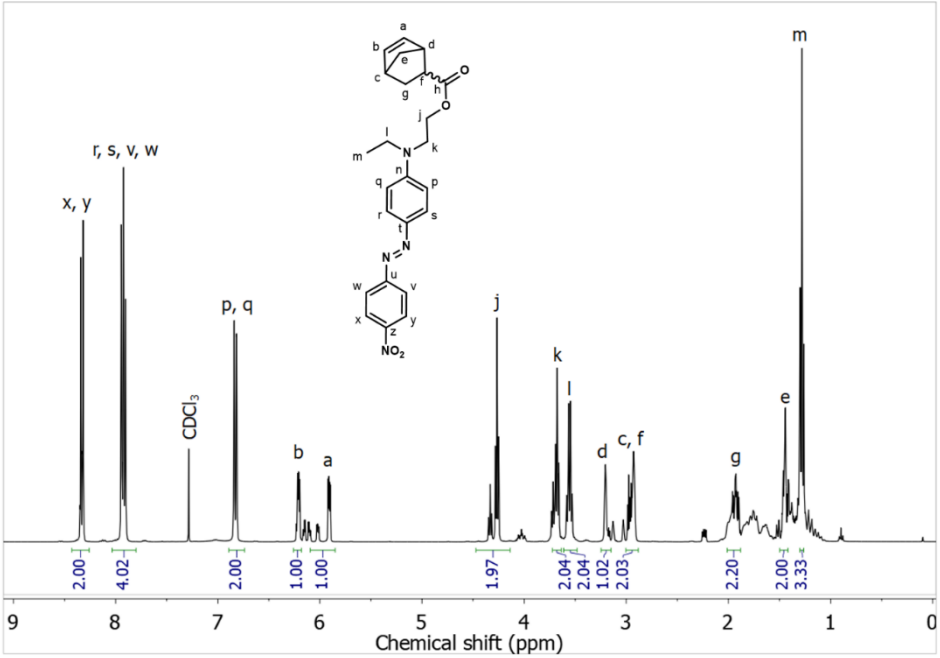

Figure S3.23 ^{1}H NMR spectrum of **NBE-3**

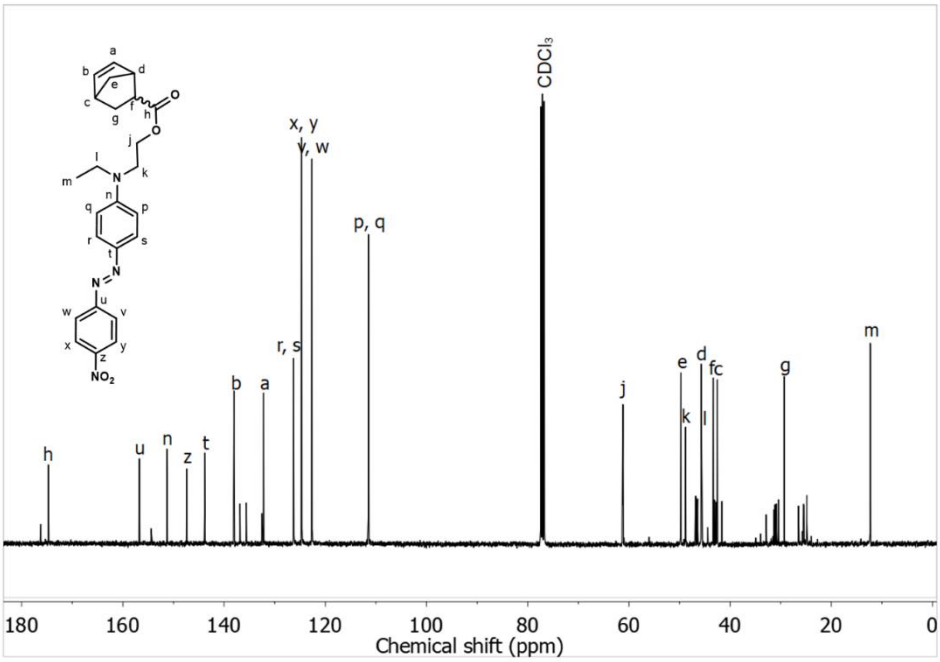

Figure S3.24 ^{13}C NMR spectrum of **NBE-3**

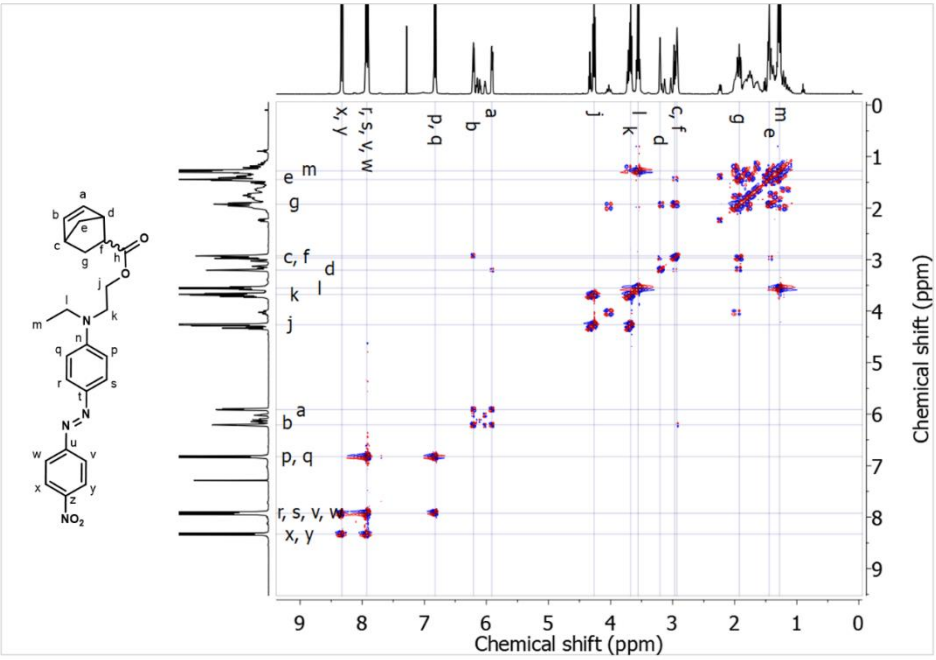

Figure S3.25 COSY of **NBE-3**

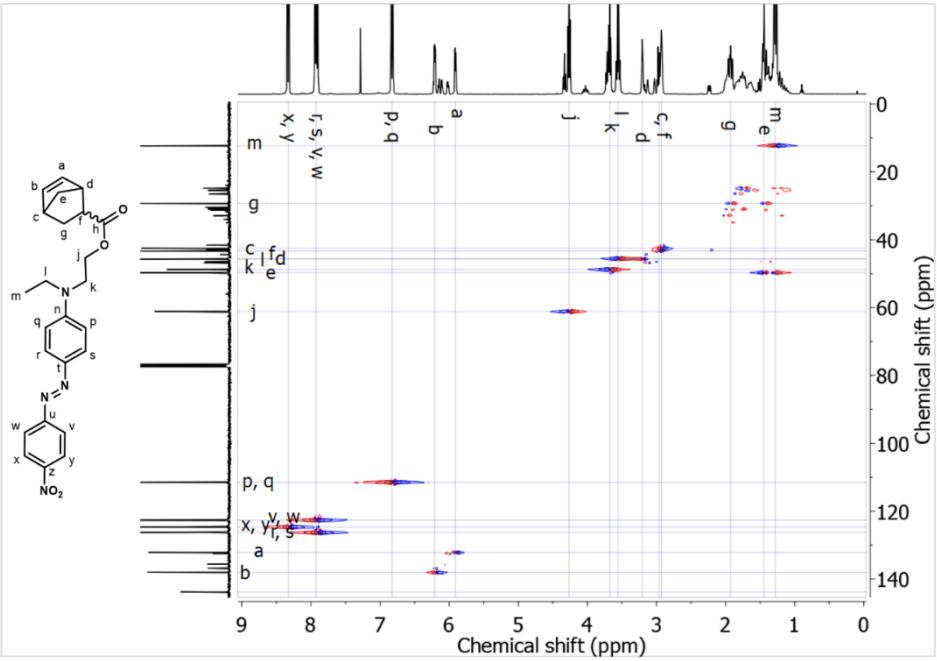

Figure S3.26 HSQC of **NBE-3**

Eidgenössische Technische Hochschule Zürich

Laboratorium für Organische Chemie

ETH-Hönggerberg - HCI E304 8093 Zürich Tel: 044/633 43 58

Mikroelementaranalyse

Name: Owusu Francis Gruppe: Opris EMPA
Labor: LA182 Tel: 058/765 48 01

Substanz: NBE-3
Molekularformel: C24 H26 N4 O4 Mr = 434.49g/mol

Schmelzpunkt:
gereinigt: ????????????????????????? getrocknet: HV

Bestimmungen: C H N

Eingang: 19.09.19 Ausgang: 19.09.19

M-166264 Operator: PK

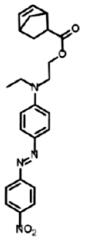

$C_{24}H_{26}N_4O_4$
M = 434.50 g/mol

Berechnete Gewichtsanteile:

[C] 66.34% [H] 6.03% [N] 12.89% [O] 14.73%

Gefundene Gewichtsanteile:

Einwaage: 0.919mg LECO TruSpec Micro
[C] 68.16% [H] 6.89% [N] 12.13% 19.09.19

Einwaage: 0.910mg LECO TruSpec Micro
[C] 67.97% [H] 6.94% [N] 12.13% 19.09.19

wegen zu grosser Abweichung werden keine weiteren Bestimmungen durchgeführt

Figure S3.27 Elemental analysis of **NBE-3**

Acquisition Parameter

Method:	ETH_HyStar_HPLC_QTOF_POS_LowMass_Loop-AS.m			Acquisition Date:	10.10.2019 16:06:14
File Name:	D:\Data\bmax0051xx\BMAX005108.d			Operator:	Daniel Wirz
Source Type	ESI	Ion Polarity	Positive	Set Nebulizer	1.6 Bar
Focus	Not active	Set Capillary	4500 V	Set Dry Heater	200 °C
Scan Begin	50 m/z	Set End Plate Offset	-500 V	Set Dry Gas	8.0 l/min
Scan End	1300 m/z	Set Collision Cell RF	200.0 Vpp	Set Divert Valve	Source

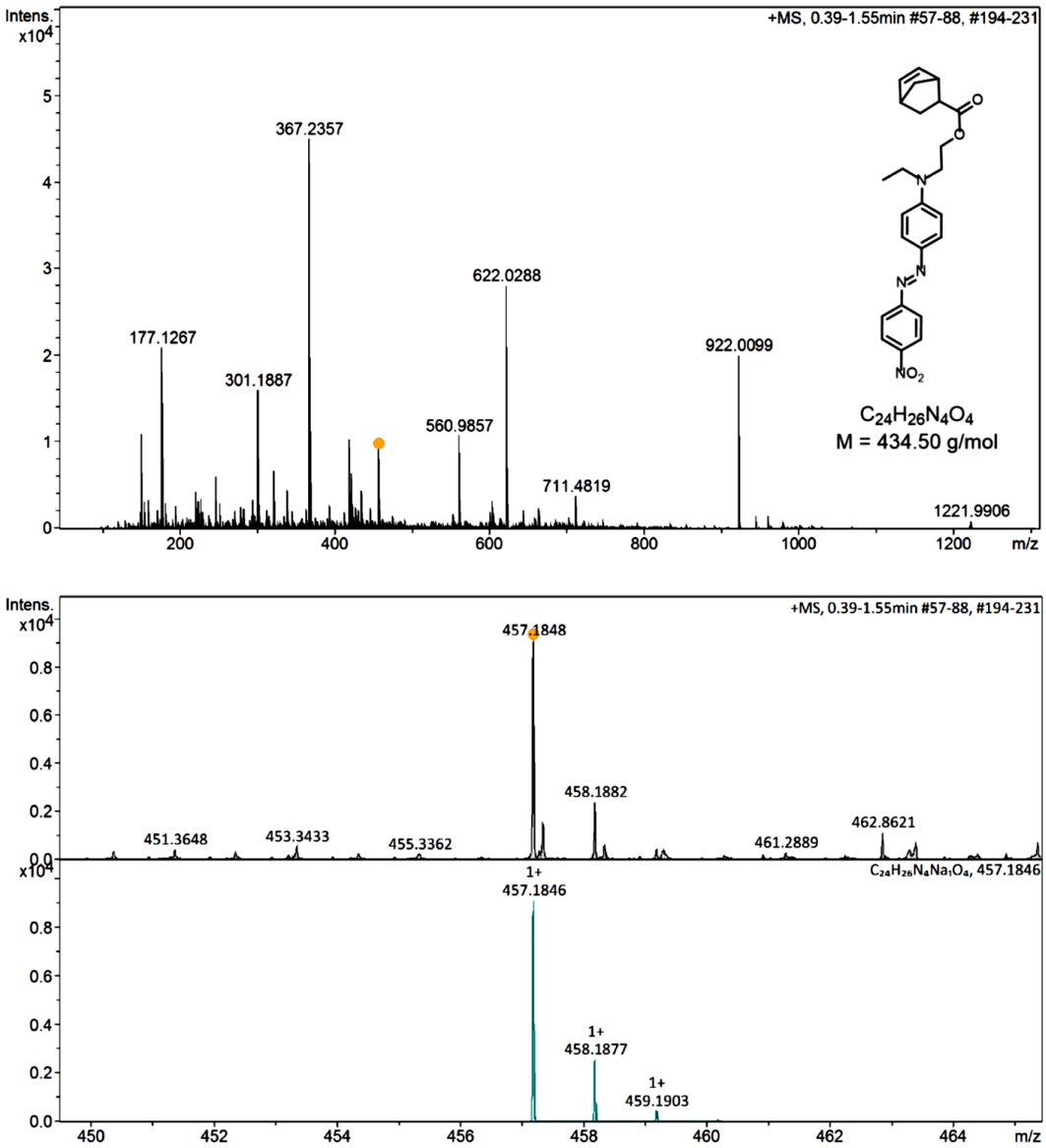

Figure S3.28 Mass spectra of **NBE-3**

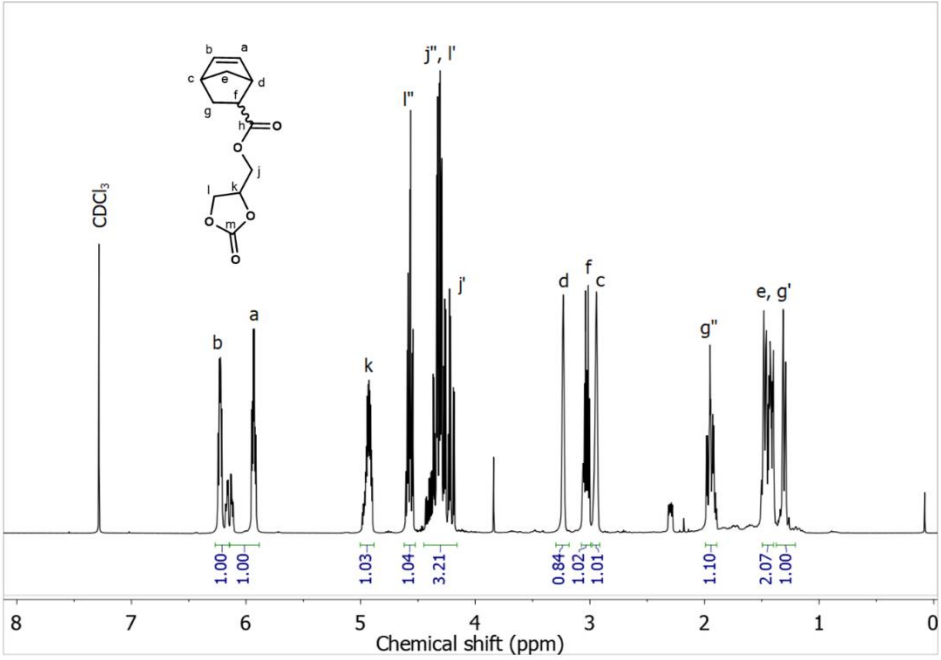

Figure S3.29 ^{1}H NMR spectrum of **NBE-4**

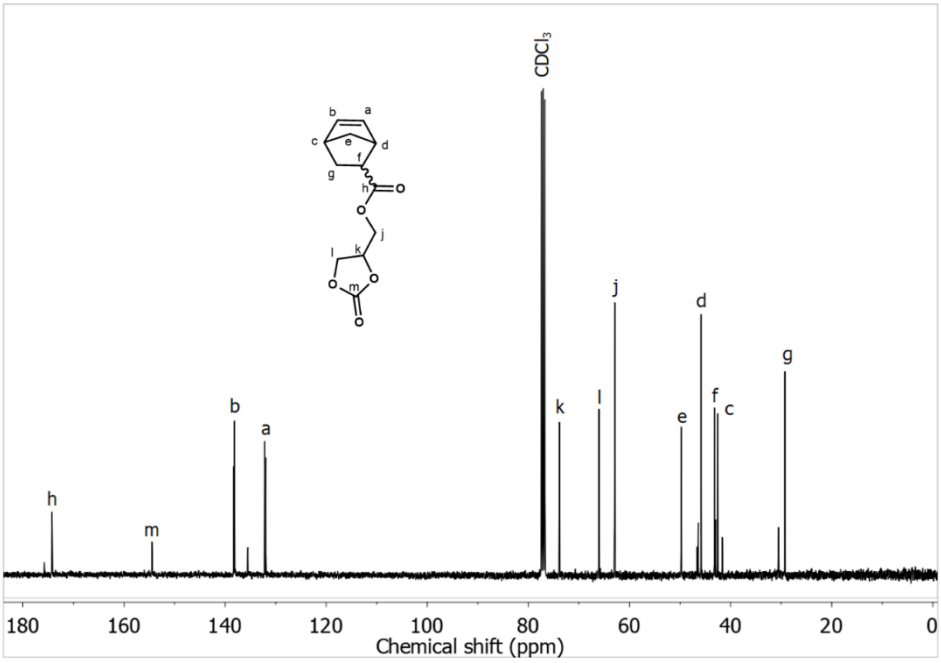

Figure S3.30 ^{13}C NMR spectrum of **NBE-4**

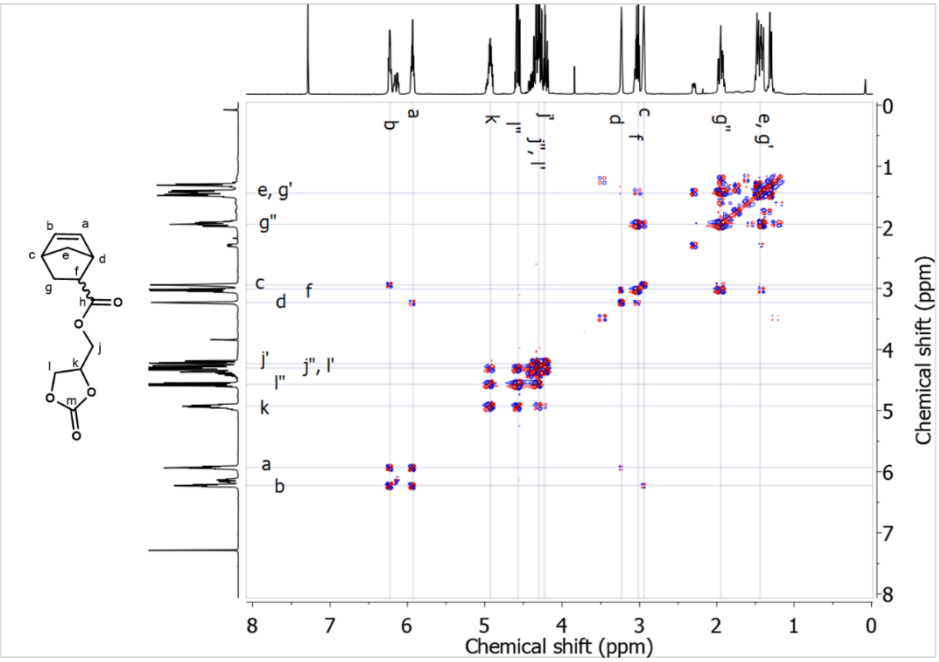

Figure S3.31 COSY of **NBE-4**

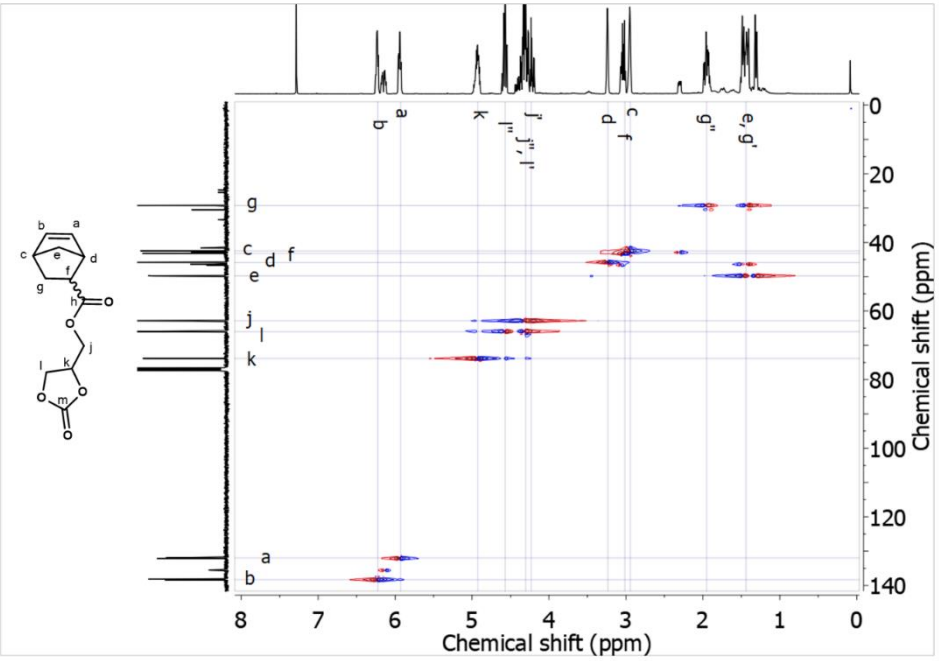

Figure S3.32 HSQC of **NBE-4**

Eidgenössische Technische Hochschule Zürich

Laboratorium für Organische Chemie

ETH-Hönggerberg - HCI E304 8093 Zürich Tel: 044/633 43 58

Mikroelementaranalyse

Name: Owusu Francis Gruppe: Opris EMPA
Labor: LA182 Tel: 058/765 48 01

Substanz: NBE-4
Molekularformel: C12 H14 O5 Mr = 238.24g/mol

Siedepunkt:
gereinigt: ???????????????????????? getrocknet: HV

Bestimmungen: C H N

Eingang: 19.09.19 Ausgang: 20.09.19

M-166265 Operator: PK

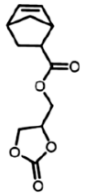

$C_{12}H_{14}O_5$
M = 238.24 g/mol

Berechnete Gewichtsanteile:

[C] 60.50% [H] 5.92% [O] 33.58%

Gefundene Gewichtsanteile:

Einwaage: 0.982mg LECO TruSpec Micro
[C] 60.78% [H] 6.44% 20.09.19

Einwaage: 0.971mg LECO TruSpec Micro
[C] 60.83% [H] 6.22% 20.09.19

Von flüssigen Proben können nur CHN bestimmt werden. Probe ist nicht homoge
n (Flüssig+Kristalle)

Figure S3.33 Elemental analysis of **NBE-4**

Acquisition Parameter

Method:	ETH_HyStar_HPLC_QTOF_POS_LowMass_Loop-AS.m			Acquisition Date:	10.10.2019 16:09:13
File Name:	D:\Data\bmax0051xx\BMAX005109.d			Operator:	Daniel Wirz
Source Type	ESI	Ion Polarity	Positive	Set Nebulizer	1.6 Bar
Focus	Not active	Set Capillary	4500 V	Set Dry Heater	200 °C
Scan Begin	50 m/z	Set End Plate Offset	-500 V	Set Dry Gas	8.0 l/min
Scan End	1300 m/z	Set Collision Cell RF	200.0 Vpp	Set Divert Valve	Source

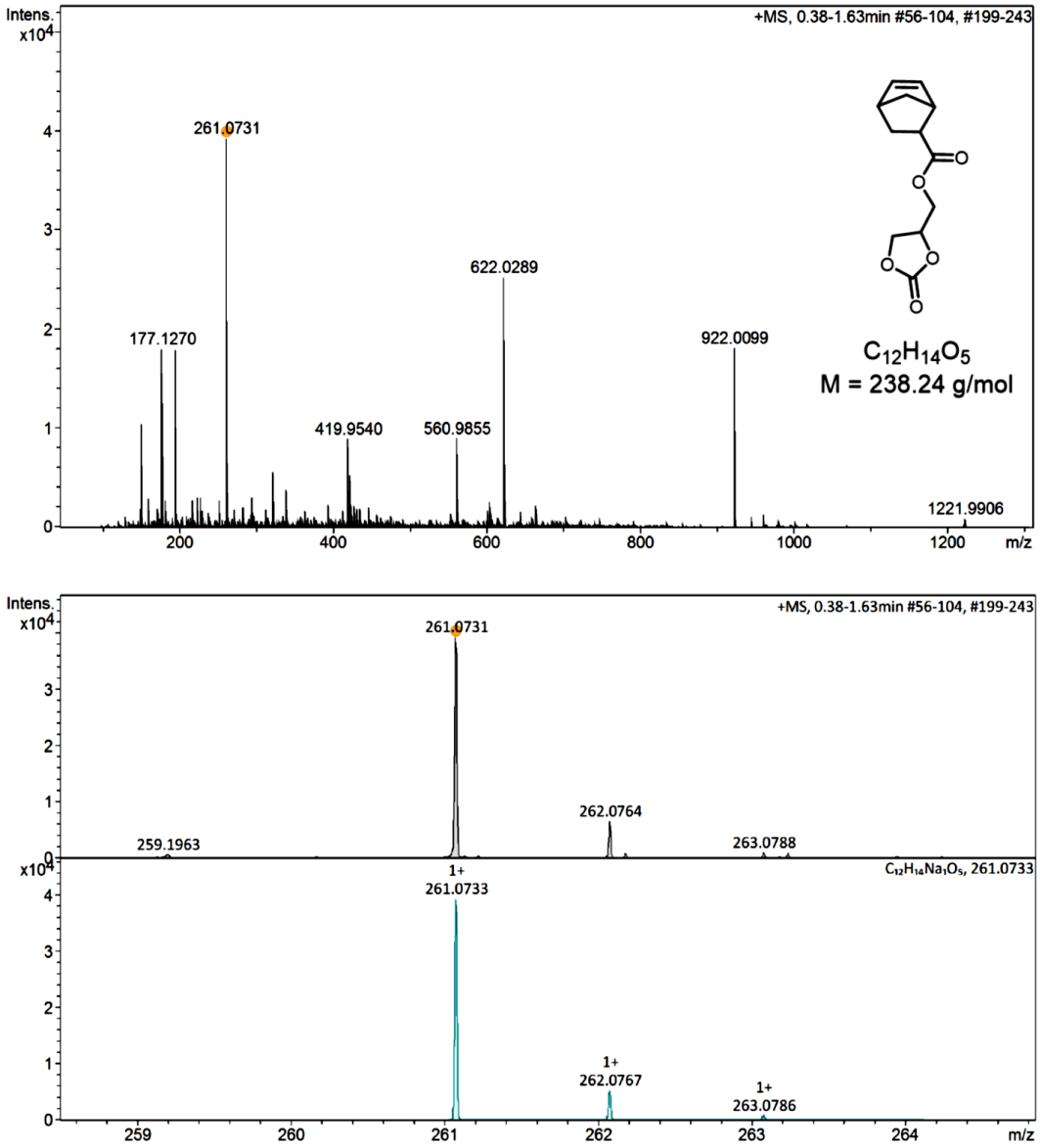

Figure S3.34 Mass spectra of **NBE-4**

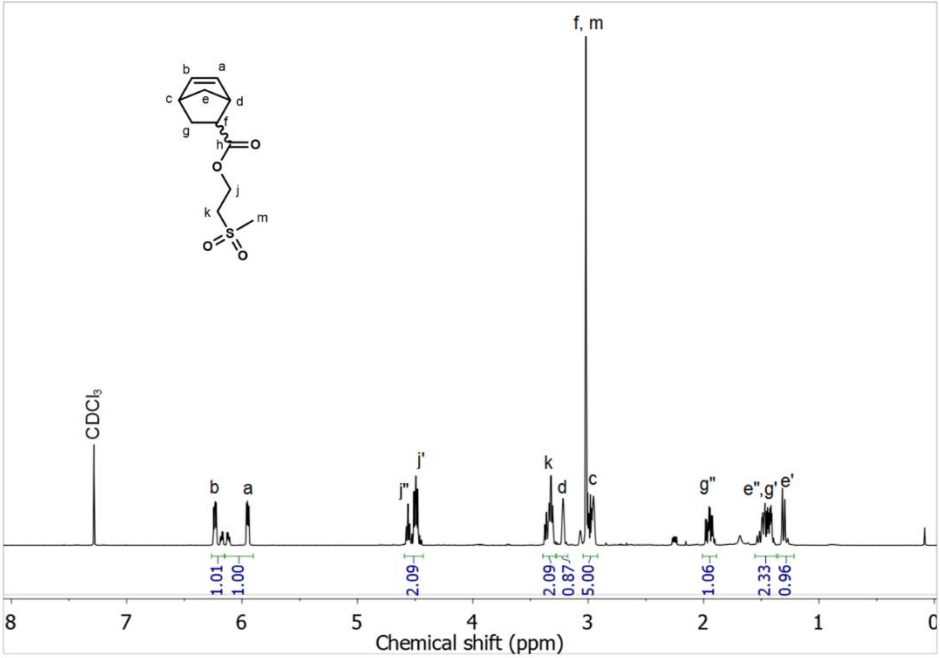

Figure S3.35 ^{1}H NMR spectrum of **NBE-5**

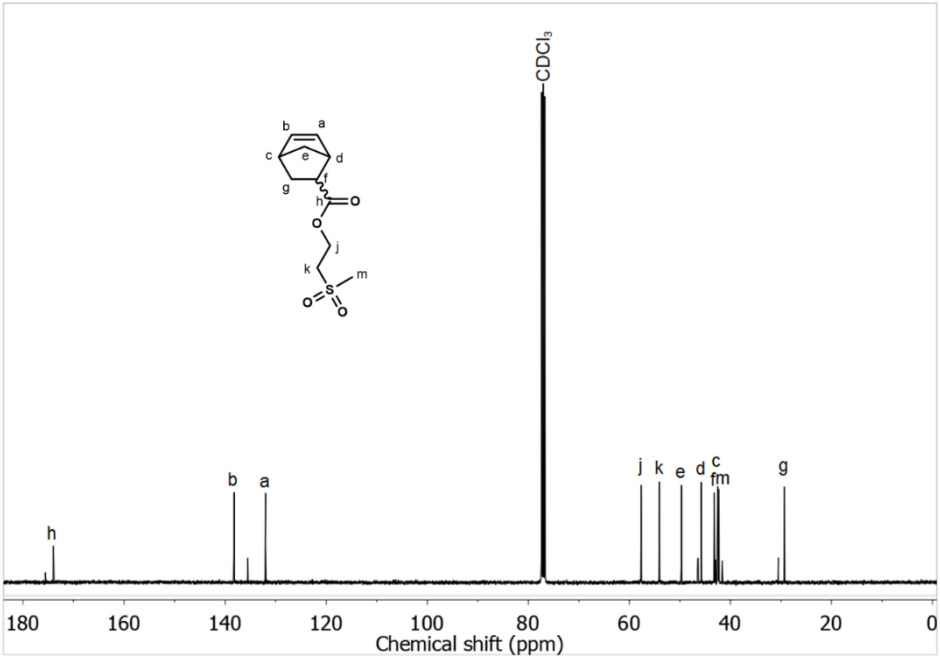

Figure S3.36 ^{13}C NMR spectrum of **NBE-5**

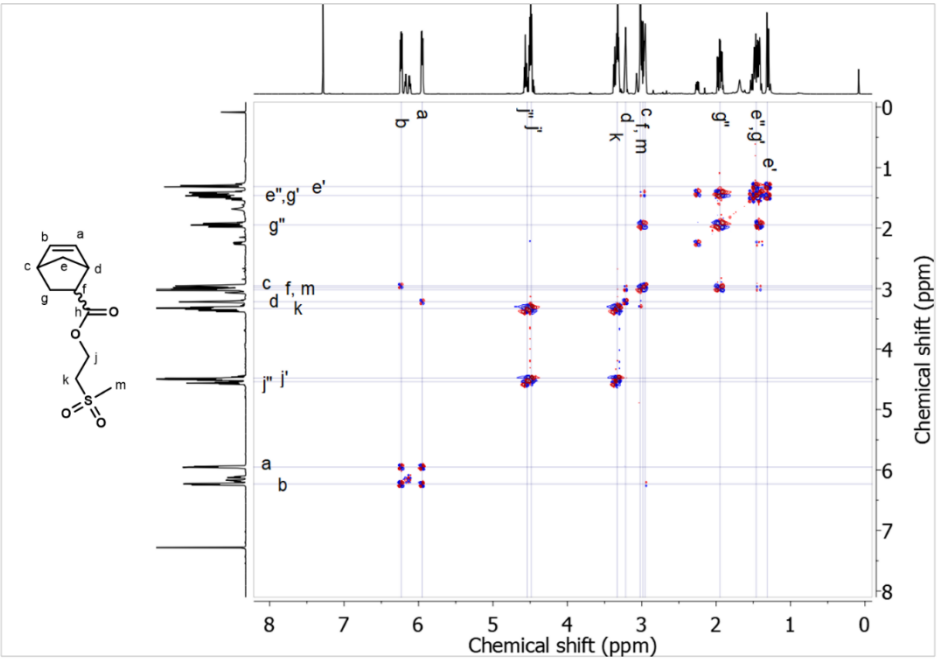

Figure S3.37 COSY of **NBE-5**

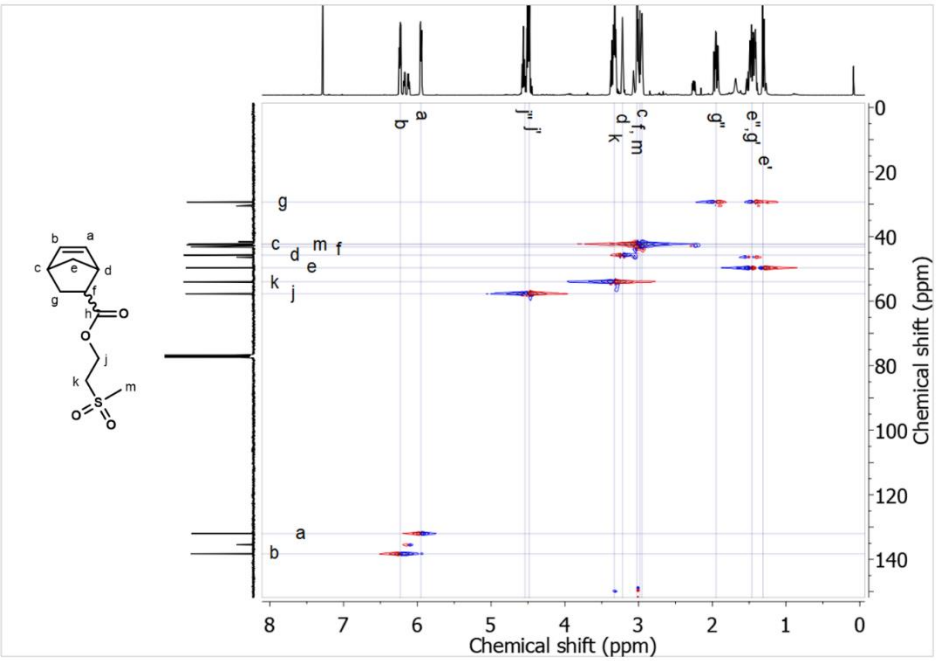

Figure S3.38 HQSC of **NBE-5**

Acquisition Parameter

Method:	ETH_HyStar_HPLC_QTOF_POS_LowMass_Loop-AS.m			Acquisition Date:	26.08.2020 13:39:31
File Name:	D:\Data\bmax0096xx\BMAX009630.d			Operator:	Michael Meier
Source Type	ESI	Ion Polarity	Positive	Set Nebulizer	1.6 Bar
Focus	Not active	Set Capillary	4500 V	Set Dry Heater	200 °C
Scan Begin	50 m/z	Set End Plate Offset	-500 V	Set Dry Gas	8.0 l/min
Scan End	1300 m/z	Set Collision Cell RF	200.0 Vpp	Set Divert Valve	Source

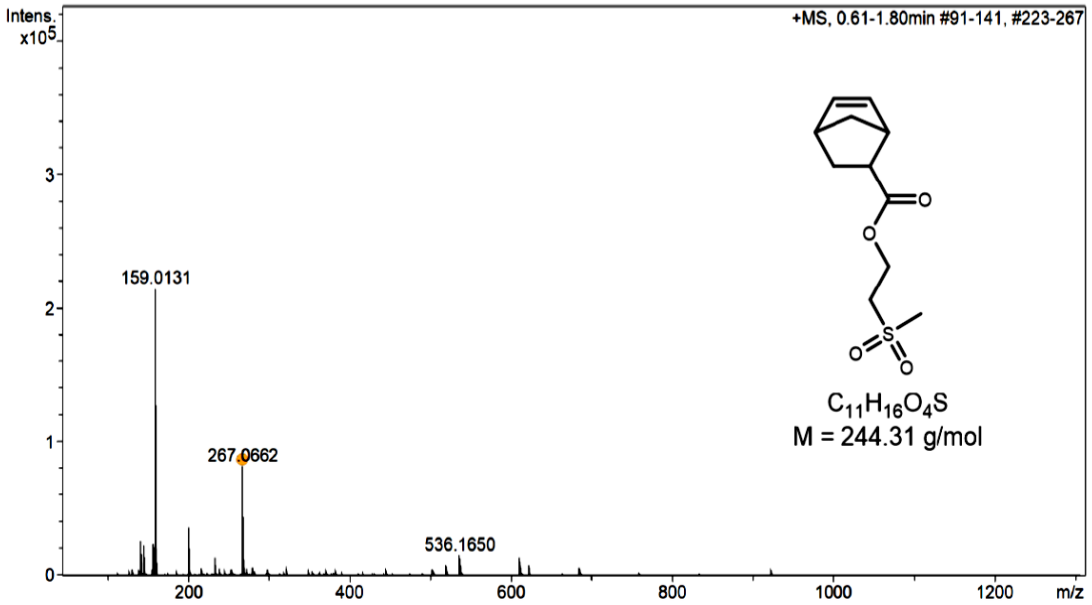

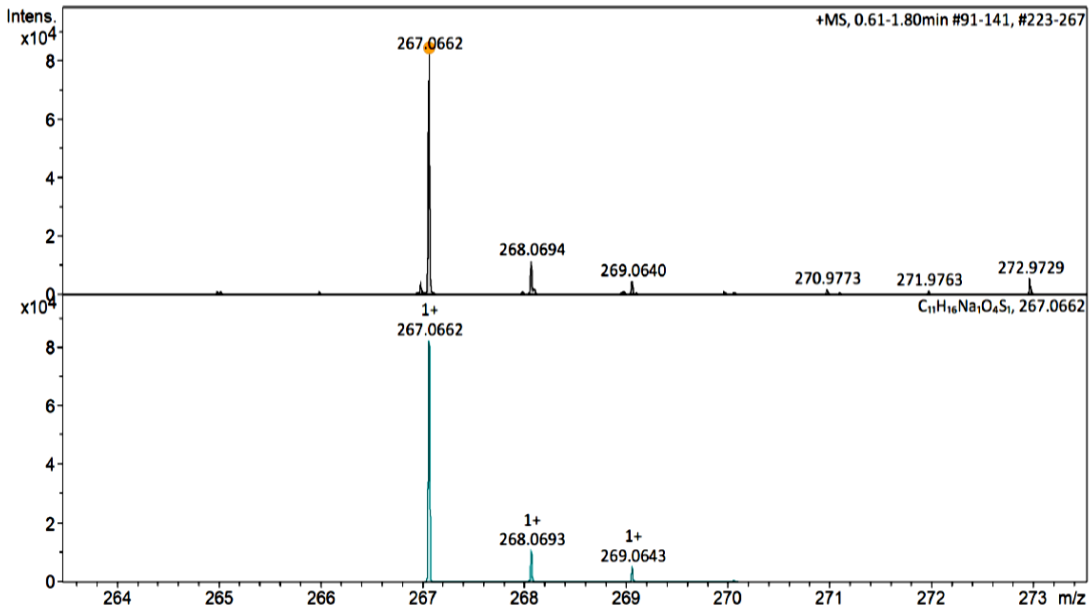

Figure S3.39 Mass spectra of **NBE-5**

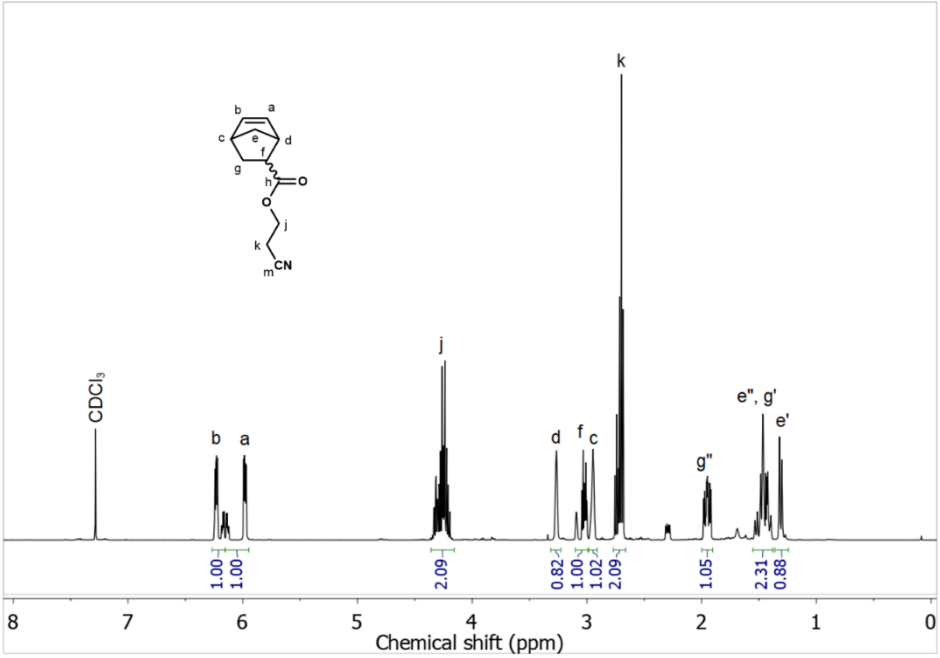

Figure S3.40 ^{1}H NMR spectrum of **NBE-6**

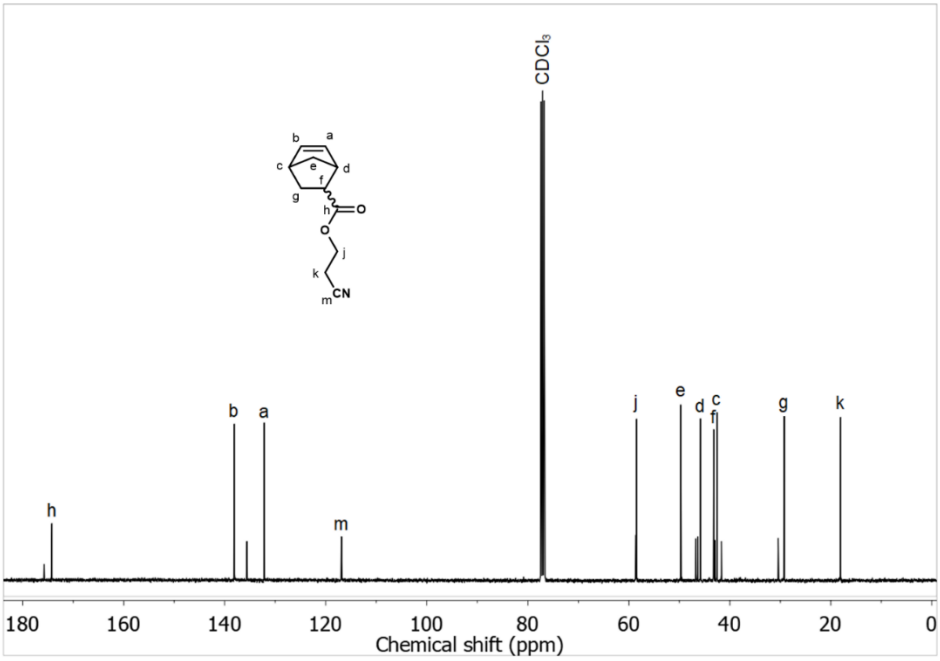

Figure S3.41 ^{13}C NMR spectrum of **NBE-6**

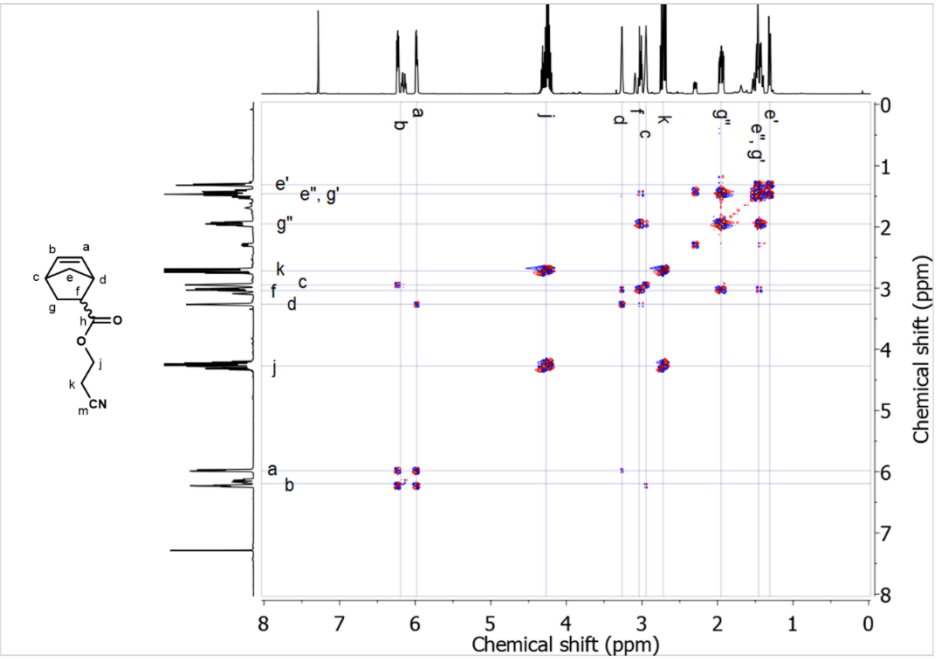

Figure S3.42 COSY of **NBE-6**

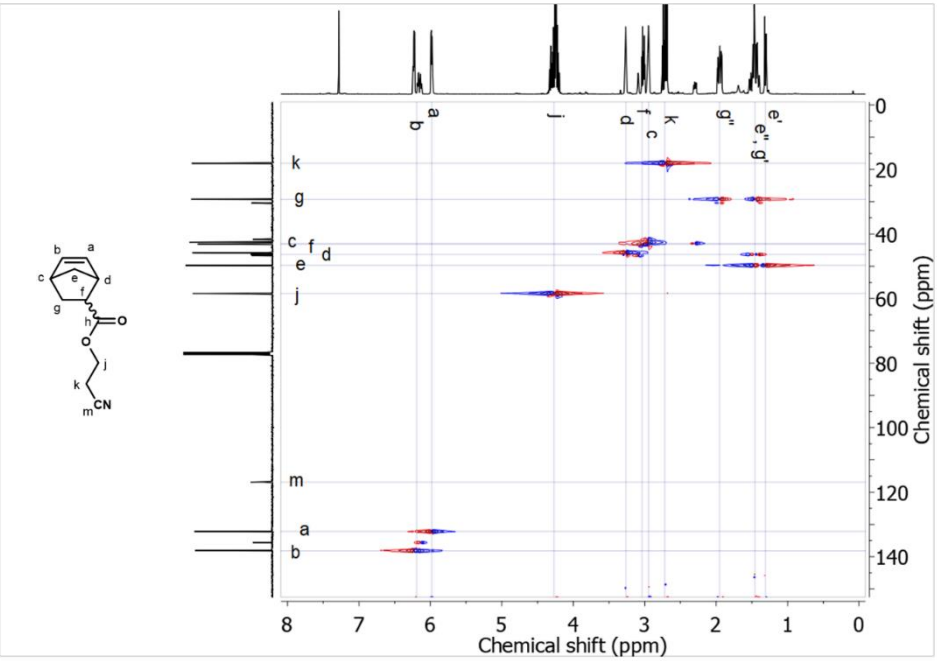

Figure S3.43 HSQC of **NBE-6**

Acquisition Parameter

Method:	ETH_HyStar_HPLC_QTOF_POS_LowMass_Loop-AS.m			Acquisition Date:	26.08.2020 13:42:29
File Name:	D:\Data\bmax0096xx\BMAX009631.d			Operator:	Michael Meier
Source Type	ESI	Ion Polarity	Positive	Set Nebulizer	1.6 Bar
Focus	Not active	Set Capillary	4500 V	Set Dry Heater	200 °C
Scan Begin	50 m/z	Set End Plate Offset	-500 V	Set Dry Gas	8.0 l/min
Scan End	1300 m/z	Set Collision Cell RF	200.0 Vpp	Set Divert Valve	Source

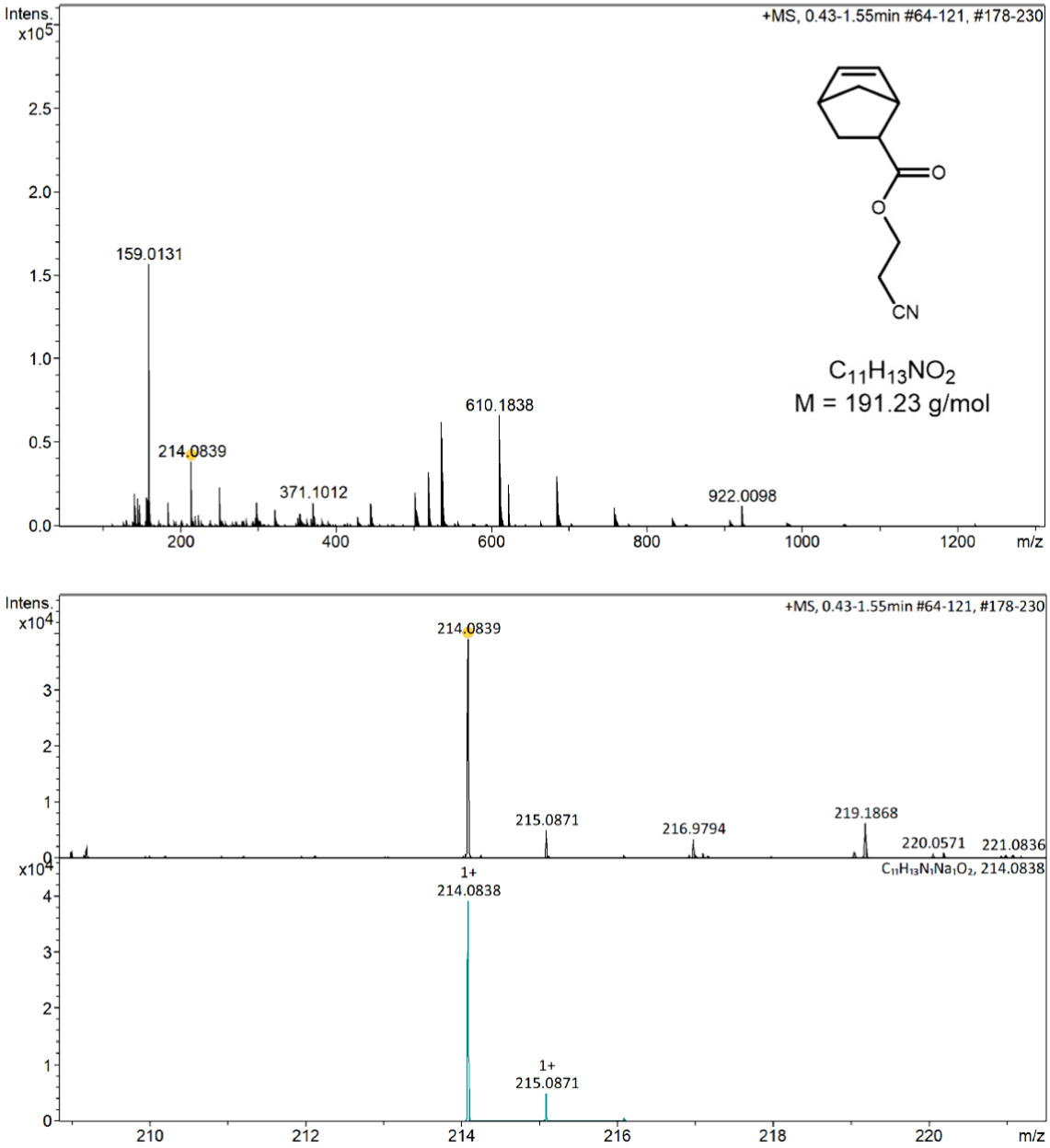

Figure S3.44 Mass spectra of **NBE-6**

3.6.6 Structure characterization of polymers

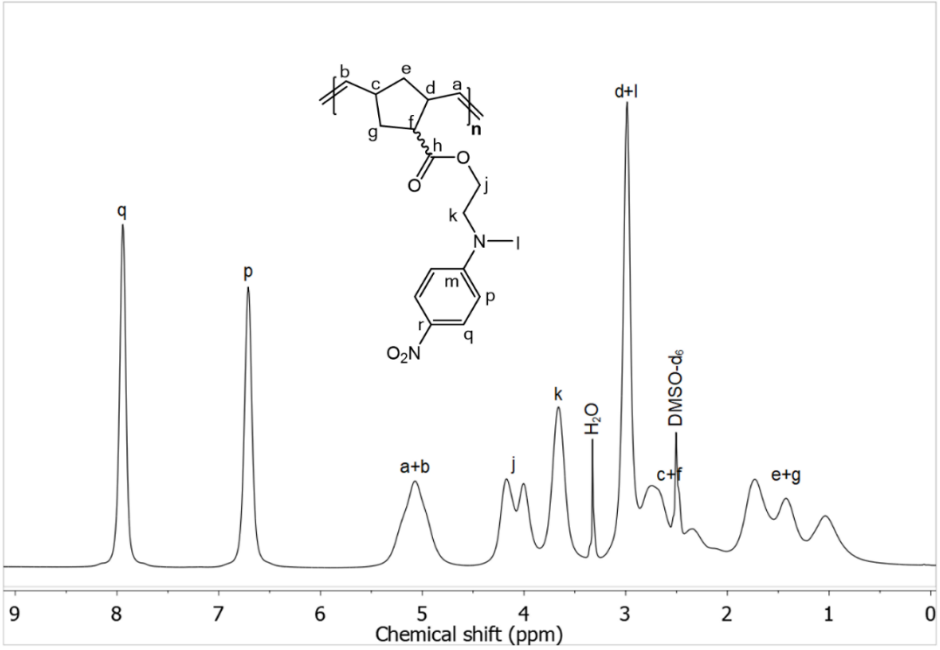

Figure S3.45 ^{1}H NMR spectrum of **PNBE-2**

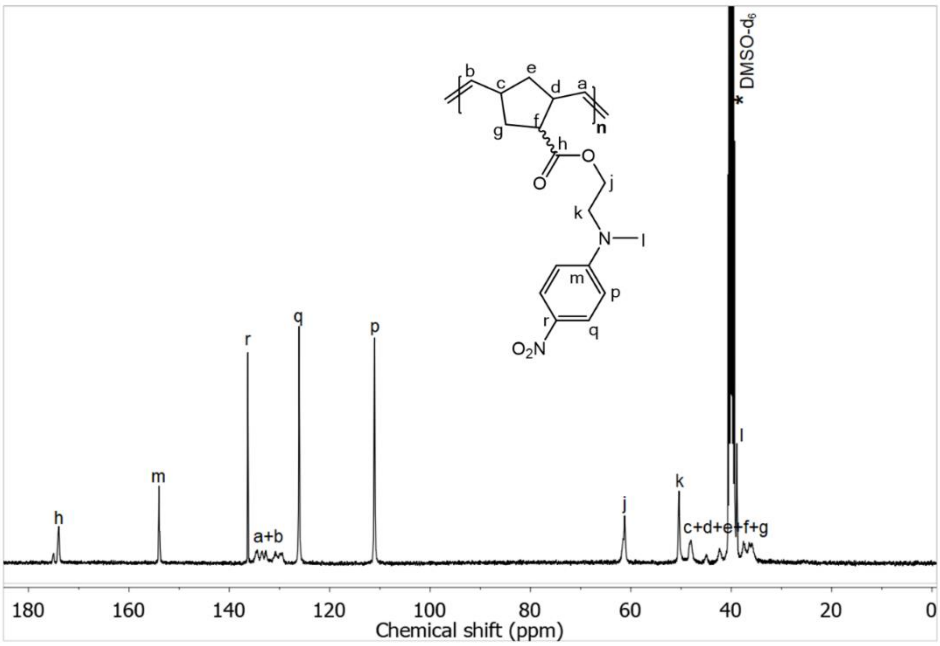

Figure S3.46 ^{13}C NMR spectrum of **PNBE-2**

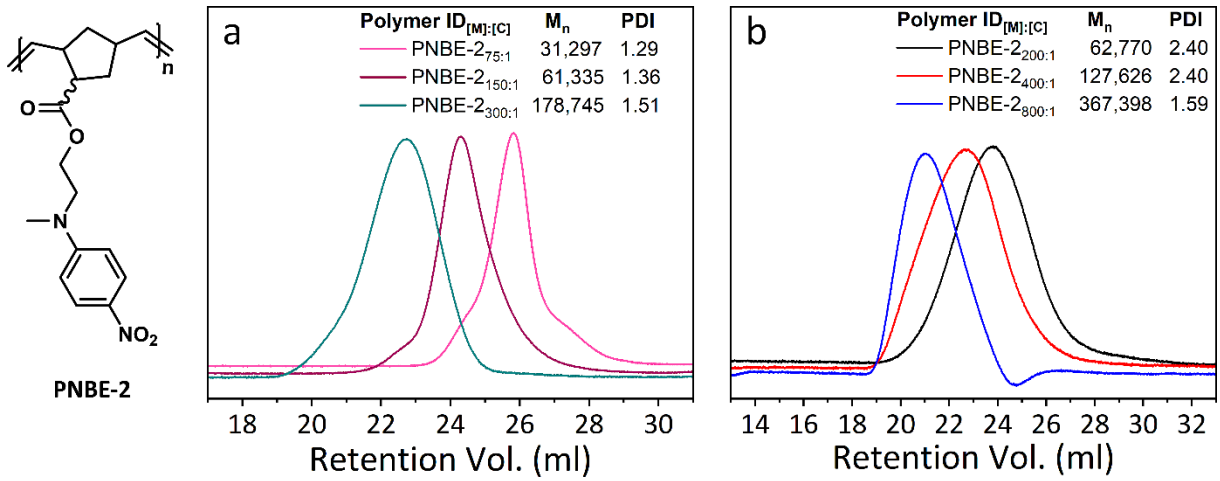

Figure S3.47 GPC elugrams of **PNBE-2** synthesized by (a) Grubb's first- and (b) third generation catalyst; in HFIP + 20 mM sodium trifluoroacetate

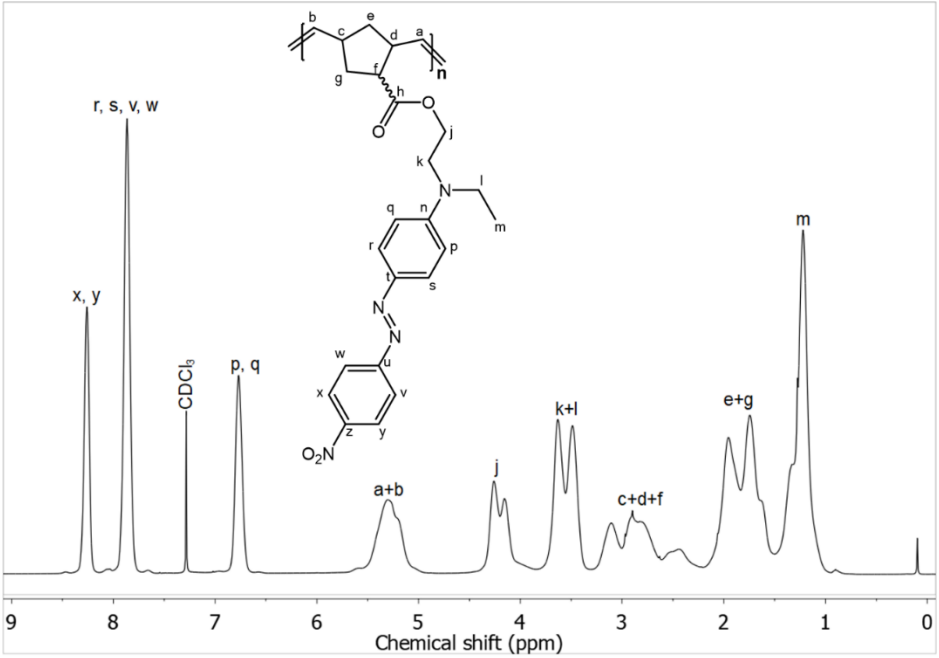

Figure S3.48 ^{1}H NMR spectrum of **PNBE-3**

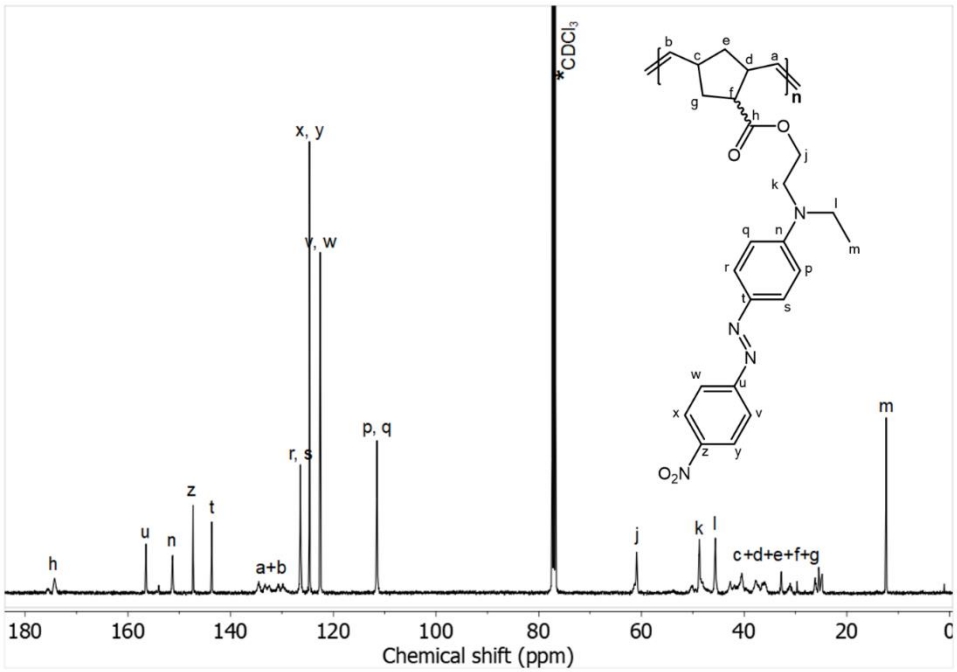

Figure S3.49 ^{13}C NMR spectrum of **PNBE-3**

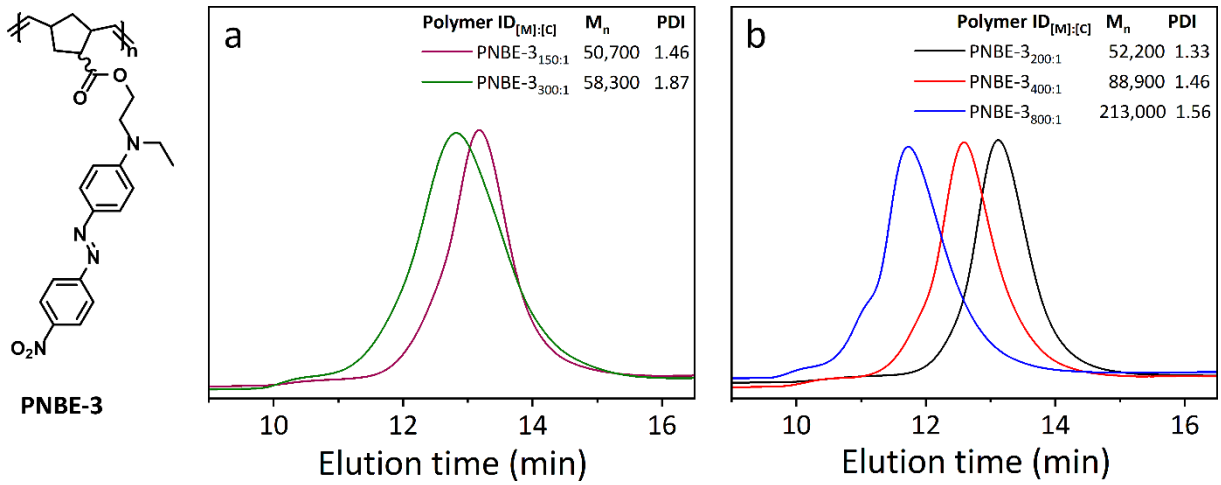

Figure S3.50 GPC elugrams of **PNBE-3** synthesized by (a) Grubb's first- and (b) third generation catalyst; in THF

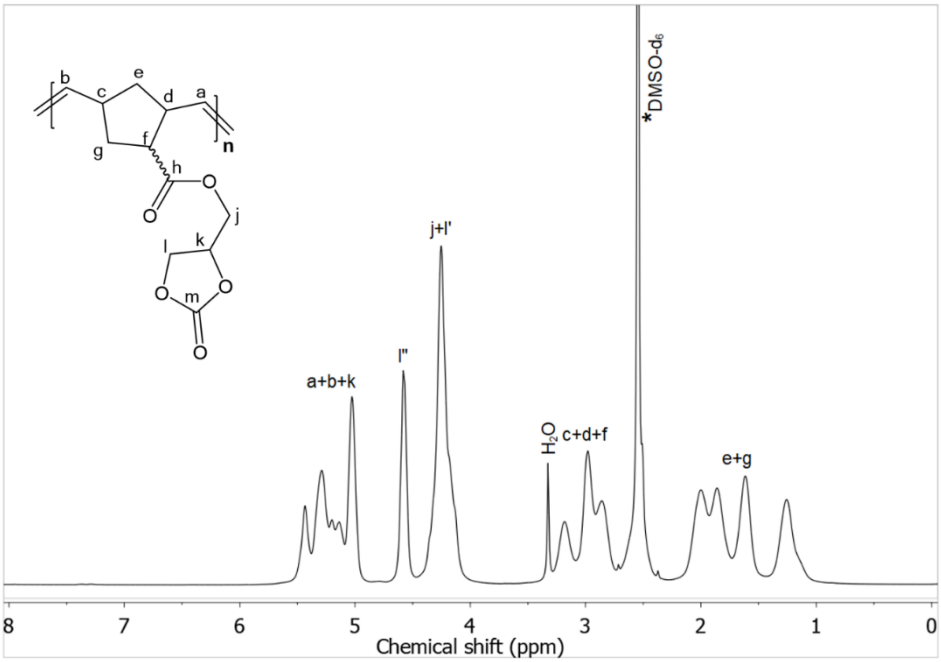

Figure S3.51 ^{1}H NMR spectrum of **PNBE-4**

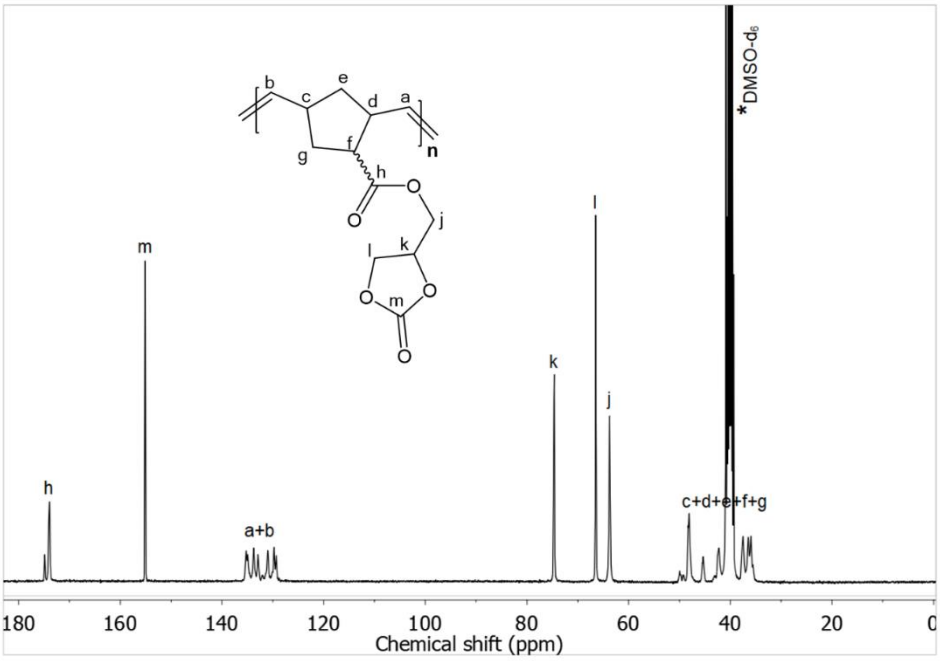

Figure S3.52 ^{13}C NMR spectrum of **PNBE-4**

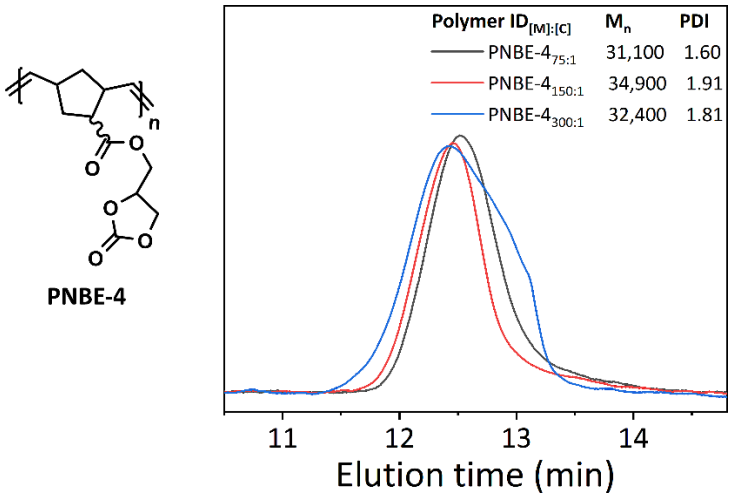

Figure S3.53 GPC elugrams of **PNBE-4** in HFIP

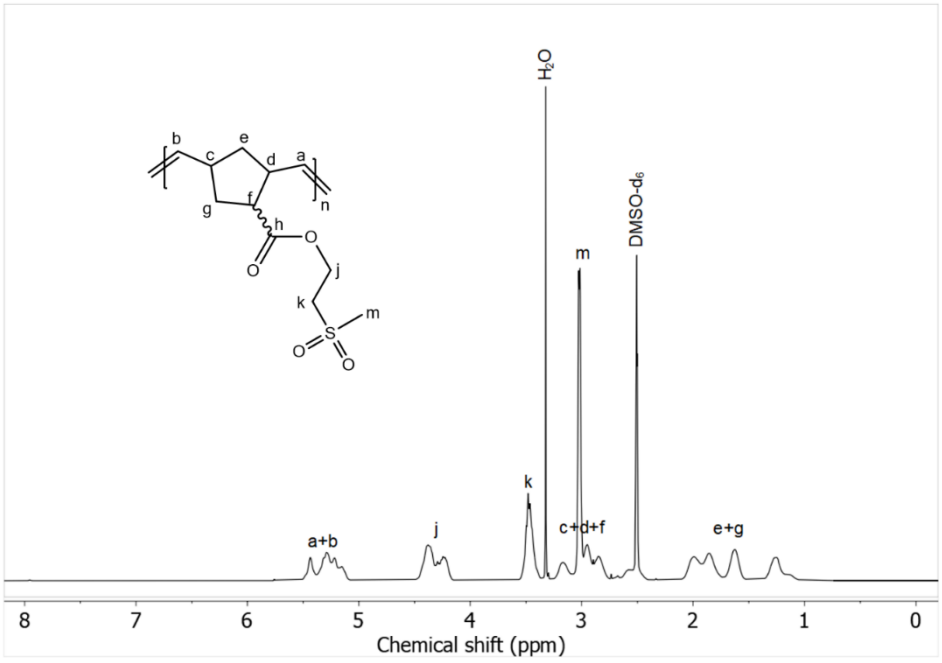

Figure S3.54 ^{1}H NMR spectrum of **PNBE-5**

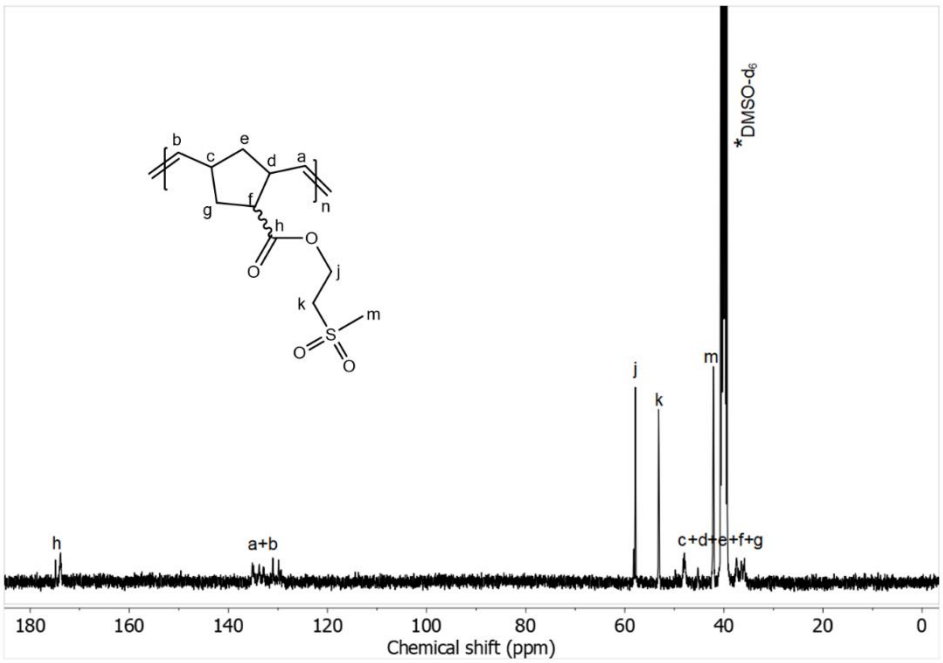

Figure S3.55 ^{13}C NMR spectrum of **PNBE-5**

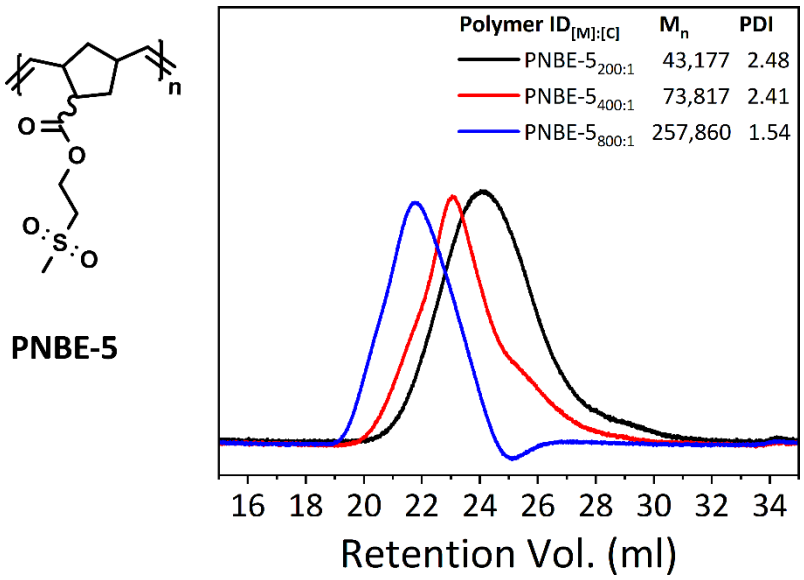

Figure S3.56 GPC elugrams of **PNBE-5** in HFIP + 20 mM sodium trifluoroacetate

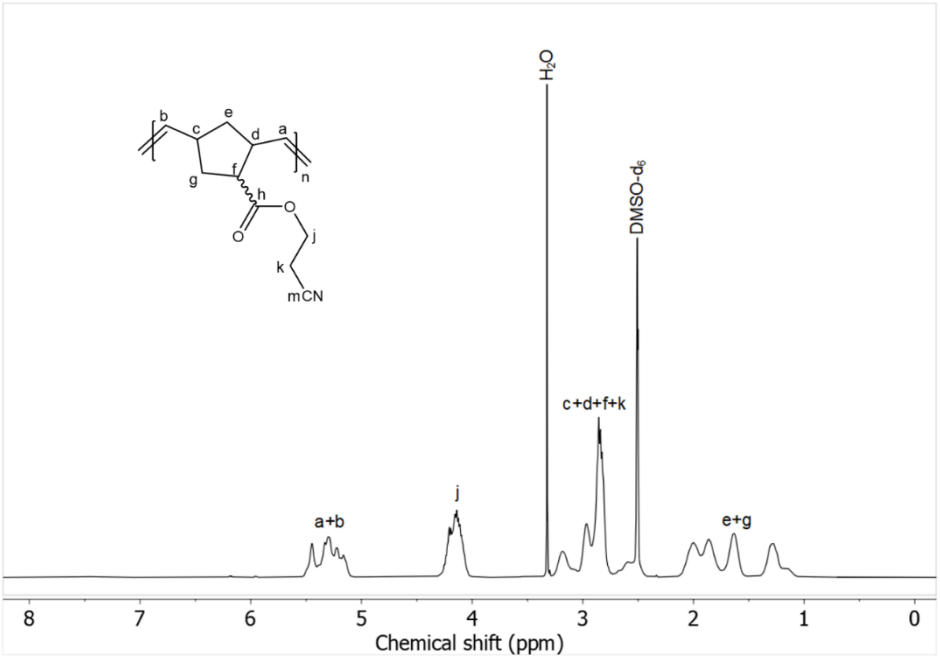

Figure S3.57 ^{1}H NMR spectrum of **PNBE-6**

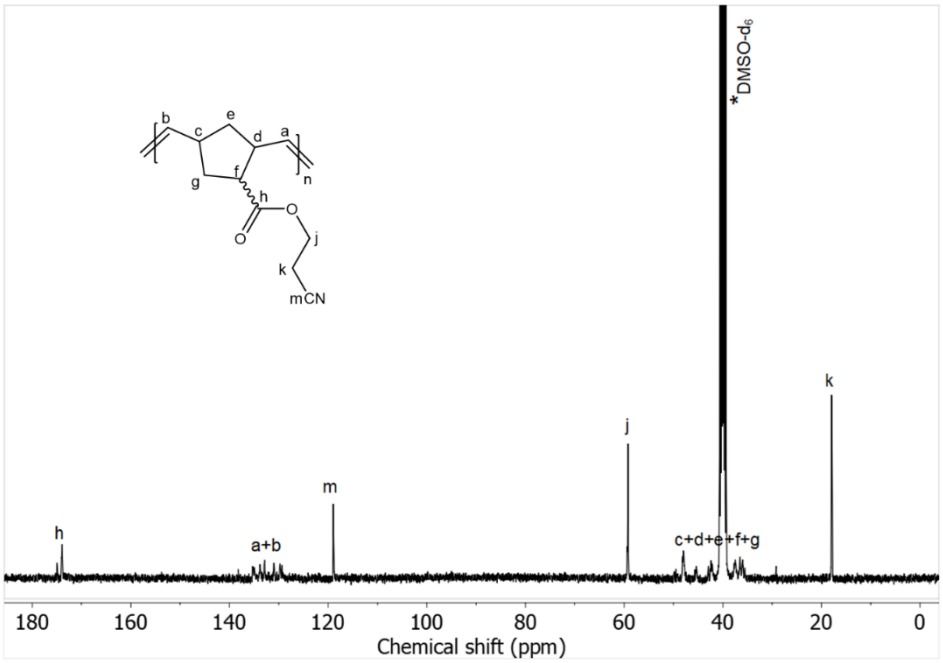

Figure S3.58 ^{13}C NMR spectrum of **PNBE-6**

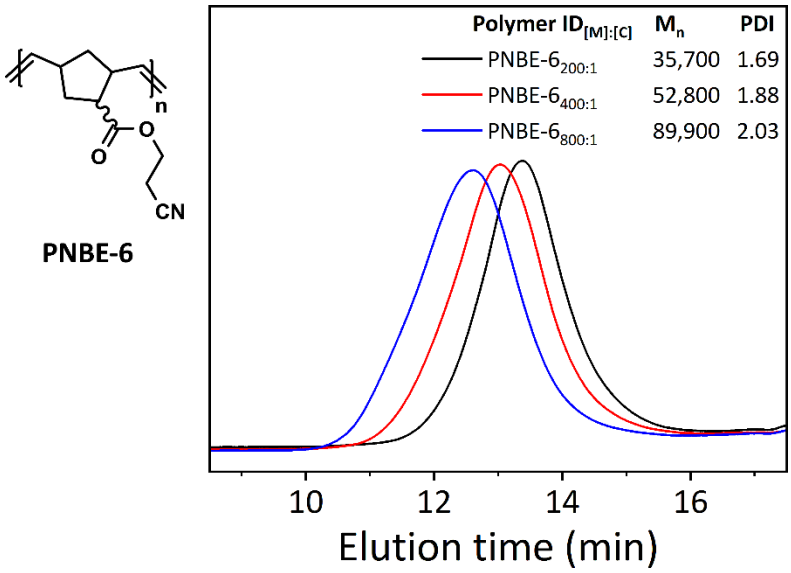

Figure S3.59 GPC elugrams of **PNBE-6** in THF

3.6.7 Thermal behaviour of polymers

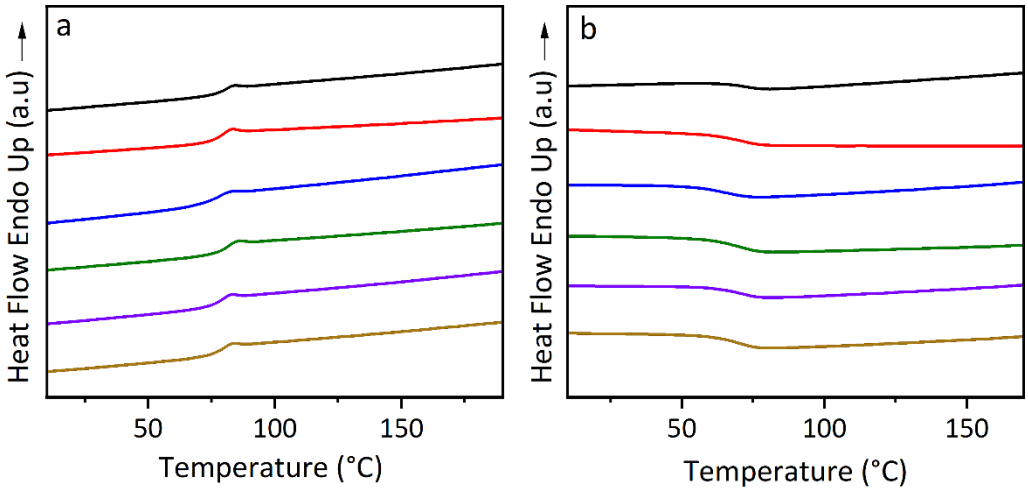

Polymer ID$_{[M]:[C]}$	T_g (°C) 2nd heating cycle [(a)]	1st cooling cycle [(b)]
PNBE-2$_{75:1}$	79	73
PNBE-2$_{150:1}$	78	69
PNBE-2$_{200:1}$	75	64
PNBE-2$_{300:1}$	80	68
PNBE-2$_{400:1}$	77	68
PNBE-2$_{800:1}$	78	70

Figure S3.60 DSC thermograms for **PNBE-2** polymer sets in (a) second heating and (b) first cooling cycle

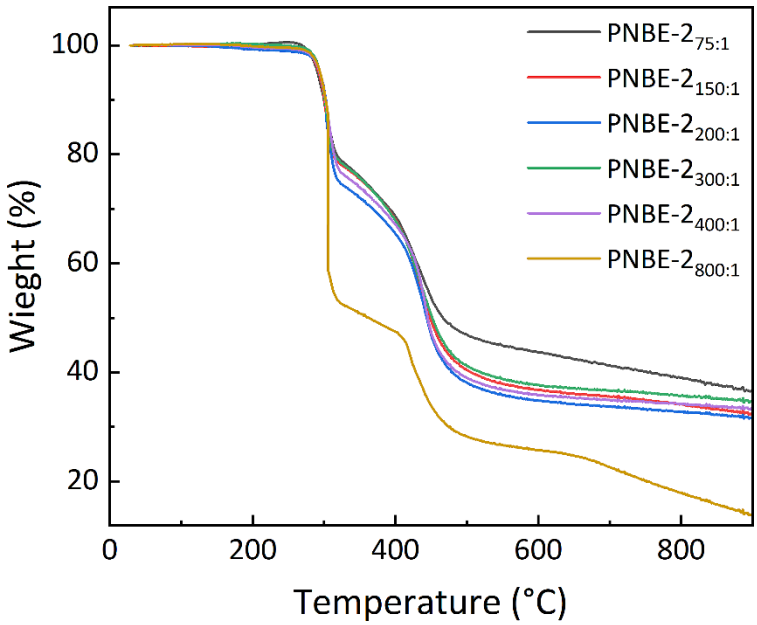

Figure S3.61 TGA curves for **PNBE-2** polymer sets

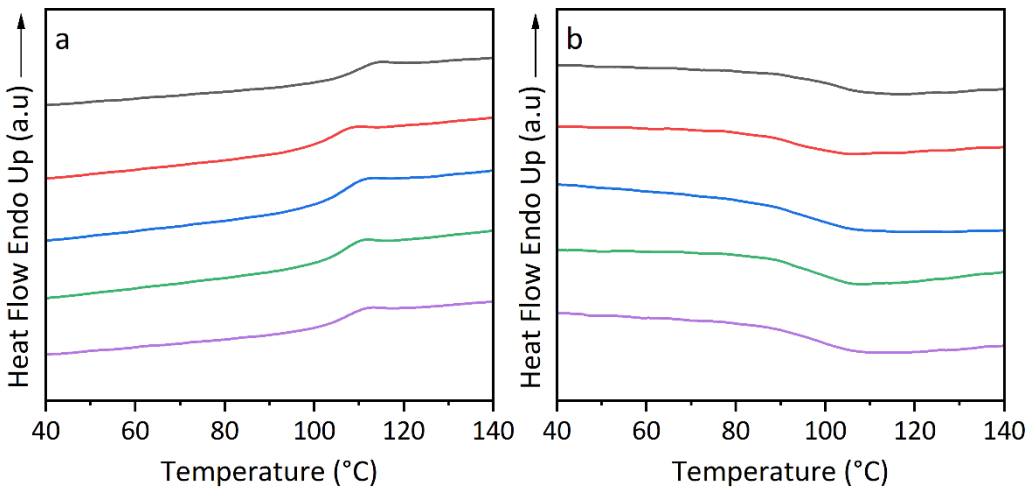

Polymer ID$_{[M]:[C]}$	T_g (°C) 2nd heating cycle [a]	1st cooling cycle [b]
PNBE-3$_{150:1}$	108	99
PNBE-3$_{200:1}$	103	92
PNBE-3$_{300:1}$	106	95
PNBE-3$_{400:1}$	106	96
PNBE-3$_{800:1}$	106	95

Figure S3.62 DSC thermograms for **PNBE-3** polymer sets in (a) second heating and (b) first cooling cycle

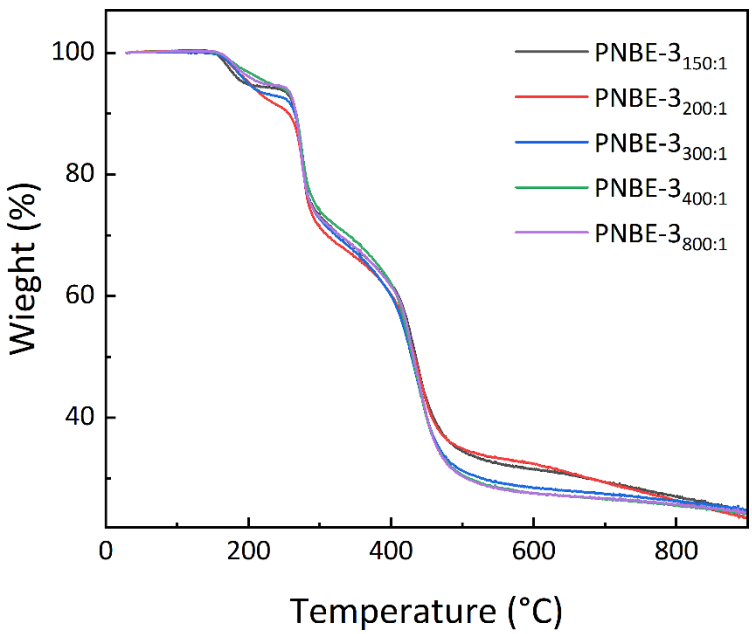

Figure S3.63 TGA curves for **PNBE-3** polymer sets

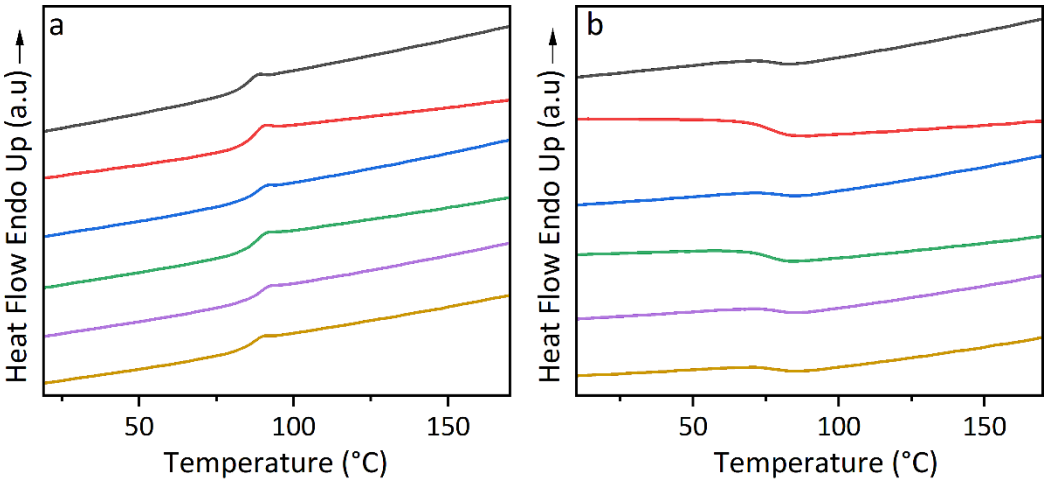

Polymer ID$_{[M]:[C]}$	T_g (°C) 2nd Heating cycle [a]	1st cooling cylce [b]
PNBE-4$_{75:1}$	84	79
PNBE-4$_{150:1}$	86	76
PNBE-4$_{200:1}$	87	80
PNBE-4$_{300:1}$	87	76
PNBE-4$_{400:1}$	88	80
PNBE-4$_{800:1}$	86	80

Figure S3.64 DSC thermograms for **PNBE-4** polymer sets in (a) second heating and (b) first cooling cycle

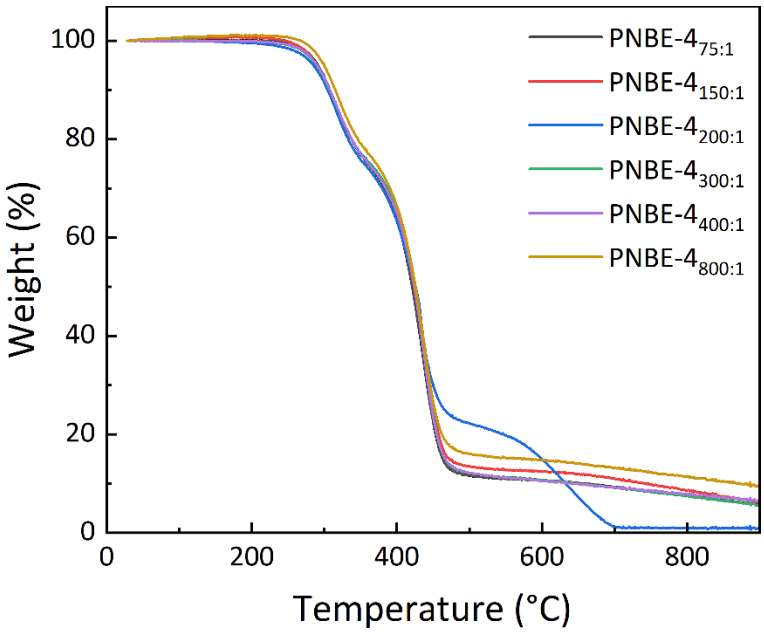

Figure S3.65 TGA curves for **PNBE-2** polymer sets

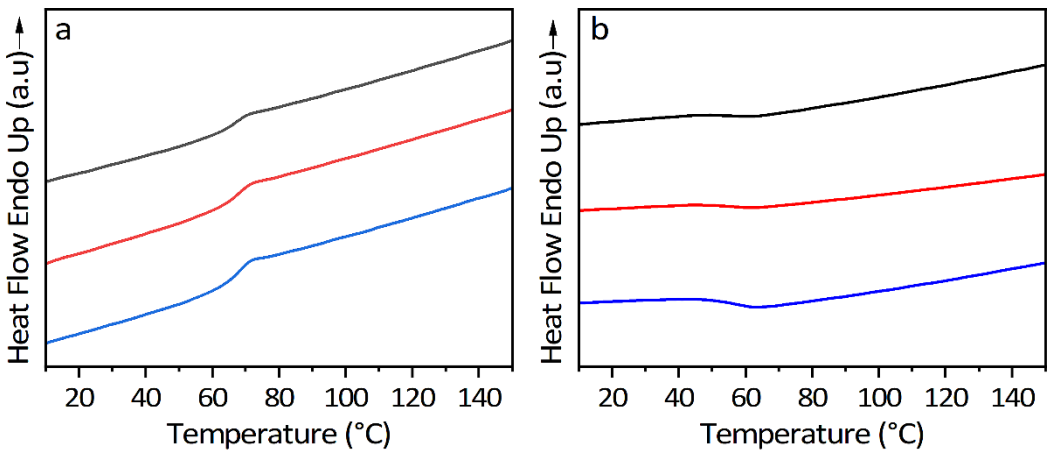

Polymer ID$_{[M]:[C]}$	T_g (°C)	
	2nd heating cycle [(a)]	1st cooling cycle [(b)]
PNBE-5$_{200:1}$	66	56
PNBE-5$_{400:1}$	68	56
PNBE-5$_{800:1}$	67	57

Figure S3.66 DSC thermograms for **PNBE-5** polymer sets in (a) second heating and (b) first cooling cycle

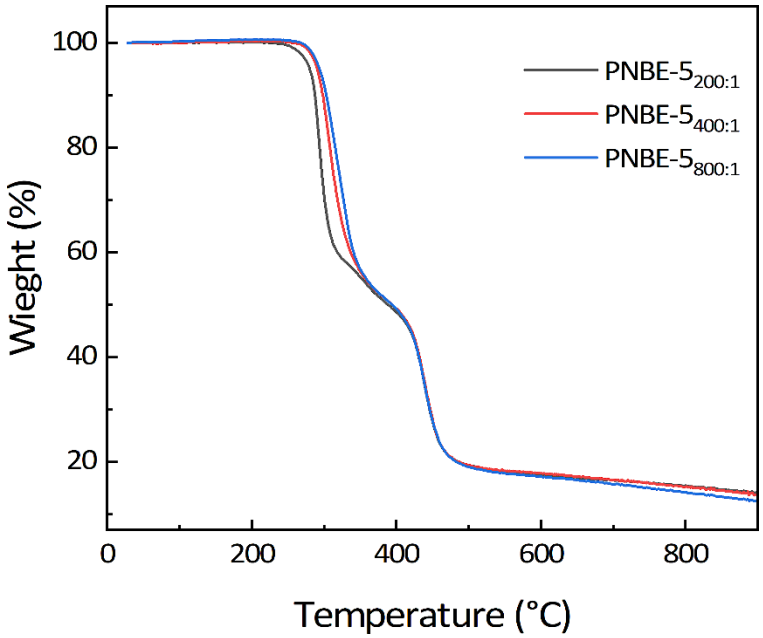

Figure S3.67 TGA curves for **PNBE-5** polymer sets

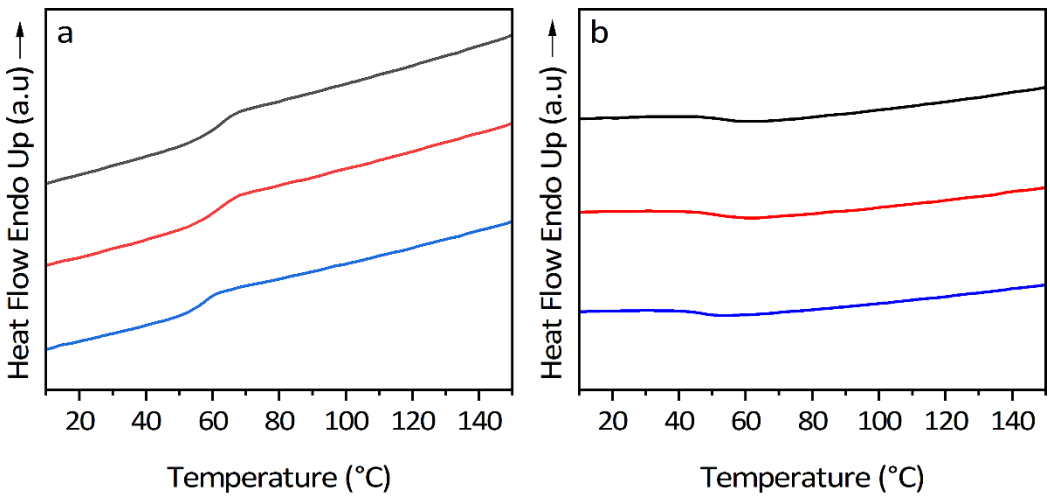

Polymer ID$_{[M]:[C]}$	T_g (°C)	
	2nd heating cycle [(a)]	1st cooling cycle [(b)]
PNBE-6$_{200:1}$	62	55
PNBE-6$_{400:1}$	62	52
PNBE-6$_{800:1}$	58	48

Figure S3.68 DSC thermograms for **PNBE-6** polymer sets in (a) second heating and (b) first cooling cycle

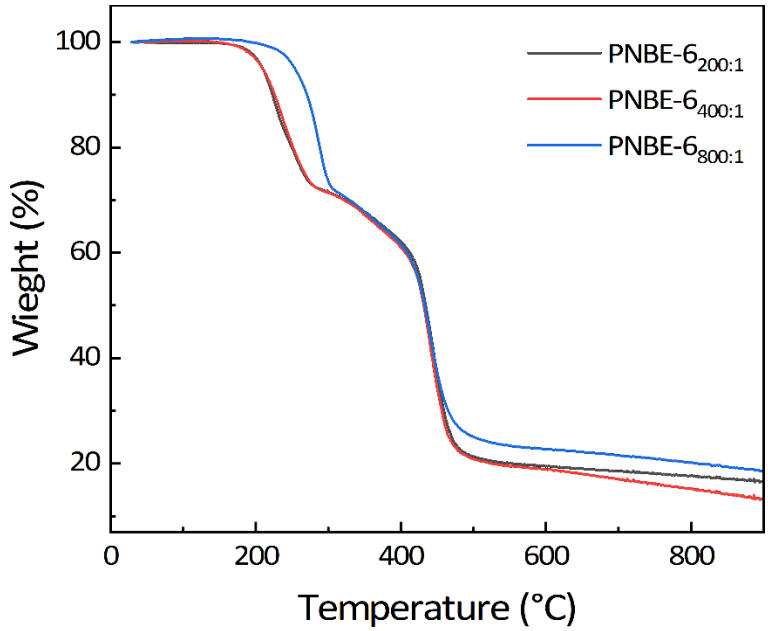

Figure S3.69 TGA curves for **PNBE-6** polymer sets

3.6.8 Dielectric properties of polymers

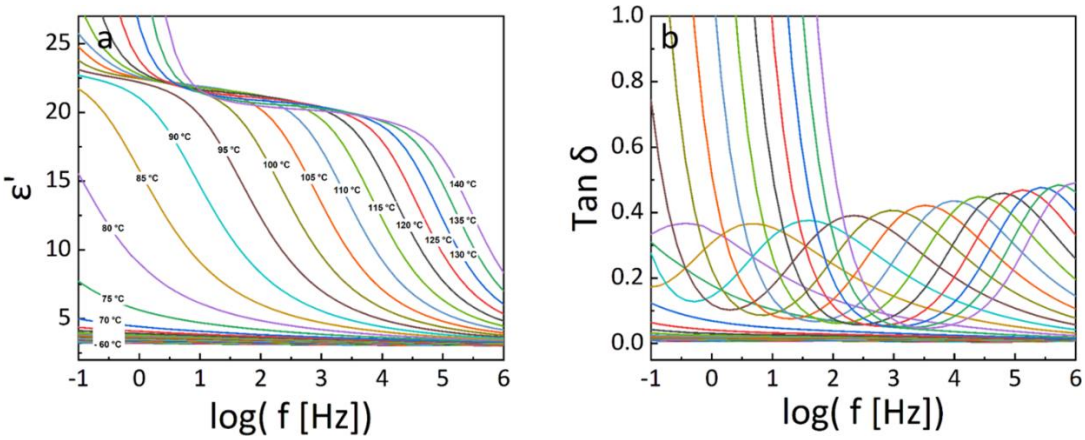

Figure S3.70 Isothermal dielectric response of **PNBE-2**; (a) real permittivity, ε'; (b) tangent loss Tan δ; of the complex dielectric function vs frequency

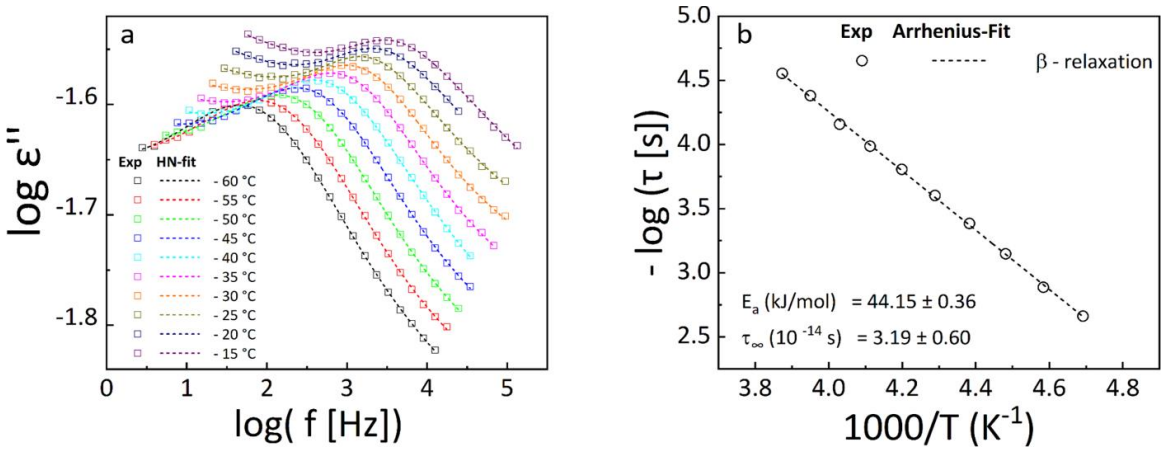

Figure S3.71 β-relaxation processes in **PNBE-2**: (a) isothermal plot of imaginary part ε″ of the complex dielectric permittivity versus frequency (b) Arrhenius plot of corresponding relaxation times obtained from Havriliak-Negami (HN)-fit versus inverse of temperature. The experimental data are represented by scattered dots and the fit functions are represented by short-dashed lines.

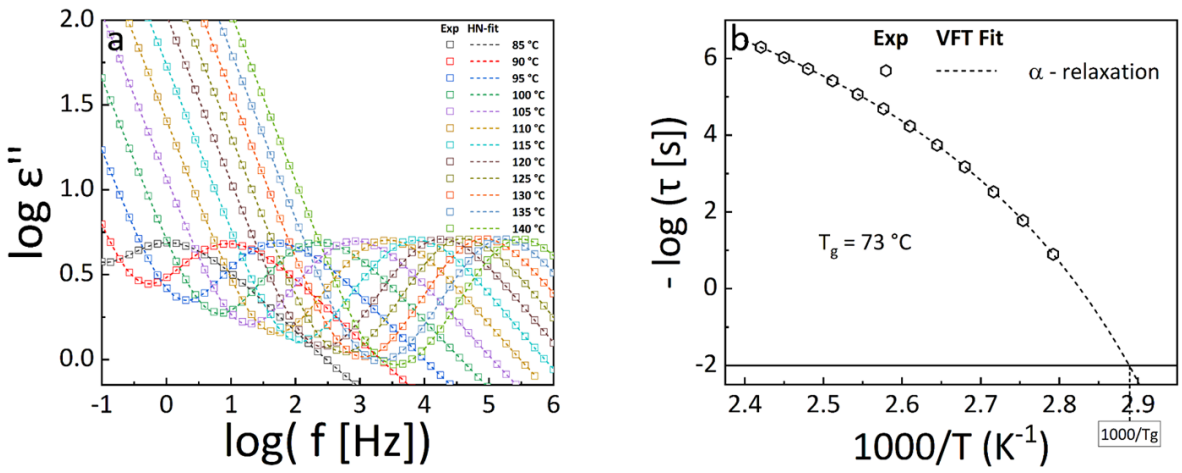

Figure S3.72 α-relaxation processes in **PNBE-2**: (a) isothermal plot of imaginary part ε″ of the complex dielectric permittivity versus frequency (b) Vogel-Fulcher-Tammann (VFT) plot of corresponding relaxation times obtained from Havriliak-Negami (HN)-fit versus inverse of temperature. The experimental data are represented by scattered dots and the fit functions are represented by short-dashed lines.

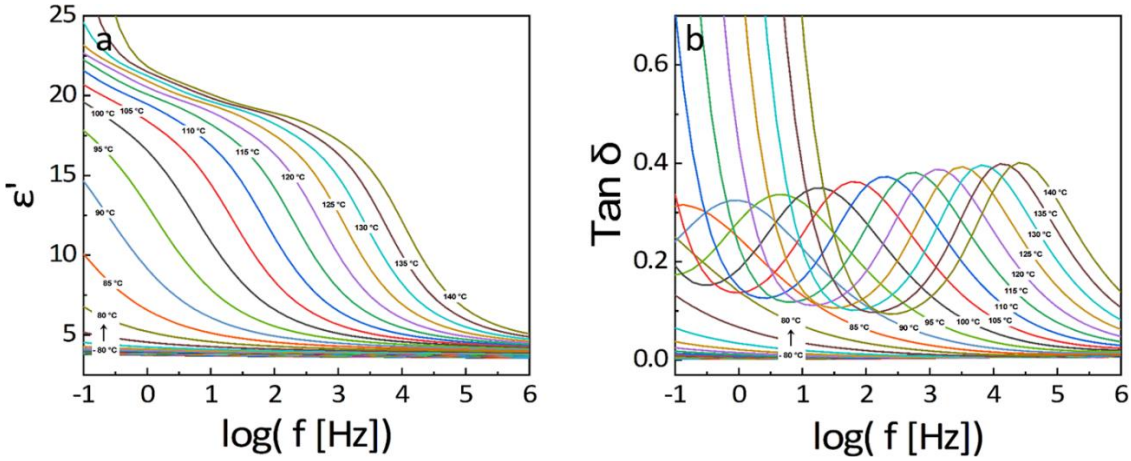

Figure S3.73 Isothermal dielectric response of **PNBE-3**; (a) real permittivity, ε'; (b) tangent loss Tan δ; of the complex dielectric function vs frequency

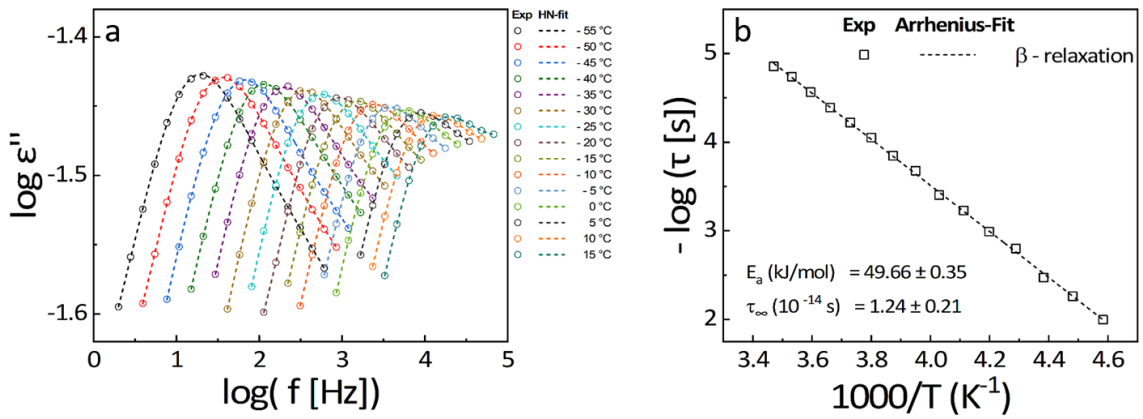

Figure S3.74 β-relaxation processes in **PNBE-3**: (a) isothermal plot of imaginary part ε″ of the complex dielectric permittivity versus frequency (b) Arrhenius plot of corresponding relaxation times obtained from Havriliak-Negami (HN)-fit versus inverse of temperature. The experimental data are represented by scattered dots and the fit functions are represented by short-dashed lines.

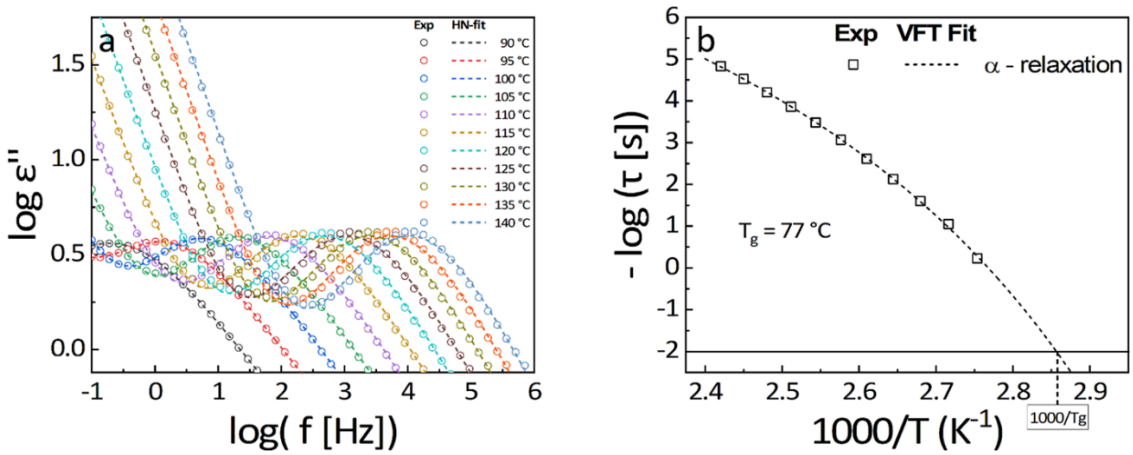

Figure S3.75 α-relaxation processes in **PNBE-3**: (a) isothermal plot of imaginary part ε″ of the complex dielectric permittivity versus frequency (b) Vogel-Fulcher-Tammann (VFT) plot of corresponding relaxation times obtained from Havriliak-Negami (HN)-fit versus inverse of temperature. The experimental data are represented by scattered dots and the fit functions are represented by short-dashed lines.

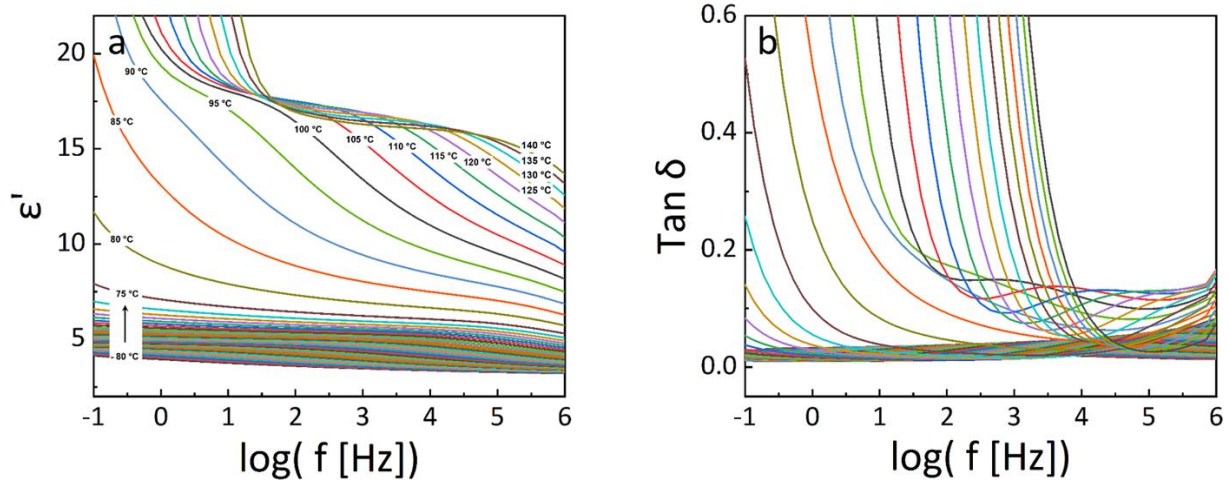

Figure S3.76 Isothermal dielectric response of **PNBE-4**; (a) real permittivity, ε'; (b) tangent loss Tan δ; of the complex dielectric function vs frequency

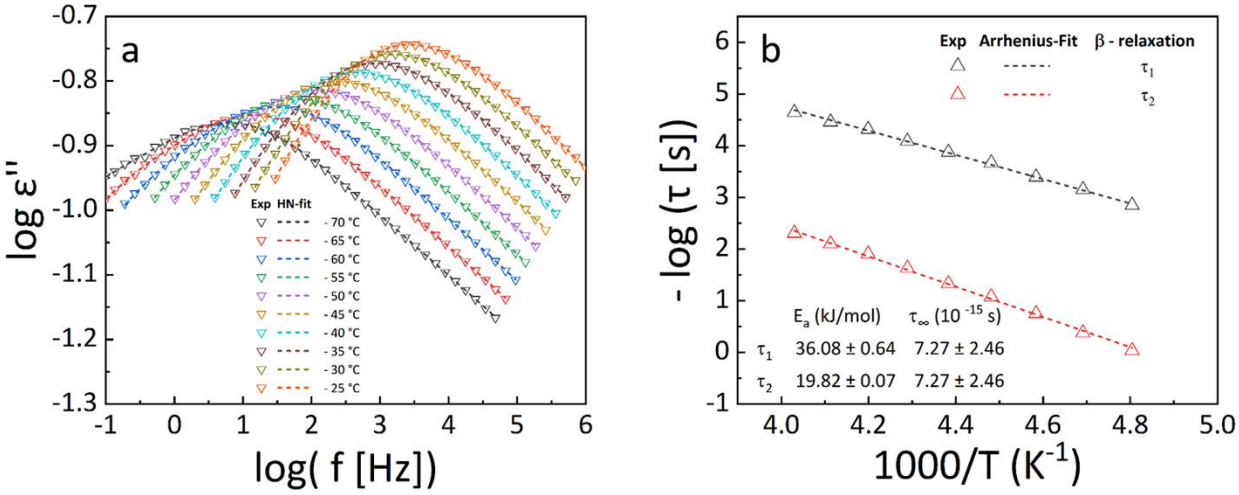

Figure S3.77 β-relaxation processes in **PNBE-4**: (a) isothermal plot of imaginary part ε″ of the complex dielectric permittivity versus frequency (b) Arrhenius plots of corresponding relaxation times obtained from Havriliak-Negami (HN)-fit versus inverse of temperature. The experimental data are represented by scattered dots and the fit functions are represented by short-dashed lines.

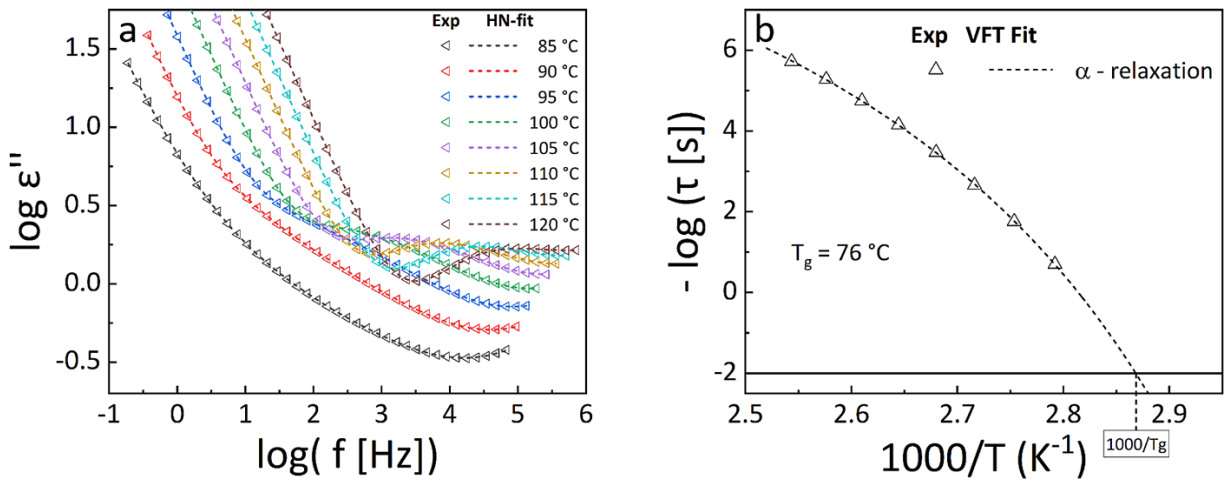

Figure S3.78 α-relaxation processes in **PNBE-4**: (a) isothermal plot of imaginary part ε″ of the complex dielectric permittivity versus frequency (b) Vogel-Fulcher-Tammann (VFT) plot of corresponding relaxation times obtained from Havriliak-Negami (HN)-fit versus the inverse of temperature. The experimental data are represented by scattered dots and the fit functions are represented by short-dashed lines.

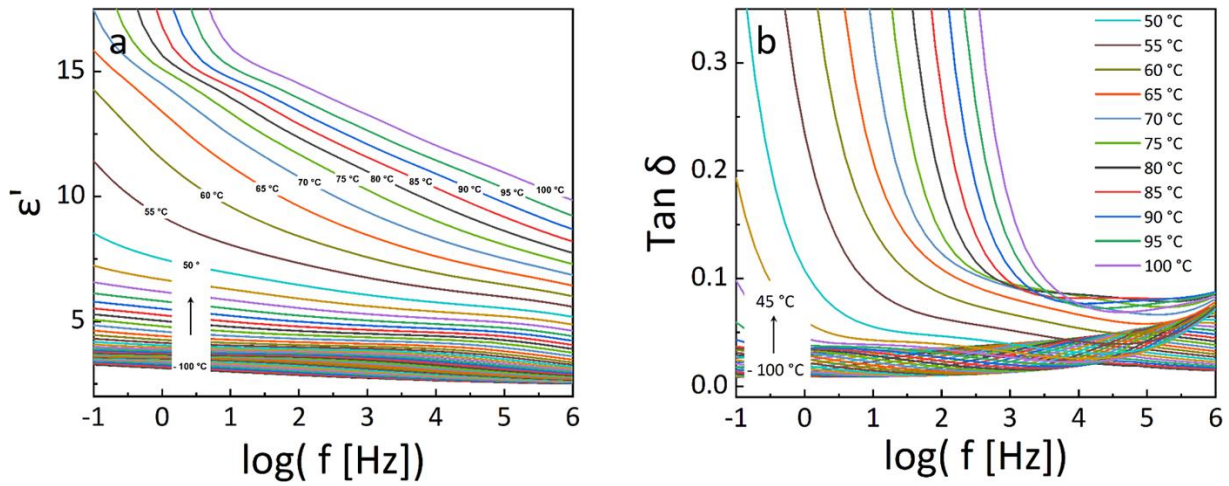

Figure S3.79 Isothermal dielectric response of **PNBE-5**; (a) real permittivity, ε'; (b) tangent loss Tan δ; of the complex dielectric function vs frequency

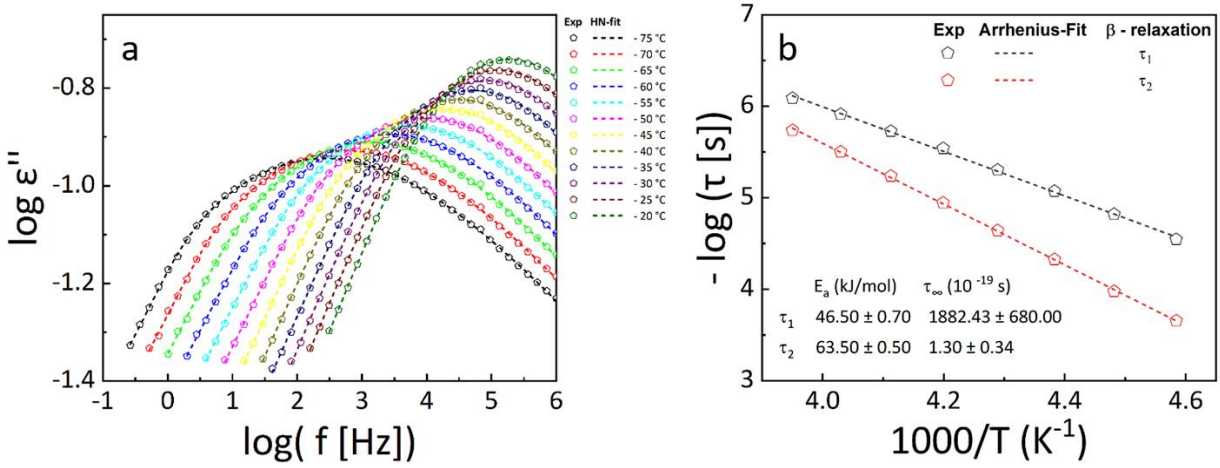

Figure S3.80 β-relaxation processes in **PNBE-5**: (a) isothermal plot of imaginary part ε″ of the complex dielectric permittivity versus frequency (b) Arrhenius plots of corresponding relaxation times obtained from Havriliak-Negami (HN)-fit versus inverse of temperature. The experimental data are represented by scattered dots and the fit functions are represented by short-dashed lines.

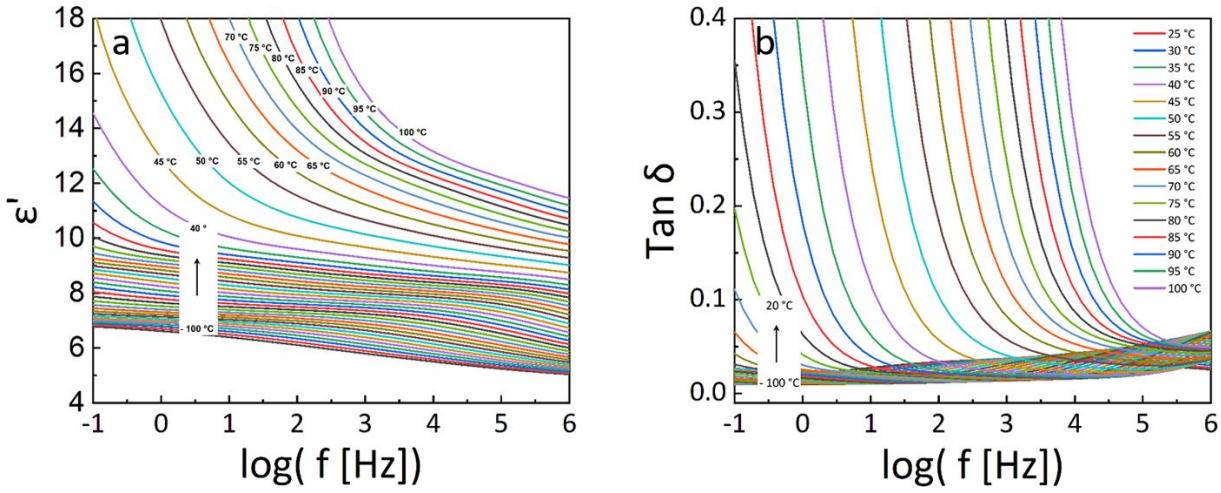

Figure S3.81 Isothermal dielectric response of **PNBE-6**; (a) real permittivity, ε'; (b) tangent loss Tan δ; of the complex dielectric function vs frequency

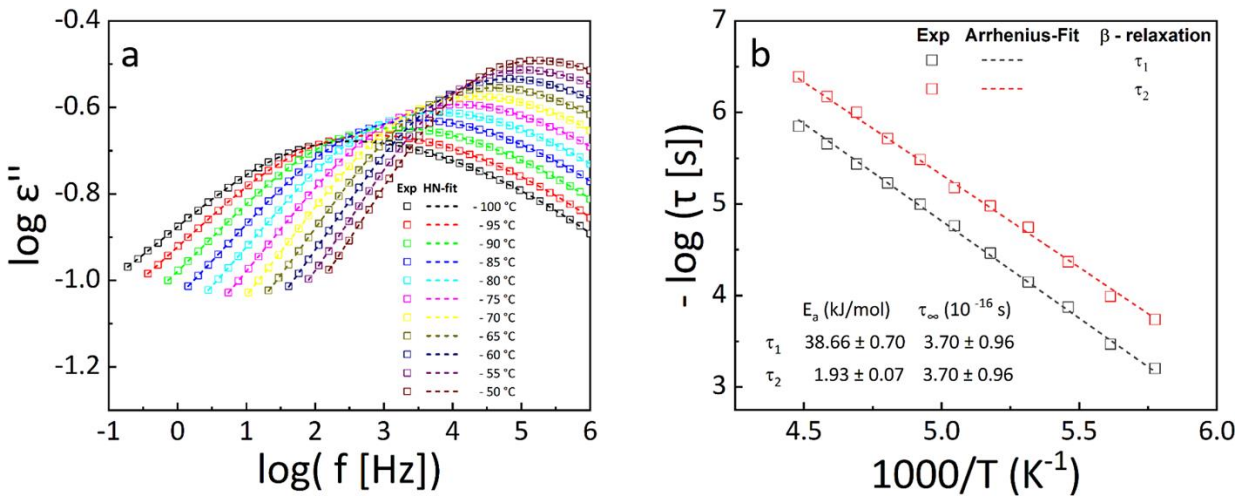

Figure S3.82 β-relaxation processes in **PNBE-6**: (a) isothermal plot of imaginary part ε″ of the complex dielectric permittivity versus frequency (b) Arrhenius plots of corresponding relaxation times obtained from Havriliak-Negami (HN)-fit versus inverse of temperature. The experimental data are represented by scattered dots and the fit functions are represented by short-dashed lines.

3.6.9 Dipole moments of monomers

NBE-X solutions of different concentrations were prepared by dissolving in chloroform. Dilute solutions of **NBE-X** were used to avoid antiparallel orientation of dipoles. Dielectric measurements on the solutions were performed using a high-resolution ALPHA analyzer (Novocontrol, Montabaur, Germany) using a liquid parallel plate sample cell BDS 1308 to avoid errors related to solvent evaporation during measurement. The dielectric permittivity ε' was recorded at a frequency of 10^5 Hz at ambient temperature. The liquid cell BDS 1308 was calibrated using chloroform.

The dipole moments of **NBE-X** were experimentally estimated according to the Hedestrand-Guggenheim – Smith equation (Eq 1) and the modified Onsager equation according to Böttcher (Eq 2):

$$\mu_2^2 = \frac{27 \cdot M_2 \cdot k_B \cdot T}{4\pi \cdot \rho_1 \cdot (\varepsilon_1 + 2)^2 \cdot N_A} \cdot \left(\frac{\partial \varepsilon_{12}}{\partial x_2} - (n_2^2 - n_1^2) \right) \tag{3.3}$$

$$\varepsilon_{12} = 1 + \frac{4\pi}{3}\frac{\varepsilon_{12}(2\varepsilon_{12}+1)(n_1^2+2)^2}{3(2\varepsilon_{12}+n_1^2)^2}\frac{\mu_1^2}{k_B T}N_1 + \frac{4\pi}{3}\frac{\varepsilon_{12}(2\varepsilon_{12}+1)(n_2^2+2)^2}{3(2\varepsilon_{12}+n_2^2)^2}\frac{\mu_2^2}{k_B T}N_2 + 3\frac{N_1}{N_A}R_1\frac{\varepsilon_{12}(n_1^2+2)}{2\varepsilon_{12}+n_1^2} + 3\frac{N_2}{N_A}R_2\frac{\varepsilon_{12}(n_2^2+2)}{2\varepsilon_{12}+n_2^2} \tag{3.4}$$

In the above equations,

μ_1	dipole moment of the solvent
μ_2	dipole moment of NBE-X monomer
M_2	molar mass of NBE-X monomer
N_A	Avogadro's constant
k_B	Boltzmann's constant
T	Temperature
ρ_1	density of the solvent
ε_1	dielectric permittivity of the solvent
ε_{12}	dielectric permittivity of the solution
x_2	molar fraction of NBE-X monomer
n_1	refractive index of the solvent
n_2	refractive index of NBE-X monomer
N_i	number density of dipoles expressed as $N_i = \frac{\rho_i}{M_i}N_A$
R_i	molecular refraction in the limit of infinite wavelength expressed as $R_i = \frac{M_i}{\rho_i}\frac{(n_i^2-1)}{(n_i^2+2)}$

3.7 References

[1] Q. M. Zhang, M. J. Serpe, *ChemPhysChem* **2017**, 18, 1451.

[2] A. S. Abd-El-Aziz, M. Antonietti, C. Barner-Kowollik, W. H. Binder, A. Böker, C. Boyer, M. R. Buchmeiser, S. Z. D. Cheng, F. D'Agosto, G. Floudas, H. Frey, G. Galli, J. Genzer, L. Hartmann, R. Hoogenboom, T. Ishizone, D. L. Kaplan, M. Leclerc, A. Lendlein, B. Liu, T. E. Long, S. Ludwigs, J.-F. Lutz, K. Matyjaszewski, M. A. R. Meier, K. Müllen, M. Müllner, B. Rieger, T. P. Russell, D. A. Savin, A. D. Schlüter, U. S. Schubert, S. Seiffert, K. Severing, J. B. P. Soares, M. Staffilani, B. S. Sumerlin, Y. Sun, B. Z. Tang, C. Tang, P. Théato, N. Tirelli, O. K. C. Tsui, M. M. Unterlass, P. Vana, B. Voit, S. Vyazovkin, C. Weder, U. Wiesner, W.-Y. Wong, C. Wu, Y. Yagci, J. Yuan, G. Zhang, *Macromolecular Chemistry and Physics* **2020**, 221, 2000216.

[3] S. Bauer, *IEEE Transactions on Dielectrics and Electrical Insulation* **2006**, 13, 953.

[4] H. Kawai, *Japanese Journal of Applied Physics* **1969**, 8, 975.

[5] Q. Li, Q. Wang, *Macromolecular Chemistry and Physics* **2016**, 217, 1228.

[6] X. Chen, X. Han, Q.-D. Shen, *Advanced Electronic Materials* **2017**, 3, 1600460.

[7] R. Gerhard, *From electrode charges on dielectric elastomers to trapped charges and electric dipoles in electrets and ferroelectrets: fundamental and applications-relevant aspects of diversity in electroactive polymers*, SPIE, **2016**.

[8] X. Qiu, W. Wirges, R. Gerhard, *Journal of Applied Physics* **2011**, 110, 024108.

[9] Y. S. Ko, F. A. Nüesch, D. Damjanovic, D. M. Opris, *Advanced Materials* **2017**, 29, 1603813.

[10] H. K. Hall Jr., A. B. Padias, G. Chu, H.-Y. Lee, I. Kalnin, M. Sansone, G. Breckenridge, *Journal of Polymer Science Part A: Polymer Chemistry* **1992**, 30, 2341.

[11] G. R. Davies, H. V. S. A. Hubbard, I. M. Ward, W. J. Feast, V. C. Gibson, E. Khosravi, E. L. Marshall, *Polymer* **1995**, 36, 235.

[12] F. Kremer, L. Dominguez, W. H. Meyer, G. Wegner, *Polymer* **1989**, 30, 2023.

[13] S. Bauer, S. B. Lang, *IEEE Transactions on Dielectrics and Electrical Insulation* **1996**, 3, 647.

[14] T. L. Choi, R. H. Grubbs, *Angew. Chem.-Int. Edit.* **2003**, 42, 1743.

[15] K.-T. Bang, T.-L. Choi, *Journal of Polymer Science* **2020**, 58, 48.

[16] S. Hilf, A. F. M. Kilbinger, *Nature Chemistry* **2009**, 1, 537.

[17] A. Leitgeb, J. Wappel, C. Slugovc, *Polymer* **2010**, 51, 2927.

[18] D. Ndaya, R. Bosire, R. M. Kasi, *Polymer Chemistry* **2019**, DOI: 10.1039/C9PY00536F.

[19] N. R. Grove, P. A. Kohl, S. A. Bidstrup Allen, S. Jayaraman, R. Shick, *Journal of Polymer Science Part B: Polymer Physics* **1999**, 37, 3003.

[20] M. A. Rahman, H. N. Lokupitiya, M. S. Ganewatta, L. Yuan, M. Stefik, C. Tang, *Macromolecules* **2017**, 50, 2069.

[21] M. S. Ganewatta, W. Ding, M. A. Rahman, L. Yuan, Z. Wang, N. Hamidi, M. L. Robertson, C. Tang, *Macromolecules* **2016**, 49, 7155.

[22] Y. Shao, C. Lavigueur, X. X. Zhu, *Macromolecules* **2012**, 45, 1924.

[23] Y. Zhu, C. Ma, H. Han, R. Sun, X. Liao, M. Xie, *Polymer Chemistry* **2019**, 10, 2447.

[24] Z. You, D. Gao, O. Jin, X. He, M. Xie, *Journal of Polymer Science Part A: Polymer Chemistry* **2013**, 51, 1292.

[25] G. O. Karpov, D. A. Alentiev, A. I. Wozniak, E. V. Bermesheva, I. V. Lounev, Y. A. Gusev, V. P. Shantarovich, M. V. Bermeshev, *Polymer* **2020**, 203, 122759.

[26] L. Fang, J. Zhou, Y. Tao, Y. Wang, X. Chen, X. Chen, J. Hou, J. Sun, Q. Fang, *ACS Sustainable Chemistry & Engineering* **2019**, 7, 4078.

[27] J. Wang, J. Zhou, L. Fang, J. Sun, Q. Fang, *Materials Chemistry Frontiers* **2018**, 2, 1467.

[28] H. Yin, P. Chapala, M. Bermeshev, A. Schönhals, M. Böhning, *ACS Macro Letters* **2017**, 6, 813.

[29] H. Han, D. Zhou, Q. Ren, F. Ma, C. Ma, M. Xie, *European Polymer Journal* **2020**, 122, 109376.

[30] S. Bonardd, A. Alegria, C. Saldias, A. Leiva, G. Kortaberria, *ACS Applied Materials & Interfaces* **2018**, 10, 38476.

[31] S. Bonardd, Á. Alegria, O. Ramirez, C. Saldías, Á. Leiva, G. Kortaberria, *Reactive and Functional Polymers* **2019**, 140, 1.

[32] Y. S. Ko, F. A. Nüesch, D. M. Opris, *Journal of Materials Chemistry C* **2017**, 5, 1826.

[33] R. H. Boyd, G. D. Smith, DOI: 10.1017/cbo9780511600319, Cambridge University Press, Cambridge 2007, Online.

[34] F. Kremer, *Broadband dielectric spectroscopy*, Springer, Berlin **2003**.

[35] C. J. F. Böttcher, *Recueil des Travaux Chimiques des Pays-Bas* **1943**, 62, 119.

[36] J. Wudarczyk, G. Papamokos, T. Marszalek, T. Nevolianis, D. Schollmeyer, W. Pisula, G. Floudas, M. Baumgarten, K. Müllen, *ACS Applied Materials & Interfaces* **2017**, 9, 20527.

[37] J. Knelles, C. Wanner, F. Schulz, M. Freund, M. A. Kolmangadi, A. Baro, P. Huber, A. Schönhals, S. Laschat, *Liquid Crystals* **2021**, DOI: 10.1080/02678292.2021.18734381.

[38] E. A. Guggenheim, *Transactions of the Faraday Society* **1951**, 47, 573.

CHAPTER 4

Stretchable High Response Piezoelectric Elastomers Based on Polable Polynorbornene Fillers in a Polydimethylsiloxane Matrix

This chapter is based on the publication

Stretchable High Response Piezoelectric Elastomers Based on Polable Polynorbornene Fillers in a Polydimethylsiloxane Matrix

by

*Francis Owusu,[a,b] Frank A. Nüesch,[a,b,c] and Dorina M. Opris [a]**

[a] *Swiss Federal Laboratories for Materials Science and Technology Empa, Laboratory for Functional Polymers, Überlandstr. 129, CH-8600, Dübendorf, Switzerland.*

[b] *Institute of Chemical Sciences and Engineering, Ecole Polytechnique Federale de Lausanne, EPFL, Station 6, CH-1015 Lausanne, Switzerland.*

[c] *Institute of Materials Science and Engineering Ecole Polytechnique Federale de Lausanne (EPFL) Station 6, Lausanne CH-1015, Switzerland.*

Reprinted with permission from

Advanced Functional Materials, 2022, 32, 2207083
DOI:10.1002/adfm.202207083
https://doi.org/10.1002/adfm.202207083

Author Contributions:

F. Owusu performed the preparation of compounds and devices as well as their characterization and contributed to the manuscript

4.1 Abstract

To advance the field of piezoelectrics it is desirable to find materials that combine high piezoelectricity with high elasticity. Applications such as self-sensors, stretchable electronics, soft robots, and energy harvesting would benefit tremendously. However, this is not an easy task neither for materials based on ceramics nor for those based on polymers. While ceramics can show strong piezoelectric effects, their mechanical response tends to be weak. Polymers instead are elastic but only few have sizeable piezoelectric effects. Additionally, they cannot keep the polarization permanently as needed for piezoelectrics. Here we synthesize an all-organic piezoelectric elastomer by blending high glass transition temperature (T_g = 104 °C) polar polynorbornene nanoparticles (NPs) with a high relaxation strength ($\Delta\varepsilon'$ = 22.4) into chemically cross-linked polydimethylsiloxane matrix. After processing the blends into thin films by doctor blading, they are poled by corona discharge at elevated temperatures. Fifteen days after poling, the materials show a stable and reversible piezoelectric response d_{31} = 37 pC/N. This, to the best of our knowledge, not only is the highest d_{31} value reported, but the response is three times that of the well-known polyvinylidene difluoride.

4.2 Introduction

Piezoelectric materials couple mechanical and electrical energy. Because of their excellent potential to generate electric charges in response to mechanical deformations, these smart materials have been widely investigated for self-powered sensors, actuators, and energy-harvesting applications.[1,2] Ceramics materials such as the famous lead zirconate titanate (PZT) family dominate commercial applications due to their outstanding piezoelectric properties. However, they exhibit drawbacks such as rigidity, brittleness, toxicity, high density, low breakdown field strength, and lack of design flexibility, limiting their extensive application in flexible and stretchable devices.[3-7] Although reported to show low piezoelectric properties compared to their ceramic counterparts, piezoelectric polymers are mechanically flexible, easier to process into complex designs, lightweight, cost-efficient, biocompatible, and possess large quasi-piezoelectric sensitivity.[8-10] There are numerous polymers reported to exhibit piezoelectric effects.[11-13] Among these, the well-investigated polyvinylidene fluoride (PVDF) and its copolymers with trifluoroethylene and tetrafluoroethylene represent the state-of-the-art in piezoelectric polymers. Besides, other polymers such as polyureas, polyamides, polyimides, polyesters, and polypeptides, to mention a few, have likewise been investigated for their piezoelectric response.[11] For instance, Takase et al. investigated the piezoelectric properties of nylon 7 and nylon 11. The recorded piezoelectric response, as a function of temperature, revealed maximal values of d_{31} = 17 pC/N for Nylon 7 and d_{31} = 14 pC/N for Nylon 11. However, moisture

uptake issues impose limitations on their application in commercial devices.[14] Vinylidene cyanide and vinyl acetate copolymers have also been reported to give a piezoelectric response comparable to PVDF.[15] However, the synthesis of these copolymers is difficult and has hindered their development. Furthermore, an amorphous polyimide made of 2,6-bis(3-aminophenoxy)benzonitrile/ 4,4′oxydiphthalic anhydride ((β-CN)APB/ODPA), containing polar functional groups has demonstrated an impressive piezoelectric response for potential application at temperatures up to 150 °C.[13] However, most bulk piezoelectric polymers have a low mechanical strain at break and are not elastic, which hamper application in areas where large deformations are required.

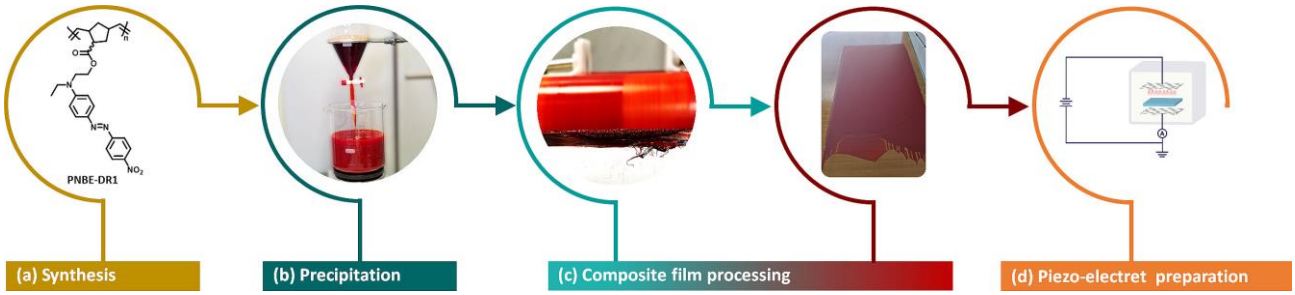

Figure 4.1 Process flow diagram showing techniques for preparing piezo-electret elastomer: a) synthesis of polar polymer; b) precipitation of polar polymer into a non-solvent; c) formation of homogenous composites using a three-roll-mill and processing it into thin films by Doctor Blading; and d) corona poling the films in a strong electric field at elevated temperatures.

Extensive research has shown that piezoelectric flexible materials can be achieved by design.[16-21] Ferroelectrets with a remarkable piezoelectric response have been reported using electrically polarized air-filled internal pores.[22-27] Their response was explained by R. Gerhard using a charge-spring model, which connects the piezoelectric coefficient with the elastic moduli of dipoles and matrix.[28] Matrices used include polyolefins,[29,30] fluoropolymers[31,32] cyclo-olefin polymers,[33] polycarbonates,[34] polyesters.[35] The most extensively studied ferroelectret, cellular polypropylene (PP), has been used in flexible devices, including actuators, sensors, and generators.[36-38] While they exhibit excellent flexibility and large d_{33} piezoelectric response, these cellular materials' response strongly depends on their thermal processing and thermal history and they lack elasticity.[17,39] Block copolymers with soft and hard blocks have also been explored, whereby the hard block served for charge trapping, and the soft block enabled elasticity.[40] Immobilizing polarized nanoparticles in a matrix of a dielectric elastomer enables the formation of stable stretchable electrets.[18,41,42] Piezoelectricity in such materials is introduced by poling in a strong electric field either by contact or corona poling.

In this work, we have prepared piezo-electret elastic materials with controlled structural and physicochemical properties using a composite approach in which a polydimethylsiloxane matrix is filled with polar high glass transition temperature (T_g) polymer nanoparticles (Figure 4.1). Processing strategies have been adopted to make these materials into stretchable films with different morphologies to meet specific requirements for advanced technological applications. A permanent polarization, responsible for the piezoelectric effect, was introduced in the films by poling them in a strong electric field at temperatures above the T_g of the filler. Corona poling was used to minimize localized arcing during poling and to enable high poling fields without dielectric breakdown. The mechanical properties, dielectric behavior, remanent polarization, and piezoelectric responses were assessed as a function of time, frequency, and strain.

4.3 Results and Discussion

Two different stereoisomeric monomers of 5-norbornene-2-carboxylic acid (mixture of *endo* and *exo* with predominantly *endo* and pure *exo*) were successfully functionalized with *N*-ethyl-*N*-(2-hydroxyethyl)-4-(4-nitrophenylazo) aniline *via* Steglich esterification (Figure 4.1(a) and Scheme S4.1) to give *endo/exo* mixture (M-A_1) and purely *exo* - (M-A_2) monomers. The synthesized polar monomers, known to exhibit a large dipole moment μ of 10-12 Debye,[43] were successfully polymerized by ring-opening metathesis polymerization (ROMP) under different conditions and using the same monomer-to-catalyst feed ratio. The two bulk polymers with regio-irregular structures were abbreviated as P-A_1 (*endo/exo* mixture) and P-A_2 (*exo*) for simplicity and clarity. The conversion rate for each polymerization was monitored over time by ^{1}H NMR spectroscopy. Comparing the semi-logarithmic plot of $[M_t]/[M_0]$ (where $[M_0]$ represents the initial monomer concentration and $[M_t]$ the concentration of monomer at a specific time) and the percentage conversion plot versus time for both monomers revealed different reaction rates for the respective polymers, P-A_1 and P-A_2. Detailed kinetic data for the polymerization can be found in supporting information (Figures S4.1-S4.4). The final polymers were isolated in a yield of over 85% and thoroughly characterized (Figures S5-S9). ^{1}H and ^{13}C NMR spectroscopy provided structural evidence of successful reaction and purification (Figures S4.5 and S4.6). Gel permeation chromatography (GPC) elugrams in THF using polystyrene standard revealed monomodal molecular weight distribution for both polymers with number average molecular weights (M_n) and polydispersity indices (PDI) as recorded in Table 4.1 (Figure S4.7). Thermogravimetric analysis (TGA) was conducted to test the thermal stability and decomposition behavior (Figure S4.8). Both polymers showed stability up to 168 °C before yielding to thermal decomposition. Differential scanning calorimetry (DSC) showed amorphous polymers (Figure S4.9). The corresponding T_g values of the transitions are likewise listed in Table 4.1. The lowest T_g of 95 °C was measured for P-A_2 and the highest of 104 °C for P-A_1.

Table 4.1 Number average molecular weight M_n, polydispersity index (PDI), values of the glass transition T_g, decomposition temperature $T_{d,1.5\%}$, room temperature dielectric permittivity ε', and dielectric relaxation strength $\Delta\varepsilon$.

Polymer ID	M_n [Da]	PDI	T_g [°C]	$T_{d,1.5\%}$ [°C]	ε' [a]	$\Delta\varepsilon_{max}$ [b]
P-A$_1$	275,000	1.30	104	168	4.3	19.5
P-A$_2$	381,500	1.25	95	168	5.5	22.4

[a] taken at 25 °C; [d] taken at maximum relaxation

Polymer nanoparticles could be generated by displacing the solvent used in preparing polymer solutions with a nonsolvent, a method known as nanoprecipitation or *Ouzo effect*, as described in the experimental section. To avoid complex nonlinear influence on the particle size distribution as reported in the literature,[44,45] the ratio between solvent and nonsolvent for all preparations was kept constant at 0.33. A comparison is made for particles prepared from the initial polymer solutions of **P-A$_1$** and **P-A$_2$** in DCM with the same concentrations and by increasing the concentration for **P-A$_1$** solutions. As expected, the same initial polymer concentration for **P-A$_1$** and **P-A$_2$** did not guarantee the same dynamics for the nanoprecipitation process, since the two polymers vary in M_n (confirmed by GPC) and stereoregular configuration (elucidated by ^{1}H NMR). Figure 4.2(a,b,d,h) shows a slight variation in the mean sizes of the particles prepared from these two polymers with the same concentrations in DCM and the same solvent/nonsolvent ratio. Thus, the difference in their macromolecular coils in solution and hydrodynamic volumes affects the particle size. Furthermore, an increment in particle sizes was observed by varying initial polymer concentrations of **P-A$_1$**. We observed that as the initial polymer concentration of **P-A$_1$** was increased, the generated particles increased in size. Thus, increasing concentration leads to a high number of molecules per solvent volume, resulting in larger particle formation. The SEM micrographs and the corresponding size distributions determined by particle count using ImageJ and DLS analyses, as shown in Figure 4.2, reveal a pronounced dependence of particle size on the initial polymer concentrations. At a concentration above 5 g L^{-1}, the precipitated particles became more polydispersed and showed broader size distributions (Figure 4.2(b,f,c,g))

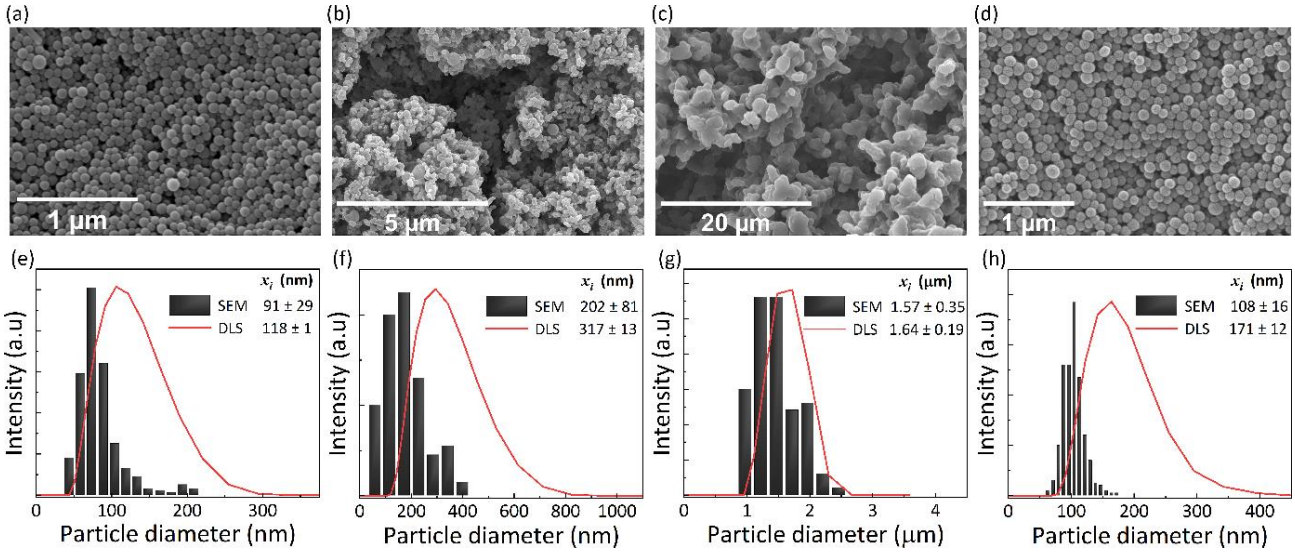

Figure 4.2 Representative SEM images and corresponding size-distributions obtained by SEM (black bars) and by DLS (red lines) made from P-A_1 concentration of: 2 g L^{-1} (a, e); 5 g L^{-1} (b, f); 10 g L^{-1} (c, g); and P-A_2 concentration of 2 g L^{-1} (d, h). Data are presented as mean ± SD ($3 \leq n \leq 300$) and $p < 0.05$.

A solution processing technique was employed to prepare composites of the polymer particles as filler in polydimethylsiloxane (PDMS) matrix. Processing steps and the solvent used are very crucial to obtaining composite films with good dispersion and excellent filler distribution in the matrix yielding desirable properties. For this reason, we employed a series of methods, including ball milling to break down large aggregates of polymer particles, homogeneous mixing of a well-dispersed filler in matrix solution by shearing in a 3-roll mill, and double-layer blade casting to minimize defects in the produced films. We successfully prepared composite films of **P-A_1** and **P-A_2** in PDMS solutions in cyclohexane with varying filler loadings and particle sizes. Table 4.2 summarizes the amount and the size of the filler used as well as the elastic modulus at different strain levels of 5% ($Y'_{5\%}$) and 50% ($Y'_{50\%}$), storage modulus (E'), dielectric permittivity, and relaxation strength ($\Delta\varepsilon$) of the materials synthesized. The obtained materials were denoted as **P-$A_{X\text{-}Y}$-Z**, where **P-A_X** represents the filler used, **Y** the size of the filler (small S, medium M, and large L), and **Z** represents the percentage weight (wt.%) of filler, respectively. Freestanding films with a typical thickness of 80 µm to 120 µm were achievable. The morphology of the produced films analyzed by SEM generally reveal evenly dispersed polymer particle fillers in the PDMS matrix. However, the extent of homogeneity and interfacial interaction between the two phases decreases with increasing filler particle size. The SEM micrographs in Figure 4.3 provide evidence of phase separation as influenced by the particle size of the polymer filler. Again increasing filler content to 40 wt.% increases the chances of introducing micro-cracks as defects in the resultant films (Figure S4.10).

Table 4.2 Summary of mechanical and dielectric properties of the prepared composites.

Composite	Filler [1]	Filler particle size	Mechanical properties				Dielectric properties	
			Tensile		DMA			
			$Y_{5\%}$	$Y_{50\%}$	$E'_{1\%}$	$E'_{10\%}$	ε' [2]	$\Delta\varepsilon$
			[MPa]					
P-A$_{1\text{-}S}$-10	10 wt. % of **P-A$_1$** with a small particle size	91 nm	1.4	0.4	1.4	1.0	2.6	0.3
P-A$_{1\text{-}S}$-20	20 wt. % of **P-A$_1$** with a small particle size	91 nm	2.8	0.6	2.6	1.4	2.7	0.7
P-A$_{1\text{-}S}$-30	30 wt. % of **P-A$_1$** with a small particle size	91 nm	5.5	0.6	6.2	2.5	2.8	1.3
P-A$_{1\text{-}M}$-30	30 wt. % of **P-A$_1$** with a medium particle size	202 nm	5.1	0.7	6.7	2.5	2.7	1.2
P-A$_{1\text{-}L}$-30	30 wt. % of **P-A$_1$** with a large particle size	1.6 µm	3.7	0.7	3.7	2.2	2.9	1.6
P-A$_{2\text{-}S}$-30	30 wt. % of **P-A$_2$** with a small particle size	108 nm	4.6	0.6	5.1	2.3	2.9	1.5
Matrix	-	-	0.6	0.2	0.5	0.5	2.4	-

[1]In PDMS cross-linked networks; [2]taken at 25 °C

Broadband dielectric spectroscopy (BDS) was employed to investigate the dipole relaxation dynamics in the polar polymers and the corresponding composites prepared. Thermally stimulated depolarization current (TSDC) as a complementary technique was also used to investigate the possibility of introducing quasi-permanent polarization in these amorphous materials. Graphical representations of how the real part ε' and imaginary part ε'' of complex permittivity, the real part of the conductivity σ', and the loss tangent $\tan\delta$ evolve with change in temperature at different frequencies for these materials can be found in the supporting information (Figure S4.11 – S4.15). The amount and size of filler have only a minor effect on the dielectric permittivity at room temperature, which is below 3, since the dipoles are frozen and cannot be polarized. However, there is a noticeable increase in ε' with increasing temperature above filler T_g over the specified frequency range. The experimental data were further interpreted by fitting with Havriliak–Negami (HN) relaxation model to understand the dielectric behavior with respect to structural and molecular motions of dipolar segments. A concise description of the dielectric behavior of such systems has already been given in another publication.[19,43] The parameters of relevance to understanding the

temperature and frequency-dependent transitions taking place at the molecular level and the possibility of polarizing these materials are the dielectric relaxation time (**τ)** and the dielectric relaxation strength (***Δε***). Figure 4 provides information on the temperature-dependent behavior of the two dielectric relaxation parameters estimated from the HN-fit function and the TSDC thermograms for the bulk polymers and their respective composites.

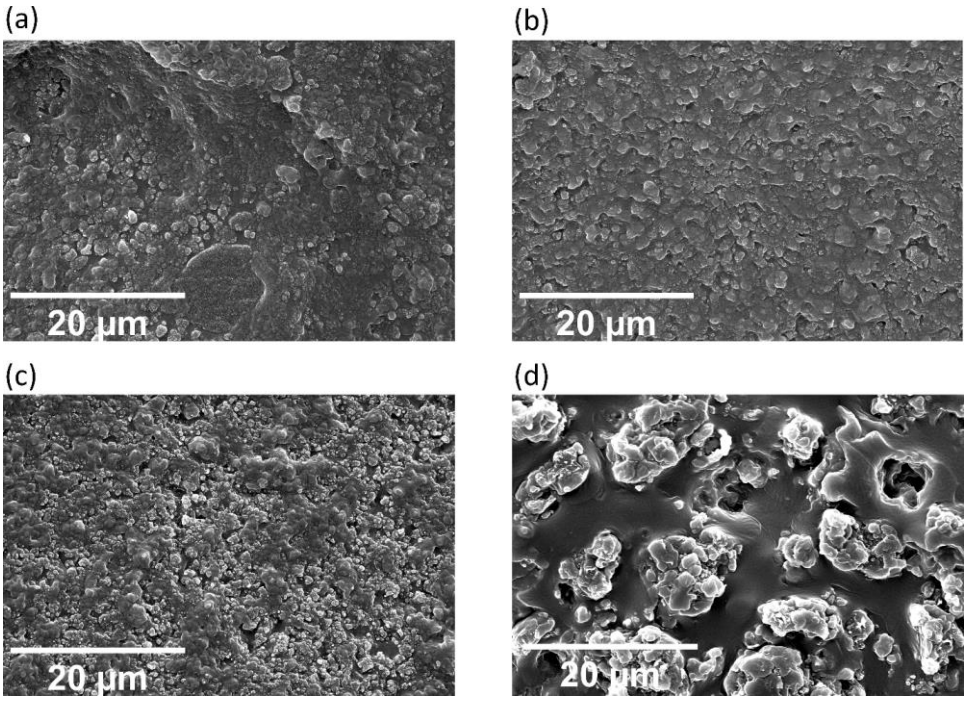

Figure 4.3 Effect of filler particle size on the morphology of prepared composites with 30 wt.% polymer particle loading in PDMS; (a) P-$A_{2\text{-}S}$-30; (b) P-$A_{1\text{-}S}$-30; (c) P-$A_{1\text{-}M}$-30 (d) P-$A_{1\text{-}L}$-30.

The two stereo-irregular polymers, **P-A$_1$** and **P-A$_2$**, though possessing the same chemical composition, reveal a slight difference in their molecular dynamics in response to an electric field, attributed to variation in the structural configuration. Additionally, **P-A$_1$** and **P-A$_2$** have relaxation strengths of 19.5 and 22.4 respectively, which are higher than the values of 16.3 reported by our group on a poly(methyl methacrylate) modified with disperse red 1 moiety.[19] The higher value for the last indicates that this polymer should give a stronger piezoelectric response. The matrix environment significantly influences the relaxation time, delaying the reorientation motion of dipoles with an electric field. Additionally, the disparity in thermal expansion coefficients and thermal conductivity of the polymer filler particles and PDMS matrix informs the resultant response in an electric field, as shown in Figure 4.4(a). Interestingly, the relaxation behavior with respect to time (***τ***) was independent of the amount of filler (Figure S4.16). The dielectric relaxation strength rather shows dependence on the amount of filler content and the stereoregular configuration of the polar

polymer particles, as plotted in Figure 4b. The complementary TSDC thermograms provided evidence of the various dipole contributions to polarization at very low frequencies and the possibility of poling the entire materials in a DC electric field. Detailed temperature-dependent poling and depolarization curves have been provided in supporting information (Figure S4.17). Figure 4.4(c,d) shows that the intensity of current density, which is also a contributing parameter to polarization, was higher in the bulk polar polymer than in their respective composites. The spike of these peak currents was observed close to the T_gs of the respective polymers. As a confirmation of the matrix effect on the dielectric relaxation behavior of these polar polymers, we could observe peak shifts in the corresponding thermograms of their respective composites.

Dielectric breakdown measurements were statistically evaluated with a Weibull probability plot on several measured data sets. Figure 4.4(e) showed an increase in the electric breakdown field (E_b) when the filler was added. This increase can be explained by the higher elastic modulus of the composites compared to the PDMS matrix. The increased breakdown field of the materials also confirms their high quality, since any film defect will lead to dielectric failure. However, a general decrease in E_b with increasing the amount of filler from 10 to 30 wt.% and the size of the filler particles was observed. Thus, the materials made with small particles performed best. The inferior performance of the materials made with larger particles is explained by the more inhomogeneous electric field in the material, which leads to earlier dielectric breakdown. A comparison between composites of the two stereo-irregular polymers with the same filler content of 30 wt.% and small particles shows different E_b. The elastic modulus of **P-A$_{2\text{-}s}$-30** ($Y'_{5\%}$ = 4.6 MPa) is slightly lower than **P-A$_{1\text{-}s}$-30** ($Y'_{5\%}$ = 5.5. MPa) and thus cannot explain the slight increase in E_b of the first. As will be discussed later, it seems that **P-A$_{2\text{-}s}$-30** is more homogenous, which will lead to a more homogenous distribution of the electric field in the material. However, it is still difficult to clarify where this difference comes from since the fillers have a different stereo-irregular structure and other extrinsic factors, such as film defects, can affect the E_b.

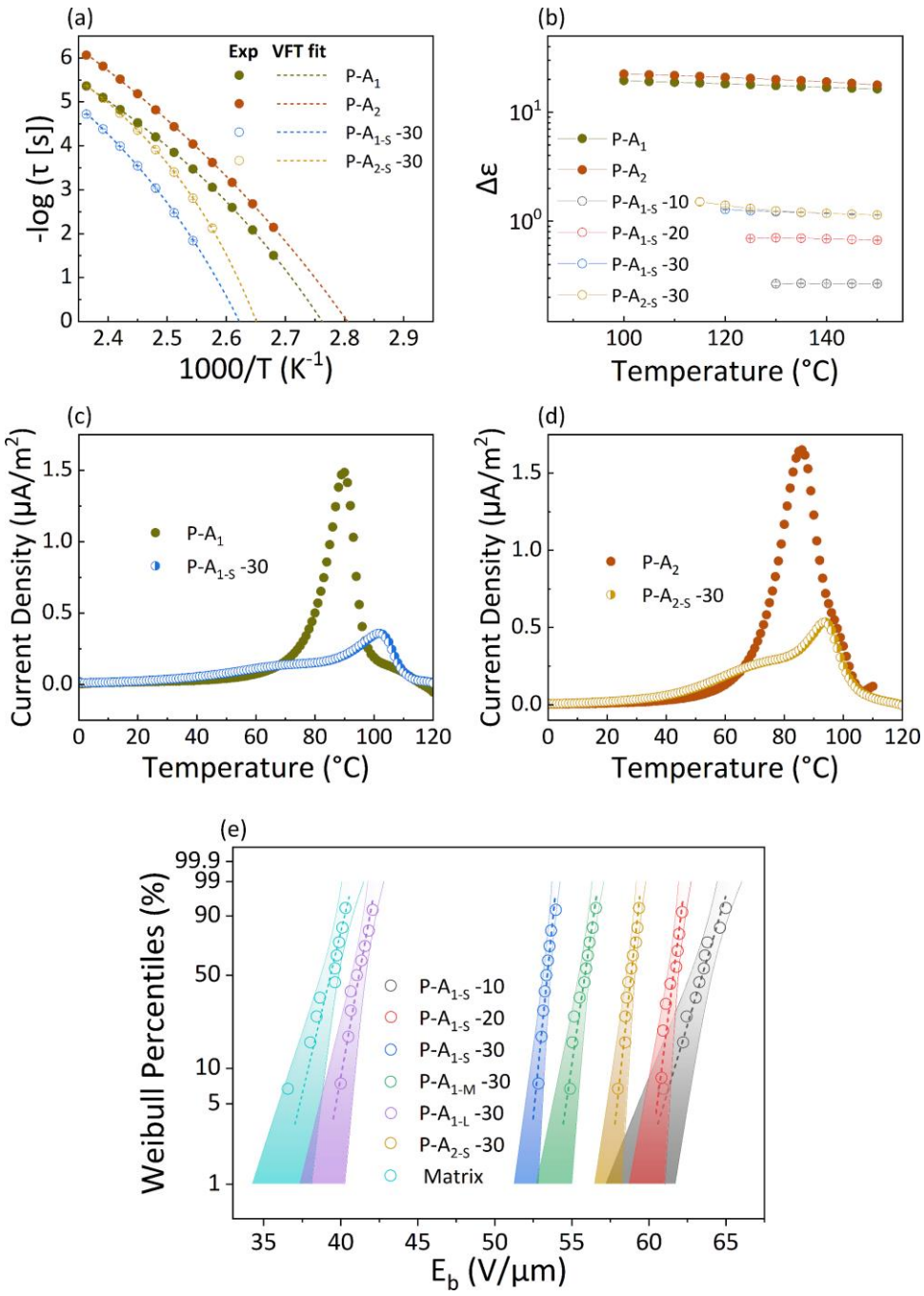

Figure 4.4 Dielectric behavior of P-A_1 and P-A_2, and their respective composites; (a) Effect of matrix on the dynamics of α-relaxation processes as shown in a Vogel-Fulcher-Tammann (VFT) plot corresponding relaxation times obtained from HN-fit versus the inverse of temperature; (b) temperature dependence of dielectric relaxation strength; (c) TSDC thermograms of P-A_1 and P-$A_{1\text{-}S}$-30; (d) TSDC thermograms of P-A_2 and P-$A_{2\text{-}S}$-30, comparing temperature-dependent depolarization current density; (e) Plot of dielectric breakdown of the composites in a two-parameter Weibull distribution and 95% confidence bands. Data are presented as mean ± SD (3≤ n ≤ 10) and $p < 0.05$.

The mechanical properties of the prepared composites were evaluated using uniaxial tensile testing, cyclic deformations, and dynamic mechanical analysis (DMA), as provided in supporting information (Figure S4.18 – S4.22). All composites proved to be elastomeric, showing pronounced dependence of mechanical response on the composition of the material. Thus, the filler type, amount, and particle size affect the bulk mechanical behavior. Increasing the amount of filler led to an increase in Young's modulus and the strain at break. Keeping the filler content constant and increasing particle size decreases Young's modulus and strain at break. The stereo-irregular polymer composites with the same amount of fillers gave similar tensile test results. The increase in Young's modulus with decreasing filler size and with increasing filler amount is explained by the increased cross-linking density due to the physical interactions between the polymer chains in the matrix and the filler. The improved tensile strength of all materials can be explained by the very good contact between the filler and the matrix, even though no compatibilizer was added. Polydimethylsiloxanes stick to most surfaces and are, therefore, often used as gluing agents. This strong adhesion may explain the improved mechanical properties of our materials. Cyclic deformation tests were also performed to further prove the mechanical integrity of these composites (Figure S4.19). We generally observed increased stress softening under larger strain deformations (Mullins effect) with increasing the filler content. Thus, materials lose stiffness after the first cycle, which is associated with the breakage of the interactions between the filler particles or filler and polymer chains.

DMA probed the viscoelastic behavior in the amplitude and frequency sweep modes (Figures S4.20 and S4.21). A slight increase in the storage modulus and a slight decrease in *tan δ* with increasing frequency was observed for all materials except for the matrix. The loss factor *tan δ* gives valuable information regarding the non-elastic component in a material. The matrix–filler interface (interfacial region) strongly affects the mechanical properties of composites and quite often it's damping level too. The *tan δ* of all materials was below 0.13 at all frequencies, which is rather low. An increase in *tan δ* with increasing the content of small particle filler content was observed, which indicates that the interaction between the matrix and the filler is less pronounced for the high filler content. Material **P-A$_{2\text{-}s}$-30** has a smaller *tan δ* than **P-A$_{1\text{-}s}$-30**, which may indicate a better interaction between the filler and the matrix for the first and may explain its increased dielectric breakdown field. However, for the materials with 30 wt.% filler, but different particles size, no clear trend was observed. Material made with medium size particles showed the highest *tan δ*. The reason behind this is unclear.

A strong dependence of the storage and loss moduli on strain amplitude with increasing filler content in composites was observed. This behavior is known as the Payne effect,[46,47] which is absent in the pristine PDMS matrix elastomer but strongly depends on the materials' filler content. At small strain amplitudes, the dynamic modulus is almost constant but decreases rapidly with increasing strain. As expected, the storage modulus increases with the amount of filler and decreasing filler size. It is

generally accepted that the dynamical break-up of filler networks is responsible for this nonlinear viscoelastic behavior of composite.

Storage modulus measurements were conducted at different temperatures from 50 to 150 °C (Figure S4.22). Below the T_g of the filler, the materials showed an increase of the storage modulus at the rubbery plateau with the amount of filler and with decreasing particle size. This increase is due to filler–polymer and filler–filler interaction in the network structure. On increasing the temperature, a drop of storage modulus was observed for all samples, corresponding to the filler nanoparticles' T_g. These measurements also reveal an increasing dependence of the damping factor with increasing filler content and a decrease with increasing particle size.

Transverse piezoelectric coefficient measurements for the composite sets were conducted with an internally built technique. The testing setup, described in previous work in our lab, couples a Zwick Z010 tensile testing machine with a Keithley 2000 multimeter.[19] It allows applying a known force while straining the sample and recording the output electrical response (current and voltage) simultaneously. To affirm the reliability of these measurements, control samples of unpoled composites and poled matrix were studied alongside. An insignificant amount of current within the noise range of the measurement technique could be detected in all instances. This confirms that piezoelectric properties in the heterogeneous composite systems could only be induced after electric poling.

Samples of the composites were then subjected to thermally assisted corona poling to induce dipole alignment and anisotropic piezoelectric behavior in d_{31} mode. The procedure for poling is described in the experimental section. Directional changes in polarization experiments were also conducted by reversing the circuit connection to electrodes on the composite samples. This resulted in the flip of the direction of charge flow and a change in sign but a similar magnitude to the recorded current. The collected charge per cycle was calculated by integrating the recorded current. The piezoelectric coefficients and electromechanical coupling constants could then be calculated according to the equations provided in the supporting information. The resulting piezo-electrets after corona poling were tested for stability regarding their piezoelectric response over one month by applying 50% mechanical strain and measuring the output current and voltage. The evaluated piezoelectric properties generally experienced a non-exponential decay over 15 days characterized by a relatively strong decrease followed by a pseudo-stable state over the study period. To prove the reason behind the piezoelectric decay, a poled sample was tested after letting it stand for three weeks. Its response was similar to the sample tested at predetermined periods, suggesting that charge migration in the soft PDMS matrix is responsible for the decay and not the rearrangement of the particles in the matrix.

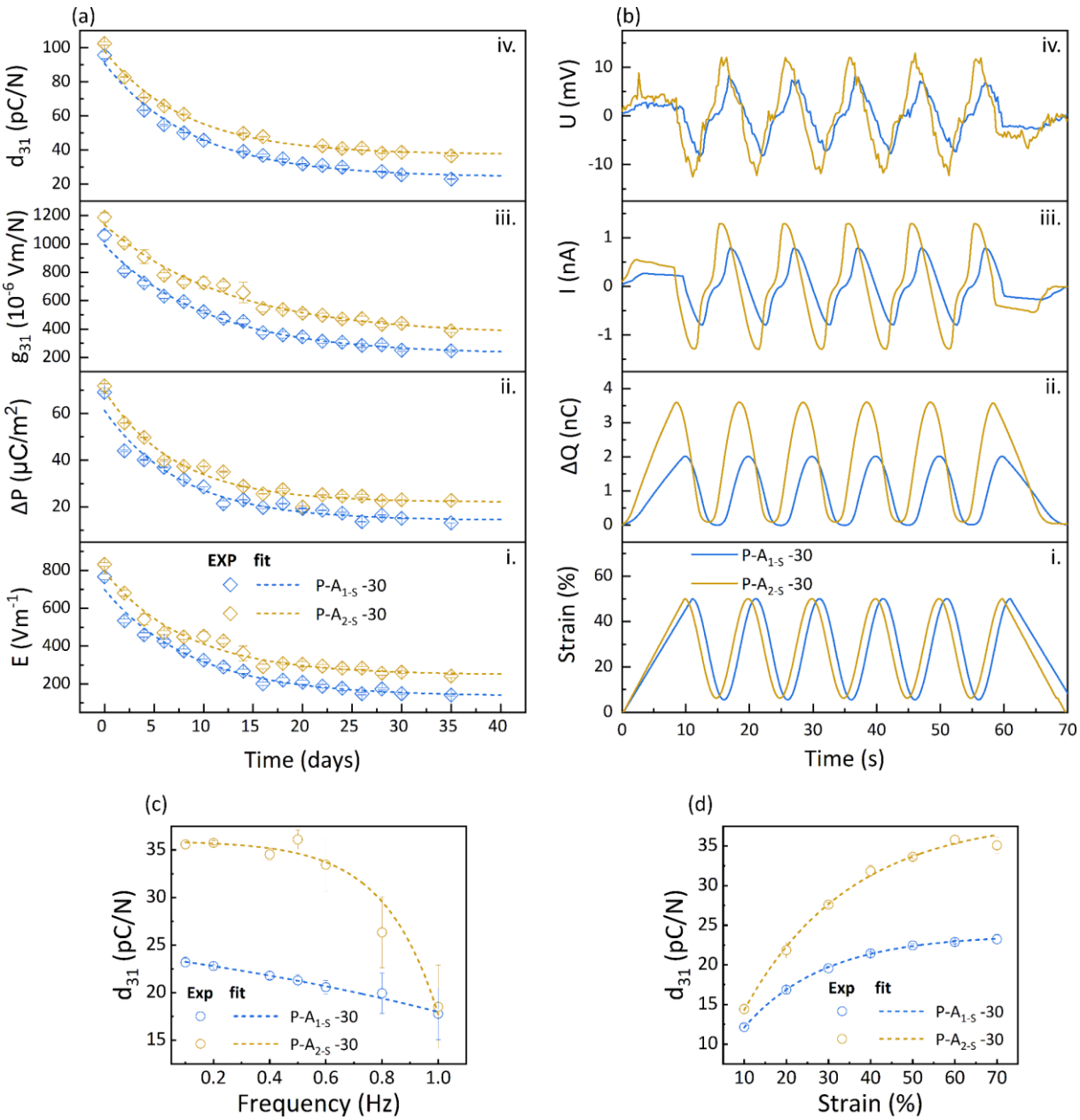

Figure 4.5 Piezoelectric response of **P-A$_{1\text{-}S}$-30** (blue) and **P-A$_{2\text{-}S}$-30** (yellow) elastomers: (a) Non-exponential decay of charges collected at 50% strain deformation cycles over time; (i) stress-induced electric field, *E*; (ii) stress-induced polarization, ΔP; (iii) estimated transverse piezoelectric voltage coefficient, g_{31} and (iv) calculated transverse piezoelectric charge coefficient, d_{31}; (b) applied strain (i.) generated charges (ii.), current (iii.) and voltage (iv.); (c) frequency dependent d_{31}; and (d) strain dependent d_{31} values. Data are presented as mean ± SD (n = 15) and $p < 0.05$.

If the creep was responsible for the decay, the sample stressed at predetermined time intervals should show a stronger decay, which was not the case. Therefore, we concluded that the decay is not due to mechanical relaxation but rather electrical. The material consists of a soft matrix with a T_g

significantly below room temperature, while the filler consists of hard particles with a high T_g. During poling at elevated temperatures, not only the dipoles from the filler particles are polarized, but ions are also moved in both the matrix and the filler. Ion relaxation is a slow process, that takes time, but the soft matrix facilitates the ion movement.

Figure 4.5(a) shows piezo-electrets of the stereoirregular polymer composites, which gave the highest performance. We further observed that piezoelectric properties were enhanced by increasing the active polar polymer filler content. That notwithstanding, the particle size of the filler plays a critical role; thus, increasing filler particle size with the same content in composite resulted in a decrease in the piezoelectric response. The piezoelectric response is explained by the charge-spring model described by:[28]

$$d_{33} = \frac{-P_3}{Y_M} + \frac{P_3}{Y_D} \tag{4.1}$$

where $P_3 = \varepsilon_0 \Delta\varepsilon(T) E_p$, Y_M is the Young's modulus of the matrix and Y_D the Young's modulus of the filler (dipole phase). Our materials have stiff dipoles since the filler has a high T_g and, thus an elastic modulus, which is several orders of magnitude higher than the elastic modulus of the matrix with a low T_g. Therefore, when the materials are stretched, the material's dipole density changes, leading to a current flow between the electrodes. The graphical proof of the above observations can be found in the supporting information (Figure S4.23 and S4.24). Figure 4.5(b) provides a typical representation of the applied sinusoidal strain and the corresponding stress-induced charges, current, and voltage generated for **P-A$_{1\text{-}S}$-30** and **P-A$_{2\text{-}S}$-30**.

To confirm the influence of poling approach on the resultant piezo-electret, we performed electrode contact poling of **P-A$_{1\text{-}S}$-30** film and evaluated the piezoelectric property. It was revealed that the corona-poled samples showed a d_{31} approximately three times higher than the electrode contact poled counterpart (Figure S4.25).

A summary of the transverse piezoelectric coefficient, d_{31}, as influenced by the filler content, particle size and stereoregular configuration of the different polar polymers for the prepared piezo-electret composites is shown in Figure 4.6(a). Material **P-A$_{2\text{-}S}$-30** exhibited the highest d_{31} of 37 pC/N at 50% strain, likely due to its larger relaxation strength. Its response is also three times larger than the one at 150% for a PDMS-based elastomer filled with poly(methyl methacrylate) modified dispersed red 1 poled by direct poling.[19]

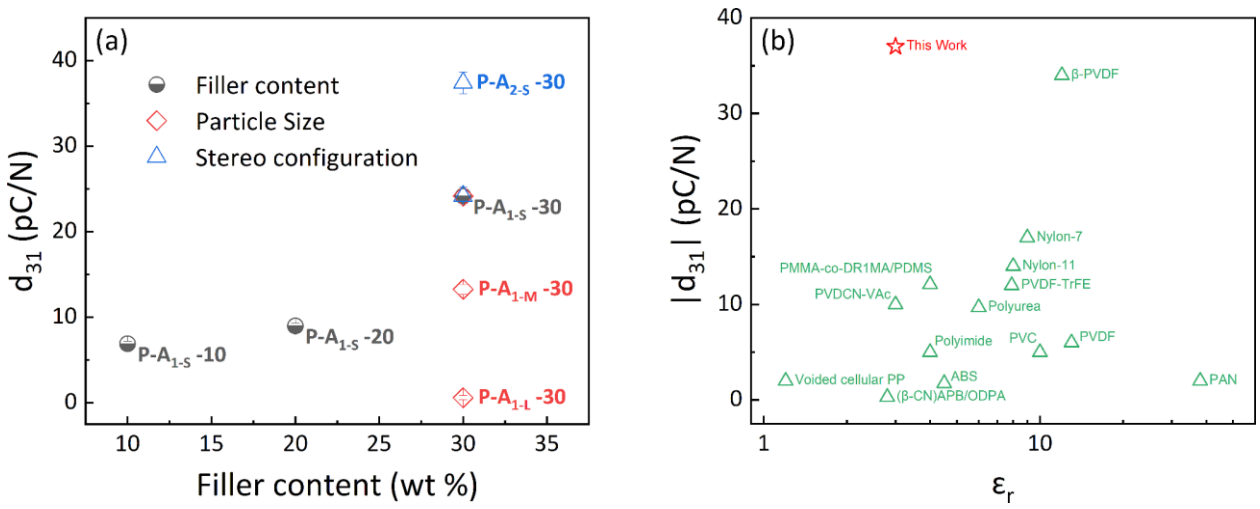

Figure 4.6. Summary: (a) Effect of different amounts and filler sizes on the d_{31} and (b) piezoelectric response of different piezoelectric polymers with different relative permittivity and of the best material developed in this work.

Many flexible piezoelectric devices have an outstanding piezoelectric response when pressed, but are made of materials with high elastic modulus, which lack elasticity.[21,48-50] Aside the advantage of this material to withstanding comparatively large mechanical deformations, the recorded d_{31} value is comparatively the highest to already investigated polymers, as presented in Figure 4.6(b). Therefore, the material developed in this work may be suitable for applications where elasticity and compliance are a must, for instance, in implants.[51]

4.4 Conclusion

This work has employed suitable synthetic and composite preparation pathways coupled with electric poling to prepare piezo-electret elastomers. Polar norbornene monomers were first polymerized by ring-opening metathesis polymerization, and the resulting polymers were processed into nanoparticles via nanoprecipitation. Blends with different content and size of polar polynorbornene NPs in polydimethylsiloxanes were processed into thin films by doctor blading and the films were chemically cross-linked. To turn the materials piezoelectric, they were poled in a strong electric field above the T_g of the filler. The piezoelectric performance revealed a strong dependence on the amount, particle size, stereoregular configuration of the reinforced polymer NPs and the electric poling technique employed. Surprisingly, a quasi-stable transverse piezoelectric coefficient, d_{31}, as high as 37 pC/N could be recorded for the best-performing material poled by corona discharge. To the best of our knowledge, this is the highest value reported for elastic electrets. In addition, these piezo-electret elastomers can withstand large mechanical deformations, a critical property rendering

them suitable for application in stretchable sensors, energy harvesting, soft robotics, and flexible electronics. Future work will be invested in increasing the piezoelectric response even further by introducing pores into the polarized films.

4.5 Experimental Section

4.5.1 Materials

All reagents were purchased from Sigma Aldrich and utilized without further purification unless otherwise stated. Linear hydroxyl end-capped polydimethylsiloxane (PDMS) (AB116665, M_w = 139,000 g mol^{-1}), ethyltriacetoxy silane crosslinker, and titanium 2-ethylhexoxide catalyst were purchased from ABCR. Dichloromethane (DCM), ethyl acetate, ethanol, methanol, heptane, cyclohexane, and tetrahydrofuran (THF) were purchased from VWR Chemicals and deuterated solvents from Deutero GmbH. DCM was dried over calcium hydride. Millipore Milli-Q system processed deionized water was taken for all experimental work-ups. Polymers **P-A$_1$** and **P-A$_2$**, and their respective monomers were synthesized according to the literature with slight modifications in reaction conditions.[43] A comprehensive overview of the syntheses with kinetic data of the polymerization can be found in supporting information (Figure S4.1 – S4.4).

4.5.2 Preparation of Polymer Particles

Particulate of the polymers **P-A$_1$** and **P-A$_2$**, with sizes in the nanometer to micrometer range, were prepared by solvent displacement technique. In practice, different polymer solutions (250 ml each) in DCM with concentrations of 5-, 8-, and 10 g L^{-1} were prepared and separately added dropwise to 750 ml of methanol under vigorous stirring. The resulting polymer/DCM/methanol ternary systems were allowed to stir further for 30 minutes and the DCM was carefully evaporated under vacuum. Subsequently, the colloidal suspensions were then filtered through a 0.22-µm pore-size Nylon membrane and the obtained polymer particles were dried under vacuum at 25 °C. Polymer particles with an average size ranging from 100 nm to 2 µm were achieved.

4.5.3 Composite Film Processing

The composite film, using the synthesized polymer particles as filler and PDMS as matrix components, was fabricated via solution processing coupled with blade casting. The filler was initially ball-milled using a Retsch MM 400 mixer mill (35 ml PTFE screw-top grinding jar and 1.25 mm diameter Zirconia grinding balls at 30 Hz for 30 minutes) to break down large aggregates and pre-dispersed in cyclohexane. The calculated amount of the matrix to give a set weight ratio of

composition was added and manually mixed with a glass rod. Further mechanical agitation by shearing was performed on an EXAKT three-roll mill with hard chromium-plated rollers (G-series) for 15 minutes to improve the homogeneity of the mixture. The resulting viscous slurry was further diluted with a small amount of cyclohexane (5 wt.% equivalence of the resulting viscous slurry) followed by the addition of ethyltriacetoxy silane crosslinker (100 µl per gram of PDMS) and subjected to stirring overnight. Titanium 2-ethylhexoxide catalyst (10 µl per gram of PDMS) was added and further stirred for 2-5 minutes. The resulting mixture was double-layer cast on Teflon coated glass substrate using a Zehntner ZUA 2000 blade. The produced film was first air-dried for 12-18 hours to complete cross-linking reaction, followed by heat treatment in a vacuum oven at 100 °C for 8 hours to remove residual solvent. Free-standing films with thicknesses ranging from 80 to 120 µm could be processed.

4.5.4 Structural Characterization

^{1}H and ^{13}C NMR spectra were recorded in $CDCl_3$ with a 400 MHz Bruker Avance-400 spectrometer at room temperature. The morphology of the synthesized polymer particles and composite films were characterized using FEI Quanta 650 ESEM. Images were taken in secondary electrons-topography mode using Everhart-Thornley Detector at 10 kV acceleration voltage. The particle size distribution in SEM images was evaluated by an average diameter count of approximately 300 particles. Dynamic light scattering (DLS) measurements were carried out on the particle suspensions produced after nanoprecipitation, using a Malvern Zetasizer at room temperature (25 °C). Measurements were conducted three times and always the average values were reported.

4.5.5 Molecular Weight Determination

Gel permeation chromatography (GPC) elugrams in THF were recorded with an Agilent 1260 Infinity, using two tandem-connected mixed-bed columns (1×PLgel 5 µm MIXED-C Guard and 2×PLgel 5 µm MIXED-C Analytical), coupled to a 390-MDS refractive index detector and calibrated with polystyrene standard. The system employed a flow rate of 1 ml min^{-1} and was kept at 30 °C.

4.5.6 Thermal Analysis

Differential scanning calorimetry measurements were performed using a Perkin Elmer DSC 8000. Samples were initially heated to 150 °C at a rate of 20 °C/min to remove any thermal history. Heat-cool-heat cycles were scanned from 0 to 150 °C at a rate of 20 °C/min unless otherwise stated. Thermogravimetric analysis (TGA) was conducted using a Perkin Elmer TGA7 at a heating rate of 10 °C/min under a nitrogen gas flow.

4.5.7 Mechanical Behavior Evaluation

Uniaxial tensile and repetitive cyclic deformation tests were performed on a Zwick Z010 universal testing machine with a 50- and 20 mm min-1 crosshead speed. Dog-bone shape test specimens with gauge width of 2 mm and length of 18 mm were prepared by die-cutting. Reported data are averages of three independent measurements. The Young modulus was estimated from the slope of the stress-strain curves using a linear fit to the data points within 10% strain. Dynamic mechanical analysis was carried out on an RSA 3 DMA from TA Instruments in the tensile mode. Stripes of samples with rectangular geometry were measured under a dynamic load of 4 g. Data in the frequency sweeps were obtained by applying 2% strain in the frequency range of 0.1–10 Hz. The amplitude scans were performed at 0.1Hz from 1 – 10 % strain. The temperature dependence measurements were conducted by applying 0.5% strain at a frequency of 0.1Hz.

4.5.8 Broadband Dielectric Spectroscopy

Temperature-dependent dielectric properties were evaluated using a Novocontrol Alpha-A Frequency Analyzer equipped with quatro cryosystem temperature control. Samples of polymers **P-A$_1$** and **P-A$_2$** were prepared by making pellets with the aid of a hydraulic press, sandwiching them between two metal electrodes with 100 µm glass fibres as spacers, and melt pressing at 120 °C. The composite films with known thickness were sandwiched between two metal electrodes. Dielectric spectra were recorded by applying an external electric field of 10 kV/m in a frequency and temperature range of 0.1 to 1 MHz and −50 to 150 °C, respectively.

4.5.9 Thermally Stimulated Depolarization Current Analysis

A Novocontrol quatro cryosystem consisting of a cryostat with a sample holder coupled to a sensitive electrometer (B2985A, Keysight technologies) with a built-in dc voltage source was used for the measurements. Samples were prepared as described in the broadband dielectric spectroscopy procedure above. In practice, each sample was heated to a set polarization temperature (T_p) and after stabilization, an electric field (E_p) of 2 V µm^{-1} was applied for a time (t_p) of 1 minute. The sample was steadily cooled at 10 °C min^{-1} while keeping the electric field until the temperature reached 0 °C. The applied electric field was then removed. The sample was subsequently heated at 5 °C min^{-1} after a delay time of 5 minutes. Currents accompanying the depolarization during this gradual heating process were recorded for analysis.

4.5.10 Dielectric Breakdown Measurement

A 12.5 kV dc high voltage power supply system (HCL 35-12500 pos, F.u.g electronic GmbH, Germany) was used for all measurements. Samples were sandwiched between two metal electrodes

with 1 mm^2 area embedded in an epoxy resin. The applied voltage was linearly increased until failure voltage was recorded on several samples. Statistical analysis was employed to evaluate the dielectric breakdown field, commonly following Weibull probability model

4.5.11 Corona Poling

Piezo-electret of the composite films were prepared by corona discharge in air atmosphere using a PolyK Technologies Corona poling system (PK-C30kV-200C). The system is equipped with a 30 kV/ 2 mA dc high voltage source, connected to a grid of corona needles mounted in an oven with digital temperature control. In practice, a specimen with a gauge width of 30 mm and a length of 60 mm is fixed on a poling frame and inserted into the poling station. The sample was then heated to a stabilized temperature of 120 °C, after which a voltage of 18 kV was applied to the grid of needles for 30 minutes. The poled film was then allowed to cool under the corona electric field for 30 minutes to room temperature. The voltage supply was finally switched off and the sample was carefully unmounted.

4.5.12 Electrode Contact Poling

Specimen of the composites was sandwiched between two carbon black compliant electrodes circularly brushed on with 14 mm diameter. A maximum electric field of 25 V/µm, beyond which the films yield electrical breakdown, could be applied at 120 °C for 10 minutes. The film was then allowed to cool to room temperature while keeping the electric field on at a rate of 10 °C/min. The field was maintained by a Stanford Research Systems PS350 high voltage source. Temperature control was facilitated by a CTS-Temperature test chamber.

4.5.13 Piezoelectric Coefficient (d_{31}) Measurements

Measurements were conducted on the same setup and following a similar procedure as described in the literature.[19]

4.5.14 Statistical Analysis

All data are evaluated by averaging several measurements without removing outliers ($n \geq 3$). The data given in the manuscript represent the mean value, mean ± standard deviation. Evaluation were performed employing descriptive statistics in the built-in functions of OriginLab. For image analysis, the built-in functions of ImageJ were used. A probability value ($p \leq 0.05$) was significantly considered during the analysis.

4.6 Supporting Information

4.6.1 Synthesis Route

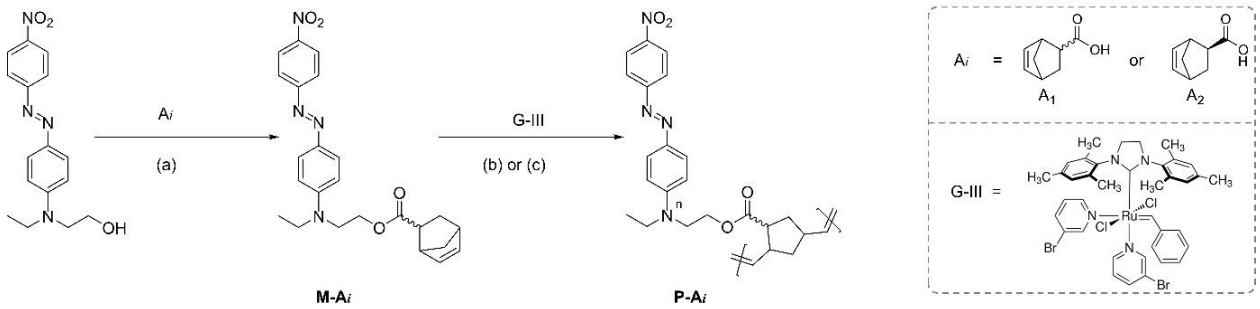

Scheme S4.1 Synthesis of M-Ai and respective P-Ai: (a) 4-dimethylaminopyridine (DMAP), N,N'-dicyclohexylcarbodiimide (DCC), dry dichloromethane (DCM), 24 h, 45 °C. Grubbs 3rd generation catalysts (G-III), dry DCM; (b) M-A_1, 40 °C for 23 h (c) M-A_2, 25°C for 2 h.

4.6.1.1 Synthesis of M-Ai

A dried 2-necked round bottom flask was charged with ether 5-norbornene-2-carboxylic acid, mixture of *endo* and *exo*, predominantly *endo* (**A_1**) or *exo*-5-norbornene-2-carboxylic acid (**A_2**) (5.00 g, 36.202 mmol), *N*-ethyl-*N*-(2-hydroxyethyl)-4-(4-nitrophenylazo) aniline (11.38 g, 36.20 mmol) and 4-dimethylaminopyridine (8.85 g, 72.40 mmol) dissolved in of anhydrous DCM (60 mL). N,N'-dicyclohexylcarbodiimide (14.94 g, 72.40 mmol) was added at 0 °C to the reaction mixture, stirred for 5 min at 0 °C, and refluxed for 24 h at 45 °C. The resulting crude mass was concentrated in vacuum and purified using column chromatography with heptane and ethyl acetate (3:2) mixture as eluent.

M-A_1 was obtained as a reddish powder (95 % yield): ^{1}H NMR (400 MHz, $CDCl_3$) δ 8.43 – 8.24 (m, 2H), 8.04 – 7.82 (m, 4H), 6.90 – 6.74 (m, 2H), 6.24 – 6.13 (m, 1H), 6.01 (ddd, J = 77.5, 5.7, 3.0 Hz, 1H), 4.30 (dt, J = 26.8, 6.3 Hz, 2H), 3.70 (dt, J = 15.8, 6.3 Hz, 2H), 3.56 (q, J = 7.2 Hz, 2H), 3.24 – 3.10 (m, 1H), 3.05 – 2.87 (m, 2H), 2.02 – 1.89 (m, 2H), 1.44 (ddd, J = 11.1, 7.6, 4.1 Hz, 2H), 1.28 (t, J = 7.1 Hz, 3H). ^{13}C NMR (101 MHz, $CDCl_3$) δ 175.69 (d, J = 106.1 Hz), 174.71, 156.76, 151.32, 147.36, 143.82, 138.14, 138.02, 136.86, 135.63, 132.53, 132.19, 126.27, 124.66, 122.64, 111.47, 61.32, 61.18, 55.94, 55.74, 49.81, 49.76, 49.70, 48.85, 48.79, 46.81, 46.57, 46.39, 45.71, 45.65, 45.61, 44.36, 43.31, 43.08, 42.75, 42.54, 41.63, 34.94, 33.97, 32.87, 32.80, 31.27, 31.14, 30.85, 30.44, 29.29, 26.48, 26.41, 25.53, 25.47, 25.40, 24.99, 24.86, 24.70, 12.30.

M-A$_2$ was obtained as a reddish powder (91 % yield): ^{1}H NMR (400 MHz, $CDCl_3$) δ 8.39 – 8.30 (m, 2H), 8.00 – 7.88 (m, 4H), 6.89 – 6.79 (m, 2H), 6.18 – 6.09 (m, 2H), 4.34 (t, *J* = 6.3 Hz, 2H), 3.72 (t, *J* = 6.3 Hz, 2H), 3.57 (q, *J* = 7.1 Hz, 2H), 3.07 – 2.99 (m, 1H), 2.97 – 2.90 (m, 1H), 2.29 – 2.19 (m, 1H), 1.91 (dt, *J* = 11.8, 4.0 Hz, 1H),1.52 (dt, *J* = 8.3, 1.6 Hz, 1H), 1.39 (dddd, *J* = 9.7, 8.4, 5.7, 2.6 Hz, 3H), 1.29 (t, *J* = 7.1 Hz, 3H). ^{13}C NMR (101 MHz, $CDCl_3$) δ 176.23, 156.62, 151.40, 147.44, 143.80, 138.52, 138.16, 136.07, 135.63, 126.41, 124.70, 122.62, 111.59, 61.30, 49.68, 48.91, 46.96, 46.84, 46.57, 46.40, 45.70, 43.79, 43.09, 41.72, 41.63, 32.88, 32.82, 32.08, 30.99, 30.86, 30.45, 26.53, 25.54, 25.37, 24.79, 12.31.

4.6.2 Polymerization Kinetics

4.6.2.1 Synthesis of P-Ai

Homopolymers of M-A*i* (M-A$_1$ and M-A$_2$) were prepared via ROMP with the same monomer-to-catalyst feed ratio ([M]:[C] = 400:1) and their rate of polymerization was studied. In an argon-filled Schlenk setup, a solution of M-A*i* (2.00 g, 4.603 mmol) in 30 mL of DCM, which was degassed in three freeze-vacuum-thaw cycles, was added to a degassed solution of G-III (10.18 mg, 0.012 mmol) in 16 mL of DCM to give a monomer concentration of 0.1 M. The reaction was allowed to proceed per conditions described in Scheme S1. The progress of polymerization was monitored at regular time intervals using ^{1}H NMR, done by taking aliquots and quenching with ethyl vinyl ether in $CDCl_3$. After confirming optimal monomer conversion by ^{1}H NMR, ethyl vinyl ether was added, and the resulting mixture was stirred for a further 1 h. The product mixture was concentrated under vacuum and then precipitated into excess methanol. The polymer was further purified by five consecutive dissolution (DCM) and re-precipitation cycles (MeOH). The obtained polymers were dried to constant weight under vacuum at 40 °C.

P-A$_1$ was obtained as a dark red solid: ^{1}H NMR(400 MHz, $CDCl_3$) **δ**: 8.26 (br d, **J** = 9.0 Hz, 2H), 7.87 (br s, 4H), 6.78 (br d, **J** = 12.2 Hz, 2H), 5.28 (br dd, **J** = 44.0, 21.3 Hz, 2H), 4.45–3.87 (br m, 2H), 3.56 (br d, **J** = 55.7 Hz, 4H), 3.26–2.61 (br m, 3H), 1.85 (br d, **J** = 86.3 Hz, 4H), 1.46–1.10 (br m, 3H). ^{13}C NMR (101 MHz, $CDCl_3$) **δ**: 174.28, 156.47, 154.00, 151.31, 147.31, 143.67, 134.52, 133.31, 132.48, 130.71, 129.80, 126.40, 124.64, 122.57, 111.50, 60.93, 50.12, 48.71, 45.61, 42.71, 40.51, 37.70, 36.10, 32.77, 31.11, 26.18, 25.45, 24.83, 12.36.

P-A$_2$ was obtained as a dark red solid: ^{1}H NMR (400 MHz, $CDCl_3$) δ 8.26 (br s, 2H), 7.86 (br s, 4H), 6.76 (br s, 2H), 5.25 (br d, *J* = 53.2 Hz, 2H), 4.25 (br s, 2H), 3.56 (br d, *J* = 60.4 Hz, 4H), 3.19 – 2.37 (br m, 3H), 2.17 – 1.47 (br m, 4H), 1.16 (br d, *J* = 40.5 Hz, 3H). ^{13}C NMR (101 MHz, $CDCl_3$) δ 175.36, 156.55, 151.27, 147.35, 143.73, 134.65, 133.55, 132.77, 131.99, 130.99, 126.40 126.33, 124.65,

122.62, 122.57, 111.48, 61.28, 50.40, 50.06, 49.63, 48.78, 45.67, 43.16, 41.94, 37.09, 32.81, 26.18, 25.43, 24.79, 12.33.

4.6.3 Theoretical consideration for calculating piezoelectric constants

The magnitude of charges, *Q*, per unit area, *A*, induced by the poled composite material on electrodes on the film surfaces is equal to the total macroscopic dipole moment, *M*, per unit volume, V, of polymer between the electrodes, which is the polarization, *P*. Thus;

$$\frac{Q}{A} = \frac{M}{V} = P \tag{4.2}$$

And

$$P = P_r + \Delta P \tag{4.3}$$

where $P_r = \varepsilon_0 \Delta\varepsilon(T) E_p$, is the remnant polarization induced by poling and ΔP is the stress-induced polarization.

Piezoelectric charge coefficient, d_{31}, is the change in Q per unit area of the electrode on the poled sample with stress, S, applied perpendicularly in the cross-sectional direction; thus,

$$S = \frac{F}{A_c} \tag{4.4}$$

where *F* is the applied force and A_c is the cross-sectional area where the force was applied.

$$d_{31} = \frac{\Delta Q}{S \cdot A_e} = \frac{\Delta Q \cdot A_c}{F \cdot A_e} = \frac{\Delta P \cdot A_c}{F} \tag{4.5}$$

Where A_e is area of the electrode on the poled sample.

Piezoelectric voltage coefficient, *g*, also called voltage output constant, is defined as the electric field, *E*, generated per unit of mechanical stress, *S*, applied and is expressed as

$$g = \frac{E}{S} \tag{4.6}$$

g_{31} and d_{31} are related to the relative permittivity from the equation:

$$g_{31} = \frac{d_{31}}{\varepsilon_r \varepsilon_0} \tag{4.7}$$

ehere ε_r is the dielectric constant of the dielectric material and ε_0 is the permittivity of vacuum (8.85×10^{-12} F·m^{-1}).

The electromechanical coupling coefficient, k_{31}, represents the conversion efficiency between electrical and mechanical energy and is a measure of the combination of piezoelectric and mechanical properties of a material, expressed as:

$$k_{31} = d_{31}\sqrt{\frac{Y_{11}}{\varepsilon_r \varepsilon_0}} \tag{4.8}$$

4.6.4 Supplementary Figures

4.6.4.1 Kinetics Data on Polymerization

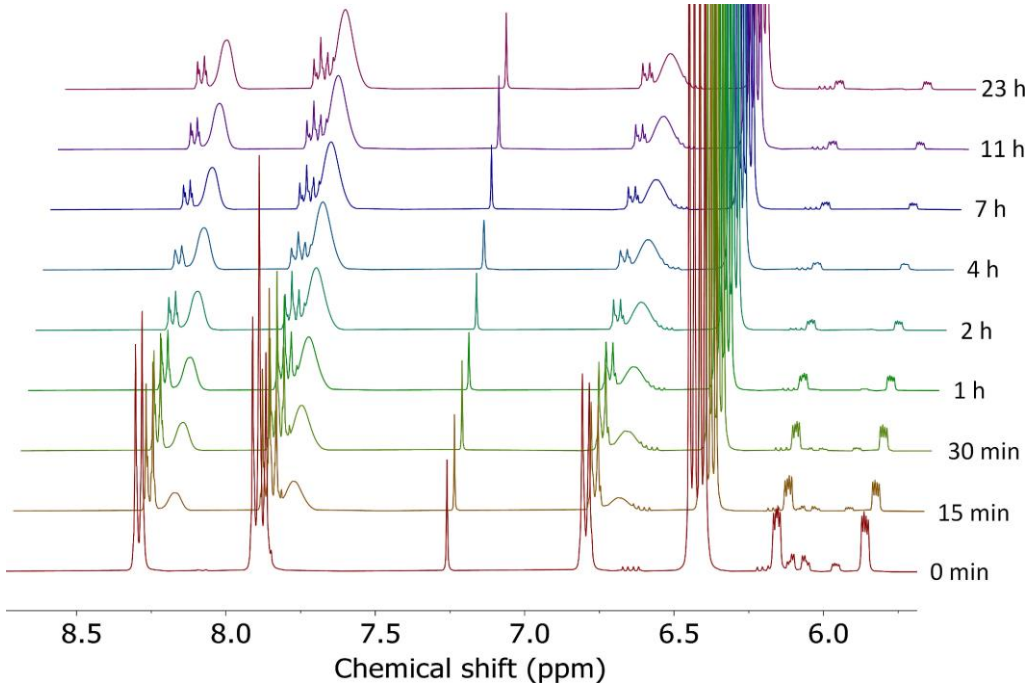

Figure S4.1 Stacked plot of ^{1}H NMR spectra for the kinetic progress of ROMP with [M-A_1]:[G-III] = 400:1

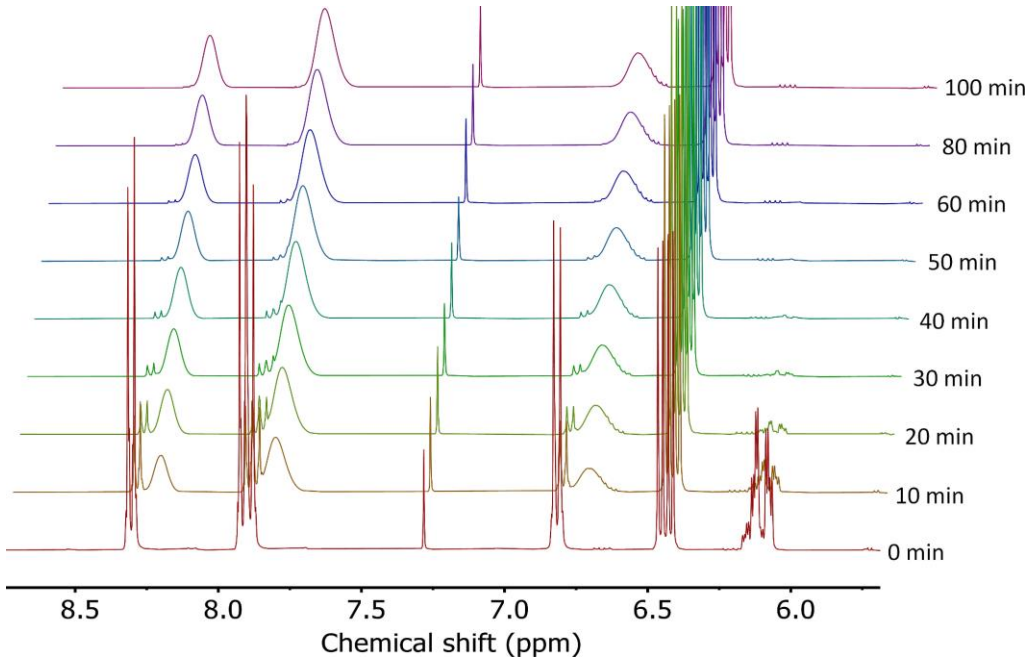

Figure S4.2 Stacked plot of ^{1}H NMR spectra for the kinetic progress of ROMP with [M-A_2]:[G-III] = 400:1

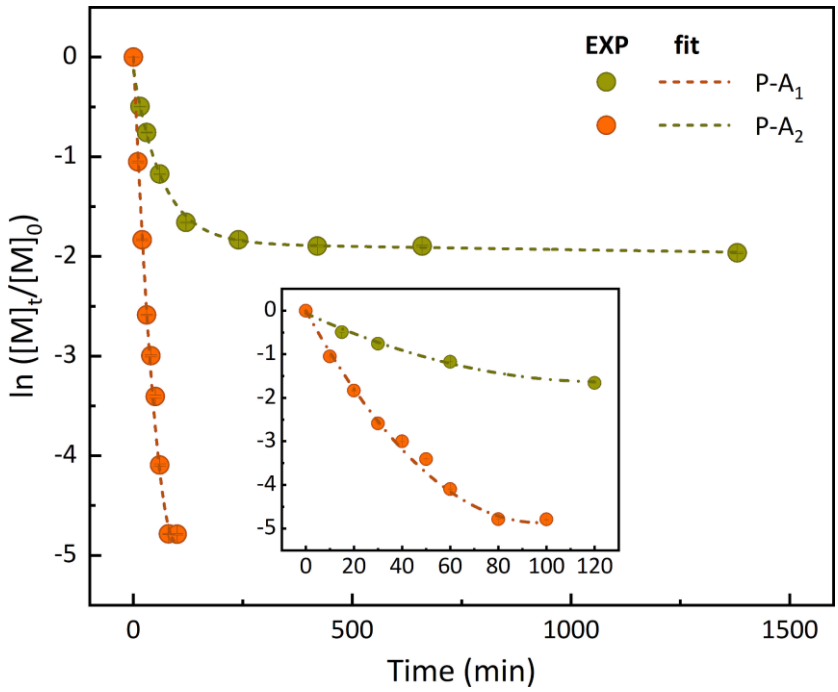

Figure S4.3 Plot of ln ($[M]_t/[M]o$) against time obtained from ^{1}H NMR spectra for **P-A$_1$** and **P-A$_2$**

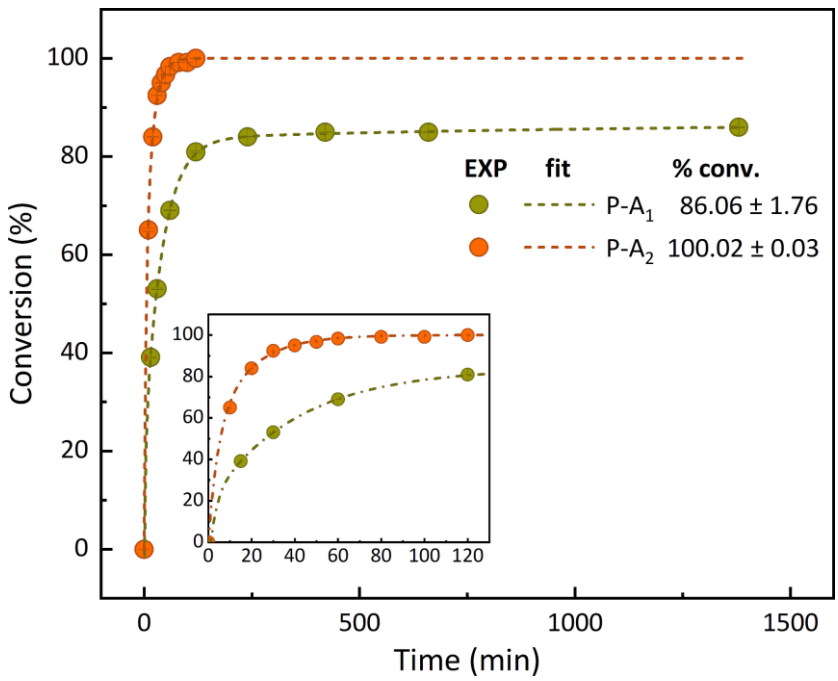

Figure S4.4 Percent conversion of **P-A$_1$** and **P-A$_2$** as a function of time as determined by ^{1}H NMR

4.6.4.2 Structure, Molecular Weight, and Thermal data

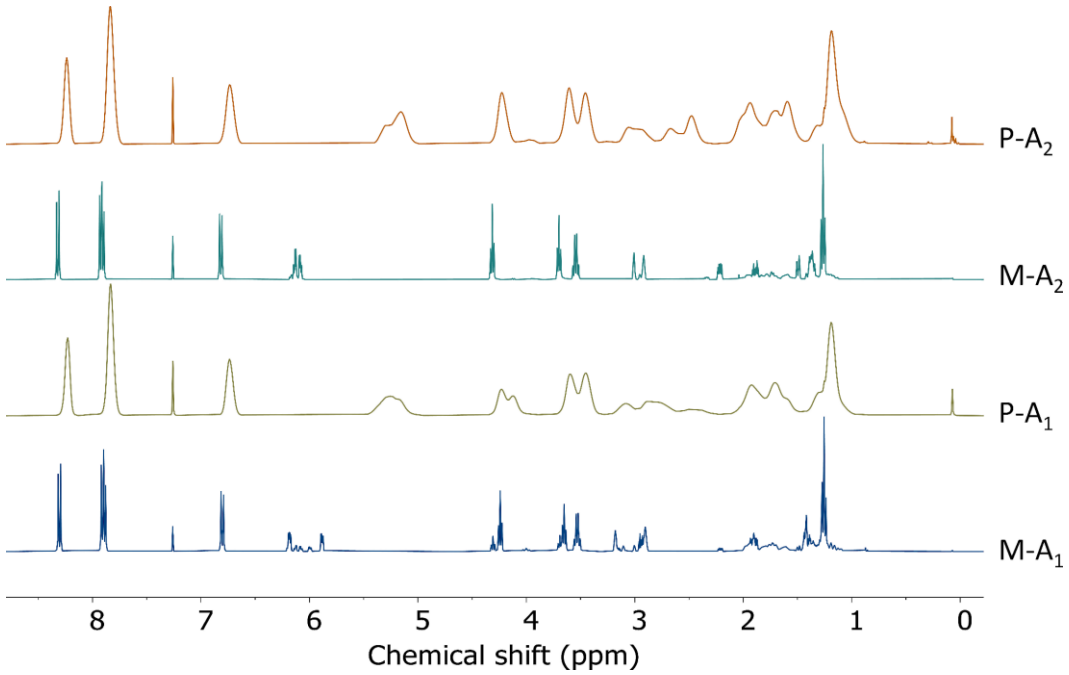

Figure S4.5 ^{1}H NMR spectra in $CDCl_3$ of monomers **M-Ai** and their corresponding polymers **P-Ai**

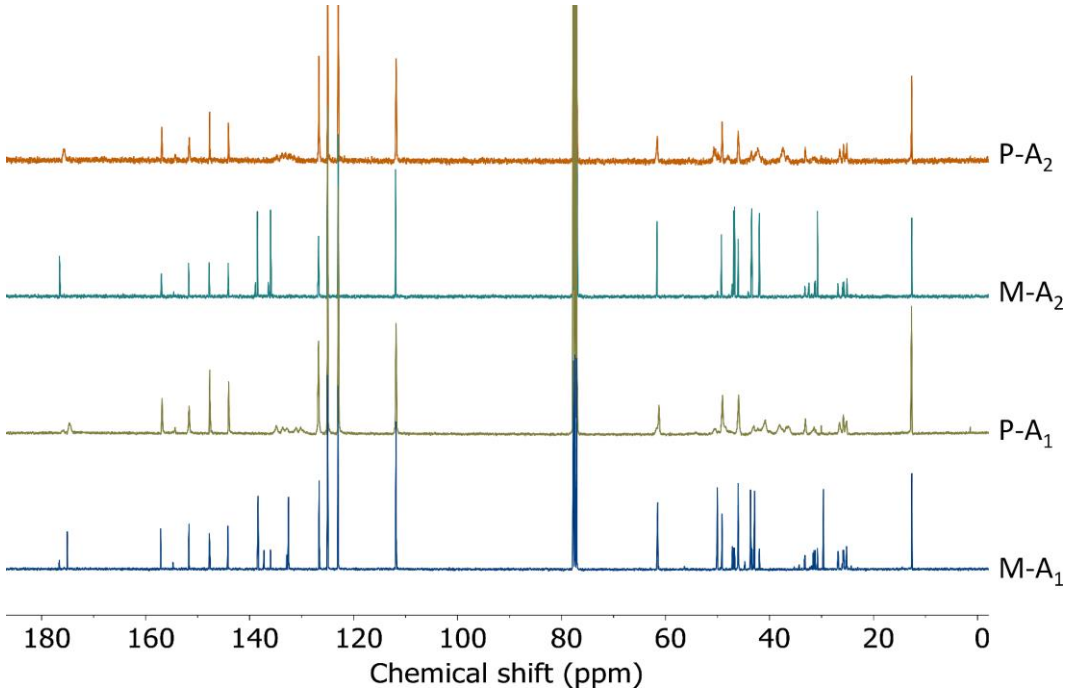

Figure S4.6 ^{13}C NMR spectra in $CDCl_3$ of monomers **M-Ai** and their corresponding polymers **P-Ai**

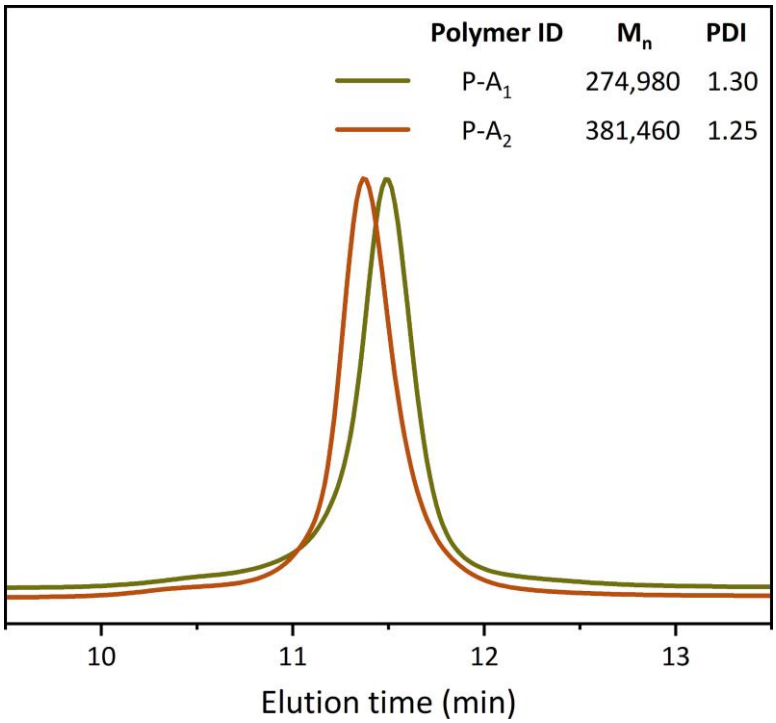

Figure S4.7 Normalized refractive index GPC traces of **P-A$_1$** and **P-A$_2$** in THF

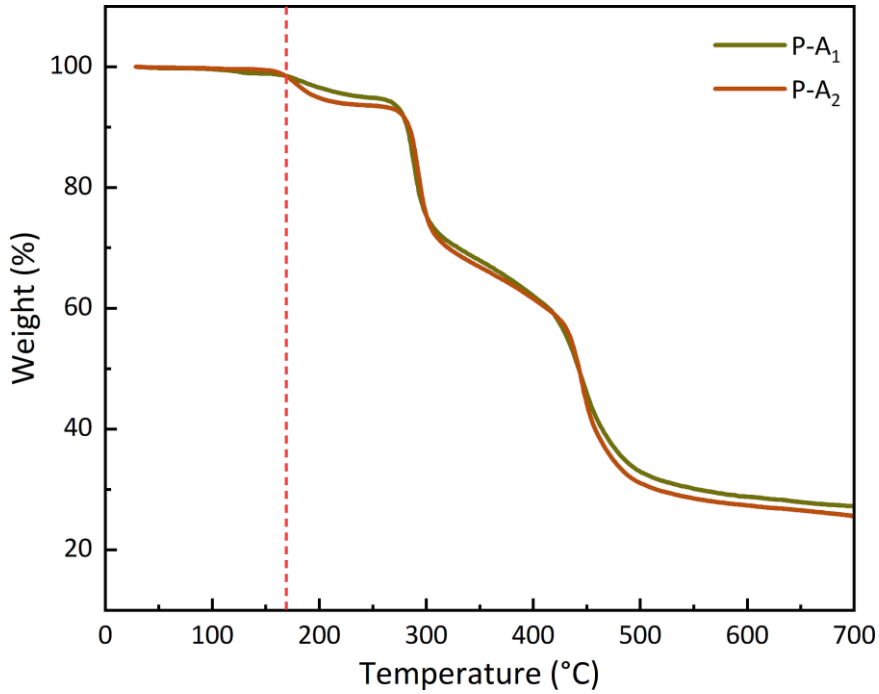

Figure S4.8 TGA thermograms of **P-A$_1$** and **P-A$_2$**. Both polymers showed stability up to 168 °C before yielding to thermal decomposition.

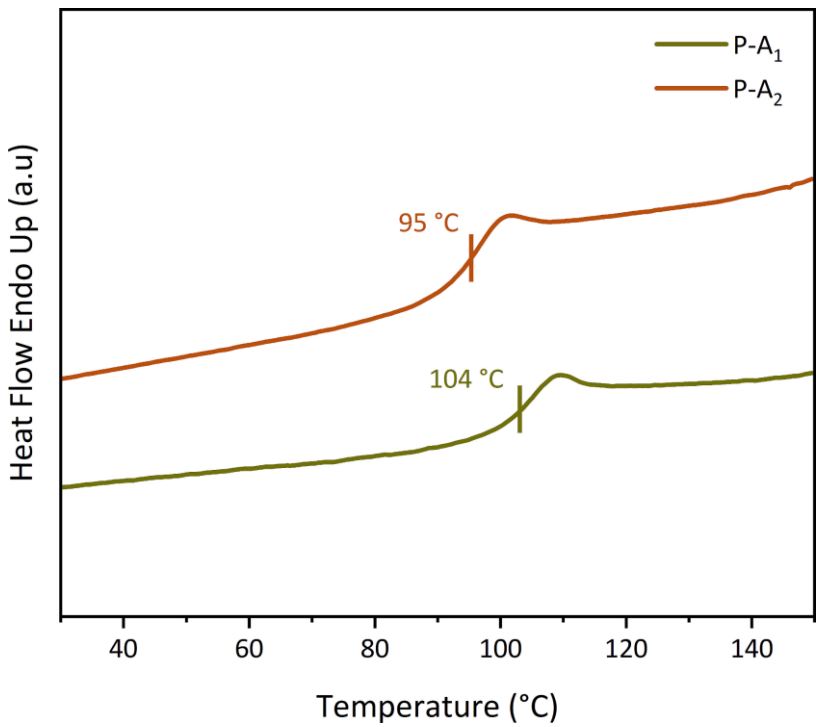

Figure S4.9 DSC curves of **P-A$_1$** and **P-A$_2$**

4.6.4.3 Composite Morphology evaluation

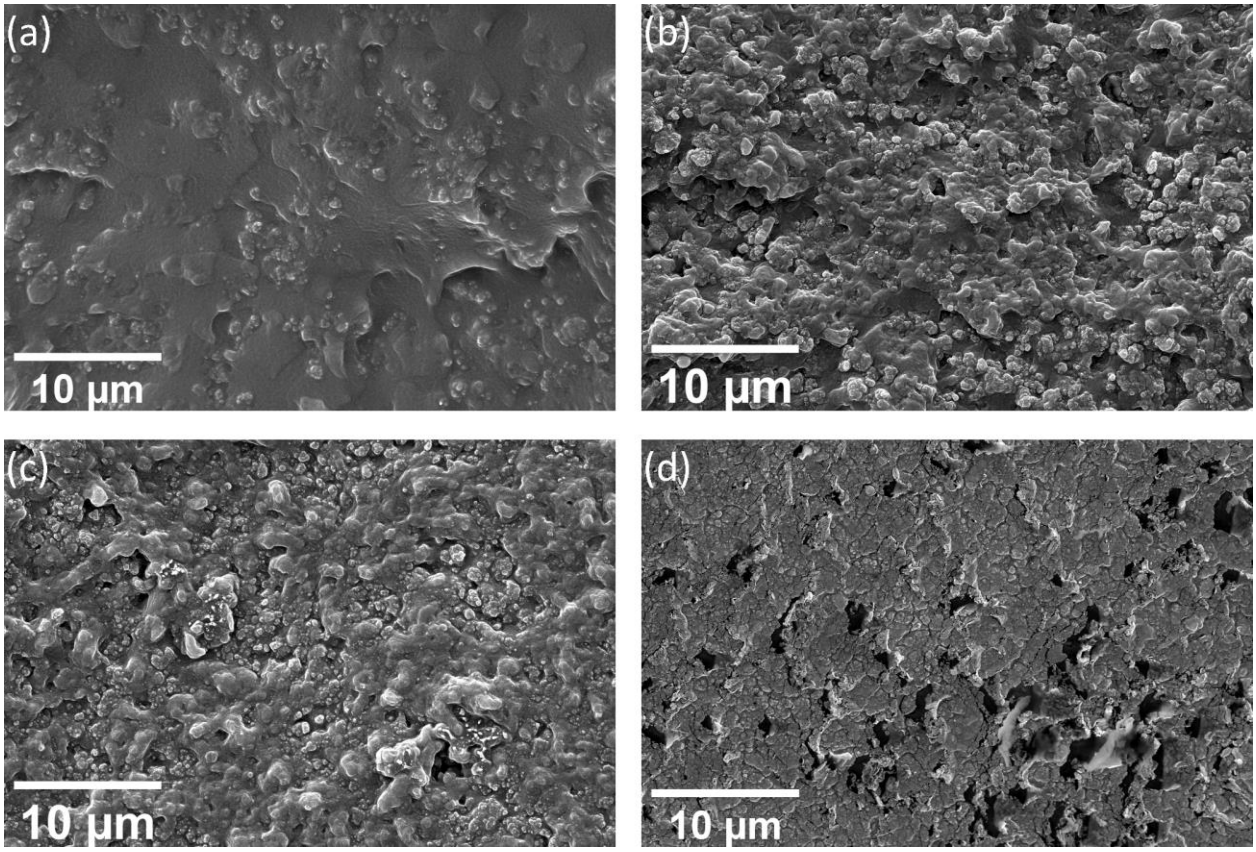

Figure S4.10 SEM image of the microstructure of composites prepared with **P-A$_{1\text{-}S}$** filler in PDMS matrix with increasing filler content: (a) **P-A$_{1\text{-}S}$-10**; (b) **P-A$_{1\text{-}S}$-20**; (c) **P-A$_{1\text{-}S}$-30** and (d) **P-A$_{1\text{-}S}$-40**

4.6.4.4 Dielectric Spectra and TSDC Thermograms

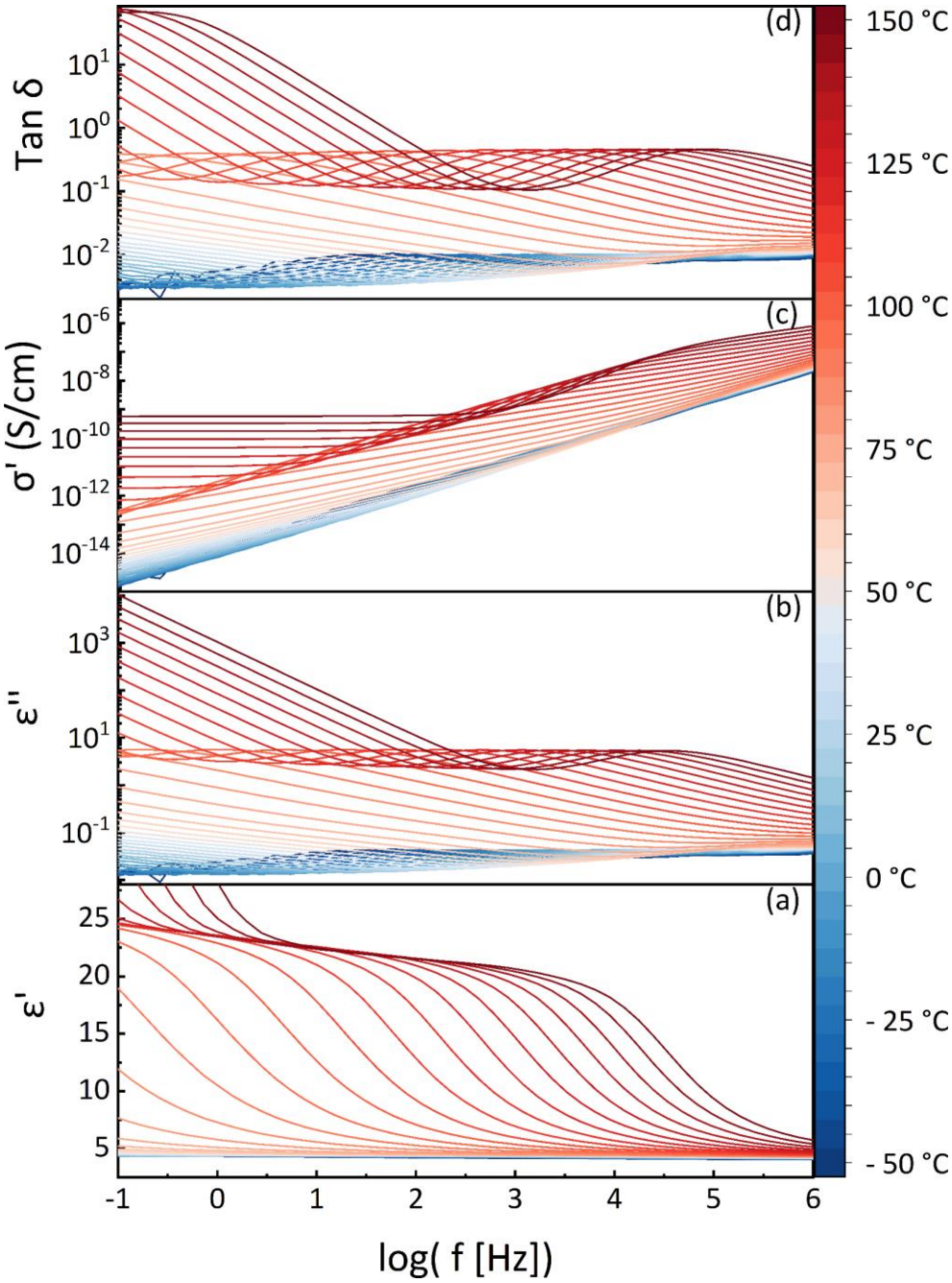

Figure S4.11 Isothermal dielectric response of **P-A₁** as a function of frequency: (a) real permittivity ε′; (b) dielectric loss ε″; (c) real conductivity σ′ and (d) loss tan δ.

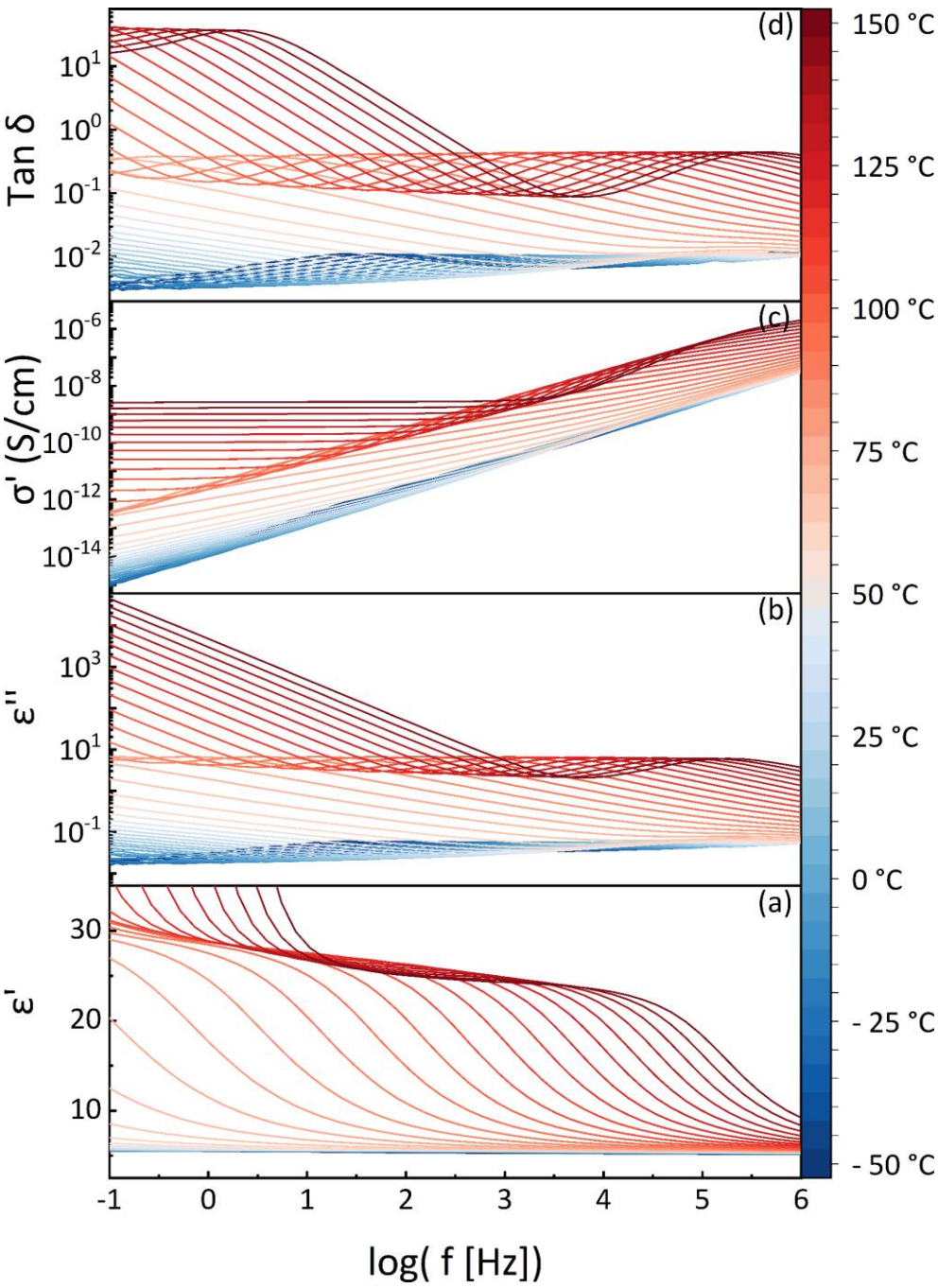

Figure S4.12 Isothermal dielectric response of **P-A$_2$** as a function of frequency: (a) real permittivity ε′; (b) dielectric loss ε′″; (c) real conductivity σ′ and (d) loss tan δ.

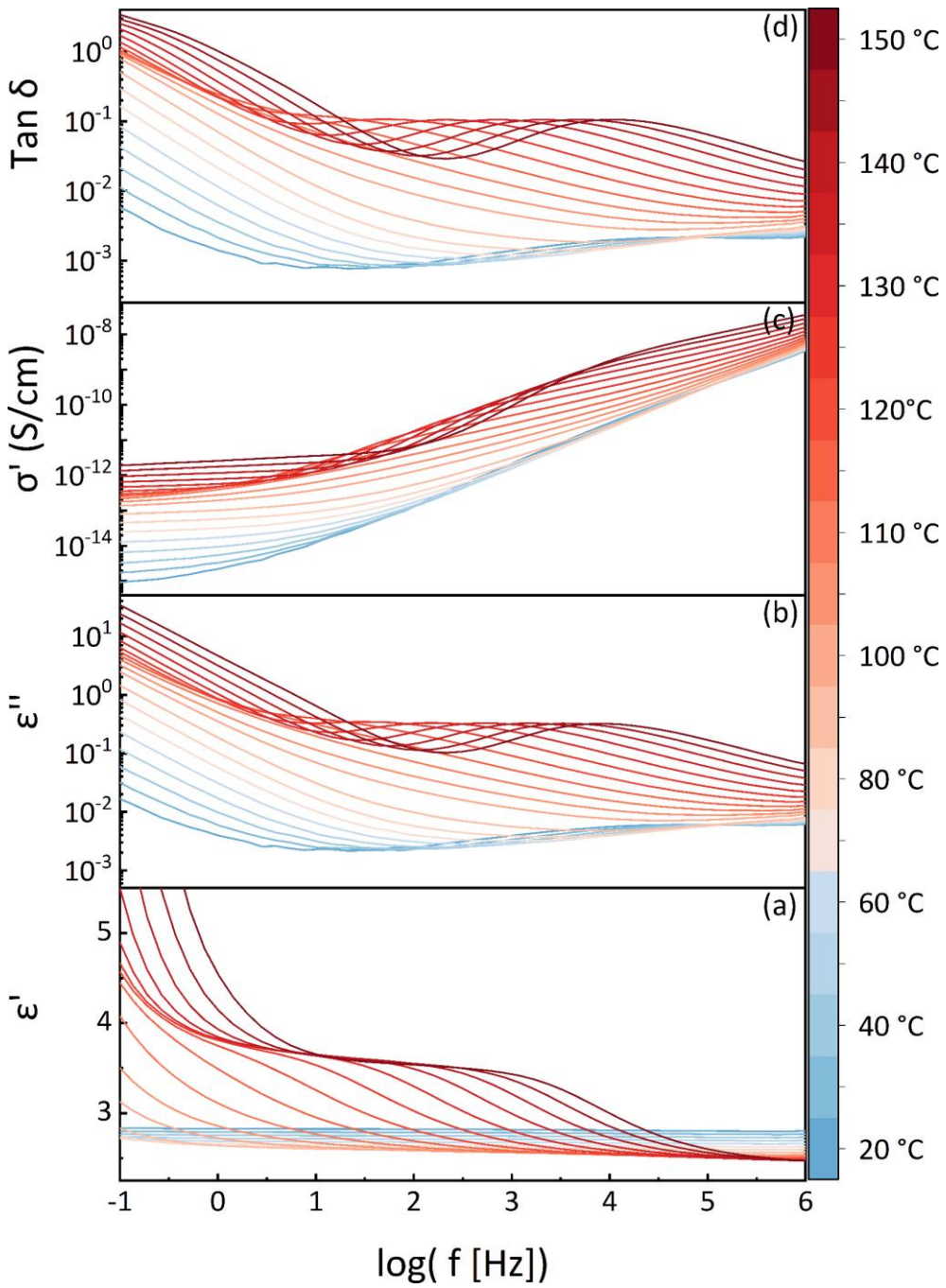

Figure S4.13 Isothermal dielectric response of **P-A$_{1\text{-}S}$ -30** as a function of frequency: (a) real permittivity ε; (b) dielectric loss ε′′; (c) real conductivity σ′ and (d) loss tan δ.

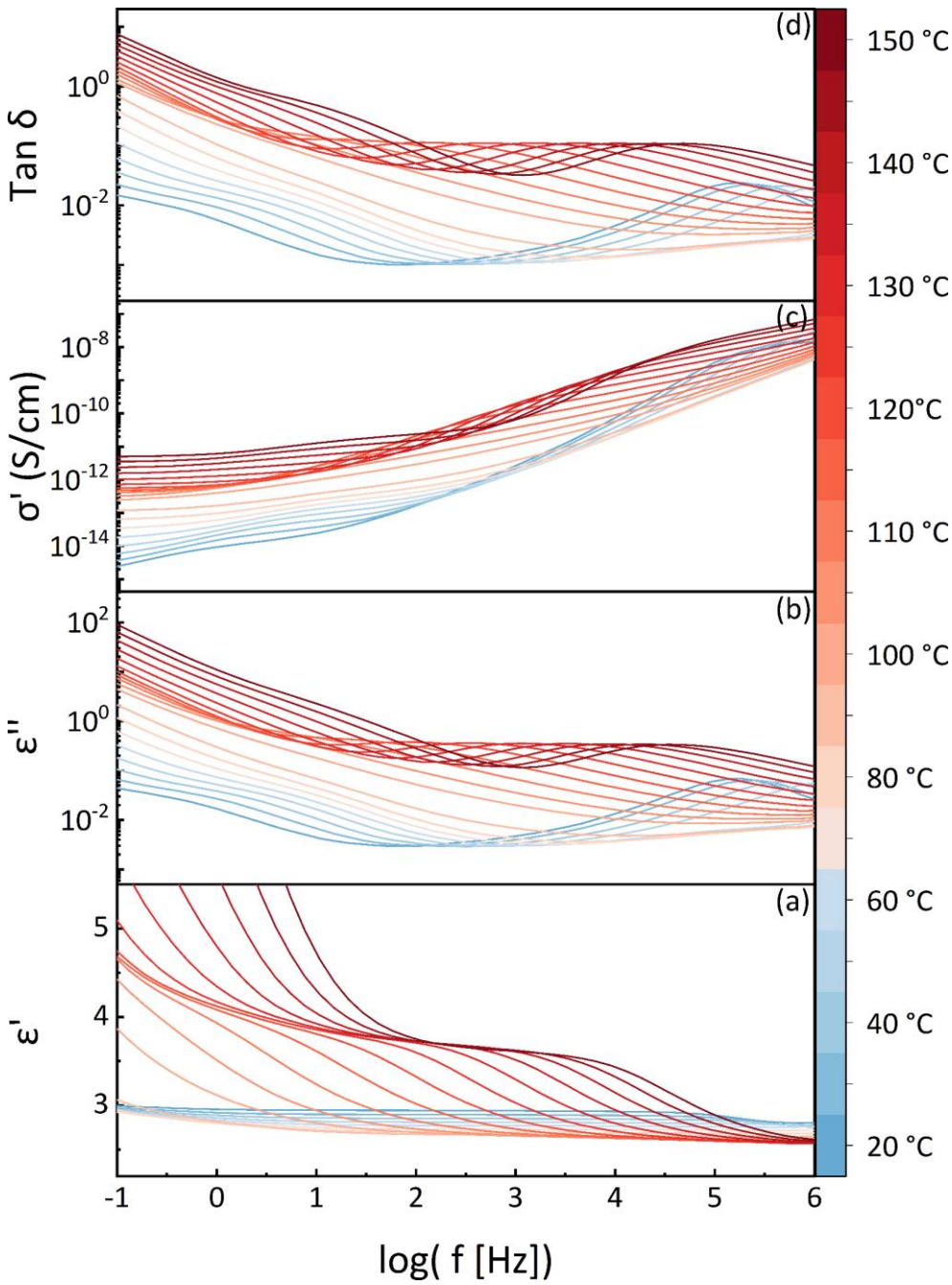

Figure S4.14 Isothermal dielectric response of **P-A$_{2\text{-}S}$ -30** as a function of frequency: (a) real permittivity ε′; (b) dielectric loss ε″; (c) real conductivity σ′ and (d) loss tan δ.

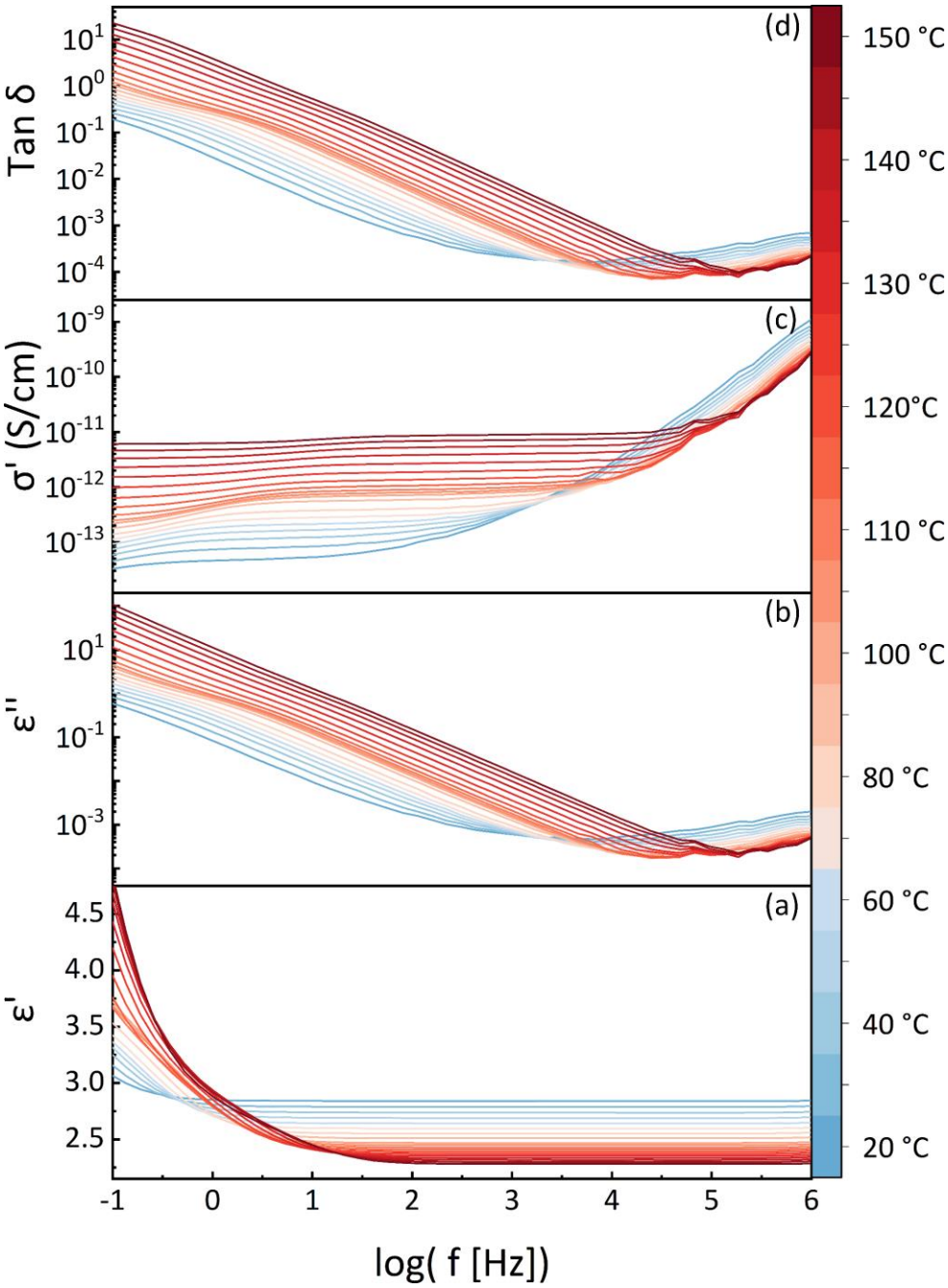

Figure S4.15 Isothermal dielectric response of PDMS matrix as a function of frequency: (a) real permittivity ε′; (b) dielectric loss ε″; (c) real conductivity σ′ and (d) loss tan δ.

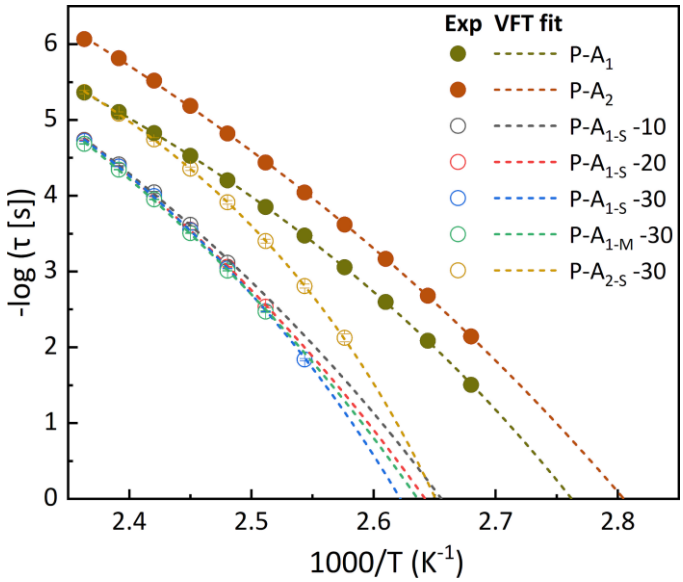

Figure S4.16 Effect of matrix on the dynamics of α-relaxation processes for polymers **P-A$_1$** and **P-A$_2$** with varying content in composites with PDMS. Vogel-Fulcher-Tammann (VFT) plot of corresponding relaxation times obtained from Havriliak-Negami (HN)-fit versus the inverse of temperature. Scattered dots represent the experimental data and the fit functions are represented by short-dashed lines

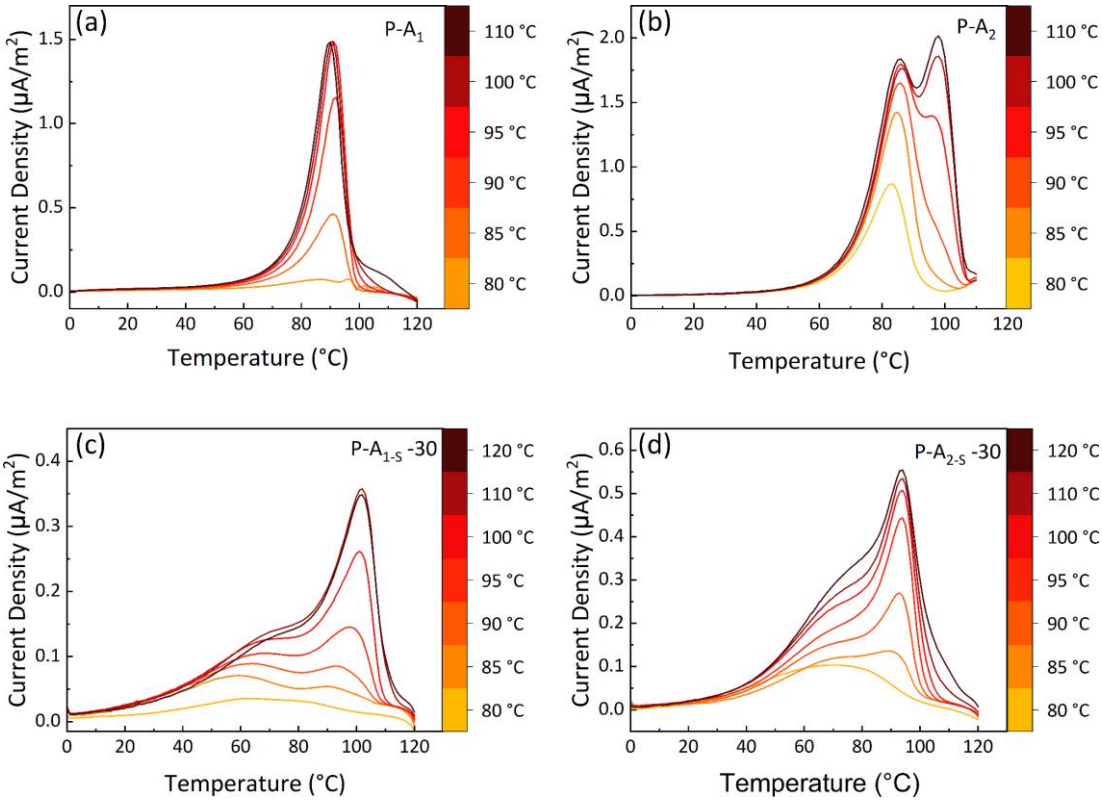

Figure S4.17 TSDC thermograms of (a) **P-A$_1$**; (b) **P-A$_2$**; (c) **P-A$_{1\text{-}S}$-30** and (d) **P-A$_{2\text{-}S}$-30**

4.6.4.5 Mechanical Property Data

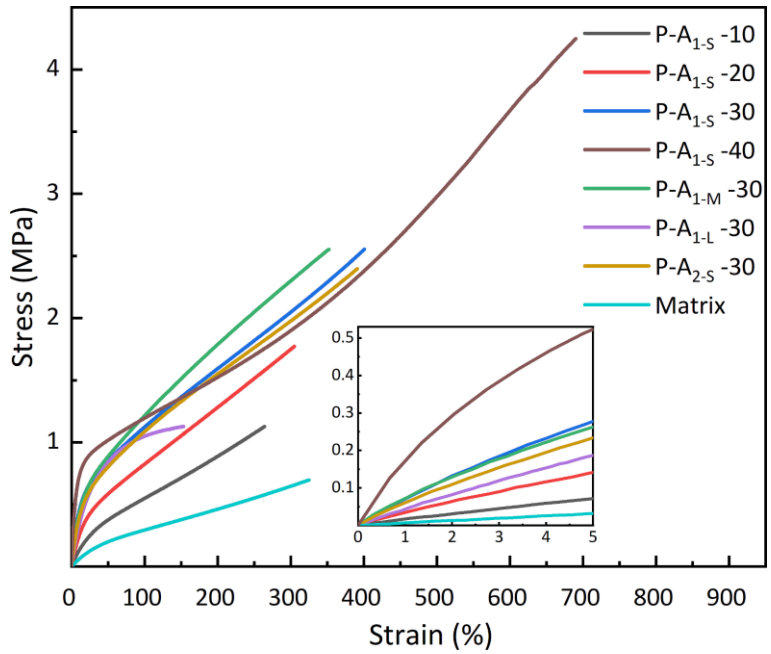

Figure S4.18 Uniaxial tensile curves of all the prepared composites and PDMS matrix. The average results of three independent measurements are as displayed.

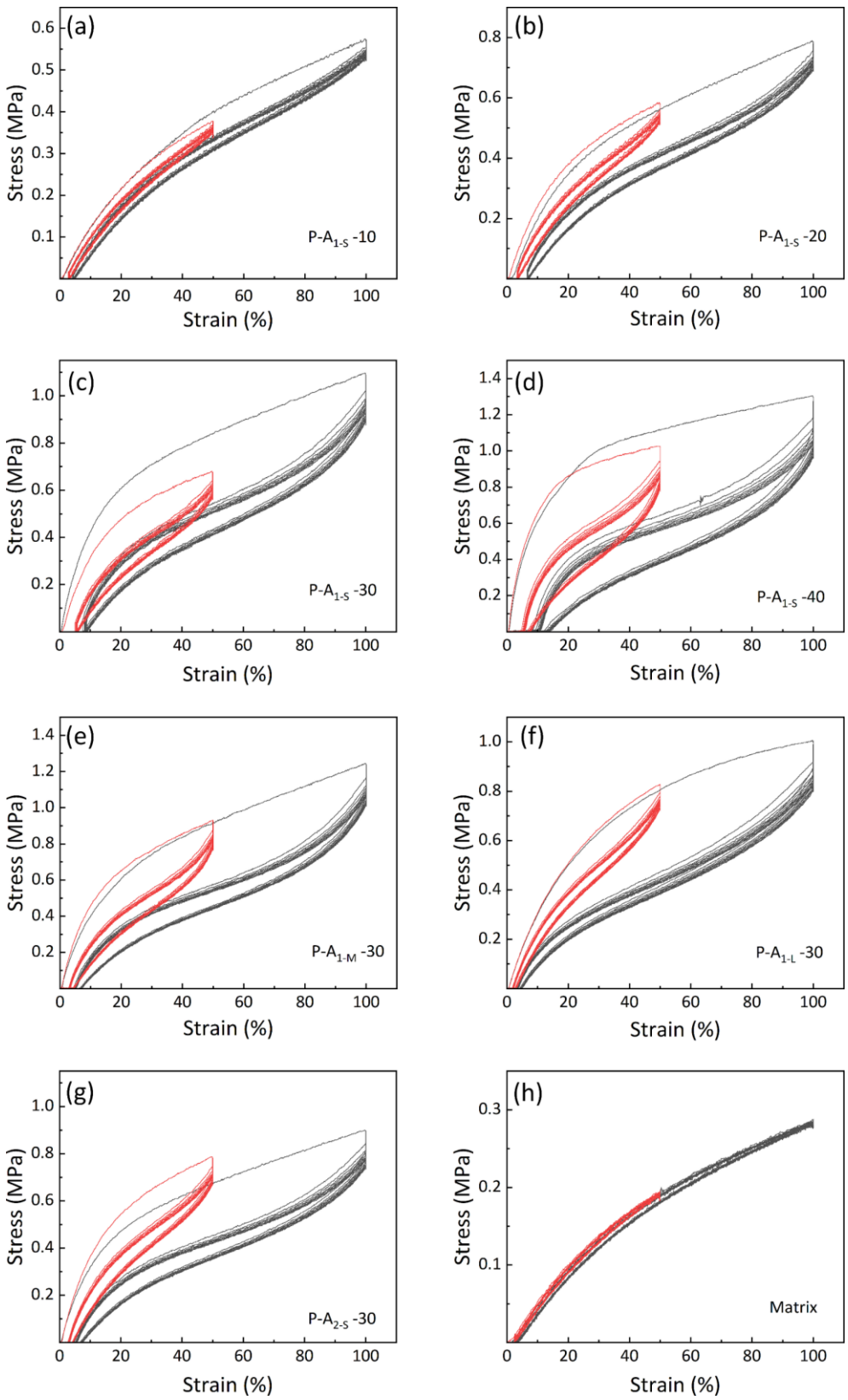

Figure S4.19 Representative uniaxial cyclic mechanical deformation of: (a) **P-A$_{1\text{-}S}$ -10**; (b) **P-A$_{1\text{-}S}$ -20**; (c) **P-A$_{1\text{-}S}$ -30**; (d) **P-A$_{1\text{-}S}$ -40**; (e) **P-A$_{1\text{-}M}$ -30**; (f) **P-A$_{1\text{-}L}$ -30**; (g) **P-A$_{2\text{-}S}$ -30**; (h) PDMS matrix

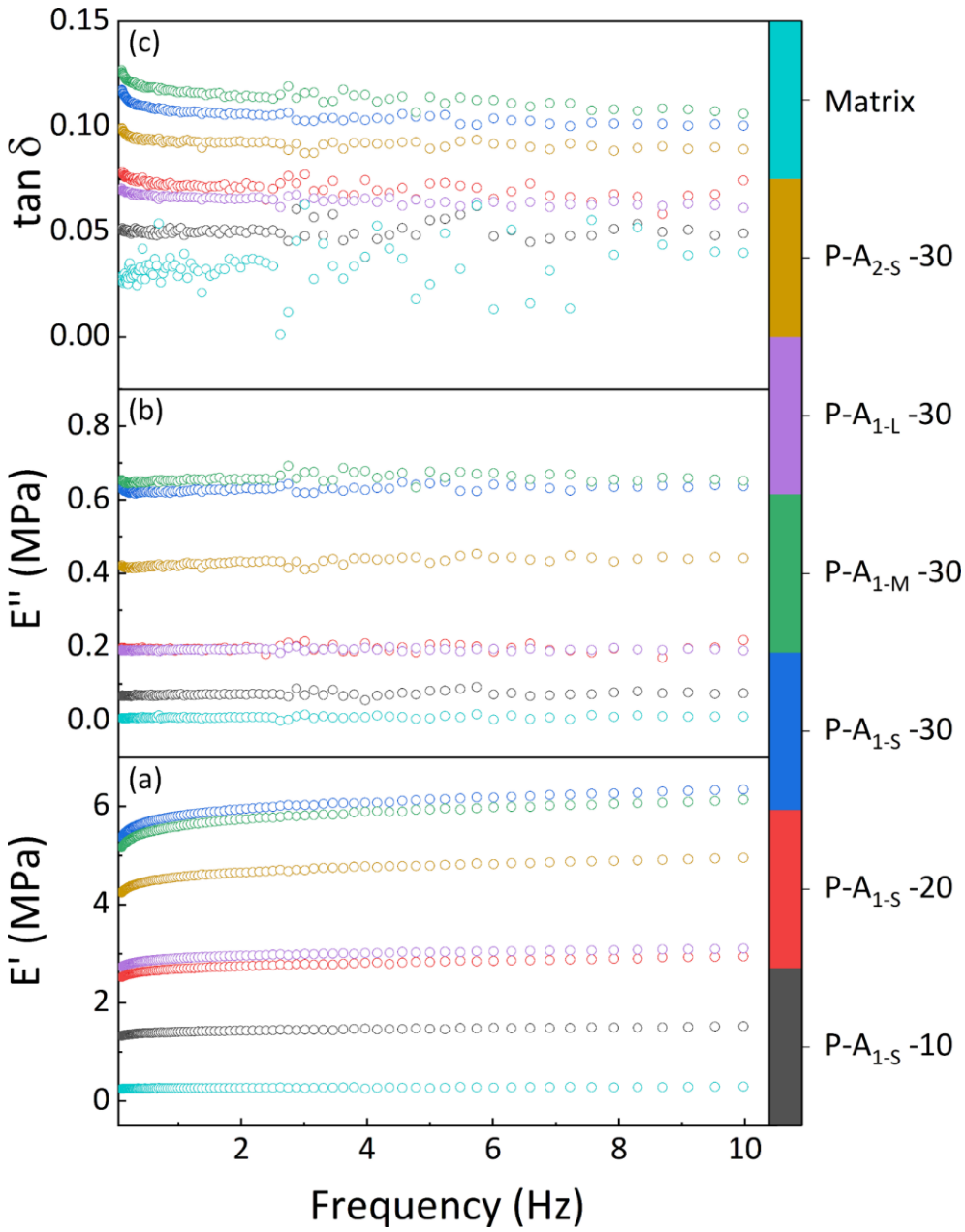

Figure S4.20 Frequency dependent DMA results obtained for composite materials and PDMS matrix: (a) storage modulus, E′; (b) loss modulus, E″; and (c) damping factor, tan δ.

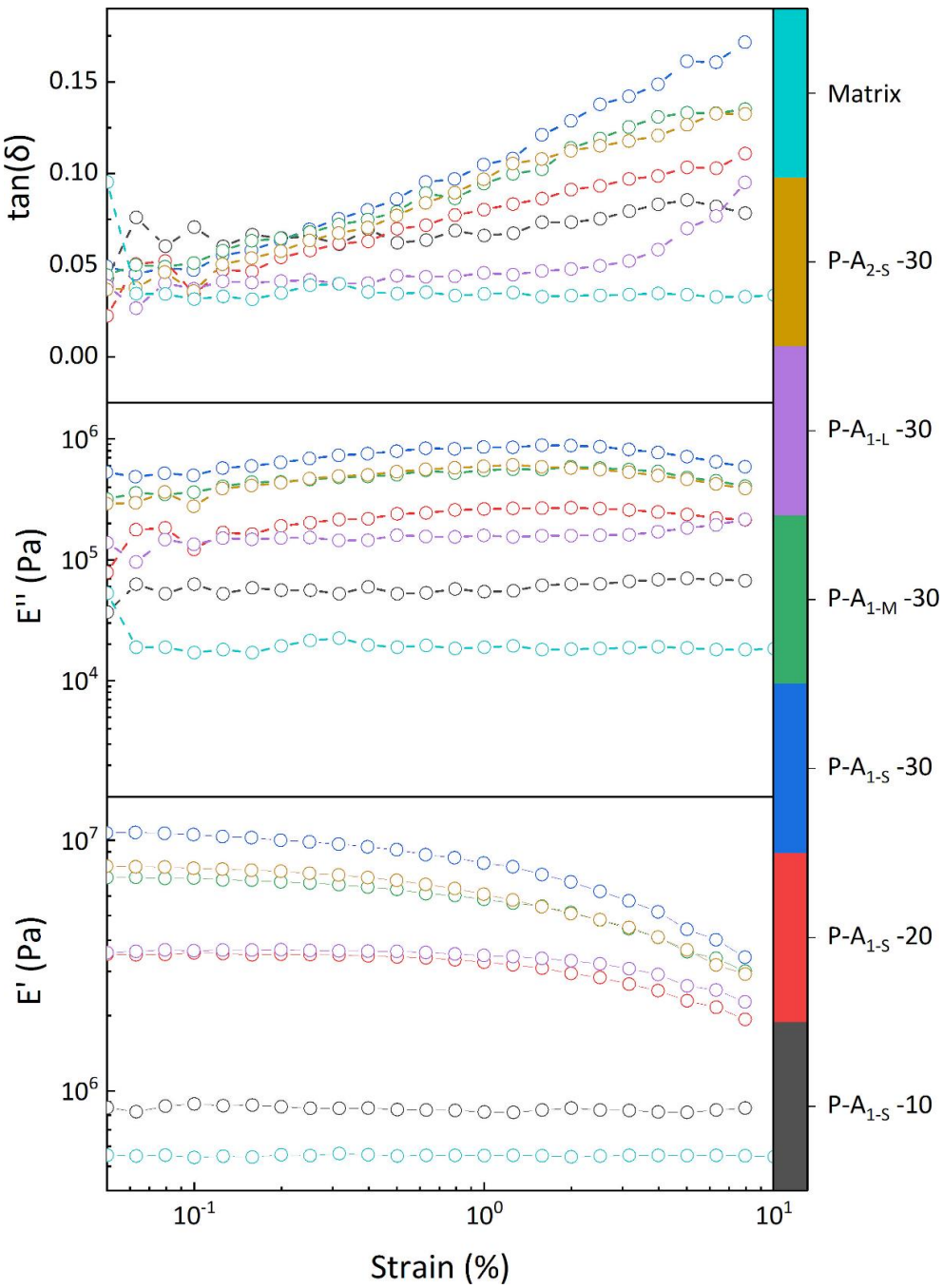

Figure S4.21 Strain dependent DMA results obtained for composite materials and PDMS matrix: (a) storage modulus, E′; (b) loss modulus, E″; and (c) damping factor, tan δ.

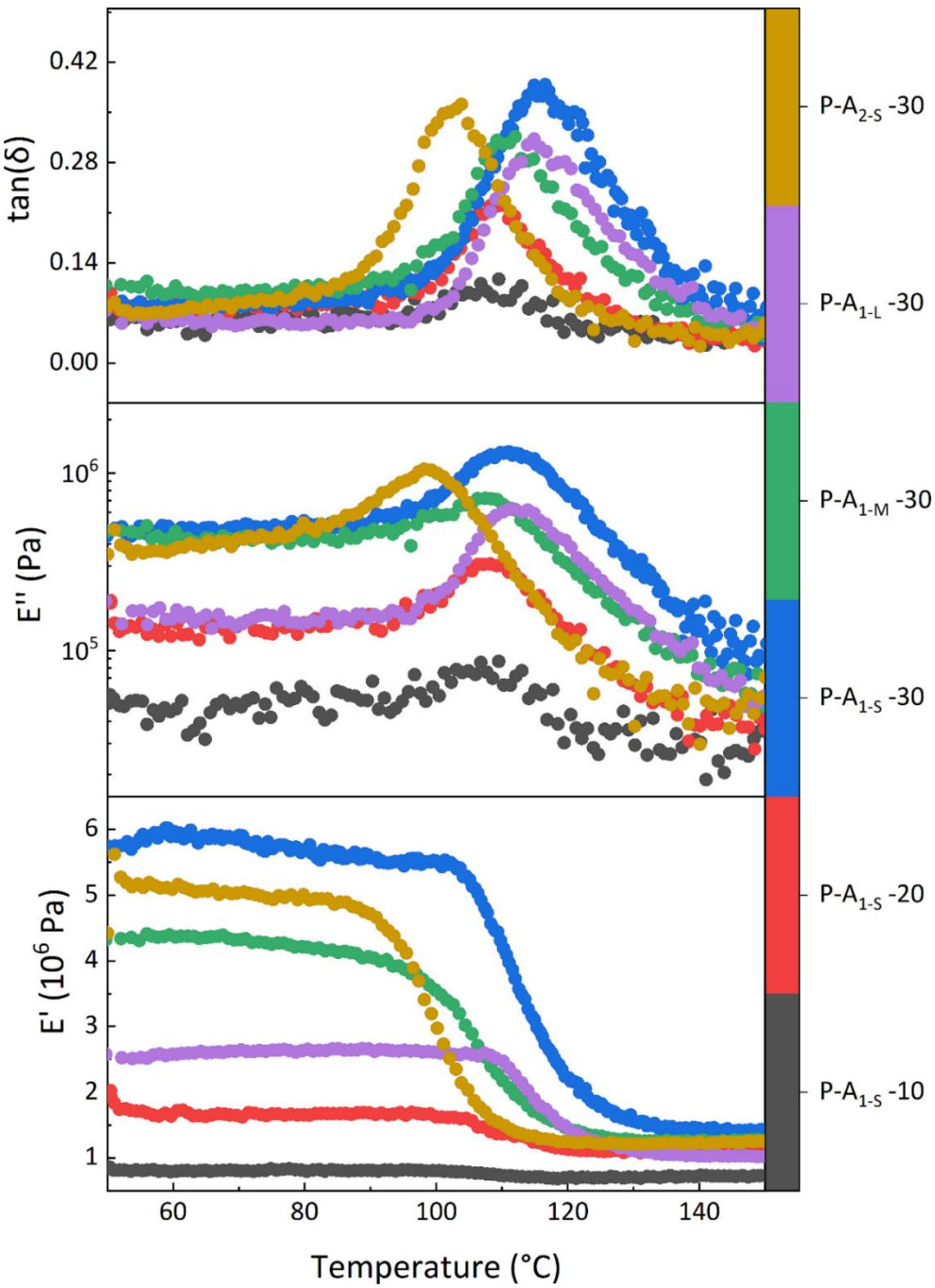

Figure S 4.22 Temperature dependent DMA for different materials were conducted by applying 0.5% strain at a frequency of 0.1 Hz: (a) storage modulus, E′; (b) loss modulus, E″; and (c) damping factor, tan δ.

4.6.4.6 Piezoelectric Coefficient (d_{31}) Data

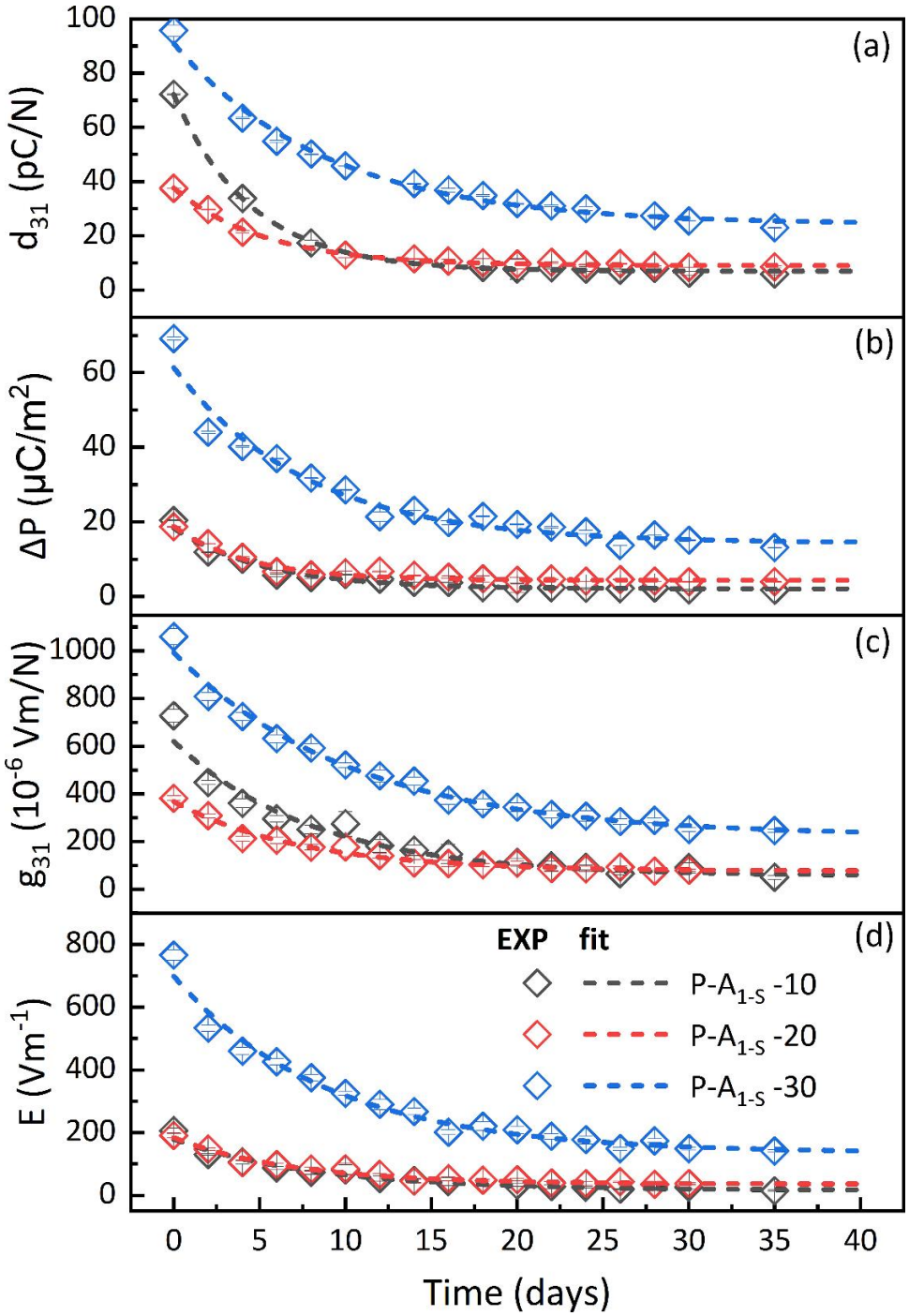

Figure S4.23 Non-exponential decay of charges collected at 50% strain deformation cycles over time for composites with increasing filler content and small particle size: (a) calculated transverse piezoelectric charge coefficient, d_{31}; (b) stress-induced polarization, ΔP; (c) estimated transverse piezoelectric voltage coefficient, g_{31} and (d) stress-induced electric field, E

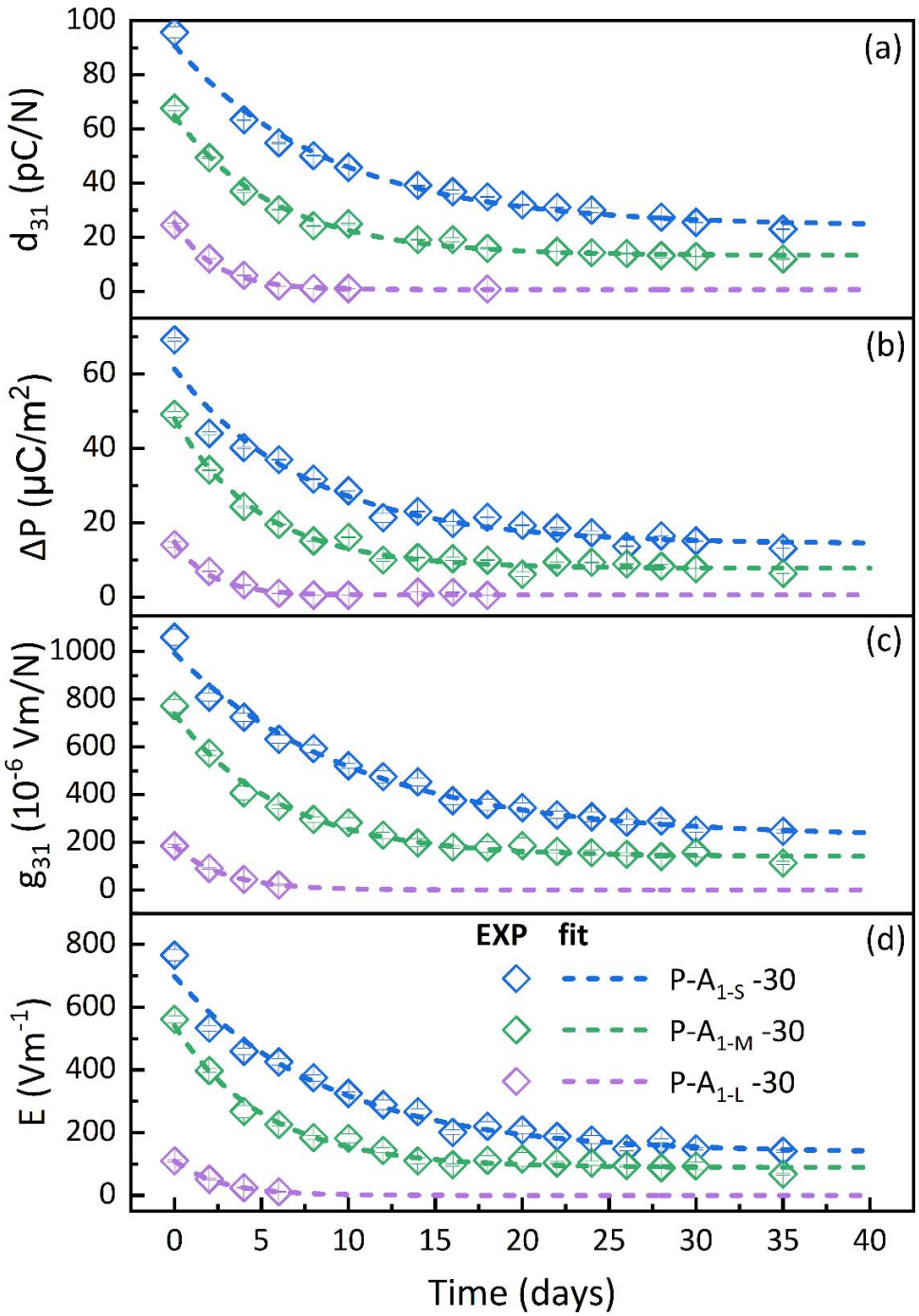

Figure S4.24 Non-exponential decay of charges collected at 50% strain deformation cycles over time for 30 wt% composites containing **P-A$_1$** with changing filler particle size: (a) calculated transverse piezoelectric charge coefficient, d_{31}; (b) stress-induced polarization, ΔP; (c) estimated transverse piezoelectric voltage coefficient, g_{31} and (d) stress-induced electric field, E

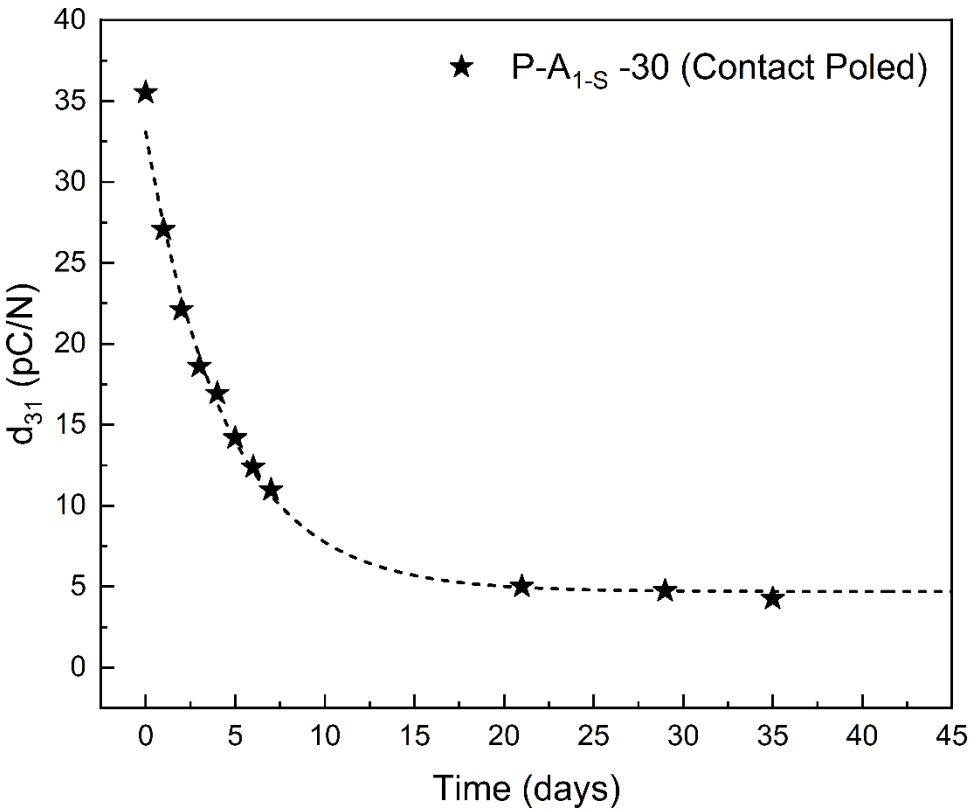

Figure S4.25 Electrode contact poled specimen of **P-A$_{1\text{-}S}$-30**; Non-exponential decay of calculated transverse piezoelectric charge coefficient, d_{31} at 50% strain deformation cycles over time.

4.7 References

[1] H. Yuan, T. Lei, Y. Qin, R. Yang, *Nano Energy* **2019**, *59*, 84.

[2] T. Mori, S. Priya, *MRS Bull.* **2018**, *43*, 176.

[3] V. L. Stuber, D. B. Deutz, J. Bennett, D. Cannel, D. M. de Leeuw, S. van der Zwaag, P. Groen, *Energy Technol.* **2019**, *7*, 177.

[4] S. Lee, Q. Shi, C. Lee, *APL Mater.* **2019**, *7*, 031302.

[5] C. Falconi, *Nano Energy* **2019**, *59*, 730.

[6] V. Jella, S. Ippili, J.-H. Eom, S. V. N. Pammi, J.-S. Jung, V.-D. Tran, V. H. Nguyen, A. Kirakosyan, S. Yun, D. Kim, M. R. Sihn, J. Choi, Y.-J. Kim, H.-J. Kim, S.-G. Yoon, *Nano Energy* **2019**, *57*, 74.

[7] Y. Liu, H. Wang, W. Zhao, M. Zhang, H. Qin, Y. Xie, *Sensors* **2018**, *18*, 645.

[8] S. Mishra, L. Unnikrishnan, S. K. Nayak, S. Mohanty, *Macromol. Mater. Eng.* **2019**, *304*, 1800463.

[9] M. Smith, S. Kar-Narayan, *Int. Mater. Rev.* **2022**, *67*, 65.

[10] N. Castro, N. Pereira, V. F. Cardoso, C. Ribeiro, S. Lanceros-Mendez, in *Frontiers of Nanoscience*, Vol. 14 (Eds: M. Benelmekki, A. Erbe), Elsevier **2019**, p. 35.

[11] Z. Ounaies, J. A. Young, J. S. Harrison, in *Field Responsive Polymers*, Vol. 726, American Chemical Society **1999**, Ch. 6, p. 88.

[12] J. S. Harrison, Z. Ounaies, in *Encyclopedia of Polymer Science and Technology*, DOI: 10.1002/0471440264.pst427 **2002**.

[13] C. Park, Z. Ounaies, K. E. Wise, J. S. Harrison, *Polymer* **2004**, *45*, 5417.

[14] Y. Takase, J. W. Lee, J. I. Scheinbeim, B. A. Newman, *Macromolecules* **1991**, *24*, 6644.

[15] S. Miyata, M. Yoshikawa, S. Tasaka, M. Ko, *Polym. J.* **1980**, *12*, 857.

[16] A. H. Rahmati, S. Yang, S. Bauer, P. Sharma, *Soft Matter* **2019**, *15*, 127.

[17] R. Gerhard, in *Electromechanically Active Polymers: A Concise Reference*, DOI: 10.1007/978-3-319-31530-0_21 (Ed: F. Carpi), Springer International Publishing, Cham **2016**, p. 489.

[18] Y. S. Ko, F. A. Nüesch, D. Damjanovic, D. M. Opris, *Adv. Mater.* **2017**, 29, 1603813.

[19] Y. S. Ko, F. A. Nüesch, D. M. Opris, *J. Mater. Chem. C* **2017**, *5*, 1826.

[20] K. Kapat, Q. T. H. Shubhra, M. Zhou, S. Leeuwenburgh, *Adv. Funct. Mater.* **2020**, *30*, 1909045.

[21] R. Ding, H. Liu, X. Zhang, J. Xiao, R. Kishor, H. Sun, B. Zhu, G. Chen, F. Gao, X. Feng, J. Chen, X. Chen, X. Sun, Y. Zheng, *Adv. Funct. Mater.* **2016**, *26*, 7708.

[22] X. Qiu, L. Holländer, W. Wirges, R. Gerhard, H. C. Basso, *J. Appl. Phys.***2013**, *113*, 224106.

[23] S. Bauer, R. Gerhard-Multhaupt, G. M. Sessler, *Phys. Today* **2004**, *57*, 37.

[24] S. R. Anton, K. Farinholt, A. Erturk, *J. Intell. Mater. Syst. Struct.* **2014**, *25*, 1681

[25] S. Gong, C. Wang, J. Zhang, C. Zhang, J. E. West, K. Ren, *Adv. Sustainable Syst.* **2018**, *2*, 1700178.

[26] A. Kachroudi, S. Basrour, L. Rufer, A. Sylvestre, F. Jomni, *Smart Mater. Struct.* **2016**, *25*, 105027.

[27] R. A. P. Altafim, X. Qiu, W. Wirges, R. Gerhard, R. A. C. Altafim, H. C. Basso, W. Jenninger, J. Wagner, *J. Appl. Phys.* **2009**, *106*, 014106.

[28] R. Gerhard, *Proc. SPIE* **2016**, *9798*, 97980T-1.

[29] M. Wegener, W. Wirges, J. Fohlmeister, B. Tiersch, R. Gerhard, *J. Phys. D: Appl. Phys.* **2004**, *37*, 623.

[30] M. Nakayama, Y. Uenaka, S. Kataoka, Y. Oda, K. Yamamoto, Y. Tajitsu, *Jpn. J. Appl. Phys.* **2009**, *48*, 09KE05.

[31] S. Zhukov, S. Fedosov, H. von Seggern, *J. Phys. D: Appl. Phys.* **2011**, *44*, 105501.

[32] P. Fang, F. Wang, W. Wirges, R. Gerhard, H. C. Basso, *Appl. Phys. A* **2011**, *103*, 455.

[33] Y. Li, C. Zeng, *Macromol. Chem. Phys.* **2013**, *214*, 2733.

[34] N. Behrendt, *IEEE Trans. Dielectr. Electr. Insul.* **2010**, *17*, 1113.

[35] W. Wirges, M. Wegener, O. Voronina, L. Zirkel, R. Gerhard, *Adv. Funct. Mater.* **2007**, *17*, 324.

[36] W. Li, D. Torres, T. Wang, C. Wang, N. Sepúlveda, *Nano Energy* **2016**, *30*, 649.

[37] N. Wu, X. Cheng, Q. Zhong, J. Zhong, W. Li, B. Wang, B. Hu, J. Zhou, *Adv. Funct. Mater.* **2015**, *25*, 4788.

[38] K. Kirjavainen, *US Patent 4 654 546*, **1987**.

[39] Y. Zhang, C. R. Bowen, S. K. Ghosh, D. Mandal, H. Khanbareh, M. Arafa, C. Wan, *Nano Energy* **2019**, *57*, 118.

[40] C.-C. Hung, S. Nakahira, Y.-C. Chiu, T. Isono, H.-C. Wu, K. Watanabe, Y.-C. Chiang, S. Takashima, R. Borsali, S.-H. Tung, T. Satoh, W.-C. Chen, *Macromolecules* **2018**, *51*, 4966.

[41] S. Zhang, Y. Wang, X. Yao, P. Le Floch, X. Yang, J. Liu, Z. Suo, *Nano Letters* **2020**, *20*, 4580.

[42] J. E. Q. Quinsaat, T. de Wild, F. A. Nüesch, D. Damjanovic, R. Krämer, G. Schürch, D. Häfliger, F. Clemens, T. Sebastian, M. Dascalu, D. M. Opris, *Composites Part B: Engineering* **2020**, *198*, 108211.

[43] F. Owusu, M. Tress, F. A. Nüesch, S. Lehner, D. M. Opris, *Mater. Adv.* **2022**, *3*, 998.

[44] S. Stainmesse, A. M. Orecchioni, E. Nakache, F. Puisieux, H. Fessi, *Colloid Pol. Sci.* **1995**, *273*, 505.

[45] I. Y. Perevyazko, J. T. Delaney, A. Vollrath, G. M. Pavlov, S. Schubert, U. S. Schubert, *Soft Matter* **2011**, *7*, 5030.

[46] K. Song, in *Progress in Rubber Nanocomposites*, (Eds: S. Thomas, H. J. Maria), Woodhead Publishing **2017**, p. 115. DOI: https://doi.org/10.1016/B978-0-08-100409-8.00004-8

[47] M. Shamonin, E. Y. Kramarenko, in *Novel Magnetic Nanostructures*, (Eds: N. Domracheva, M. Caporali, E. Rentschler), Elsevier **2018**, p. 221. DOI: https://doi.org/10.1016/B978-0-12-813594-5.00007-2

[48] F. R. Fan, W. Tang, Z. L. Wang, *Adv. Mater.* **2016**, *28*, 4283.

[49] N. Wang, R. Daniels, L. Connelly, M. Sotzing, C. Wu, R. Gerhard, G. A. Sotzing, Y. Cao, *Small* **2021**, *17*, 2103161.

[50] T. Vijayakanth, D. J. Liptrot, E. Gazit, R. Boomishankar, C. R. Bowen, *Adv. Funct. Mater.* **2022**, *32*, 2109492.

[51] V. Jarkov, S. J. Allan, C. Bowen, H. Khanbareh, *Int. Mater. Rev.* **2021**, 1-51.

[52] M. G. Broadhurst, G. T. Davis, *Ferroelectrics* **1984**, 60, 3.

[53] E. Fukada, *Annals of the New York Academy of Sciences* **1974**, 238, 7.

CHAPTER 5
Conclusions and Outlook

The purpose of this thesis was to further investigate an established concept in the design of piezoelectric elastomers using an all-organic compositing approach. To achieve this, polar polymers in which the dipolar moieties could be electrically oriented via thermal assistance were synthesized and processed into particles with sub-micrometer sizes. The polymer particles are subsequently used as reinforcements in an elastomeric matrix and the resulting composite is rendered piezoelectric by poling in a strong electric field. Observably from the first proven concept, there was a reported time-dependent decay in the piezoelectric response of materials prepared by this technique.[1] Therefore, we aimed to thoroughly investigate the underlying mechanisms for the decay in piezoelectric response of such piezoelectric elastomer composites.

In the first phase of this study, we employed ring-opening metathesis polymerization (ROMP) to successfully synthesize novel polar amorphous polymers bearing different dipole moieties as side chains. This was accomplished by carefully selecting a monomer that could be easily functionalized with polar moieties while retaining high enough ring strain to be polymerized after a thorough literature review. A 2-substituted norbornene monomer (5-norbornene-2-carboxylic acid) was chosen as a precursor because it is readily available and easy to synthesize via Diels-Alder cycloaddition reaction.[2-3] Additionally, this monomer can tolerate a wide range of functional groups and still exhibit good reactivity. Polymers obtained from such monomer derivatives also show superior chemical properties, high glass transition temperature (T_g) and high thermal stability. Beforehand, the precursor was then functionalized with different polar groups via conventional esterification to afford six (6) polar norbornene monomers. Structural elucidation was performed on the synthesized monomers using NMR, spectroscopy, LC-MS and elemental analysis. Five (5) out of the six (6) pre-modified monomers were successfully polymerized by ROMP using Grubb's catalyst (1st and 3rd generation). Chemical structures of the corresponding polar polymers were verified by NMR spectroscopy, molecular weights determined by gel permeation chromatography (GPC), and thermal properties evaluated by thermogravimetric analysis (TGA) and differential scanning calorimetry (DSC). Structure-property relations, with respect to dielectric behaviors of the prepared polar polymers, could be established. The polymers, which showed relatively good dielectric relaxation strength ($\Delta\varepsilon$), high T_g enough to sustain macroscopic polarization at room

temperature when electrically poled, and ease of processing into micrometer-sized particles were used as a filler in composite preparation with PDMS.

The chosen polar polymer with promising functionalities was the polynorbornene containing disperse red 1 (N-ethyl-N-(2-hydroxyethyl)-4-(4-nitrophenylazo) aniline) dipole moiety as a pendant group. Therefore, we synthesized norbornene monomers functionalized with disperse red 1 from two different stereoisomeric precursors (*exo*-5-norbornene-2-carboxylic acid, and 5-norbornene-2-carboxylic acid, mixture of *endo* and *exo*, predominantly endo). The monomers were subjected to the same feed-to-catalyst ratio during polymerization and yielded two polar polymers with different regio-irregularity backed by structural, molecular weight and thermal evidence. Monitoring the reaction kinetics of the monomers over time by ^{1}H NMR spectroscopy confirmed the high reactivity of *exo*-isomer over the predominated *endo*-isomer.[4-6] The dielectric properties of these polymers were further characterized by broadband dielectric spectroscopy and thermally stimulated depolarization current experiments. As a necessary requirement, nanoprecipitation technique was deployed to process the two polar polymers into sub-micrometer particles. This method enabled the production of polymer particles without the use of colloidal stabilizing agents. Particle sizes ranging from 90 nm to 2 µm could be prepared depending on the initial concentration of polymer solution, and the ratio between solvent and non-solvent used in creating the ternary polymer/solvent/non-solvent system.

The polar polymer particles were dispersed in PDMS via solution processing and the resulting elastic hybrid materials were electrically poled to induce piezoelectric activity. As previously mentioned, we intentionally selected polymers containing double bonds in their main chains to understand the time-dependent decay process in piezoelectric response. The rationale is to introduce enough rigidity in the structure of the polar polymer, which was hypothesized to help limit dipolar relaxations possibly caused by a high degree of intramolecular chain rotations. However, the observed piezoelectric properties generally revealed similar time-dependent decay. Hence, the reason for introducing double bonds in the polar polymer main chains to limit depolarization could not be substantiated. This likewise confirms that thermodynamic instability or quasi-stable state is generally an intrinsic behavior exhibited in oriented structures of polar polymers.[7-8] Immense theoretical simulations will be required to understand these molecular dynamics in more detail. Furthermore, we investigated the influences of particle size and interfaces created between polar polymer fillers and PDMS matrix on the piezoelectric response decay. Interestingly, the piezoelectric responses were observed to increase with decreasing particle size of the polar polymer filler particles. The observed behavior is likely due to good dispersion and effective stress transfer in composite systems with smaller filler particles than larger ones. Additionally, large interfacial boundaries present in composites with smaller filler particles possibly serve as charge traps to retain polarization. Another investigation was carried out to understand the possible effect of interfacial relaxation on charge decay, which may be

caused by periodic mechanical strains during operation. One was periodically strained for three weeks and the other left stands after poling. The recorded piezoelectric responses were similar, suggesting that charge decay in the prepared piezoelectric elastomer composite is not significantly influenced by the mechanism of mechanical deformation. Also, the type of poling treatment on polarization and the eventual piezoelectric performance was evaluated. This investigation revealed that samples subjected to corona poling showed higher piezoelectric properties compared to the ones treated by contact poling. Comparatively, the piezoelectric response recorded for the best system in this current work was threefold higher than previously reported in the first proof of concept. The reasons can be due to several factors such as the variation in the dipole densities of the difference active filler polymers used and their polarizability. Again, the filler particles size-dependent properties and the kind of poling treatment employed could cause variation in the induced polarization and hence the piezoelectric effects. The piezoelectric properties exhibited a time-dependent decay, which we evaluated to be mostly caused by the partial dipole randomization within the polar polymer particles than the mechanical deformation induced inter-particle randomization. However, our investigation did not cover contributions from interfacial depolarization, which may be present as a result of ionic impurities. This can also significantly reflect in the initial drastic decay in piezoelectric activity and can be considered for further investigation.

Going forward, the chemistry and molecular dynamics at the filler-matrix interfaces of such piezoelectric composite systems should be further understood in order to close the gap between the established concept and technological implementation.

The piezoelectric performance of the prepared elastic composites showed strong dependence on the amount, particle size, stereo-regular configuration of the polar polymer particles used and the electric poling technique employed. However, a quasi-stable transverse piezoelectric coefficient (d_{31}) of 37 pC N^{-1} could be recorded for the best-performing material poled by corona discharge. In addition, these piezoelectric materials could withstand large mechanical deformations as a peculiar advantage when compared with the favorable piezoelectric polymer and ceramic materials.

A number of advantages can be outlined by using this versatile approach in the development of piezoelectric elastomers. For example, the incredible tunability with respect to relevant material properties can be carefully engineered via suitable synthetic routes. And again, since polymers generally have high dielectric strength, they, for the same reason, hold a high tendency to withstand poling with minimal chance of electrical breakdown. However, some peculiarities exhibited in the performance of the resulting piezoelectric elastomers will require optimization. The first is the realization of elastic materials with comparatively high piezoelectric response. Ceramics materials meet the criterion of high piezoelectric activity but remain challenging to fabricate stretchable devices from them due to their rigid and brittle nature. Polymers and polymer composites are readily processable with a high degree of freedom to be fabricated into stretchable devices but their

piezoelectric response remain weak. It will be ideally strategic to investigate the tradeoff between piezoelectricity and elasticity through careful material domain and interfacial engineering. Another hurdle is the prevailing requirement for compatible electrodes, which will be suitable for conforming to deformations when large strains are applied. Therefore, designing elastic electrodes to follow the mechanical dynamisms whiles retaining excellent conductivity will be important to look into. Also, devising techniques which allow simultaneous poling and crosslinking can improve piezoelectric activity in elastic composites materials. Polarization can be thereby enhanced in the filler particles due to the less restrictions in uncrosslinked state of the elastic matrix. The chemically locked elastic networks of the matrix following curing can additionally contribute to holding the filler particles in the polarized state. Lastly, the possibility to build multiple piezoelectric elastomer stacks using compatible electrodes can provide another excellent avenue to improving piezoelectric activity.

In summary, this study has provided further investigation into piezoelectric elastomers prepared by an all-organic composite processing technique. The already established concept for designing such smart materials extends the possibilities of fabricating stretchable electronic devices for relevant applications in implantable sensors, energy harvesting, and soft skin for robotics.

5.1 References

[1] Y. S. Ko, F. A. Nüesch, D. M. Opris, *Journal of Materials Chemistry C* **2017**, 5, 1826.

[2] K. Mizuta, S. Fukutomi, K. Yamabuki, K. Onimura, T. Oishi, *Polymer Journal* **2010**, 42, 534.

[3] M. Kanao, A. Otake, K. Tsuchiya, K. Ogino, *International Journal of Organic Chemistry* **2012**, Vol.02 No.01, 4.

[4] C. Slugovc, *Macromolecular Rapid Communications* **2004**, 25, 1283.

[5] Alexey Lyapkov, Stanislav Kiselev, Galina Bozhenkova, Olga Kukurina, Mekhman Yusubov, F. Verpoort, *IntechOpen* **2017**, DOI: 10.5772/intechopen.71085.

[6] M. G. Hyatt, D. J. Walsh, R. L. Lord, J. G. Andino Martinez, D. Guironnet, *Journal of the American Chemical Society* **2019**, 141, 17918.

[7] Z. Ounaies, J. A. Young, J. S. Harrison, in *Field Responsive Polymers*, Vol. 726, American Chemical Society **1999**, Ch. 6, p. 88.

[8] G. M. Sessler, *Journal of Electrostatics* **2001**, 51-52, 137.

Curriculum Vitae

Name	|	Francis Owusu
Date of Birth	|	26th May 1987
Nationality	|	Ghanaian
E-mail	|	ofadroit@yahoo.com
URLs	|	orcid.org/0000-0001-8419-1032
		linkedin.com/in/francis-owusu

EDUCATION

Doctoral Thesis	École polytechnique fédérale de Lausanne (EPFL)
Since 03/2019	Lausanne, Switzerland
MSc Materials Chemistry	Chalmers University of Technology (CTH)
08/2016 – 10/2018	Göteborg, Sweden
BSc Chemistry	Kwame Nkrumah University of Science and Technology (KNUST)
08/2006 – 06/2010	Kumasi, Ghana

WORK HISTORY

Research Scientist	Swiss Federal Laboratories for Materials Science and Technology (EMPA), *Laboratory for Functional Polymers*
Since 03/2019	Dübendorf, Switzerland
Research Assistant	Chalmers University of Technology, Applied Chemistry, *Wang's research group*
10/2018 – 01/2019	Göteborg, Sweden
Quality Officer	Ernest Chemist Limited, *Quality Control and Quality Assurance Department*
09/2011 – 08/2016	Tema, Ghana

AWARDS AND SCHOLARSHIPS

2021 First Runner-up Poster Presentation Award, Advanced Materials and Surfaces Department Day, Empa, Dübendorf (Switzerland)

2016 Swedish Institute Scholarship for Master's Programme (2016 – 2018)

PUBLICATIONS

2022 **Owusu, F.**, Nüesch, F. A. & Opris, D. M. Stretchable High Response Piezoelectric Elastomers Based on Polable Polynorbornene Fillers in a Polydimethylsiloxane Matrix. *Advanced Functional Materials* **32**, 2207083 (2022). https://doi.org:https://doi.org/10.1002/adfm.202207083

2022 **Owusu, F.**, Tress, M., Nüesch, F. A., Lehner, S. & Opris, D. M. Synthesis of polar polynorbornenes with high dielectric relaxation strength as candidate materials for dielectric applications. *Materials Advances* **3**, 998-1006 (2022). https://doi.org:10.1039/D1MA00704A

2022 Sosa, M. D., Levy, I. K., **Owusu, F.**, Nüesch, F., Opris, D., Negri, R. M., & Saleh Medina, L. M. Stress effects on the impedance and ferroelectricity of PVDF- BiFeO3-MWCNT films using xanthan gum as dispersant. *Materials Chemistry and Physics* **286**, 126175 (2022). https://doi.org:https://doi.org/10.1016/j.matchemphys.2022.126175

2022 Levy, I. K., **Owusu, F.**, Geiger, T., Clemmens, F., Nüesch, F., Opris, D. M., & Negri, R. M. Dielectric properties of 3-3 flexible composites by infiltration of elastomers into porous ceramic structures using cellulose scaffold. *European Polymer Journal* **180**, 111616 (2022). https://doi.org:https://doi.org/10.1016/j.eurpolymj.2022.111616

2022 Sheima, Y., von Szczepanski, J., Danner, P., **Owusu, F.**, Iacob, M., Perju, E., Nüesch, F., & Opris, D. High dielectric permittivity elastomers: synthesis, processability, and device manufacturing. *Electroactive Polymer Actuators and Devices* Vol. PC12042 SS (SPIE, 2022). https://doi.org/10.1117/12.2610572

2019 Wiberg, C., **Owusu, F.**, Wang, E. & Ahlberg, E. Electrochemical Evaluation of a Napthalene Diimide Derivative for Potential Application in Aqueous Organic Redox Flow Batteries. *Energy Technol.* **7**, 1900843 (2019). https://doi.org:https://doi.org/10.1002/ente.201900843